

Strategies towards Realization of High Performance Solar-blind Photodetectors based on Gallium Oxide Thin Films

Doctoral Thesis

by

Damanpreet Kaur

(2018PHZ0010)



DEPARTMENT OF PHYSICS

INDIAN INSTITUTE OF TECHNOLOGY ROPAR

April 2024

Strategies towards Realization of High Performance Solar-blind Photodetectors based on Gallium Oxide Thin Films

A Thesis Submitted

In Partial Fulfilment of the Requirements for the Degree of

DOCTOR OF PHILOSOPHY

by

Damanpreet Kaur

(2018PHZ0010)



DEPARTMENT OF PHYSICS

INDIAN INSTITUTE OF TECHNOLOGY ROPAR

April 2024

Damanpreet Kaur: *Strategies towards Realization of High Performance Solar-blind Photodetectors based on Gallium Oxide Thin Films*

Copyright © 2024, Indian Institute of Technology Ropar

All Rights Reserved

DEDICATED

TO

MY PARENTS

(Sdn. Gurmeet Kaur & S. Jaspal Singh Maanipur)

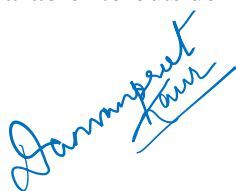
&

MY SIBLINGS

(Kamalpreet & Harpreet)

Declaration of Originality

I hereby declare that the work which is being presented in the thesis entitled “**Strategies towards Realization of High Performance Solar-blind Photodetectors based on Gallium Oxide Thin Films**” has been solely authored by me. It presents the result of my own independent investigation/research conducted during the time period from January 2019 to April 2024 under the supervision of Dr. Mukesh Kumar, Associate Professor, and Indian Institute of Technology Ropar. To the best of my knowledge, it is an original work, both in terms of research content and narrative, and has not been submitted or accepted elsewhere, in part or in full, for the award of any degree, diploma, fellowship, associateship, or similar title of any university or institution. Further, due credit has been attributed to the relevant state-of-the-art and collaborations (if any) with appropriate citations and acknowledgments, in line with established ethical norms and practices. I also declare that any idea/data/fact/source stated in my thesis has not been fabricated/ falsified/ misrepresented. All the principles of academic honesty and integrity have been followed. I fully understand that if the thesis is found to be unoriginal, fabricated, or plagiarized, the Institute reserves the right to withdraw the thesis from its archive and revoke the associated Degree conferred. Additionally, the Institute also reserves the right to appraise all concerned sections of society of the matter for their information and necessary action (if any). If accepted, I hereby consent for my thesis to be available online in the Institute’s Open Access repository, inter-library loan, and the title & abstract to be made available to outside organizations.



Signature:

Name: Damanpreet Kaur

Entry Number: 2018PHZ0010

Department: Physics

Indian Institute of Technology Ropar

Rupnagar, Punjab 140001

Date: April 7, 2024

Certificate

This is to certify that the thesis entitled “**Strategies towards Realization of High Performance Solar-blind Photodetectors based on Gallium Oxide Thin Films**” submitted by Damanpreet Kaur (2018PHZ0010) for the award of the degree of Doctor of Philosophy of Indian Institute of Technology Ropar, is a record of bonafide research work carried out under my guidance and supervision. To the best of my knowledge and belief, the work presented in this thesis is original and has not been submitted, either in part or full, for the award of any other degree, diploma, fellowship, associateship or similar title of any university or institution. In my opinion, the thesis has reached the standard of fulfilling the requirements of the regulations relating to the Degree.



Signature:

Name: Dr. Mukesh Kumar

Department: Physics

Indian Institute of Technology Ropar

Rupnagar, Punjab 140001

Date: April 7, 2024

Acknowledgments

Behind every triumphant venture is a team of people who are responsible for its success. Thus, before beginning the thesis, I would like to thank the people who have contributed immensely to its completion. Any inadvertent omission on my part in this acknowledgment is deeply regretted.

I would like to express my heartfelt gratitude to my thesis supervisor, Dr. Mukesh Kumar, whose unwavering support, guidance and motivation played a pivotal role. His undeterred faith and constant belief in me helped me in pushing my boundaries. His mentoring skills, professionalism and discipline are some of the virtues which I would like to imbibe in the future. I don't think that I can ever thank him enough for everything, big or small, which has led to the fruition of this work. Thank you Sir from the bottom of my heart. I would also like to thank my doctoral committee members (Dr. Asoka Biswas, Prof. Rajendra Srivastava, Dr. Sandeep Gautam and Dr. Rajesh V. Nair) for their timely guidance and suggestions, which proved very useful towards the realization of this thesis.

I am also thankful to my collaborators, both at IIT Ropar and outside, at IIT Bhilai, IIT Delhi, NPL Delhi, IUAC New Delhi, Binghamton University (USA), Syracuse University (USA), Russian Academy of Sciences, Tomsk State University (Russia), without whom I could not have achieved any of this. I am also thankful to the CRF facility and Department of Physics, IIT Ropar for providing the characterization facilities and resources required for carrying out the research work. A special thanks to FREM lab (all the past and present members) for their immense contribution towards this thesis. I have learnt a lot from all of you.

I think it would be very unfair if I did not acknowledge people who have contributed behind the scenes immensely. My first and foremost thanks to my parents and siblings, for always believing in me and encouraging me to do my best. The support and love that I have received from my family has been the backbone to all my achievements in life and they remain a constant source of inspiration for me. I love you with all my heart and soul. In addition, I would like to thank my nephew, Sehaj, who with all his antics and frolics made sure of amusing me throughout my PhD journey. A special thank you to Dr. Gurpreet, Arjun and Gurjot for being a part of this journey. As for my family at IIT Ropar, I am indebted to my friends – Rakhi, Sanjay and Raghvendra. Thank you for being there for all my ups and downs during the past five years, both personally and professionally. Our lunches, snacks and dinners together have

been sort of “therapy sessions” which were much needed after hard and tiring days. Rakhi, especially, has always been like a sister to me and I cannot fathom my PhD life without her. It has been great spending time with you all and hope that this continues for life. I am also indebted to my lab family – the “core of the core” group – Riya, Rohit, Vinit, Badri and Priya. Having seen tumultuous times together, I think my bond with Riya and Rohit, grew quite strong. The late-night lab sessions and the sometimes long-working hours became more bearable and enjoyable with you. Vinit and Badri are like two little kids who make everything more joyful. I will always remember the leg-pulling and teasing sessions with all of them which made my day brighter and the lab atmosphere more enjoyable.

Last but not the least, I am most thankful to God for everything that he has bestowed upon me. Waheguru ji has been very gracious and generous with me (sometimes too generous, I would say!), providing me opportunities as well as means to achieve so much in life. Thank you for all that you have given me and blessing me with much more than I deserve.

Lay Summary

This thesis aims to develop high performance photodetectors which can sense only the UV-C light based on a next-generation semiconductor material – gallium oxide. These devices find use in flame detection, non-line-of-sight communication, ozone hole monitoring etc. where conventional semiconductor devices show less reliability and are more expensive. Now, the photodetectors based on gallium oxide are still far from commercialization due to their sub-par performance. This thesis aims to achieve high performance (in terms of detecting weak signals at faster speeds) by employing different strategies. A simple thin-film photodetector consists of a substrate, active layer (which absorbs the light) and contacts or electrodes. The present work aims to address all these three components and refine them for achieving high performance. Each component, stand-alone or in synergy with others, is optimized to maximize the photodetection capabilities. As one of the main achievements of this work, we have been able to fabricate devices which work in the sub-millisecond regime while employing only ~ 3nm of active layer, thereby improving the performance manifold. Also, since the film itself has high chemical and thermal stability, it may be used for high temperatures operations but under such extreme environments, the contacts usually fail. Therefore, we have also studied the temperature resilience of the devices under high temperatures and under high energy radiation as well, to mimic the actual working conditions of a harsh environment.

Abstract

The UV-C (< 280 nm of wavelength) part of the solar spectrum is highly dangerous to living organisms, with exposure often causing changes in their genetic make-up. Thankfully, the ozone layer in the atmosphere absorbs almost all of this radiation, thereby providing us with natural protection. The complete absorption leads to a very low background signal of UV-C on earth. This unique characteristic can be exploited in the fabrication of highly sensitive photodetectors which are responsive to UV-C only from other sources on earth, leading to the development of the so-called solar-blind photodetectors (SBPD). Therefore, SBPDs have applications ranging from civil to medical uses which includes ozone-hole monitoring, flame detection, space exploration, UV sterilization systems, non-line-of-sight communications and hydrogen flame detection. Gallium oxide is a new, ultra-wide Band Gap (UWBG) material with properties that are promising for its use as a functional material in the fabrication of SBPDs. It has an apt band gap of 4.6-5.3 eV (depending on the polymorph) making it intrinsically solar-blind. Moreover, it is highly chemically and thermally stable (m.p. $\sim 1730^{\circ}\text{C}$), has a high breakdown voltage and is extremely radiation hardened and hence it can be employed for use in extreme environment applications (high temperature and high radiation conditions). For photodetection, however, the trade-off between two key parameters viz. responsivity and response time has become one of the main bottlenecks in achieving high performance. Herein, we aim to develop high performance gallium oxide based SBPDs and study its use in extreme environment applications.

The thesis begins by optimizing the active layer of gallium oxide. First, polycrystalline thin films are optimized on different orientations of Si substrate and the strain induced differences in photodetector performance were studied. Polycrystalline films were also optimized on the sapphire *c*-plane sapphire substrate which has a lower lattice mismatch ($\sim 6.6\%$) with Ga_2O_3 by depositing varying thicknesses via RF magnetron and it was found that thicker films have a lower number of oxygen vacancies and a better stoichiometric ratio and hence can be utilized for fabricating better and faster optoelectronic devices. We have also found room temperature crystallinity in Ga_2O_3 by using a facile fabrication with conventional sputtering technique. The subsequently grown photodetectors show an ultra-high photo-to-dark current ratio of over 10^5 at a moderate bias of 10 V bias under 254 nm illumination.

In the second part of the thesis, the speed of the amorphous Ga_2O_3 photodetectors were enhanced by using surface modification. First, we have modified the surface of a 300 nm amorphous Ga_2O_3 film by nanopatterning it using 500 eV Ar^+ ion beam sputtering. The defects

introduced in the system act as recombination centers for the charge carriers bringing about a reduction in the decay time of the devices, even at zero-bias. Second, instead of modifying the active layer, we have modified the surface of the substrate used underneath and conformally coated an ultra-thin amorphous Ga_2O_3 on top. Ion-beam sputtering (500eV Ar^+) is utilized to nanopattern SiO_2 coated Si substrate leaving the topmost part rich in elemental Si, which enhances the carrier conduction by increasing n -type doping of the subsequently coated Ga_2O_3 films. The metal-semiconductor-metal (MSM) photoconductor devices fabricated on doped, rippled films show superior properties with responsivity increasing from 6 mAW^{-1} to 433 mAW^{-1} while having fast detection speeds of $861 \mu\text{s}/710 \mu\text{s}$ (rise/fall time).

The third part of the present thesis focusses on utilizing heterostructures for improving the performance. The amalgamation of two different materials is highly dependent on the interface between the two materials. The end result of how two different materials will integrate is highly dependent on their interface chemistry. This is shown by interfacing amorphous Ga_2O_3 with two different sulfide materials – CdS and PtS. For the CdS- Ga_2O_3 heterostructure, the resultant devices remain solar-blind and outperform the singular bare photodetectors. For the PtS- Ga_2O_3 heterostructure, even though the band alignment still remains type I, the resultant devices show a broadband photoresponse instead of the solar-blind nature. Thus, this shows that the interfacing of two materials for enhanced photodetection requires a thorough and complete understanding of the interfacial dynamics and charge transfer from one material to another and therefore, warrants careful consideration of optimization parameters before implementation.

In the last part of the thesis, we try to look at the impact of extreme environments such as high temperatures and swift heavy ion radiation on the fabricated photodetectors, since the active layer itself is extremely resilient to extreme temperatures and high radiation doses. In the first part, we study the origin of the near-failure of conventional Au contacts to $\beta\text{-Ga}_2\text{O}_3$ at high temperatures using interfacial studies. Next, an unconventional transparent conducting oxide contact of indium zinc oxide (IZO) to $\beta\text{-Ga}_2\text{O}_3$ is studied under high temperatures. The devices show a unique conversion from Schottky to Ohmic by annealing at an optimized temperature of 650°C , while changing back to Schottky at higher temperatures. Finally, the radiation hardness of gallium oxide is checked against swift heavy ions Ag^{7+} of 100 MeV and the device performance judged under control and irradiated conditions.

Table of Contents

Acknowledgments	ix
Lay Summary	xi
Abstract	xiii
List of symbols, and abbreviations	xix
List of Figures	xxi
List of Tables.....	xxvii
Chapter 1: Introduction.....	1
1.1 Background.....	1
1.2 Basics of Photodetector.....	3
1.3 Gallium oxide – Material properties and design	7
1.4 Open challenges in the field of Ga ₂ O ₃	10
1.4.1 <i>p</i> -type doping	10
1.4.2 Poor thermal conductivity.....	12
1.4.3 Trade-off between responsivity and response time	13
1.4.4 Application-based challenges.....	13
1.5 Current scenario in the field of Ga ₂ O ₃ based SBPDs.....	14
1.6 Basic device architecture.....	14
1.7 Objectives of the thesis	15
1.8 Outline of the thesis.....	15
References.....	18
Chapter 2: Fabrication and characterization techniques	21
2.1 Magnetron sputtering	21
2.2 Characterization techniques	22
2.2.1 Crystal structure characterizations	22
2.2.2 Morphological characterizations	23
2.2.3 Optical characterizations	23
2.2.4 Chemical composition analysis and band alignment studies	24
2.3 Device fabrication and characterization	24
2.3.1 Contacts for devices.....	24
2.3.2 Photodetector device characterization.....	25
References.....	27
Chapter 3: Dependence of performance on the growth of active layer.....	29
3.1 Strain induced performance difference	29
3.1.1 Experimental section	31
3.1.2 Results and Discussion	32

3.1.3 Conclusions	42
3.2 Optimizing thickness of β -Ga ₂ O ₃ film on sapphire substrates.....	42
3.2.1 Experimental section	43
3.2.2 Results and Discussion	43
3.2.3 Conclusions	47
3.3 Room temperature crystallinity	48
3.3.1 Experimental details	48
3.3.2 Results and discussion.....	48
3.3.3 Conclusions	51
References.....	52
Chapter 4: Enhancing performance using surface modification	55
4.1 Nanopatterning the active layer	55
4.1.1 Experimental details	56
4.1.2 Results and discussion.....	57
4.1.3 Conclusions	62
4.2 Nanopatterning the substrate below.....	63
4.2.1 Experimental details	64
4.2.2 Results and discussion.....	64
4.2.3 Conclusions	75
References.....	77
Chapter 5: Interface engineering via heterostructures of gallium oxide	81
5.1 CdS – amorphous Ga ₂ O ₃ heterointerface	81
5.1.1 Experimental details	82
5.1.2 Results and discussion.....	82
5.1.3 Conclusions	92
5.2 PtS – amorphous Ga ₂ O ₃	92
5.2.1 Experimental details	93
5.2.2 Results and discussion.....	93
5.2.3 Conclusion	99
References.....	100
Chapter 6: Photodetectors under extreme environments.....	103
6.1 Au contacts under high temperatures.....	103
6.1.1 Experimental details	104
6.1.2 Results and discussion.....	104
6.1.3 Conclusions	110
6.2 Indium Zinc Oxide (IZO) contact under high temperatures	110
6.2.1 Experimental details	111

6.2.2 Results and discussion.....	111
6.2.3 Conclusions.....	116
6.3 Radiation hardness under swift heavy ions	117
6.3.1 Experimental details.....	118
6.3.2 Results and discussion.....	119
6.3.3 Conclusions.....	126
References.....	127
Chapter 7: Summary and Scope for Future Studies.....	131
7.1 Summary	131
7.1.1 Dependence of performance on the growth of active layer	131
7.1.2 Enhancing performance using surface modification.....	132
7.1.3 Interface engineering via heterostructures of gallium oxide.....	132
7.1.4 Photodetectors under extreme environments	133
7.2 Scope for future studies.....	134
List of Publications	135
Conferences/Workshops Attended.....	137
Curriculum Vitae.....	139

List of symbols, and abbreviations

Symbol/ abbreviations	Description
2D	Two-dimensional
TMDs	Transition metal dichalcogenides
S	Sulfur
Ga ₂ O ₃	Gallium oxide
Pt	Platinum
Au	Gold
Ag	Silver
In	Indium
JCPDS	Joint Committee of Power Diffraction Standards
VBM	Valence band maximum
CBM	Conduction band minimum
SEM	Scanning electron microscope
EDX	Energy dispersive X-ray spectroscopy
XPS	X-ray photoelectron spectroscopy
AFM	Atomic force microscopy
KPFM	Kelvin probe force microscopy
PL	Photoluminescence
GIXRD	Grazing incidence X-ray diffraction
PVD	Physical vapor deposition
SP	Surface potential
V _{CPD}	Contact potential difference
ϕ_B	Schottky barrier height
ϕ	Work function
CBO	Conduction band offset
VBO	Valence band offset
E_g	Bandgap
E_F	Fermi Energy
FWHM	Full width half maxima
Ar	Argon
O ₂	Oxygen
q	Electronic charge
RT	Room temperature
UV	Ultraviolet
Vis	Visible
NIR	Near-infrared

nm	Nanometer
k	Boltzmann constant
T	Temperature
FFT	Fast Fourier Transform
I_{ph}	Illumination current (Current under light conditions)
I_{dark}	Dark current
PDCR	Photo-to-dark current ratio
$P_{optical}$	Incident optical power
A	Active area
A*	Richardson constant
R	Responsivity
D*	Specific detectivity
EQE	External quantum efficiency
h	Planck constant
T _r	Rise time
T _f	Fall time
DC	Direct current
RF	Radio frequency
A	Absorbance
α	Absorption coefficient
IBS	Ion beam sputtering
SHI	Swift heavy ions
MSM	Metal-semiconductor-metal
REELS	Reflection electron energy loss spectroscopy

List of Figures

Figure 1.1 Schematic representing the complete absorption of UV-C by the ozone layer along with the potential uses of SBPDs.	2
Figure 1.2 The five different polymorphs of gallium oxide along with their crystal structures and their space groups.	7
Figure 1.3 The unique properties of gallium oxide which makes it a promising candidate for SBPDs.	8
Figure 1.4. Various morphologies of Ga_2O_3 on which SBPDs have been fabricated	9
Figure 1.5 Band structure of $\beta\text{-Ga}_2\text{O}_3$. The k points are $\Gamma=(000)$, $A=(0,0,1/2)$, $Z=(1/2,1/2,0)$, $M=(1/2,1/2,1/2)$, $L=(0,1/2,1/2)$ and $V=(0,1/2,0)$	10
Figure 1.6 Schematic showing the different device geometries which have been utilized for the fabrication of gallium oxide based SBPDs.	12
Figure 1.7 Performance comparison of the current scenario in (a) gallium oxide based and (b) gallium oxide heterostructures based photodetectors	14
Figure 1.8 Basic device architecture showing the three integral components.	15
Figure 2.1 (a) Schematic illustration of the sputtering system (b) RF magnetron sputtering equipment used for growing Ga_2O_3 thin films.	22
Figure 2.2 Physical shadow mask used for electrode deposition in the (a) interdigitated geometry and (b) strip geometry. (c) Thermal evaporator system used for depositing metal contacts (d) Testing equipment used to characterize the photodetector devices along with the probe station equipped with UV-C lamp used shown in the inset.	25
Figure 2.3 Experimental set-up for the testing equipment used to characterize fast photodetection.	26
Figure 3.1 (a) Schematic of the growth of gallium oxide on Si substrates and of the temperature profile followed for the depositions of (b) (100), (110) and (111) and (c) HSL (111).	32
Figure 3.2. Atomic arrangement of atoms in the Si crystal structure for the (a) Si (100) plane, (b) Si (110) plane, (c) Si (111) plane and (d) crystal structure of $\beta\text{-Ga}_2\text{O}_3$ in the (-401) plane. Produced using VESTA software.	32
Figure 3.3 AFM micrographs of $\beta\text{-Ga}_2\text{O}_3$ thin films grown on Si (100), (110) and (111), respectively.	33
Figure 3.4 AFM micrographs with the watershed mask determined in Gwyddion software along with the grain size distribution calculated from the above watershed mask for $\beta\text{-Ga}_2\text{O}_3$ grown on (a,d) Si (100), (b,e) Si (110) and (c,f) Si (111).	34
Figure 3.5. (a-b) GIXRD data of the three samples showing the formation of $\beta\text{-Ga}_2\text{O}_3$ on all three orientations of Si. The zoomed-in view of the dominant peaks are fitted using a Voigt function and shows the least FWHM (and hence strain) for (111). (c-e) W-H plots of the three samples with the linear fit showing the crystallite size and strain in the three films.	35
Figure 3.6 Device performance of the PDs fabricated on Si (100), (110) and (111). (a) Comparative dark current of the three devices, (b) Log I vs. V of the devices showing the maximum photoresponse of (111) to 254 nm incident light, (c) Responsivity vs. wavelength of	

the devices showing excellent solar blindness and (d) temporal response of the devices to repeated switching of incident light. Single cycle photoresponse of the devices of Ga₂O₃ on (e) Si (100), (f) Si (110) and (g) Si (111) to 254 nm incident light with their respective rise and fall times. 37

Figure 3.7 Comparison of the crystallite size and strain with the device performance of the polycrystalline Ga₂O₃ based solar-blind photodetectors. 39

Figure 3.8 (a) GIXRD data of with and without seed layer samples of β -Ga₂O₃ on Si (111). The zoomed-in view of the dominant peaks shows a reduced FWHM (and hence reduced strain) upon introduction of a seed layer and (b) W-H plot of HSL (111) sample showing reduced strain and increased crystallite size. 40

Figure 3.9 AFM micrographs of (a) with and (b) without seed layer samples of β -Ga₂O₃ on Si (111), (c) watershed mask used for calculating the grain size distribution which is shown in (d). 40

Figure 3.10 Device performance comparison of with and without seed layer in β -Ga₂O₃ on Si (111). (a) Responsivity vs. wavelength showing enhanced performance, (b) improved response times and (c) improved photoresponse. 41

Figure 3.11 Device performance showing excellent stability even after 2100 hours using an optical chopper and oscilloscope. The T_r and T_d represents the rise time and the fall time of the devices, respectively. The x-axis and the y-axis represent different scales for all the four datasets. The data is recorded at 5 V bias under 254 nm UV-C light. 41

Figure 3.12 (a) GIXRD data of the films of varying thickness showing the formation of β -Ga₂O₃ on *c*-plane sapphire. (b) Transmittance data recorded using UV-Vis spectrophotometer and (c) band gap calculations using Tauc plot for varying film thickness. 43

Figure 3.13. AFM micrographs showing the morphology for (a) 5nm, (b) 20 nm, (c) 50 nm, (d) 100 nm and (e) 300 nm. (f) variation of the calculated RMS roughness for the varying thickness of β -Ga₂O₃ thin films. 44

Figure 3.14 (a) Device Schematic. I-V curves under dark and light conditions (254 nm, 365 nm, 532 nm, 650 nm incident light) for devices fabricated on (b) 5nm, (c) 20 nm, (d) 50 nm, (e) 100 nm and (f) 300 nm thick films of β -Ga₂O₃. 45

Figure 3.15 (a) Temporal photoresponse of the devices with calculated rise and fall time. Reduction in the PPC effect can be clearly seen with increasing β -Ga₂O₃ film thickness. XPS core level spectra for the (b) Ga 3d and (c) O 1s peaks for the varying film thickness of β -Ga₂O₃. 46

Figure 3.16 (a) Correlation of the photo-to-dark current ratio (PDCR), ratio of O(II)/(O(I) + O(II)) (depicting the oxygen-related defects) and Ga³⁺/Ga⁺ for the varying film thicknesses and (b) schematic representing the trapping of charge carriers leading to a delayed recombination which is responsible for the observed PPC effect. 47

Figure 3.17 (a) XRD spectra for the thin films grown on *c*-plane sapphire at room temperature but different RF powers and deposition pressure. (b) TEM image of the RT-150W sample with the inset showing the SAED pattern. (c) HRTEM image with insets showing the corresponding FFT analysis of Ga₂O₃ and sapphire substrate. The zoomed-in image shows a mapping of the bi-phase polycrystalline films. 49

Figure 3.18 (a) AFM micrograph image showing the morphology of RT-150 W. (b) Absorbance spectra with the inset showing the Tauc plot for band gap calculation. XPS core

level spectra of (c) Ga 3d and (d) O 1s. (e) VBM calculation using the valence band spectra. 50

Figure 3.19 For the RT-150W photodetector device, (a) I-V graphs under dark and illuminated conditions. (b) responsivity versus wavelength graph showing the solar-blind nature (c) temporal response of the device to repeated switching of 254 nm incident light. 51

Amorphous Ga_2O_3 thin films (approx. 300 nm thickness) were deposited on SiO_2 coated Si substrate by RF Magnetron Sputtering using a Gallium oxide target (99.99% purity, supplied by K. J. Lesker). 56

Prior to deposition, the substrates were cleaned ultrasonically in soap solution, de-ionized water, acetone and propanol for 30 minutes each and finally dried with N_2 gun. After achieving a base vacuum of 8×10^{-7} Torr, deposition was done at room temperature with 100 W RF power and 3 mTorr working pressure using Ar gas. The films were then nanopatterned using a broad ion beam inside a vacuum chamber housing a Kaufman ion source and irradiated at room temperature with 500 eV Ar^+ ions at an incident angle of 67° with respect to the surface normal for 15 minutes. The experimental set-up for the irradiation process can be found in a previously reported study.[14] An unirradiated sample was kept as a control for the measurements. Subsequently, photodetectors were fabricated on the control and irradiated samples (henceforth named “bare” and “rippled”) by forming Cr/Au strip electrodes (with an interspacing of 3.5 mm in between) via a physical shadow mask using a thermal evaporator (see Figure 4.1). The diffuse reflectance spectra were recorded using an UV–Vis spectrophotometer (Perkin Elmer, Lambda 950), and the bandgap was calculated by using the Kubelka-Munk function. 56

Figure 4.1 (a) Schematic depicting atomic level changes during ion-matter interaction. (b) Schematic for the growth of amorphous gallium oxide thin film with subsequent nanopatterning by broad Ar^+ ion beam sputtering (IBS). The photodetectors were fabricated to evaluate the effect of nanopatterning on device performance. 57

Figure 4.2 (a,b) AFM scans ($1\mu\text{m} \times 1\mu\text{m}$) of amorphous Ga_2O_3 thin film (bare) and irradiated thin film (rippled), respectively, showing the formation of nanopatterns using IBS. The top-right insets represent the corresponding 3-D mapping while the bottom-left insets depict the FFT of the corresponding AFM images. The black arrow indicates the direction of the incident ion beam. (c) log-log plot of power spectral density (PSD) versus the spectral frequency q as extracted from the AFM data. (d) The diffuse reflectance spectra of the thin films on SiO_2/Si substrate. The estimated band gap of (e) bare and (f) rippled gallium oxide thin films. 58

Figure 4.3. (a) Photoluminescence spectra and (b) time-resolved PL of amorphous Ga_2O_3 films before and after IBS. 60

Figure 4.4 (a) Schematic of “perpendicular” and “parallel” oriented device structures of rippled surfaces of amorphous Ga_2O_3 (b) I-V characteristics. Responsivity versus wavelength of the fabricated solar-blind photodetectors at (c) 0 V bias and (d) 5 V bias. 61

Figure 4.5. (a) Temporal response at zero-bias (b) single-cycle for the temporal response at zero-bias (c) decay edges showing the fall time at zero-bias (d) decay edges showing the fall time at 5 V bias for the fabricated SBPDs under 254 nm illumination. 62

Figure 4.6 (a) Schematic showing the fabrication of nanoripples and the consequent majority carrier MSM photoconductor devices. $3\mu\text{m} \times 3\mu\text{m}$ AFM micrographs for the irradiation times of (b) 0 min (or bare substrate), (c) 5 min, (d) 10 min and (e) 15 min. Bottom-left insets of the respective micrographs shows the FFT images showing the periodicity of the nanoripples while the top-right insets show the magnified images of the nanoripples. Black arrow depicts the direction of the incident ion beam. (f) Log-log plot of power spectral density versus spatial

frequency q as extracted from AFM data. (g) Variation of RMS roughness with increasing ion beam sputtering times. 66

Figure 4.7 (a) $1\mu\text{m} \times 1\mu\text{m}$ AFM micrographs for the varying irradiation times without and with Ga_2O_3 coating showing the conformality of the films. Below the micrographs are the respective line scans showing that the Ga_2O_3 films get conformally-coated (for 5-15min) since the nature of the ripples remain same before and after Ga_2O_3 deposition. (b) EDX mapping of the 5 min rippled substrates with Ga_2O_3 showing the uniformity of the films. 67

Figure 4.8. (a) XPS core level spectra of Ga 3p and Si 2p for the non-rippled and rippled 5 minute with Ga_2O_3 samples showing the additional peak of elemental silicon in the latter (b) XPS core level spectra of Ga 3p and Si 2p for rippled 10 and 15 minute with Ga_2O_3 samples (c) Valence band maxima of the various samples showing increasing n -type doping. 68

Figure 4.10. (a) Dark current and light current (under 254 nm illumination) of the devices of rippled substrates with Ga_2O_3 along with a zoomed-in image. (b) Responsivity versus wavelength of the bare and rippled devices with Ga_2O_3 . The erosion of the SiO_2 layer exposes the underlying Si substrate leading to a response in the visible spectrum for the 15 min rippled devices. (c) Temporal response of the non-rippled and rippled devices to repeated switching of the incident 254 nm wavelength of light. (d) XPS core level spectra of O1s of the non-rippled and rippled samples with Ga_2O_3 and its deconvolution into three peaks corresponding to oxygen bonded to Ga, Si and the oxygen vacancies. (e) Temporal response of the devices after prolonged storage in air ambient showing high stability and robustness of the fabricated device. 72

Figure 4.11. (a) Experimental reflectance data showing the difference in reflectance for non-rippled and 5 min rippled samples with Ga_2O_3 and (b) its simulated reflectance data. (c) Experimental reflectance spectra of non-rippled SiO_2 coated Si substrate with and without Ga_2O_3 . (d) Simulated reflectance spectra of non-rippled SiO_2 coated Si substrate with and without Ga_2O_3 . (e) Experimental reflectance spectra of rippled 5 min SiO_2 coated Si substrate with and without Ga_2O_3 . (f) Simulated reflectance spectra of rippled 5 min SiO_2 coated Si substrate with and without Ga_2O_3 . (g) Model used for carrying out FDTD calculations and (h) side-view of the model used for simulations showing the rippled substrate and conformally-coated Ga_2O_3 73

Figure 4.12 Simulated reflectance spectra using FDTD simulations for (a) non-rippled SiO_2/Si (~ 280 nm thick) and (b-h) rippled SiO_2/Si for varying thicknesses of SiO_2 from 280 nm to 95 nm. (i) FESEM image of rippled 5nm with Ga_2O_3 showing the reduction in thickness after irradiation. 74

Figure 5.1 (a) Schematic of the device structure showing the pristine and annealed interface. (b) Temporal response of the bare Ga_2O_3 , bare CdS and Ga_2O_3 -CdS heterostructure based solar-blind photodetectors under 254 nm illumination and 5 V bias. 83

Figure 5.2. (a) Cross-sectional image of the thin film structure. Optical images of (b) pristine and (c) annealed interface. Atomic concentration of the (d) pristine and (e) annealed interfaces as determined by XPS depth profiling. (f) I-V graph under dark conditions and (g) log I vs. V plot under dark and 254 nm illumination for the pristine and annealed interface based devices. 84

Figure 5.3. (a) PDCR for different applied voltages for the pristine and annealed interface. Inset shows the responsivity vs. wavelength plot at 5 V bias and (b) temporal response under 254 nm illumination with the rise and fall times for the pristine and annealed interface based devices. 85

Figure 5.5. XPS core level spectra and valence band maxima calculation at the bulk and interface for (a) pristine and (b) annealed interfaces. (c) Band alignment diagrams for the pristine and annealed interfaces found using the binding energy measurements carried out via XPS and VBS spectra (d) Band alignments along with the obtained band bending.	88
Figure 5.7. Surface potential maps in dark of (a) CdS and (b) Ga ₂ O ₃ - CdS pristine interface along with the corresponding (c) surface potential distribution. Surface potential maps in dark of (d) CdS and (e) Ga ₂ O ₃ - CdS annealed interface along with the corresponding (f) surface potential distribution. (g) Surface potential distribution under dark conditions of the Ga ₂ O ₃ - CdS pristine and annealed interface.	90
Figure 5.8. Surface potential distribution of the bare CdS (a) pristine and (b) annealed interface showing almost negligible change under dark and light conditions. Surface potential maps under illumination of (c) CdS and (d) Ga ₂ O ₃ - CdS pristine interface along with the corresponding (e) surface potential distribution. Surface potential maps under illumination of (f) CdS and (g) Ga ₂ O ₃ - CdS annealed interface along with the corresponding (h) surface potential distribution.	91
Figure 5.9. (a) Schematic showing the growth of PtS and PtS-Ga ₂ O ₃ thin films and photodetectors thereof. (b) Optical image of the actual thin film heterostructure. (c) Raman spectra showing the B _{1g} peak proving the formation of PtS. (d) AFM micrographs showing the surface morphology of PtS and PtS-Ga ₂ O ₃ films along with the height profiles to measure the thickness of Ga ₂ O ₃ film.	94
Figure 5.10. Core-level spectra of (a) Pt 4f, (b) S 2p, (c) Ga 3d and (d) O 1s for the PtS-Ga ₂ O ₃ heterostructure measured during XPS depth profiling.	95
Figure 5.12 Working principle of heterojunction device under dark and illumination. (b) Experimental set-up for high speed photodetection measurements. (c) Temporal response of the heterojunction device to different wavelengths of incident light using the mentioned set-up. (d) Temporal response of PtS-Ga ₂ O ₃ heterojunction devices to different wavelengths of incident light after 7500 hours of ambient storage.	98
Figure 6.1 (a) Device schematic used for this study. Optical images of the actual devices showing finger electrodes for (b) room temperature as-deposited, (c) 450°C, (d) 650°C and (e) 850°C annealed devices. Atomic concentration profiles as determined by XPS depth profile for (f) room temperature as-deposited, (g) 450°C, (g) 650°C and (i) 850°C annealed devices..	105
Figure 6.2 (a) Dark current of the devices without illumination, (b) I-V curves under dark and light conditions (254 nm), (c) Log I vs. voltage graph showing the relative increment in the photocurrent, (d) photo-to-dark-current ratio for the devices, (e) temporal response of the devices to repeated switching of incident light and (f) time-cycles of the devices showing excellent stability.	106
Figure 6.3 XPS core level spectra of Au 4f for increasing depths for (a) room temperature as-deposited, (b) 450°C, (c) 650°C and (d) 850°C annealed devices.	108
Figure 6.4 XPS core level spectra of Ga 3d for increasing depths for (a) room temperature as-deposited, (b) 450°C, (c) 650°C and (d) 850°C annealed devices	108
Figure 6.5 (a) Variation in the VBM values as a function of depth for the different samples (b) Specific detectivity of the different device and (c) schematic representing the diffusion and alloy formation at the interface.	109
Figure 6.6. (a) Device schematic of the experimental conditions. Here green colour represents Ga ₂ O ₃ while purple colour is indicative of IZO. (b) Dark current of the devices using IZO	

electrodes annealed under different temperatures (c) Photoresponse of the devices to 254 nm incident light (e) temporal response of the devices to repeated switching of incident light. 112

Figure 6.7 (a) Optical images of the devices showing physical damage after annealing. Atomic concentrations of various elements with increasing depth found using XPS depth profile for (b) room temperature (c) 450°C (d) 650°C and (e) 850°C annealed samples. 113

Figure 6.9 (a) Variation in the valence band maxima values for the different samples. Absorbance spectra of (b) Ga₂O₃ and (b) IZO with the insets showing the corresponding band gaps using Tauc plot method. Calculated band alignments for the (d) room temperature (e) 450°C, (f) 650°C and (g) 850°C annealed samples. 116

Figure 6.10 (a) Schematic of the device under testing. (b) Variation in responsivity of the different samples and (c) temporal response of the devices showing resilience under high temperature annealing. 116

Figure 6.11 (a) Schematic for the growth amorphous and polycrystalline gallium oxide thin film and irradiation procedure with swift heavy ion irradiation. The photodetector was fabricated for final performance measurement. (b) GIXRD of control and irradiated amorphous and polycrystalline gallium oxide thin films. FE-SEM images of (c) control a-Ga₂O₃, (d) irradiated a-Ga₂O₃, (e) control pc-Ga₂O₃ and (f) irradiated pc-Ga₂O₃ thin films. 118

Figure 6.12 EDX Spectra of (a) a-Ga₂O₃ control (b) a-Ga₂O₃ irradiated (c) pc-Ga₂O₃ control and (d) pc-Ga₂O₃ irradiated. The absence of silver in any of these shows that all the Ag⁷⁺ ions simply pass through without getting deposited in the samples. (e) Variation of the electronic energy loss (S_e) and nuclear energy loss (S_n) of 100 MeV Ag⁷⁺ ions incident on gallium oxide film as a function of film thickness. The inset shows the almost constant and dominated value of electronic energy loss for entire thickness of gallium oxide deposited on silicon substrate. 120

Figure 6.14 (a,b) Comparison of transient photoresponse and (c,d) fitted single cycle photoresponse of amorphous and polycrystalline based SBPD. 122

Figure 6.16 Comparison of peak responsivity @ 250 nm (at 5 V bias) for (a) amorphous Ga₂O₃ based photodetector and (b) polycrystalline Ga₂O₃ based photodetector, respectively. The responsivity values are reported for control and irradiated samples along with those after annealing. 125

List of Tables

Table 1.1: Comparison of the solar-blind photodetectors based on different materials.	6
Table 4.1: Comparison of the photodetectors in the present work with those reported in literature.....	74

Chapter 1: Introduction

Starting with a brief introduction to solar-blind photodetectors, the chapter aims to give insight into the principle working, advantages and applications of the field. The basics of a simple photodetector along with the pertinent performance parameters is elucidated. Then, the material of interest – Gallium Oxide – is introduced along with its material properties, followed by the open challenges in the field. A brief discussion about the current scenario in the field of Ga_2O_3 based solar-blind photodetectors comprehensively elucidates the research gap and finally, the chapter concludes with the outline of the present thesis.

1.1 Background

Ultraviolet radiation of the solar spectrum is highly dangerous, with impact on all life forms. With wavelength spreading beyond the visible spectrum from 100-400 nm, it is broadly classified into UV-A (320-400 nm), UV-B (280-320 nm) and UV-C (100-280 nm). In particular, UV-C is notoriously dangerous, with exposures often leading to a change in the genetic make-up of living organisms. This fact is exploited in its use for sterilization purposes. Especially with the rise of the recent COVID pandemic, the use of UV sterilizers is rampant and so are the dangers associated with it. The Sun emits the entire range of spectrum, however, thankfully, the ozone layer in the atmosphere absorbs almost all of the UV-C, thus forming a protective shield against its perils. This essentially means that there is almost negligible UV-C signal reaching the earth from sunlight and this fact can be exploited for the development of the so-called Solar-Blind Photodetectors (SBPDs), otherwise known as deep-UV (DUV) photodetectors (Figure 1.1).[1] These photodetectors (PDs) show response to only wavelengths less than 280 nm and give no response when placed in natural sunlight. They can thus detect any other source of UV-C radiation present on earth with extreme sensitivity. Apart from its application in safety systems against the possible leaks in UV sterilizers, SBPDs are also employed in space applications for UV imaging. They can also be employed in ozone-hole monitoring and flame detection. The high scattering of the UV light leads to its potential use in non-line-of-sight (NLOS) communications, thereby generating a demand for highly efficient and sensitive transmitters and receivers.[2] The usage of UV light in curing of polymer composites is also widely known besides its use in medical fields for sterilization and water disinfection.[3] These detectors are also used in safety systems in buildings for arc detection to automatically switch off the current in case arcing occurs. A similar application is the continuous monitoring of the degraded power cables at power stations against any possible

Chapter 1: Introduction

corona discharge of air. With the advent towards clean energies, especially hydrogen fuel, the use of solar-blind photodetectors has become crucial to avoid large scale accidents. A well-known fact is the auto-combustion of hydrogen gas (above a certain percentage) in air with a flame that is completely invisible to the naked eye. Herein lies the power of these detectors which can detect such “invisible” flames easily and in real-time, thereby averting any major catastrophe.

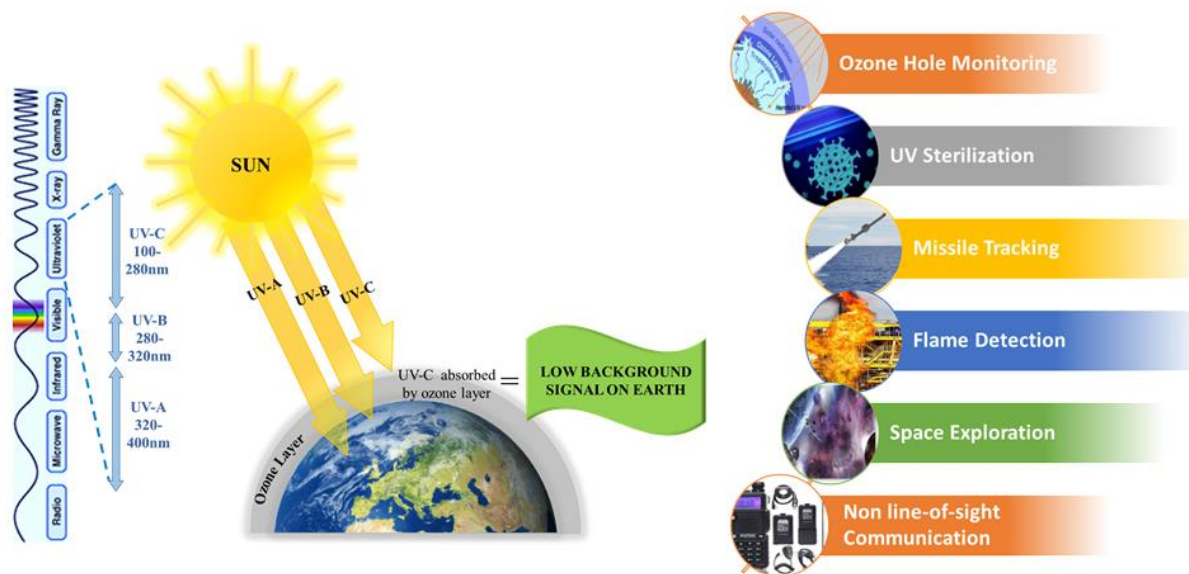


Figure 1.1 Schematic representing the complete absorption of UV-C by the ozone layer along with the potential uses of SBPDs.[1]

Traditionally, SBPDs were fabricated using mature technology such as silicon. However, the band gap of 1.1 eV renders the devices formed to have a broadband spectral response which was undesirable. To overcome this, use of optical filters (such as Wood's Filters) became necessary.[4-6] These filters work by transmitting UV light while blocking or removing the visible part of the solar spectrum. Such filters are not just costly (thereby increasing the cost of the device) but also have the problem of “solarization” i.e. developing visible light leaks after prolonged usage, thus decreasing the lifetime of the device. In addition, filters such as those based on dielectric interference films or metal-dielectric based filters have low transmittance in the UV region.[6] This gave an impetus to look for newer materials free from these constraints and the answer lay in materials with a band gap much greater than that of silicon – the WIDE BAND GAP (WBG) materials.

Materials with a band-gap greater than traditional semiconductors (~ 3 eV) and less than that of insulators (~ 7 eV) are classified as wide band gap materials. Using these, one can design

photodetectors sensitive to the entire UV spectrum (210 – 400 nm), thereby making the use of optical filters and the problem of solarization redundant. Materials such as 4H-SiC ($E_g = 3.2$ eV)[7], ZnO ($E_g = 3.37$ eV)[8], GaN ($E_g = 3.4$ eV)[9], AlGaN ($E_g = 3.4 - 6.2$ eV)[10], Ga₂O₃ ($E_g = 4.6 - 5.3$ eV)[11], Diamond ($E_g = 5.5$ eV)[12] and BN ($E_g = 6.4$ eV)[13], all classify as WBG and hence are often used as absorber materials. Most of these have different forms and polytypes which makes their band gap spread to a range of values. For the special case of deep-UV optoelectronics, corresponding to a wavelength of less than 280 nm, the band gap required has to be greater than 4.4 eV. This pre-requisite disqualifies some of the WBG materials, leaving behind a few worthy candidates, the so called Ultra Wide Band Gap (UWBG) materials. Among these, AlGaN, though having a tunable band gap (tuned by the percentage of Al present), has the disadvantage of complex growth. It is very difficult to grow these over GaN substrates, often leading to high dislocations, and defect density. Also the growth is highly composition dependent, making the whole process quite tricky and unreliable. Others such as those based on diamond are excessively costly and difficult to fabricate on large area and do not possess the flexibility of a tunable band gap (diamond has a fixed band gap of 5.5 eV and hence a sensitivity below 228 nm).[14] Ternary oxides such as MgZnO[15], Zn₂GeO₄[16], In₂Ge₂O₇[17] and ZnGa₂O₄[18] have also been employed to design UV-C photodetectors, however, the difficult and complex alloying process leads to unwanted defects, hindering the overall performance of the device. In addition, these also suffer from phase segregation in the alloyed materials. Therefore, gallium oxide turns up as one of the more viable materials that can be used to model and fabricate these deep-UV devices.[19] With a band gap of 4.6 – 5.3 eV (depending on the polymorph), it possess intrinsic solar-blindness along with other suitable properties such as high chemical and thermal stability, an absorption cut-off wavelength of 260-280 nm, high breakdown voltage and excellent radiation hardness.[20, 21] The metal-oxide has a relatively facile fabrication with no need for complex alloying processes or passivation of the functional material. Other properties of gallium oxide such as a high breakdown field voltage (~ 8 MV cm⁻¹) and a high Baliga's figure-of-merit of ~ 3412 has made it possible for the use of gallium oxide in high frequency (RF) and high power devices.[22, 23] In addition, the intrinsic radiation hardness of the material allows its usage in extremely harsh environments such as space exploration.[24, 25]

1.2 Basics of Photodetector

Photodetectors are devices which convert light energy into an electrical one. The operation of any such device includes basically three processes: (1) generation of photo-generated carriers

by incident light, (2) the transport of photo-generated carriers along with any multiplication by the current-gain mechanism (if present), and (3) Charge carrier extraction at the end electrode to provide the output signal.[26] They work on the principle of absorption of photons of energy equal to or greater than the fundamental band gap of the material. The light absorption depends upon a few material properties such as the band gap, the absorption coefficient and the thickness of the absorber. Most of the incident light needs to be absorbed within the length of the material and hence one requires optimal thickness. Fortunately, for the case of DUV optoelectronics, the ultraviolet light gets absorbed within a few μm of the material.[26, 27] This means that the devices need not be too thick and the use of thin films and nanostructures is possible. The simplest architecture for these devices comprises of an absorber material and electrodes along with the external circuitry to provide a detectable output signal. The absorber material can be in various configurations such as wafers, or thin films on suitable substrates or even nanostructures. Each of these configurations lends different properties to the fabricated photodetector that helps in enhancing one particular figure-of-merit or another. To characterize any device on the basis of its performance, one requires certain parameters. For a photodetector, the characteristics which judge its worth are mentioned below:

1. Dark Current – It is the residual current that flows in the detector even in the absence of any incident light. It is measured in Amperes.
2. Responsivity – The responsivity of the photodetector is the ratio of generated photocurrent and incident optical power, and is determined by Equation (1.1):

$$R = \frac{I_{ph} - I_{dark}}{P_{optical}} \quad (1.1)$$

where I_{ph} is the photocurrent at incident illumination, I_{dark} is the current in the dark condition and $P_{optical}$ is the incident optical power. Usually measured in Ampere per Watt (A W^{-1})

3. Response Time – The time it takes for the detector output to change in response to changes in the input light intensity is called its photoresponse (or response time). It is usually measured in two separate components viz. the rise time and the decay time. The rise time is the time taken for the photodetector output level to change from 10% to 90% of the peak output level while the decay time is the time taken for the output level to change from 90% to 10% of the peak output level. Alternatively, the response can be

found by fitting the photoresponse with a suitable fitting function having rise and decay time constants. It is measured in seconds.

4. Specific Detectivity (D^*) – It characterizes how well a weak signal can be detected compared to the detector noise. D^* is expressed by Equation (1.2):

$$D^* = \sqrt{\frac{A_{op}}{2eI_{dark}}} R \quad (1.2)$$

where A_{op} is the effective area under illumination, I_{dark} is the dark current, e is the electronic charge and R is the responsivity in $A W^{-1}$. It is usually measured in Jones ($cm Hz^{1/2} W^{-1}$). Alternatively, it is also expressed as the inverse of Noise Equivalent Power (NEP) which is the minimum input power required for an output signal-to-noise ratio of 1 at a bandwidth of 1 Hz.

5. Quantum Efficiency – Ability of the photodetector to convert the input light to an output electrical signal is called its quantum efficiency. The two sub-components are the internal and external quantum efficiency. Internal quantum efficiency (IQE) is defined as ratio of the number of electron-hole pairs generated in the semiconductor to the number of incident photons per second whereas external quantum efficiency (EQE) represents the ratio of the number of electron-hole pairs collected (contributing to the photocurrent) to the number of incident photons per second. Both IQE and EQE are measured in terms of percentages. Usually, EQE is the preferred figure-of-merit in gallium oxide based photodetectors and is determined by Equation (1.3):

$$EQE = \frac{Rh c}{e \lambda} \quad (1.3)$$

where R , h , c , e and λ are the responsivity, Planck's constant, speed of light, electronic charge and the wavelength of the incident light, respectively.

Since solar-blind photodetectors can be made using different semiconductors with suitable bandgaps, it becomes imperative to draw a comparison between their performances. Table 1.1 represents a comparison between different materials that may be employed for solar-blind photodetectors. These include materials ranging from inorganic simple oxides to ternary oxides and also includes diamond. The nitrides such as AlN and AlGaN also make good active materials for solar-blind photodetection but are often plagued with difficulty in tuning suitable bandgap. Also included are perovskite which are a new class of materials whose band gap can be tuned but they suffer from stability issues.

Table 1.1: Comparison of the solar-blind photodetectors based on different materials.

Material name	Wavelength (nm)	Bandgap (eV)	I _{dark} (nA)	R (AW ⁻¹)	τ _r (s)/ τ _d (s)	Ref
β-Ga ₂ O ₃	255	4.98	0.26 (20 V)	17	-	[28]
α-Ga ₂ O ₃	254	5.15	1.02 (10 V)	1.50 x 10 ⁻²	> 1	[29]
MgZnO	238/266	5.10	1.60 x 10 ⁻² (15 V)	0.27	-/1.67 x 10 ⁻⁶	[30]
ZnMgO	270	4.20	5 x 10 ⁻³ (3 V)	4.50 x 10 ⁻³	>1	[31]
B-doped GaN	266	-	4.68 x 10 ⁵ (10 V)	0.03	1.50 x 10 ⁻ 8/4.40 x 10 ⁻⁸	[32]
Al _{0.4} Ga _{0.6} N	280	-	5 x 10 ⁻⁶ (10 V)	9.3 x 10 ⁻²	>1	[33]
AlN/AlGa(In))N	260	-	(2-3) x 10 ⁻⁴ (0V)	2.50 x 10 ⁻²	-	[34]
Diamond	210	5.50	4 x 10 ⁻³ (100 V)	2	2.50 x 10 ⁻⁴ /-	[35]
Diamond/grapehene	220	5.45	-	1.4	-	[36]
Ni _{0.54} Mg _{0.46} O	250	-	<25 (10V)	1.20 x 10 ⁻²	-/7.69	[37]
Zr _{0.5} Ti _{0.5} O ₂	250	-	1.7 x 10 ⁻²	0.62	0.42/0.15	[38]
In ₂ Ge ₂ O ₇	230	4.43	-	3.90 x 10 ⁵	4 x 10 ⁻³ /6.93 x 10 ⁻³	[17]
Zn ₂ GeO ₄	260	4.68	1 (1V)	5.11 x 10 ³	0.01/1.30 x 10 ⁻²	[16]
Cs ₃ Cu ₂ I ₅	265	-	-	158	0.034/0.045	[39]

1.3 Gallium oxide – Material properties and design

Gallium oxide as a material has very unique properties. It is an intrinsically n -type material and exists in five different polymorphs (same composition but different crystal structures depending on how it was grown) – α , β , γ , δ and ϵ . The different polymorphs with their crystal structure and space groups are shown in Figure 1.2. The β -phase has monoclinic structure and is the most stable thermally and chemically with all the other phases changing into it at high temperature and pressure. The stability makes it possible to grow and process the polymorph at higher temperatures. Owing to this fact, it is the most widely researched phase with commercially available wafers up to 4" in diameter grown via the edge-defined film fed growth.[40] The melting point of β - gallium oxide is 1720 °C and it has a wide band gap of 4.6-4.9 eV.[41] Although the band gap is reported to be an indirect band gap (4.9 eV), it has been suggested that the direct band gap lies very near at 4.6 eV. With a difference of only 0.03-0.04 eV from the indirect one, it is virtually a direct band gap material with potential application in fabricating deep-UV LEDs.[42] Also, the direct optical transitions imply that only a thin film of the material is required to absorb most of the incoming light.[43]

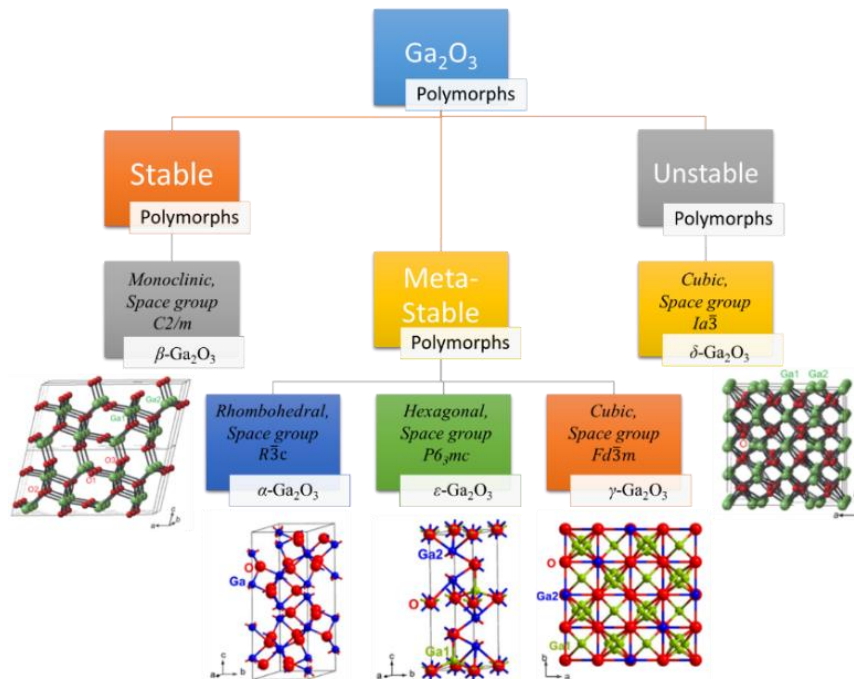


Figure 1.2 The five different polymorphs of gallium oxide along with their crystal structures and their space groups.[1]

However, β - phase is highly anisotropic in regards to some of its material properties. Electronic structure calculations have predicted that due to the asymmetry in the monoclinic crystal structure, the properties in different crystal directions are bound to vary.[44] Studies have

suggested that although the electron effective mass is nearly isotropic, properties such as thermal conductivity, optical absorption edge and optical constants show huge anisotropy.[45] Guo et al. have reported different thermal conductivities in the [010] and [100] crystal direction at room temperature. Anisotropy in the electric and optical properties in single crystals has also been reported by Ueda et al.[46] Moreover, the single crystals are also prone to cleaving easily in the [100] or [010] planes due to the inherent asymmetry. This has, however, not hampered the fabrication of photodetectors based on monoclinic Gallia. The fact that the single crystal easily cleaves is employed in fabricating PDs with single crystal flakes obtained via the relatively easy mechanical exfoliation process.[47] The optical anisotropy in the *b*- and *c*-axes of the crystal is employed in fabrication of polarization sensitive detectors.[48] Poor thermal conductivity does remain a challenge with the only remedial solution being the employment of heat sinks.



Figure 1.3 The unique properties of gallium oxide which makes it a promising candidate for SBPDs.[1]

Because of the asymmetry, there has been an interest in the other polymorphs of gallium oxide exhibiting higher symmetric crystal structures (such as cubic or hexagonal). The other phases, although meta-stable or unstable, have been reported in literature.[49, 50] The α -phase is a metastable phase with trigonal lattice which changes to the stable β -phase at temperatures above 400 °C. Other metastable phases include the ε -phase with a hexagonal crystal structure and the cubic γ -phase.[51] These phases have the advantage of having the either the same crystal structure as *c*-plane sapphire (corundum structure of α -phase) or having a smaller lattice mismatch, thereby facilitating and favoring their epitaxial growth. Also these phases have structures similar to other WBG, such as ZnO and AlN, therefore these can be used successfully

in fabricating heterostructures or band gap tuning through the alloying process. The synthesis of the metastable γ -phase has proven to be much more difficult with only nanostructures being formed via the solution method. δ -Ga₂O₃ is another phase with body-centered cubic structure which has been studied but found to be unstable and greater efforts are required for its advancement. A transient κ -Ga₂O₃ has also been reported by Playford et al. which is analogous to orthorhombic κ -Al₂O₃. [52] Figure 1.3 shows the unique properties of gallium oxide which are useful for its photodetection applications.

Apart from the crystalline phases, another form of gallium oxide is making headways in the field of research – the amorphous phase. The simplicity of a lower-cost, room-temperature and uncomplicated growth without the hassle of achieving epitaxy or single crystal has added to its charm. Additionally, it can be fabricated on larger and more diverse kinds of substrates leading to a universal applicability, including that of flexible wearable devices. In addition to the standalone phases serving as the functional material, there has been growing research on making phase junctions with the different polymorphs of gallium oxide. Being essentially the same material leads to a much smaller lattice mismatch and the slight differences in their band gap gives the advantage of a built-in electric field which helps in the segregation of the photogenerated carriers. Owing to this, phase junctions of α/β -phase and amorphous/ β phase has been developed recently. [53, 54]

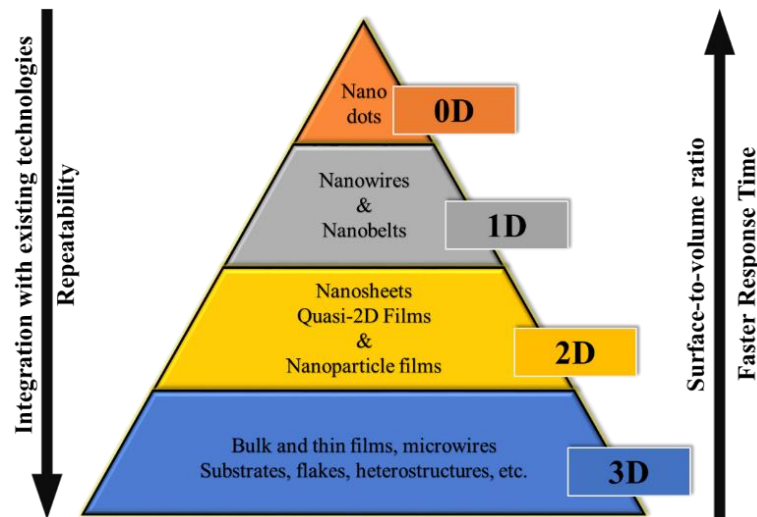


Figure 1.4. Various morphologies of Ga₂O₃ on which SBPDs have been fabricated. [1]

The different dimensionalities of gallium oxide which have been employed for the fabrication of SBPDs range from the bulk crystals to epilayers or thin films grown on different substrates. Nanostructures of Ga₂O₃ include nanowires, nanobelts, nanoflowers, nanoribbons, etc. Even

0D nanodots have also been fabricated and utilized for photodetection applications.[55] According to the dimensionality, gallium oxide structures for the fabrication of deep-UV photodetectors is shown in Figure 1.4.

1.4 Open challenges in the field of Ga_2O_3

As with every material, there are certain challenges in the field of gallium oxide, which need to be resolved for its proper utilization.

1.4.1 *p*-type doping

Gallium oxide is an intrinsically *n*-type material. Whether it is wafers, thin films or nanostructures, all of these turn out to be *n*-type even without any intentional doping. The *n*-type conductivity is often attributed to the oxygen vacancies which act as shallow donor centers.[56] Doping with acceptors such as Mg, Zn, etc. has not had any success with the generation of *p*-type conductivity since these end up acting as deep acceptors. The primary reason for the elusiveness of *p*-type doping is the relative flatness of the valence band in its band structure. DFT calculations have shown the band structure of gallium oxide to have an almost flat valence band maximum, thereby implying the high effective mass of holes, and a curved conduction band minimum making the effective mass of electrons smaller. Figure 1.5 shows the band structure of gallium oxide as calculated by He et al.[57]

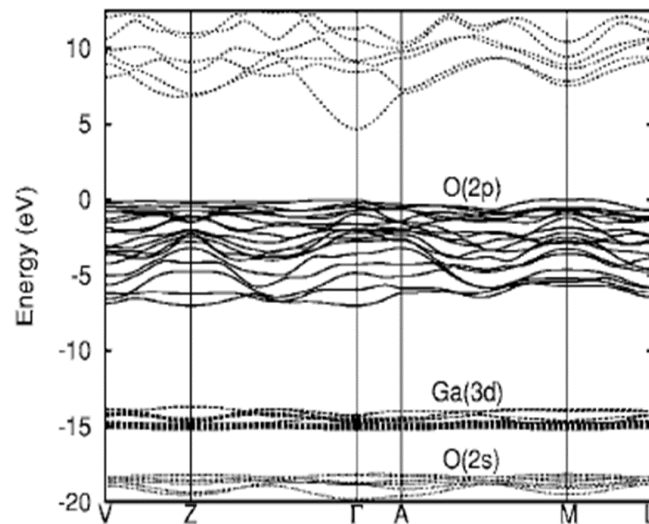


Figure 1.5 Band structure of $\beta\text{-Ga}_2\text{O}_3$. The k points are $\Gamma=(000)$, $A=(0,0,1/2)$, $Z=(1/2,1/2,0)$, $M=(1/2,1/2,1/2)$, $L=(0,1/2,1/2)$ and $V=(0,1/2,0)$. [57]

Hybrid functional calculations by Varley et al. point to the existence of self-trapped holes (STHs) which are more favorable energetically than the delocalized, free holes in the valence

band of WBGs like Ga_2O_3 . [58] This is also corroborated by experimental studies wherein it has been reported that the holes are indeed immobile and exist as STHs. [59] In making a *p*-type material, where the majority carriers are holes, there are two major requirements. First is the presence of a large number of holes (much more than the electrons) and then making these holes take part in the conduction of charge carriers i.e. the actual current in the semiconductor. In metal oxides, the conduction-band states are derived from metal-atoms (thereby they have electron related properties) whereas the valence-band states are derived from the $2p$ orbital of the oxygen atom (thereby having a small dispersion, large effective mass and high density of states). [58] In gallium oxide, as previously mentioned, there have not been suitable dopants which have acceptor states near the valence band contributing to increasing the number of holes. Even if one were to somehow achieve the high concentration of holes in gallium oxide, the high effective mass of these charge carriers along with their tendency to form STHs render it almost impossible to achieve high conductivity with holes. As soon as we get holes in the material, they tend to form small polarons at the local lattice distortions such as oxygen vacancies (i.e. they get trapped) as opposed to the delocalized holes which are free to participate in conduction in the case of conventional semiconductors. [58] This tendency to form polarons (and sometimes bound excitons with the electrons from the defect level states) rises with an increase in the defect density of the material. Ironically, it is these same STHs which are responsible for the high photoconductive gains in detectors. [60] In the present scenario, with a dearth of *p*-type doping, achieving a pure gallium oxide bipolar photodetector is far-off and we need to look for alternatives.

One such alternative is the use of unipolar devices such as photoconductors. Photoconductors are devices which have a semiconductor active material and Ohmic electrodes. Upon the incidence of light, electron-hole pairs are generated and these then move to generate a photocurrent. The Ohmic electrodes pose no barrier to the flow of carriers and hence, there is a constant influx of charge carriers from the external circuitry into the PD under applied potential. This leads to a very high dark current and slower response time. Other ways to circumvent the absence of *p*-type doping is the use of other methods for effective separation of charge carriers such as the utilization of Schottky barrier photodiodes, or Metal-Semiconductor-Metal (MSM) PDs or even the use of heterostructures. Schottky barrier is formed at the interface of an *n*-type material and a suitable metal which leads to a barrier to the flow of charge carriers. This barrier leads to a reduced dark current and a faster response time. MSM PDs are planar devices which employ two such back-to-back Schottky barriers, usually

in an interdigitated configuration to effectively separate the charge carriers. The increased photoactive area gives rise to an increased photoresponse while the barrier gives rise to a shorter response time. Heterostructures of Ga_2O_3 with other p -type materials such as p -Si or p -GaN, helps in the realization of a built-in potential at the interface which helps in charge separation. However, the interface is often replete with defects which leads to a charge pile-up and subsequently a slower response time. Figure 1.6 shows the different types of device geometries which are utilized for the fabrication of Ga_2O_3 based SBPDs.

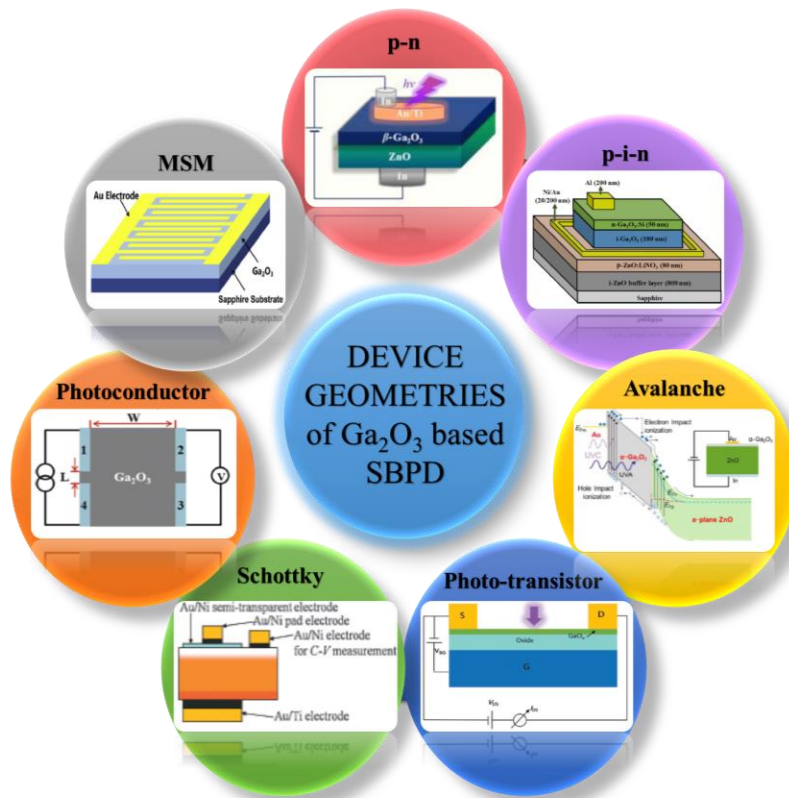


Figure 1.6 Schematic showing the different device geometries which have been utilized for the fabrication of gallium oxide based SBPDs.[1]

1.4.2 Poor thermal conductivity

Ga_2O_3 has poor thermal conductivity $0.1\text{-}0.3 \text{ W cm}^{-1} \text{ K}^{-1}$ almost 8 times less than its counterpart GaN. $\beta\text{-Ga}_2\text{O}_3$ even exhibits anisotropy in this property. This poses a problem in both optoelectronics as well as power electronics. One can circumvent this by either employing the use of substrates which have better thermal conductivity or by bringing size effects into picture (like thinning down the material to enhance the phonon-boundary scattering resulting in better thermal transport).

1.4.3 Trade-off between responsivity and response time

There is a huge trade-off between response time and responsivity. The methods that are employed to increase responsivity end up increasing the response time of the photodetector as well and vice-versa. These are two competing parameters which are closely related to each other. The main cause of photoconductive gain in gallium oxide is attributed to the trapping of holes near the oxygen vacancies which helps in increasing the responsivity of the photodetector. However, this same fact becomes the cause for the slower response time due to their prolonged life-times. So a reduction in the trap density gives rise to a faster response but at the expense of a smaller gain. Similarly, for the remedial step to increase responsivity by using transparent conducting oxides increases the overall active area, but then the holes generated under cathode and the electrons generated under anode take a longer time to reach the other electrode, thereby increasing the response time. If one employs the use of heterostructures to increase the responsivity (by forming a built-in potential), the response time of the photodetector decreases due to a charge pile-up at the interface. Even annealing of the substrate leads to an enhanced responsivity owing to suppression of impurity scattering due to structural disorders while degrading the response time because of a decrease in carrier recombination.[61] So, it is very difficult to achieve both high responsivity and a fast response time simultaneously. However, not all is lost. Remedial solutions such as using single layer graphene as an electrode improves both responsivity (by allowing the majority of the light to reach the contact area) and response time (by offering an easy channel carrier for the transport of electrons and holes).[62] More research is needed in this direction to come up with unique ways to improve the responsivity and response time together.

1.4.4 Application-based challenges

It is a well-established fact that Ga_2O_3 is radiation hardened and hence it can be employed in extreme environment applications (high radiation and high temperature). Potential harsh environments include space exploration, nuclear reactors, geothermal applications, hydrogen energy, automotive engines etc. The high radiation hardness is due to the stronger bonding in Ga_2O_3 . Their wider energy gap requires higher energy photons or ions transiting the material to achieve ionization of electrons and holes in the semiconductor as compared to Si. Also for high temperature, Si based devices can go only up to 150°C operating temperatures whereas GaN based devices operate upto 600°C . It is expected that Ga_2O_3 based devices can have

operations upto 1000°C. However, both these aspects have remained unexplored. Testing these devices for extreme environment applications still remains an open challenge.

1.5 Current scenario in the field of Ga₂O₃ based SBPDs

Figure 1.7 shows the progress in research so far and highlights the inevitable trade-off between the two key parameters – responsivity and response time – in the case of gallium oxide and gallium oxide heterostructures based PDs, respectively.

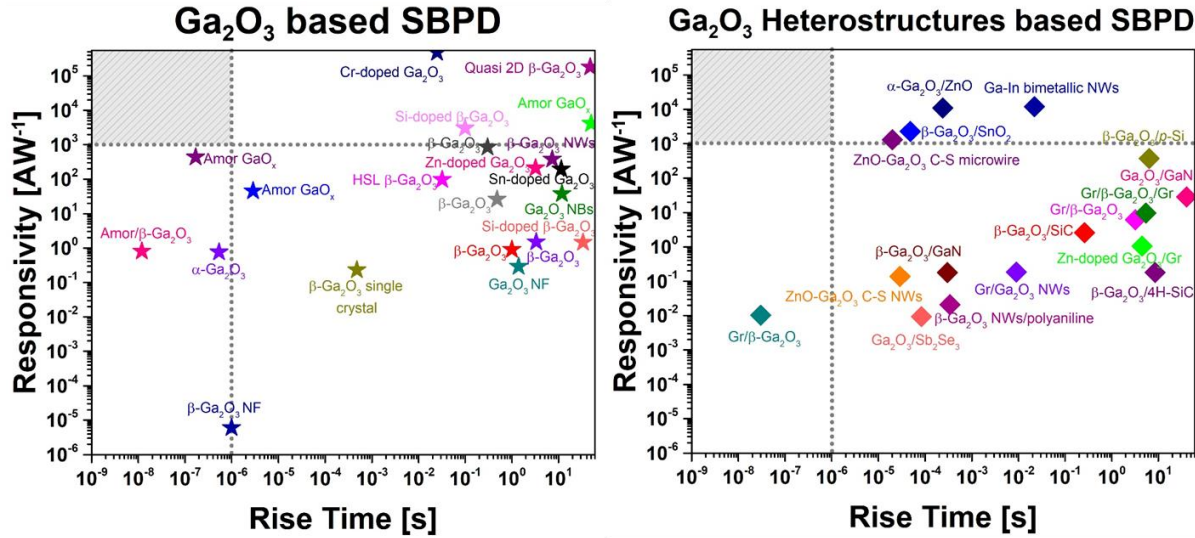


Figure 1.7 Performance comparison of the current scenario in (a) gallium oxide based and (b) gallium oxide heterostructures based photodetectors.[1]

The rectangular enclosed area on the left hand corner represents the desired performance of these PDs which needs to be targeted for achieving commercialization and making the switch from the existing technology.

1.6 Basic device architecture

For fabrication of solar-blind photodetectors based on thin-films, the simplest architecture that can be employed is depicted in Figure 1.8. It consists of three different components – the substrate used (which determines the growth of the overlying thin film), the active layer (where absorption of photons and generation of electron-hole pairs occurs) and the electrical contacts (which take out the photogenerated charge carriers into the external circuit for a measureable signal). All the three components together make up the device and a synergy between them is of the utmost importance. In the present thesis, the substrate, active layer and electrodes are optimized (alone or in combination) to achieve high performance solar-blind photodetection based on gallium oxide thin films.

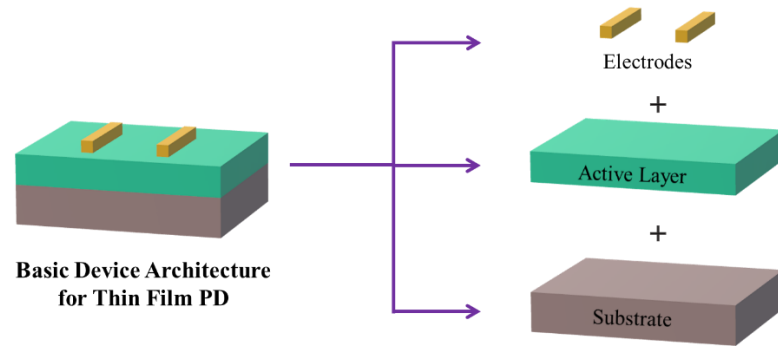


Figure 1.8 Basic device architecture showing the three integral components.

1.7 Objectives of the thesis

The aim of this research thesis is to employ unique and novel methods to develop high performance photodetectors based on the wide bandgap material – gallium oxide. The main objectives of the present thesis are as follows:

1. Optimizing the active layer for both crystalline and amorphous Ga_2O_3 for an enhanced performance.
2. Fabrication of fast speed SBPDs by employing surface modification.
3. To investigate the charge carrier dynamics of Ga_2O_3 based heterostructures and study the behavior of their photodetectors thereof.
4. Studying the impact of the extreme environments such as high temperatures and radiation on contacts and Ga_2O_3 thin films and analyse their performance limitations.

1.8 Outline of the thesis

The thesis is organized into the following seven chapters to accomplish the proposed objectives.

Chapter 1: Introduction

The introductory chapter gives a brief insight into the world of solar-blind photodetectors based on gallium oxide. The basic understanding about the need for such PDs, the background of active material involved and the existing reported literature on the said topic serves as a framework for the present thesis. The motivation behind the undertaken research is also elucidated along with the objectives that need to be realized.

Chapter 2: Fabrication and characterization techniques

This chapter states and discusses the various fabrication and deposition methods that were used in developing gallium oxide based PDs. It also elaborates on the testing equipment utilized as

Chapter 1: Introduction

well as the characterization techniques that were employed for successfully carrying out the current research work.

Chapter 3: Dependence of performance on the growth of active layer

This chapter investigates systematically the active layer involved – gallium oxide. It begins by building upon the growth of polycrystalline β -Ga₂O₃ on different orientations of Si substrate and studying how the performance changes with the strain produced in the films. This is followed by optimizing the growth of β -Ga₂O₃ on a more lattice matched substrate – sapphire – by varying the thickness of the film and studying its impact on PDs. Additionally, a facile fabrication of mixed-phase ($\alpha - \beta$) is done on room temperature on sapphire substrates, thus, opening the doors for room temperature crystallinity being achieved in Ga₂O₃.

Chapter 4: Enhancing performance using surface modification

In this chapter, surface modification of amorphous films of gallium oxide are undertaken in two different approaches. First, the surface of amorphous Ga₂O₃ film is modified and nanoripples are created using ion beam sputtering and the dependence on photodetector performance is studied. In the second approach, ultra-thin Ga₂O₃ film is conformally coated on a nanopatterned substrate, giving rise to fast speed photodetectors.

Chapter 5: Interface engineering via heterostructures of Gallium oxide

This chapter studies the importance of interfaces, charge carrier dynamics and energy level alignment in the heterostructures of Ga₂O₃, taking the case of sulfide materials. The first part includes the study of a heterostructure of amorphous Ga₂O₃ with CdS, giving rise to a solar-blind photodetector while the second part deals with a heterostructure of amorphous Ga₂O₃ with PtS but now giving a broadband photoresponse. The reasons for why the heterostructure devices show this different nature is also discussed.

Chapter 6: Photodetectors under extreme environments

This chapter touches upon the extreme environment applicability of Ga₂O₃. Although the material itself is extremely thermally stable, the devices sometimes fail due to other components of the PD. In the first part, a study on the origin of near-failure of Au contacts to β -Ga₂O₃ at high temperatures is studied. The second part involves the change in the behaviour of IZO transparent electrodes from Schottky-Ohmic-Schottky upon increasing the temperatures, studied using interfacial studies. The third part involves the radiation hardness

Chapter 1: Introduction

resilience of Ga₂O₃ films against swift heavy ions of 100 MeV energy and photodetectors thereof.

Chapter 7: Summary and scope for future studies

This chapter summarizes the entire thesis work and presents future directions for the further development of gallium oxide and its solar-blind photodetectors.

References

1. Kaur, D., et al., A Strategic Review on Gallium Oxide Based Deep-Ultraviolet Photodetectors: Recent Progress and Future Prospects. *Advanced Optical Materials* **2021**, 9(9), 2002160.
2. Debbie, K., et al., Subsea ultraviolet solar-blind broadband free-space optics communication. *Optical Engineering* **2009**, 48(4), 1-7.
3. Würtele, M.A., et al., Application of GaN-based ultraviolet-C light emitting diodes – UV LEDs – for water disinfection. *Water Research* **2011**, 45(3), 1481-1489.
4. Wood, R.W., Remarkable Optical Properties of the Alkali Metals. *Physical Review* **1933**, 44(5), 353-360.
5. Razeghi, M., et al., Semiconductor ultraviolet detectors. *Journal of Applied Physics* **1996**, 79(10), 7433-7473.
6. Mu, J., et al., Design and fabrication of a high transmissivity metal-dielectric ultraviolet band-pass filter. *Applied Physics Letters* **2013**, 102(21), 213105.
7. Chen, X., et al., High-performance 4H-SiC-based ultraviolet p-i-n photodetector. *Journal of Applied Physics* **2007**, 102(2), 024505.
8. Du, X., et al., Controlled Growth of High-Quality ZnO-Based Films and Fabrication of Visible-Blind and Solar-Blind Ultra-Violet Detectors. *Advanced Materials* **2009**, 21(45), 4625-4630.
9. Butun, B., et al., High-performance visible-blind GaN-based p-i-n photodetectors. *Applied Physics Letters* **2008**, 92(3), 033507.
10. Tut, T., et al., Solar-blind AlGaIn-based p-i-n photodetectors with high breakdown voltage and detectivity. *Applied Physics Letters* **2008**, 92(10), 103502.
11. Arora, K., et al., Ultrahigh Performance of Self-Powered β -Ga₂O₃ Thin Film Solar-Blind Photodetector Grown on Cost-Effective Si Substrate Using High-Temperature Seed Layer. *ACS Photonics* **2018**, 5(6), 2391-2401.
12. Lin, C.-N., et al., Diamond-Based All-Carbon Photodetectors for Solar-Blind Imaging. *Advanced Optical Materials* **2018**, 6(15), 1800068.
13. Liu, H., et al., High-performance deep ultraviolet photodetectors based on few-layer hexagonal boron nitride. *Nanoscale* **2018**, 10(12), 5559-5565.
14. Liao, M., et al., Thermally stable visible-blind diamond photodiode using tungsten carbide Schottky contact. *Applied Physics Letters* **2005**, 87(2), 022105.
15. Zheng, Q., et al., MgZnO-based metal-semiconductor-metal solar-blind photodetectors on ZnO substrates. *Applied Physics Letters* **2011**, 98(22), 221112.
16. Zhou, X., et al., High-Performance Solar-Blind Deep Ultraviolet Photodetector Based on Individual Single-Crystalline Zn₂GeO₄ Nanowire. *Advanced Functional Materials* **2016**, 26(5), 704-712.
17. Li, L., et al., Ultrahigh-Performance Solar-Blind Photodetectors Based on Individual Single-crystalline In₂Ge₂O₇ Nanobelts. *Advanced Materials* **2010**, 22(45), 5145-5149.
18. Shen, Y.-C., et al., Power Saving High Performance Deep-Ultraviolet Phototransistors Made of ZnGa₂O₄ Epilayers. *ACS Applied Electronic Materials* **2020**, 2(2), 590-596.
19. Ji, Z., et al., Gallium oxide films for filter and solar-blind UV detector. *Optical Materials* **2006**, 28(4), 415-417.
20. Pearton, S.J., et al., A review of Ga₂O₃ materials, processing, and devices. *Applied Physics Reviews* **2018**, 5(1), 011301.
21. Kaur, D., et al., Phase dependent radiation hardness and performance analysis of amorphous and polycrystalline Ga₂O₃ solar-blind photodetector against swift heavy ion irradiation. *Journal of Applied Physics* **2020**, 128(6), 065902.

22. Higashiwaki, M., et al., Gallium oxide (Ga₂O₃) metal-semiconductor field-effect transistors on single-crystal β -Ga₂O₃ (010) substrates. *Applied Physics Letters* **2012**, *100*(1), 013504.
23. Hwang, W.S., et al., High-voltage field effect transistors with wide-bandgap β -Ga₂O₃ nanomembranes. *Applied Physics Letters* **2014**, *104*(20), 203111.
24. Wei, T., et al., See-Through Ga₂O₃ Solar-Blind Photodetectors for Use in Harsh Environments. *IEEE Journal of Selected Topics in Quantum Electronics* **2014**, *20*(6), 112-117.
25. Yang, G., et al., Influence of High-Energy Proton Irradiation on β -Ga₂O₃ Nanobelt Field-Effect Transistors. *ACS Applied Materials & Interfaces* **2017**, *9*(46), 40471-40476.
26. Sze, S.N., K.K., *Photodetectors and Solar Cells*, in *Physics of Semiconductor Devices*. 2006. p. 663-742.
27. Quimby, R.S., *Optical Detectors*, in *Photonics and Lasers*. 2006. p. 223-247.
28. Hu, G.C., et al., High gain Ga₂O₃ solar-blind photodetectors realized via a carrier multiplication process. *Optics Express* **2015**, *23*(10), 13554-13561.
29. Guo, D.Y., et al., Epitaxial growth and solar-blind photoelectric properties of corundum-structured α -Ga₂O₃ thin films. *Materials Letters* **2016**, *164*, 364-367.
30. Han, S., et al., Photoconductive gain in solar-blind ultraviolet photodetector based on Mg_{0.52}Zn_{0.48}O thin film. *Applied Physics Letters* **2011**, *99*(24), 242105.
31. Liu, K.W., et al., The growth of ZnMgO alloy films for deep ultraviolet detection. *Journal of Physics D: Applied Physics* **2008**, *41*(12), 125104.
32. Srour, H., et al., Solar blind metal-semiconductor-metal ultraviolet photodetectors using quasi-alloy of BGaN/GaN superlattices. *Applied Physics Letters* **2011**, *99*(22), 221101.
33. Biyikli, N., et al., Solar-blind AlGaN-based p-i-n photodiodes with low dark current and high detectivity. *IEEE Photonics Technology Letters* **2004**, *16*(7), 1718-1720.
34. Kuryatkov, V., et al., Solar-blind ultraviolet photodetectors based on superlattices of AlN/AlGa(In)N. *Applied Physics Letters* **2003**, *82*(9), 1323-1325.
35. Gorokhov, E.V., et al., Solar-blind UV flame detector based on natural diamond. *Instruments and Experimental Techniques* **2008**, *51*(2), 280-283.
36. Wei, M., et al., A Solar-Blind UV Detector Based on Graphene-Microcrystalline Diamond Heterojunctions. *Small* **2017**, *13*(34), 1701328.
37. Mares, J.W., et al., Deep-ultraviolet photodetectors from epitaxially grown NixMg_{1-x}O. *Applied Physics Letters* **2010**, *97*(16), 161113.
38. Zhang, M., et al., High response solar-blind ultraviolet photodetector based on Zr_{0.5}Ti_{0.5}O₂ film. *Applied Surface Science* **2013**, *268*, 312-316.
39. Ma, J., et al., Kinetically regulated growth of Cs₃Cu₂I₅ single-crystalline thin films for highly responsive and stable deep-ultraviolet photodetectors. *Nano Today* **2023**, *52*, 101970.
40. Blevins, J.D., et al., Development of Large Diameter Semi-Insulating Gallium Oxide (Ga₂O₃) Substrates. *IEEE Transactions on Semiconductor Manufacturing* **2019**, *32*(4), 466-472.
41. Stepanov, S.I.N., V. I.; Bougrov, V. E.; Romanov, A. E., Gallium Oxide: Properties and Applications - A Review. *Reviews on Advanced Materials Science* **2016**, *44*, 63-86.
42. Peelaers, H., et al., Brillouin zone and band structure of β -Ga₂O₃. *physica status solidi (b)* **2015**, *252*(4), 828-832.

43. Bube, R.H., *Photoelectronic properties of semiconductors*. 1992, Cambridge ; New York: Cambridge University Press.
44. Schubert, M., et al., Anisotropy, phonon modes, and free charge carrier parameters in monoclinic β -gallium oxide single crystals. *Physical Review B* **2016**, *93*(12), 125209.
45. Guo, Z., et al., Anisotropic thermal conductivity in single crystal β -gallium oxide. *Applied Physics Letters* **2015**, *106*(11), 111909.
46. Ueda, N., et al., Anisotropy of electrical and optical properties in β -Ga₂O₃ single crystals. *Applied Physics Letters* **1997**, *71*(7), 933-935.
47. Oh, S., et al., Quasi-two-dimensional β -gallium oxide solar-blind photodetectors with ultrahigh responsivity. *Journal of Materials Chemistry C* **2016**, *4*(39), 9245-9250.
48. Chen, X., et al., Highly Narrow-Band Polarization-Sensitive Solar-Blind Photodetectors Based on β -Ga₂O₃ Single Crystals. *ACS Applied Materials & Interfaces* **2019**, *11*(7), 7131-7137.
49. Zhang, J., et al., Recent progress on the electronic structure, defect, and doping properties of Ga₂O₃. *APL Materials* **2020**, *8*(2), 020906.
50. Wang, X., et al., Discovery of New Polymorphs of Gallium Oxides with Particle Swarm Optimization-Based Structure Searches. *Advanced Electronic Materials* **2020**, *6*(6), 2000119.
51. Sharma, A., et al., Nano-structured phases of gallium oxide (GaOOH, α -Ga₂O₃, β -Ga₂O₃, γ -Ga₂O₃, δ -Ga₂O₃, and ϵ -Ga₂O₃): fabrication, structural, and electronic structure investigations. *International Nano Letters* **2020**, *10*(1), 71-79.
52. Playford, H.Y., et al., Structures of Uncharacterised Polymorphs of Gallium Oxide from Total Neutron Diffraction. *Chemistry – A European Journal* **2013**, *19*(8), 2803-2813.
53. Wu, C., et al., Vertical α/β -Ga₂O₃ phase junction nanorods array with graphene-silver nanowire hybrid conductive electrode for high-performance self-powered solar-blind photodetectors. *Materials Today Physics* **2020**, *12*, 100193.
54. Wang, Y., et al., One-Step Growth of Amorphous/Crystalline Ga₂O₃ Phase Junctions for High-Performance Solar-Blind Photodetection. *ACS Applied Materials & Interfaces* **2019**, *11*(49), 45922-45929.
55. Kan, H., et al., Ultrawide Band Gap Oxide Nanodots ($E_g > 4.8$ eV) for a High-Performance Deep Ultraviolet Photovoltaic Detector. *ACS Applied Materials & Interfaces* **2020**, *12*(5), 6030-6036.
56. Yamaga, M., et al., Donor structure and electric transport mechanism in β -Ga₂O₃. *Physical Review B* **2003**, *68*(15), 155207.
57. He, H., et al., First-principles study of the structural, electronic, and optical properties of β -Ga₂O₃ in its monoclinic and hexagonal phases. *Physical Review B* **2006**, *74*(19), 195123.
58. Varley, J.B., et al., Role of self-trapping in luminescence and p -type conductivity of wide-band-gap oxides. *Physical Review B* **2012**, *85*(8), 081109.
59. Kananen, B.E., et al., Self-trapped holes in β -Ga₂O₃ crystals. *Journal of Applied Physics* **2017**, *122*(21), 215703.
60. Armstrong, A.M., et al., Role of self-trapped holes in the photoconductive gain of β -gallium oxide Schottky diodes. *Journal of Applied Physics* **2016**, *119*(10), 103102.
61. Qian, L.X., et al., β -Ga₂O₃ solar-blind deep-ultraviolet photodetector based on annealed sapphire substrate. *Vacuum* **2017**, *140*, 106-110.
62. Qu, Y., et al., Enhanced Ga₂O₃/SiC ultraviolet photodetector with graphene top electrodes. *Journal of Alloys and Compounds* **2016**, *680*, 247-251.

Chapter 2: Fabrication and characterization techniques

This chapter provides insight into the fabrication and characterization techniques which are utilized in completing the research work presented in this thesis. First, a brief introduction of the sputtering technique is provided, which is the main deposition technique used for the fabrication of gallium oxide thin film. This is followed by a list of characterization techniques used to characterize the films. In particular, X-ray photoelectron spectroscopy and its use in depth profiling for band alignment studies is elucidated. The photodetector characterization set-up used to conduct optical measurements is discussed along with the arrangements for high speed device testing.

2.1 Magnetron sputtering

Sputtering is a type of physical vapour deposition which employs the ejection of the target material by using energetic ions.[1] A potential difference is applied across the target (cathode) and the sample stage (anode) which ionizes the gas present inside the chamber, thereby forming a plasma. The presence of a high vacuum ensures that the mean free path of the atoms increases and the inter-atomic collisions are minimized and the sputtered material gets deposited onto the samples kept at the anode (see Figure 2.1 (a)). An addition of magnets behind the target kept at cathode leads to a confinement of the plasma near the target and increases the sputter rate by directing the plasma due to the generated magnetic field. This variation of confining the plasma is known as Magnetron sputtering. DC fields may be applied to generate the electric potential between the anode and cathode, but for insulating targets, such as Ga_2O_3 in the present thesis, this usually leads to a space-charge region being created. Since the target is at negative potential, positively charged Ar ions tend to get crowded at the cathode. In the absence of any charge re-distribution (which usually happens for conducting targets), positive ions start collecting near the cathode. The positively charged Ar ions and the negatively charged target creates a space-charge region which does not allow the electric field to sustain and hence the plasma extinguishes, thereby stopping the deposition via sputtering. As a remedy to this, high frequency AC sources, such as the radiofrequency is employed. This oscillating field tends to attract the Ar ions in the negative cycle but prohibits the formation of a space charge region by repelling the ions in the positive cycle. Thus, insulating targets can also be easily sputtered using RF Sputtering.[2]

Chapter 2: Fabrication and characterization techniques

In the present thesis, RF magnetron sputtering (make - EXCEL INSTRUMENTS, India) is utilized for the fabrication of Ga_2O_3 thin films with RF source of 13.56 MHz and 0-300W power. Figure 2.1 (b) shows the equipment used which is equipped with Pfeiffer ACP 15 dry pump for rough vacuum generation, Pfeiffer HiPace Turbomolecular pump for achieving high vacuum and suitable gauges to check the vacuum levels. Controllable gas flows of Ar and O_2 is provided using mass flow controllers while a PID (Proportional-Integral-Derivative) controller interfaced with heater assembly is utilized to increase the substrate temperatures up to 800°C . For a better and more uniform deposition, the substrate holder may be rotated by using a, attached DC motor assembly.

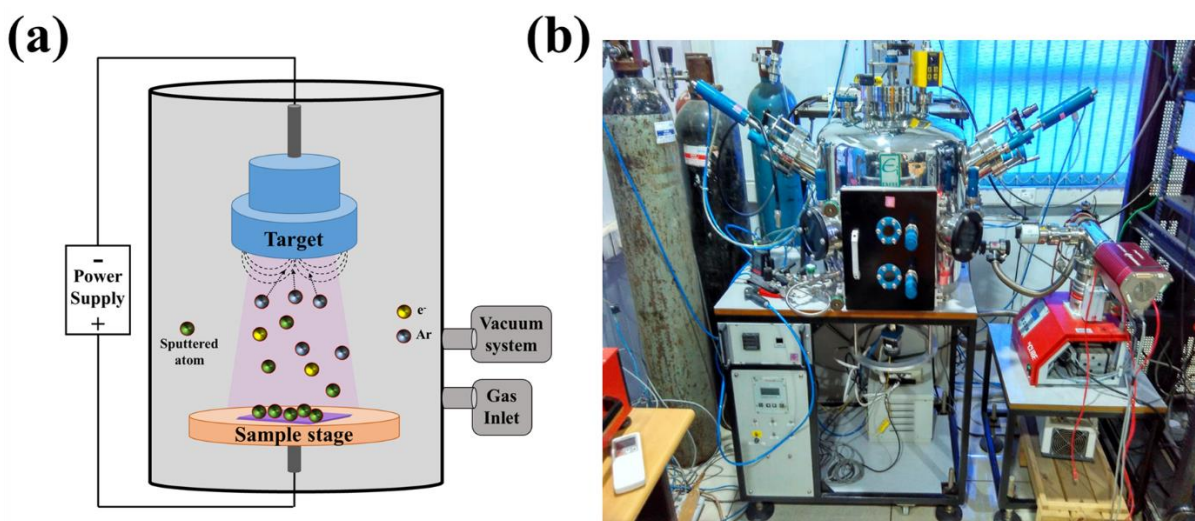


Figure 2.1 (a) Schematic illustration of the sputtering system (b) RF magnetron sputtering equipment used for growing Ga_2O_3 thin films.

2.2 Characterization techniques

During the course of the thesis, several characterization techniques were utilized which is elucidated in the list below:

2.2.1 Crystal structure characterizations

X-ray diffraction (XRD) was used to determine the crystalline structure and quality of the thin films.[3] In this technique, the electrons in the crystalline material when irradiated with X-rays, interact with the light waves and shows constructive interference at specific angles, i.e., whenever Bragg's condition is fulfilled.

$$2d \sin\theta = n\lambda$$

where d is the interplanar spacing, θ is the angle of incidence with respect to the crystal planes, n is the order of reflection, and λ is the wavelength of the X-ray source. Ga_2O_3 films were

Chapter 2: Fabrication and characterization techniques

characterized using a multipurpose diffractometer (PANalytical X-pert pro) and/or a PXRD, Bruker D8 instrument, both equipped with high-intensity $\text{CuK}\alpha$ (0.154 nm). The obtained XRD data was compared to a standard database (JCPDS data card number – 00-041-1103 for β - Ga_2O_3 , 00-006-0503 for α - Ga_2O_3). HRTEM images were recorded using Jeol JEM 2100 PLUS TEM (JEOL USA, Inc., Peabody, MA, USA).

2.2.2 Morphological characterizations

Scanning Electron Microscope (SEM) was utilized to characterize the morphology of the films.[4] For the ultra-thin films of Ga_2O_3 in Chapter 4, the SEM and energy dispersive x-ray (EDX) was recorded using JEOL Model – JSM7610F Plus. The irradiated films in chapter 6 were characterized using TESCAN instrument (MIRA II LMH) while EDX detector from OXFORD (INCAPentaFET3) attached to the above instrument was used for elemental analysis of the thin films.

Atomic Force Microscopy images provided in the thesis were recorded using Bruker Multimode 8 Scanning Probe Microscope in the tapping mode. The quantitative information about the various topological parameters such as RMS roughness, Fast-Fourier transform, line profiles, power spectral density (PSD) curve, etc. were extracted using the Gwyddion software. Specifically, for the images provided in Chapter 5, Agilent 5500 scanning probe microscopy was used to take the atomic force microscopy images. KPFM measurements were carried out by amplitude modulation using a Budget Sensor Cr/Pt-coated Multi 75-EG tip. The force constant was 3 N m^{-1} , and the tip resonance frequency was 75 kHz, respectively. The electrostatic force between the tip and the sample was induced by the electrical oscillation of the tip, which was nullified by a DC offset to the scanning tip. A Dolan-Jenner MI-150 fiber optic illuminator was used for the KPFM measurement under illumination.

The optical images presented in the thesis were recorded using Nikon ECLIPSE LV100ND.

2.2.3 Optical characterizations

Photoluminescence spectra and time resolved photoluminescence for the thin films was conducted using a double monochromatic fluorescence spectrometer (model: FLS-980 D2D2, Edinburgh Instruments) equipped with a 266 Crylas TCSPC laser. Raman spectra was recorded using LabRAM Horiba Scientific.

UV-Vis spectroscopy studies were carried out using Perkin Elmer Lambda 950 UV-Vis-NIR spectrophotometer and Shimadzu UV-1800 UV/visible spectrophotometer.

2.2.4 Chemical composition analysis and band alignment studies

X-ray photoelectron spectroscopy is a surface-sensitive technique which is used to study the elemental composition in different samples. X-rays are incident from a source which are absorbed by the atoms in the sample leading to ejection of electrons from the core level of the atoms which give characteristic peaks in the XPS spectra, allowing for the quantification and study of the chemical environment of elements across the material.[5, 6] In the present thesis, XPS analysis is carried out using Al K α x-ray source in Thermo-Fischer Scientific ESCALAB Xi+. In the case of CdS-Ga₂O₃ samples in Chapter 5, the measurements were carried out using PHI 5000 VersaProbe II Scanning ESCA system from Physical Electronics.

Since the penetration depth in XPS is only ~ 10 nm, XPS depth profiling is often employed to study the variation in elemental composition across the thickness of the samples. Ar ions are used to etch the surface upto a certain depth and then data is recorded. This is repeated till the desired depth of probing is reached. After recording the data, analysis is performed across the interface to study the band alignment between two interfaces. Using the Kraut's rule[7], which takes into account the band-bending at the interface as well, the valence band offset can be determined from the core level spectra of either the cations or the anions of the two different materials A and B as:

$$VBO = \left(E_{core\ level\ A}^{A(bulk)} - E_{VBM\ of\ A}^{A(bulk)} \right) - \left(E_{core\ level\ B}^{B(bulk)} - E_{VBM\ of\ B}^{B(bulk)} \right) + \Delta E_{CL}(interface) \quad (2.1)$$

where, $\Delta E_{CL}(interface) = (E_{core\ level\ B(i)}^{interface} - E_{core\ level\ A(i)}^{interface})$ is the binding energy difference between In 3d and Ga 2p_{3/2} core levels at the interface. The term $\left(E_{core\ level\ A}^{A(bulk)} - E_{VBM\ of\ A}^{A(bulk)} \right)$ and $\left(E_{core\ level\ B}^{B(bulk)} - E_{VBM\ of\ B}^{B(bulk)} \right)$ represent valence band edges with reference to core levels of material A and B, respectively.

Using the band gap values for the two materials A and B, the conduction band offset was calculated as:

$$CBO = E_g^A - E_g^B + VBO \quad (2.2)$$

2.3 Device fabrication and characterization

2.3.1 Contacts for devices

Metal contacts for the devices were deposited using thermal evaporation in interdigitated geometry or strip geometry as shown in Figure 2.2 (a,b) via physical shadow masks using the thermal evaporation system (make - EXCEL Instruments, India) shown in Figure 2.2 (c). The

Chapter 2: Fabrication and characterization techniques

metal-alternate contacts such as Indium Zinc Oxide were deposited using (RF + DC) sputtering as given in previously reported literature.[8]

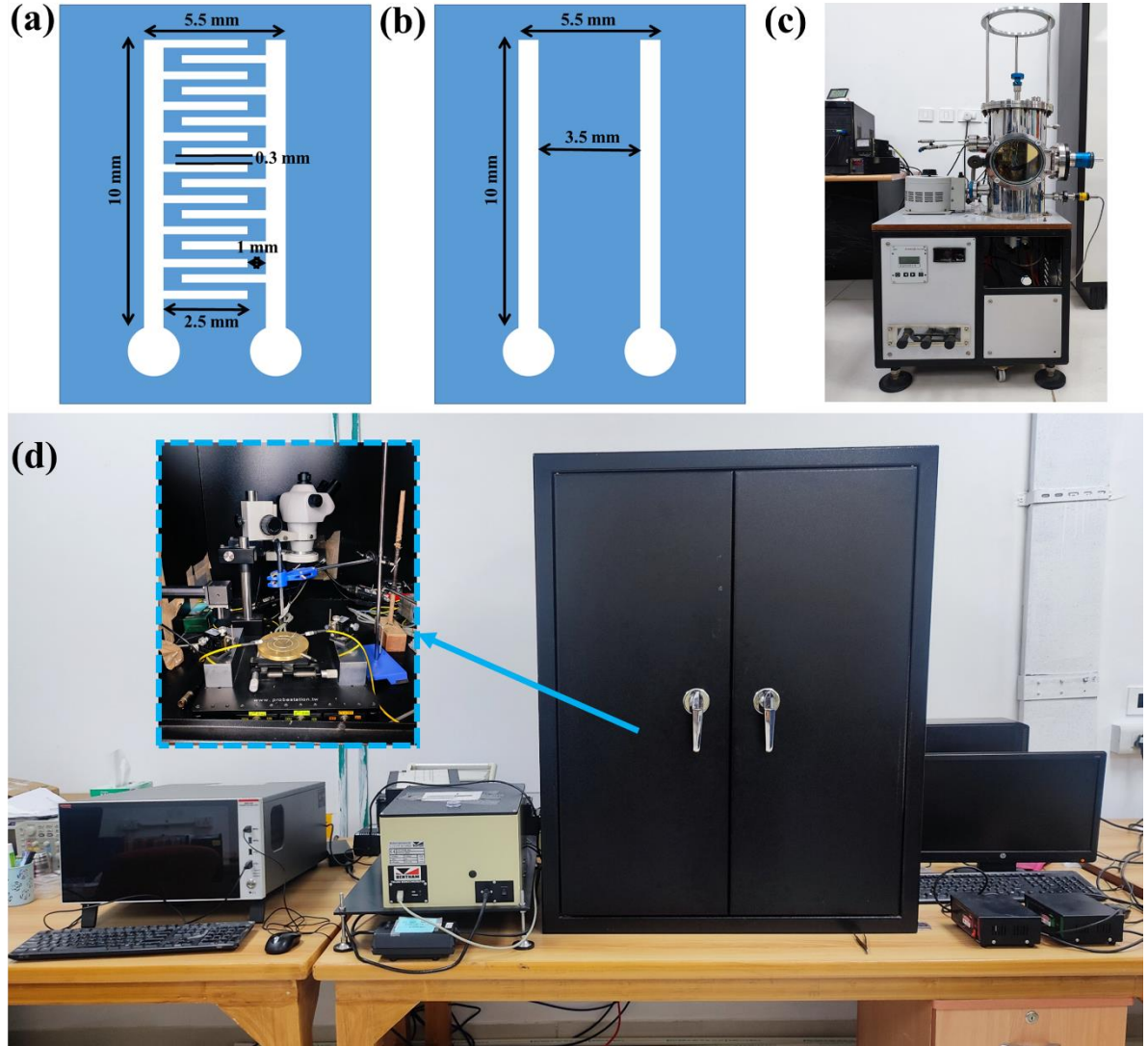


Figure 2.2 Physical shadow mask used for electrode deposition in the (a) interdigitated geometry and (b) strip geometry. (c) Thermal evaporator system used for depositing metal contacts (d) Testing equipment used to characterize the photodetector devices along with the probe station equipped with UV-C lamp used shown in the inset.

2.3.2 Photodetector device characterization

The performance of the Ga_2O_3 based solar-blind photodetectors was judged by characterizations using the equipment shown in Figure 2.2 (c,d). It consists of a monochromator (Bentham TMc -300) interfaced with a probe-station with micro-positioners and Keithley 4200 A SCS. The optical power of different incident wavelengths was calibrated using a standard Si (model: DH_Si_29987) photodiode. The other light sources used include 254 nm pen-ray UV-C lamp (Cole-Parmer, 4.4 mW cm^{-2} intensity), 365 nm handheld UV lamp (Cole-Parmer, $17 \mu\text{W cm}^{-2}$ intensity) and 532 nm and 650 nm lasers (Holmarc, 5 mW power). The PD

Chapter 2: Fabrication and characterization techniques

measurements were carried in an optically enclosed chamber to avoid any interference from ambient light.

The high speed measurements were carried out using the arrangement shown in Figure 2.3. While using the optical chopper (Scitech Instruments) during measurements, a digital oscilloscope (Tektronix MDO32) was used with a preamplifier (Ametek SR 5113 Instrument), to measure high speed photodetection.

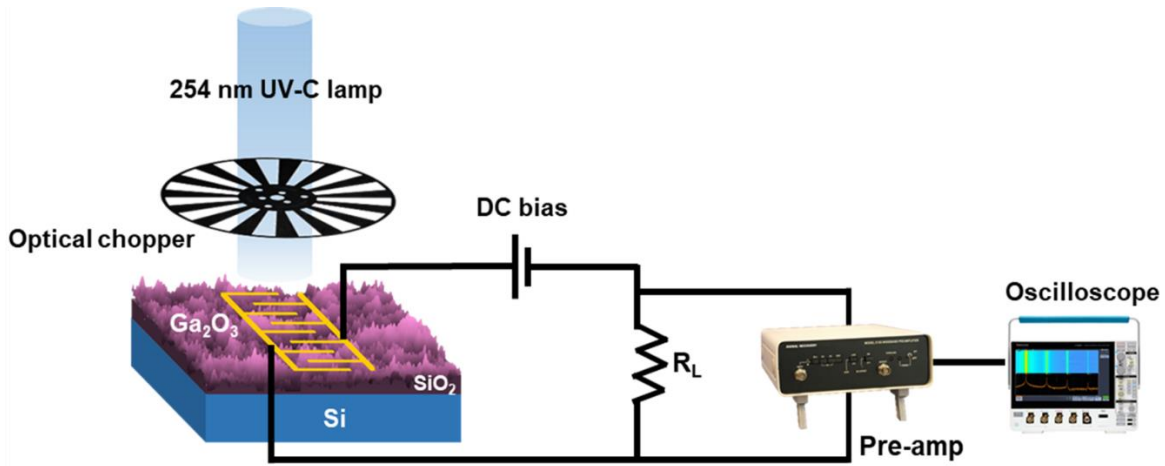


Figure 2.3 Experimental set-up for the testing equipment used to characterize fast photodetection.

References

1. Mattox, D.M., *Handbook of physical vapor deposition (PVD) processing*. 2010: William Andrew.
2. Ohring, M., The materials science of thin films. *Appl. Opt* **1992**, *31*(34), 7162.
3. Cullity, B., et al., *Elements of x-ray diffraction*, Prentice Hall. *Upper Saddle River, NJ* **2001**, 388.
4. Dehm, G., et al., *In-situ electron microscopy: Applications in physics, chemistry and materials science*. 2012: John Wiley & Sons.
5. Chastain, J., et al., *Handbook of X-ray photoelectron spectroscopy*. *Perkin-Elmer Corporation* **1992**, *40*, 221.
6. Stevie, F.A., et al., Introduction to x-ray photoelectron spectroscopy. *Journal of Vacuum Science & Technology A* **2020**, *38*(6), 063204.
7. Kraut, E.A., et al., Precise Determination of the Valence-Band Edge in X-Ray Photoemission Spectra - Application to Measurement of Semiconductor Interface Potentials. *Physical Review Letters* **1980**, *44*(24), 1620-1623.
8. Kumar, N., et al., Design of low surface roughness-low residual stress-high optoelectronic merit a-IZO thin films for flexible OLEDs. *Journal of Applied Physics* **2016**, *119*(22), 225303.

Chapter 3: Dependence of performance on the growth of active layer

This chapter begins by optimizing the active layer of gallium oxide. From the reported literature, it has already been established that both crystalline and amorphous phases may be employed for the fabrication of solar-blind photodetectors. The films may be deposited on various substrates, some of which have a higher lattice mismatch than the others. This would mean that the strain which is introduced in the films would vary with the change in the atomic arrangement of the atoms on the substrate itself. Thus, we first try to find the strain induced differences in optoelectronic performance of polycrystalline β -Ga₂O₃ on different orientations of silicon substrate. For this, three different orientations (100), (110) and (111) were used for the growth of gallium oxide films and their consequent photodetector performances were compared. Subsequently, polycrystalline films were also optimized on the sapphire *c*-plane sapphire substrate which has a lower lattice mismatch (~6.6%) with Ga₂O₃ by depositing varying thicknesses via RF magnetron sputtering at 500 °C under 1% O₂ ambient by varying the deposition time. Photodetectors fabricated for different thicknesses show excellent solar-blindness but the response time improves with increasing thickness. The persistent photoconductivity in the devices is directly correlated with the quality of the films and the oxygen-related defects in the system as studied by XPS. Next in this chapter, we also found mixed-phase, polycrystallinity in sputtered Ga₂O₃ thin films deposited on *c*-plane sapphire at room temperature which also boasts of a high performance even with facile fabrication.

3.1 Strain induced performance difference

β -Ga₂O₃ has been extensively studied for the fabrication of solar-blind photodetectors.[1-5] It can be grown homoepitaxially as well as heteroepitaxially on β -Ga₂O₃ and sapphire substrates, respectively.[6, 7] They have also been grown as heterostructures on foreign substrates such as GaN, SiC, mica, etc.[8-10] but the cost is quite high and the technology still a long way from development. Silicon technology is quite mature and growing beta gallium oxide on Si would lead to an easy integration with the existing technology leading to more cost-effectiveness and easier commercialization. The quality of thin films grown on a substrate depends on multiple factors such as their lattice parameters, the stability of the film itself, its bonding with the substrate below, method of deposition, etc.[11-13] One of the major contributing factors is the surface energy of the substrate and its correlation with the surface energy of the grown thin

Chapter 3: Dependence of performance on the growth of active layer

film. The growth kinetics, nucleation rate, and the subsequent mode of growth determines the quality of the film grown.[14, 15] Generally, it has been observed, especially in the case of polycrystalline semiconductor films that larger grain size depicts a good film growth. But the actual growth of the films is a complicated process with far too many parameters to be considered simultaneously. In particular, the growth becomes even more complicated in case of high lattice mismatch between the film and the substrate. Such is the case for gallium oxide deposition on Si substrates. Growing β -Ga₂O₃ on Si is often challenging because of the high lattice mismatch between the two, leading to the growth of amorphous or poorly crystalline films. There have been reports of the successful growth of polycrystalline β -Ga₂O₃ thin films on Si substrate.[16, 17] Kim et al. have reported that amorphous films with very small crystallites were observed when gallium oxide was grown on Si (100) using MOCVD.[18] Guo et al., on the other hand, fabricated good (-201) oriented films on Si (100) using laser molecular beam epitaxy.[17] Arora et al. have fabricated solar-blind photodetectors on RF Magnetron sputtered β -Ga₂O₃ films on Si (100) with high responsivity by employing a high temperature seed layer which increases the crystallinity of these thin films.[19]

Usually, the room temperature fabrication of Ga₂O₃ on Si leads to amorphous films because of the high lattice mismatch but providing thermal energy during growth (in the form of high temperature to the substrate) leads to polycrystalline nature. The grown films may have varied orientations and are usually reported on Si (100). Since the surface energy for different orientations of Si is different, it is expected that the growth would be varied on the different planes.[20-22] Yen et al. have studied the role of interfacial oxide layer on the preferred orientation for the growth of the gallium oxide on Si.[23] Gu et al. have studied the microstructure of gallium oxide on different Si orientations. They have shown that the lattice mismatch of the grown films with Si is the highest with (110) orientation as compared to the other orientations. Also, it was found that the growth can be further improved by annealing and/or introducing a seed layer.[24] On the other hand, Yadav et al. have also fabricated gallium oxide thin films on Si (100) and Si (111) and have shown that growth is better on Si (100) because of its rectangle projections as compared to the hexagonal projections of Si (111).[25] The literature of Ga₂O₃ on Si, especially the role of the orientations of the substrate, is still divisive. Moreover, the correlation of the film growth on differently-oriented substrate with the photodetector performance is still lacking.

The growth of thin films is an unpredictable and complicated process, governed by factors such as the non-equilibrium processes of deposition rate and atomic arrangement, grain growth and

coalescence and the subsequent formation of continuous thin film.[26] All these processes depend heavily on the interfacial energy between the thin film material and the substrate. Once deposition starts occurring, the rate of the incoming atoms and the atomic rearrangement on the surface of the substrate leads to a non-equilibrium competitive process, often resulting in stress and strain to develop in the film.[14] Any thermal energy provided to the substrate will lead to alteration of these growth kinetics. Grains forming on the substrate start to coalesce and form a continuous film which may lead to increased strain due to the structural changes as the films grow.[27] With increasing thickness, grain boundaries start to fill up and there occurs another transformative strain (especially in polycrystalline aggregates) because the grains are now attached to the substrate below.[14] This implies that the final outcome of any thin film deposition is dependent on the growth kinetics which is dominated by the interfacial energies between the film material and the substrate. Considering this in mind, it becomes interesting to see the role that interfacial surface energy of the substrate has on the gallium oxide thin film growth and its fabricated PDs. To investigate this, polycrystalline β -Ga₂O₃ was grown on three differently oriented *p*-Si – (100), (110) and (111) – at a high substrate temperature of 750°C. The temperature was chosen to overcome the lattice mismatch and help in the growth of crystalline films by providing enough thermal energy to the sputtered material to be able to relax and rearrange on the substrate itself. The nomenclature of the films and devices is based on the orientation of the Si substrate used.

3.1.1 Experimental section

p-Si of three different orientations [(100), (110) and (111)] were cleaned ultrasonically for 30 minutes sequentially in soap solution, de-ionized water, acetone and propanol, and finally blown-dry with N₂ gun. Polycrystalline Ga₂O₃ films (approx. 300 nm thick) were then deposited by RF Magnetron Sputtering using a Gallium Oxide target (99.99% purity, supplied by K. J. Lesker). The base pressure of the vacuum chamber was kept at 8×10^{-7} Torr while the depositions were done at 750°C at 100 W RF power and 3 mTorr working pressure using Ar gas. Extreme care was taken to ensure that all the parameters (except for the surface energy based on different orientations) was kept same for all the three samples. The schematic of the growth along with the temperature profile is shown in Figure 3.1 (a,b). For the introduction of a high temperature seed layer, the temperature profile as shown in Figure 3.1 (c) was adopted. The Ga₂O₃ seed layer thickness is about 15 nm. Subsequently, photodetectors were fabricated on the samples using Cr/Au (5nm/120nm) interdigitated electrodes (IDE) using a thermal

Chapter 3: Dependence of performance on the growth of active layer

evaporator and physical shadow mask. The devices are henceforth named as “(100)”, “(110)” and “(111)”, respectively, based on the growth of β -Ga₂O₃ on different orientations of Si.

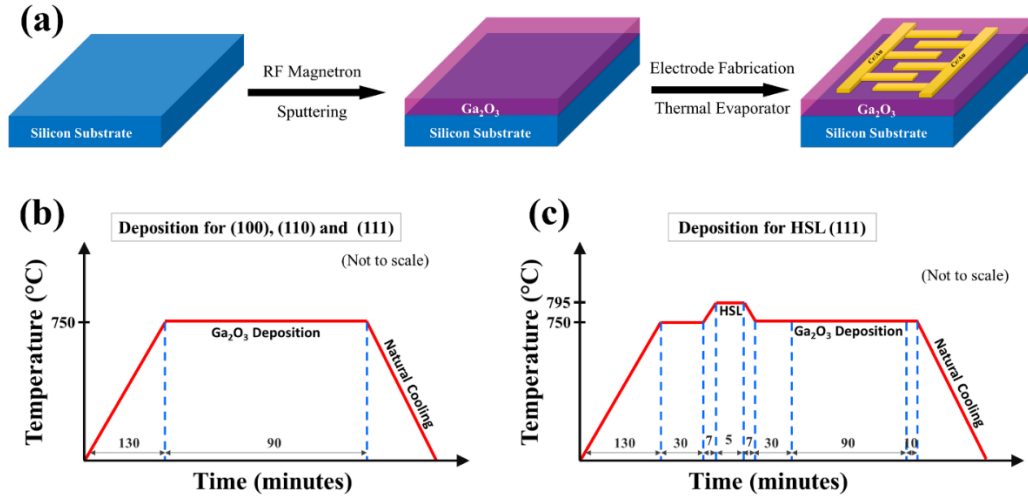


Figure 3.1 (a) Schematic of the growth of gallium oxide on Si substrates and of the temperature profile followed for the depositions of (b) (100), (110) and (111) and (c) HSL (111).

3.1.2 Results and Discussion

Silicon occurs in a diamond structure and the different planes of orientation offer different properties.

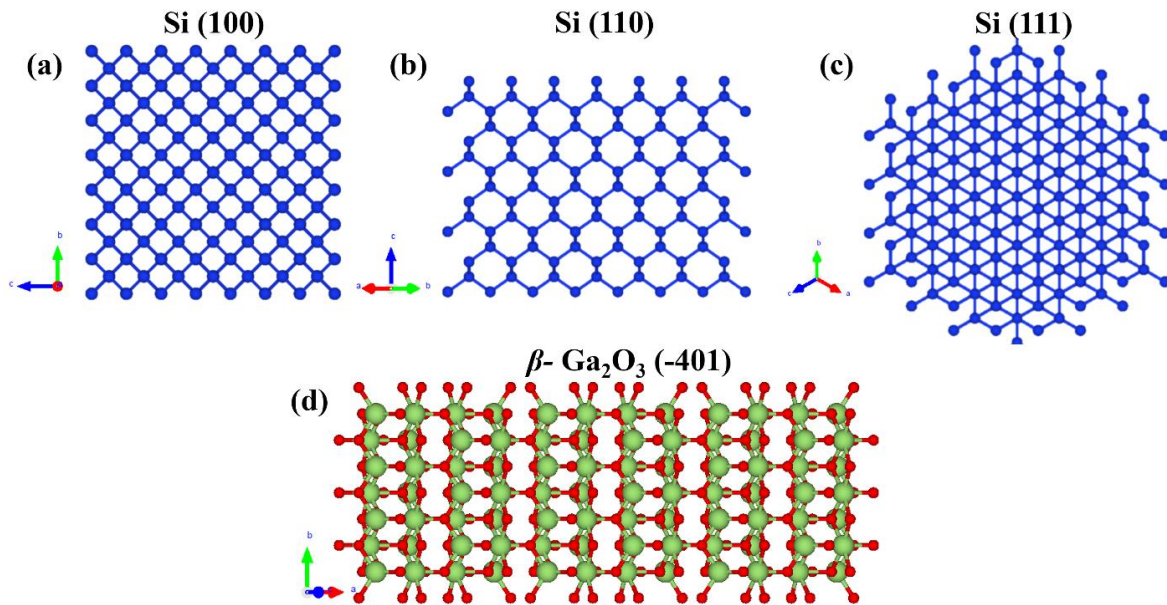


Figure 3.2. Atomic arrangement of atoms in the Si crystal structure for the (a) Si (100) plane, (b) Si (110) plane, (c) Si (111) plane and (d) crystal structure of β -Ga₂O₃ in the (-401) plane. Produced using VESTA software.[28]

Chapter 3: Dependence of performance on the growth of active layer

The atomic arrangement of Si atoms along the various planes changes as shown in Figure 3.2 (a-c). The varied arrangements lead to differences in the number of dangling bonds, free surface energy, oxidation rate, etc., all of which play an important role in the growth of thin films on Si. The surface energy of Si (100), (110) and (111) varies as 2130, 1510 and 1230 ergs cm⁻². [29]

The surface morphology of the thin films grown on varied orientations of Si was studied using Atomic Force Microscopy (AFM) images. Figure 3.3 shows the AFM micrographs of 1 μ m x 1 μ m scan size. The morphologies of the films are diverse with Ga₂O₃ on the Si (100) and (111) showing coarser grains while that on Si (110) showing much smoother and rounder grains. The RMS roughness of the films decreases in the order of Si (100) > Si (110) > Si (111) having the values of 2.54 ± 0.03 nm, 2.47 ± 0.09 nm and 2.31 ± 0.06 nm, respectively.

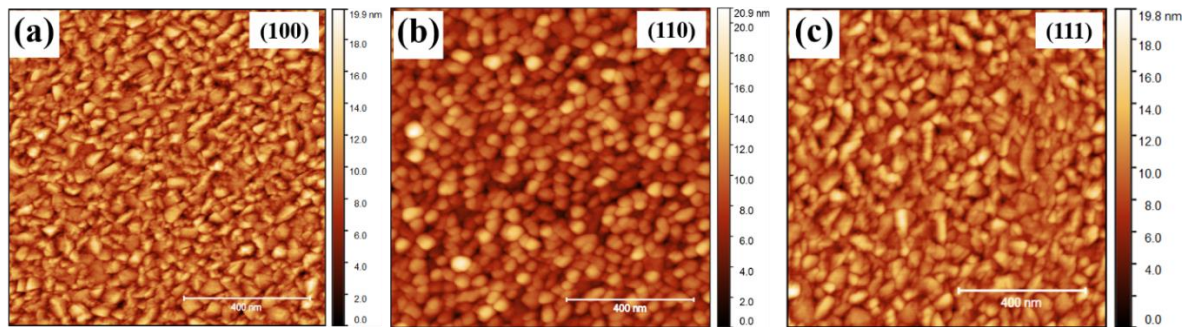


Figure 3.3 AFM micrographs of β -Ga₂O₃ thin films grown on Si (100), (110) and (111), respectively.

To compare the quality of thin film growth, grain size distribution has been calculated for all the samples using the watershed algorithm as applicable in Gwyddion software.[30] The grain size here represents the actual visible grains and not the crystallographic grains of the polycrystalline thin films. AFM is a unique technique which, unlike other 2D morphological techniques, gives height along with the spatial information. This implies that algorithms which are employed for calculating the grain size distributions can take advantage of the information in z -direction to give a better approximation of the individual grain size. Generally, for large-sized, individual grains, thresholding (using parameters such as height, slope, curvature, etc.) is used but for complicated data structures, these give very poor results. Watershed algorithm, on the other hand, is employed for local minima detection and image segmentation. Figure 3.4 (a-c) shows the grain marking on the AFM micrographs using the watershed mask. Once marked, the statistical diameter for the grain size distribution is shown in Figure 3.4 (d-f). The grain size distribution for (100) shows the smallest mean grain size as compared to (110) and

(111). The largest grains are present for the (111) thin film implying that the best growth in terms of grain size is for the gallium oxide grown on Si (111).

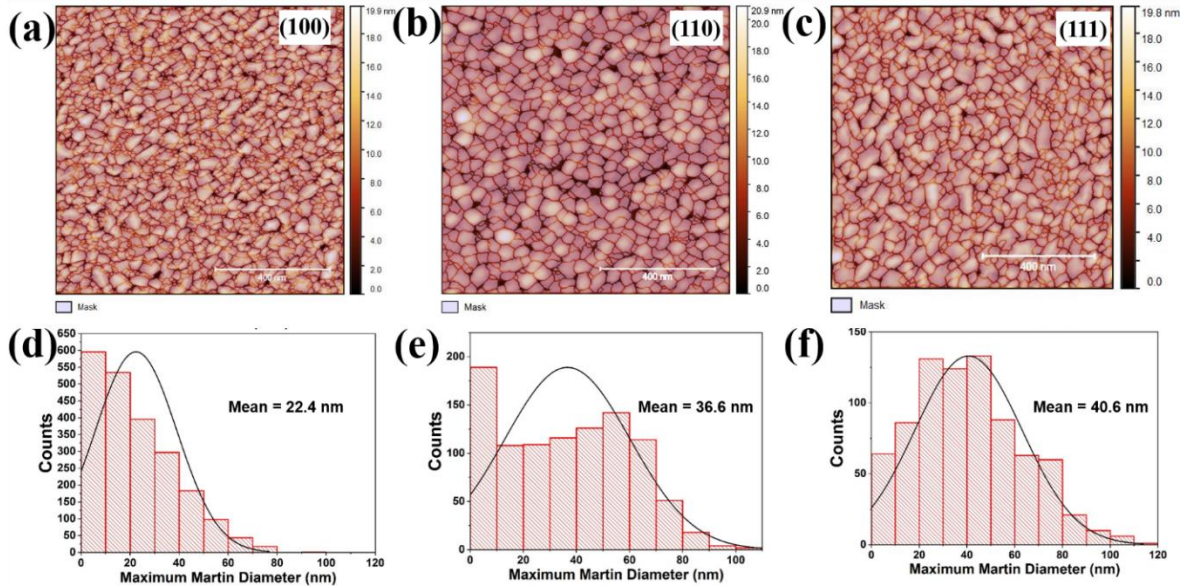


Figure 3.4 AFM micrographs with the watershed mask determined in Gwyddion software along with the grain size distribution calculated from the above watershed mask for β -Ga₂O₃ grown on (a,d) Si (100), (b,e) Si (110) and (c,f) Si (111).

In addition to the morphological characterizations, the structural changes for all the samples were checked using Grazing Incidence X-ray Diffraction (GIXRD). Figure 3.5 (a) shows the GIXRD data recorded for $\omega = 1.5^\circ$. All the samples show polycrystalline nature of Ga₂O₃ with the dominant peak being at 30.463° corresponding to (-401) peak of β -Ga₂O₃ (JCPDS Card No. – 041-1103). The peaks on all the three samples show a shifting towards the lower 2θ implying a tensile strain leading to an increase in the lattice constant. The shift is maximum for Si (100) while being the minimum for Si(111) orientation, indicating that the film grown on (111) plane is the least strained. The crystallinity of the film and the nature of the strain can also be judged by the broadening of the XRD peaks. For this purpose, a closer inspection of the dominant peak is shown in the zoomed-in view of Figure 3.5 (b). The peaks are de-convoluted into two peaks with both showing the least full width at half maxima (FWHM) for Si (111) and hence, the lowest non-uniform strain in the Ga₂O₃ on this orientation.

Strain and stress in the thin films can be measured by two different ways – deflection techniques based on determining the radius of curvature of the substrates and by direct measurements of interplanar spacings using XRD techniques. The former includes optical interferometry, laser

scanning and double-crystal diffraction topography while the latter includes grazing incidence X-ray scattering (GIXS) and high resolution X-ray diffraction techniques.[31]

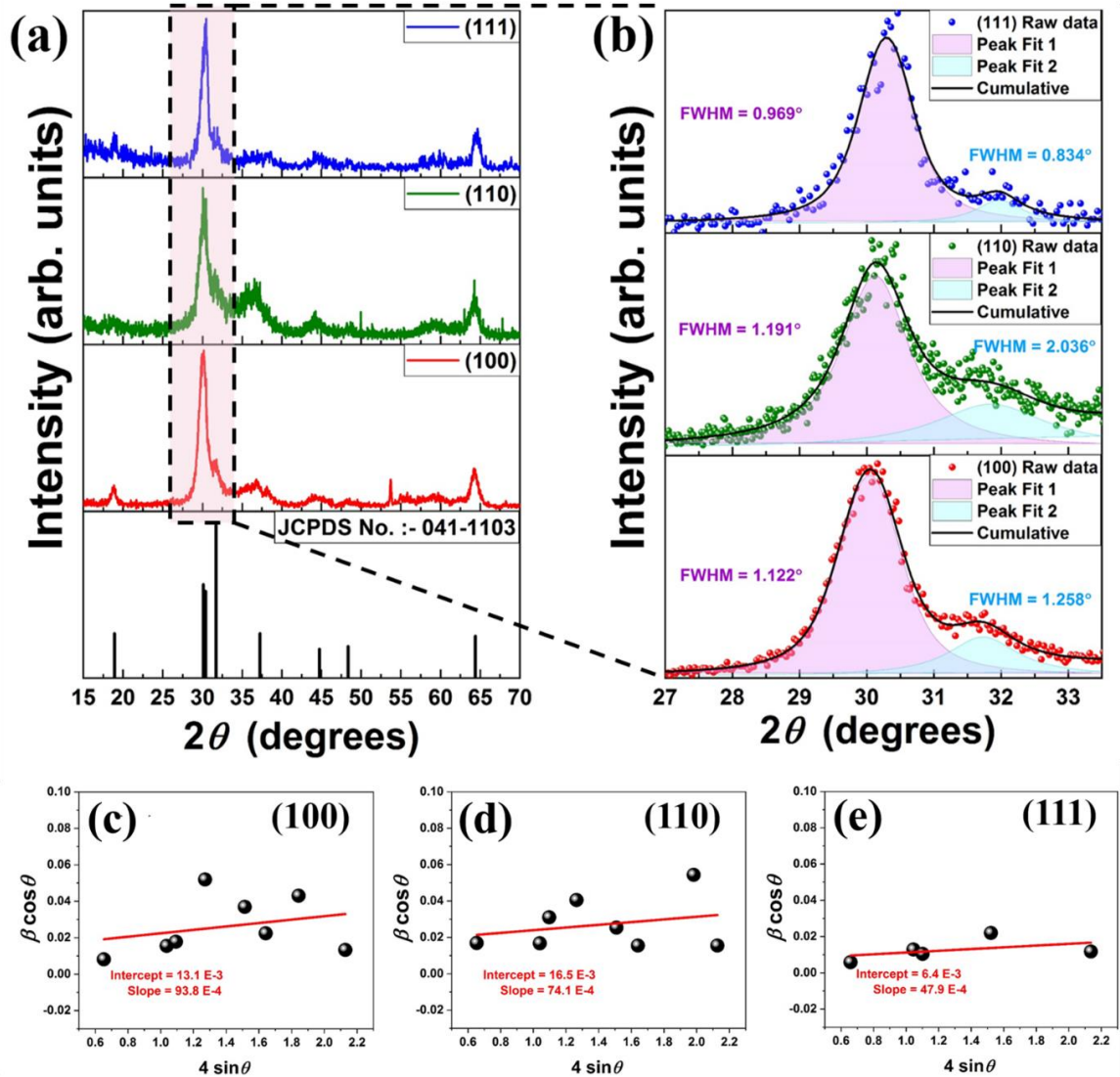


Figure 3.5. (a-b) GIXRD data of the three samples showing the formation of β -Ga₂O₃ on all three orientations of Si. The zoomed-in view of the dominant peaks are fitted using a Voigt function and shows the least FWHM (and hence strain) for (111). (c-e) W-H plots of the three samples with the linear fit showing the crystallite size and strain in the three films.

The microstrain present in the thin films and the crystallite size can be estimated from the Williamson-Hall (W-H) method. In general, peak broadening of the XRD peaks can depend on both the crystallite size and lattice microstrain.[32] Crystallite size measures the size of domains which diffract coherently. Smaller crystallite size leads to more broadening of peaks. Since diffraction occurs from parallel planes and the number of these parallel planes reduces with reducing crystallite size, the peaks become broadened. For the lattice strain, any imperfection in the lattice such as defects, dislocations, non-uniform lattice distortions, etc.,

Chapter 3: Dependence of performance on the growth of active layer

lead to a change in the lattice parameters leading to peak broadening. Both the factors contributing to broadening can be separated by using the W-H method.

Here, the size broadening and strain broadening are both independent of each other and vary differently with the Bragg angle θ . [33] According to the Scherrer equation, the broadening due to crystallite size (β_D) depends on θ as:

$$\beta_D = \frac{K\lambda}{D \cos\theta} \quad (3.1)$$

where, K is a proportionality constant depending on the peak shape and crystallite habitat, with value close to unity (in our case $K = 0.92$), λ is the wavelength of the X-ray used ($= 1.54 \text{ \AA}$) and D is the crystallite size. The strain broadening (β_ε), on the other hand, is given by:

$$\beta_\varepsilon = 4\varepsilon \tan\theta \quad (3.2)$$

where, ε represents the microstrain. The total broadening is a sum of these two individual broadenings (especially in the case of W-H isotropic strain model) and hence $\beta_T = \beta_\varepsilon + \beta_D$ can be modified in the form of:

$$\beta_T \cos\theta = 4\varepsilon \sin\theta + \frac{K\lambda}{D} \quad (3.3)$$

Performing a linear fit on the graph between $4 \sin\theta$ vs. $\beta_T \cos\theta$ gives the approximate crystallite size using the obtained y-intercept whereas the strain is determined from the slope of the linear fit. Another major factor contributing in the broadening is the instrumental broadening which has to be subtracted from the total broadening to get the actual sample broadening. [32] This exclusion has been carried out by correcting the peaks using a standard sample in the same configuration of the instrument as the actual datasets. To find the broadening (or the full width at half maxima (FWHM)), a non-linear function Voigt is used which is a combination of Lorentzian and Gaussian functions and it calculates the FWHM (β_O) as:

$$\beta_O = 0.5346 \times W_L + \sqrt{(0.2166 \times W_L^2 + W_G^2)} \quad (3.4)$$

where, β_O is the observed FWHM, W_L is the Lorentzian width and W_G is the Gaussian width. Since the peaks are fitted with a convolution of the Lorentzian and Gaussian profiles, a geometric mean is used to eliminate the instrumental broadening:

$$\beta_T = \left[(\beta_O - \beta_i) \sqrt{(\beta_O^2 - \beta_i^2)} \right]^{1/2} \quad (3.5)$$

Chapter 3: Dependence of performance on the growth of active layer

where β_i is the instrumental broadening. Using the above method, W-H plots for all three samples are shown in Figure 3.5 (c-e) where the intercept is related to the crystallite size while the slope determines the strain. The values of the crystallite size obtained for (100), (110) and (111) are 11 nm, 8.8 nm and 22 nm while the strain is 9.4, 7.4, and 4.8 ($\times 10^{-3}$) %, respectively.

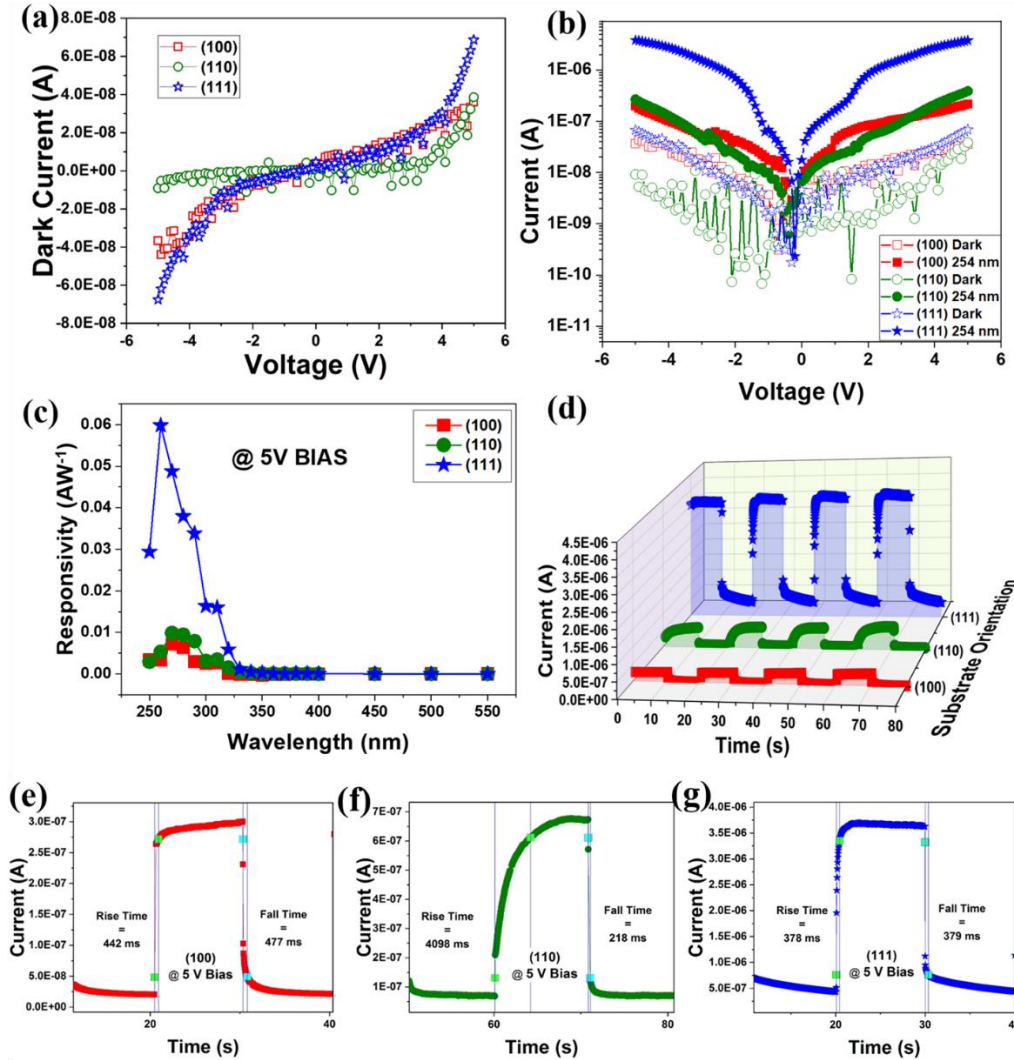


Figure 3.6 Device performance of the PDs fabricated on Si (100), (110) and (111). (a) Comparative dark current of the three devices, (b) Log I vs. V of the devices showing the maximum photoresponse of (111) to 254 nm incident light, (c) Responsivity vs. wavelength of the devices showing excellent solar blindness and (d) temporal response of the devices to repeated switching of incident light. Single cycle photoresponse of the devices of Ga₂O₃ on (e) Si (100), (f) Si (110) and (g) Si (111) to 254 nm incident light with their respective rise and fall times.

To investigate any correlation between the different growth of gallium oxide and the photodetector performance, interdigitated MSM photodetectors were fabricated on all three samples and performances compared. Figure 3.6 shows the performance of the different

Chapter 3: Dependence of performance on the growth of active layer

devices. Figure 3.6 (a) shows that the dark current is quite low (in the range of nA) for all the three devices with (111) exhibiting the highest dark current among the three. The Schottky nature of all the three devices is almost similar. Figure 3.6 (b) depicts the dark current and the corresponding photocurrent and although the (111) exhibits highest dark current, it also exhibits the highest photocurrent as well.

One of the main parameters of quantifying PD performance is responsivity (R) which is a measure of the electrical output per optical input. It is calculated as:

$$R = \frac{I_{ph} - I_{dark}}{P_{optical}} \quad (3.6)$$

where I_{ph} is the current under illumination, I_{dark} is the current under no illumination and $P_{optical}$ is the incident optical power falling on the device. All the three devices show excellent solar-blind nature with (111) showing highest responsivity of 0.6 A W^{-1} at 5 V bias (Figure 3.6 (c)). Another important parameter to judge a PD is the response of the device to repeated switching of the incident light. The temporal response of the devices is shown in Figure 3.6 (d) under 254 nm illumination (4.4 mW cm^{-2} intensity) with an on-off cycle of 10 sec intervals at 5V bias, which again corroborates the superior performance of (111) as compared to (110) and (100).

The rise time (and fall time) of the devices is characterized as the time taken for the device to go from 10% to 90% of the maximum current (90% to 10% of the maximum current) when the light is switched-on (switched-off). Figure 3.6 (e-g) shows a single cycle of temporal response demonstrating the better performance of (111).

Upon comparing the device, it is clearly visible that $\beta\text{-Ga}_2\text{O}_3$ grown on Si (111) outperforms those on Si (100) or Si (110). The only difference in these devices was the orientation of the underneath substrate. This implies that one of the key factors that could affect device performance – the actual growth of the gallium oxide thin film – is correlated to the surface energy. Since the various orientations have different atomic arrangements and varied dangling bond densities, they offer different free surface energies during growth of the thin film. Figure 3.7 shows the comparative plot between strain, crystallite size and PDCR for all the three samples of $\beta\text{-Ga}_2\text{O}_3$ grown on different orientations of Si. It clearly depicts that decreasing strain leads to an increase in the crystallite size and an enhanced performance of the fabricated device. The PDCR is calculated from the response to 254 nm of light (4.4 mW cm^{-2} intensity) using the formula:

$$PDCR = \frac{I_{ph} - I_{dark}}{I_{dark}} \quad (3.7)$$

To further validate the effect of strain on the performance of the device, a well-known method of reducing the strain further was employed – the use of a seed layer.

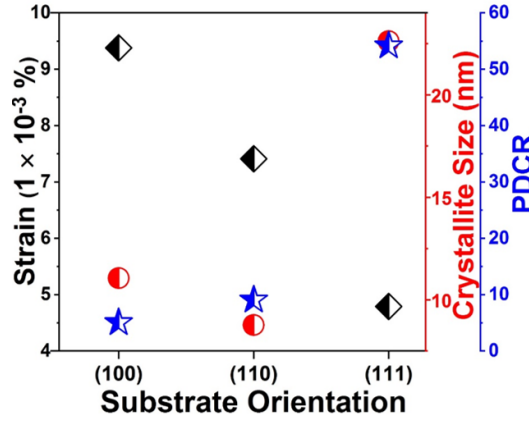


Figure 3.7 Comparison of the crystallite size and strain with the device performance of the polycrystalline Ga_2O_3 based solar-blind photodetectors.

Seed layers are often utilized to reduce the lattice mismatch between the substrate and the actual thin film and also to provide nucleation germs for the subsequent growth. This leads to an enhanced crystallinity in the deposited film by providing a sort of template for the growth above leading to better growth of films due to a lowered strain. To achieve this, a thin, high-temperature seed layer of gallium oxide was grown on *p*-type Si (111) substrate by using the temperature profile as given in Figure 3.1 (c). The grown films were characterized as above and the results of GIXRD are shown in Figure 3.8 (a). As seen from the zoomed-in peaks, the FWHM further decreases from 0.969° to 0.891° for the seed layer implying a reduced strain as compared to W/o SL. Even the W-H plots (Figure 3.8 (b)) shows the relative reduction in strain on the seed layer film with an increased crystallinity. Figure 3.9 shows the AFM micrographs of the HSL gallium oxide thin films. The RMS roughness of the HSL (111) is 1.65 ± 0.02 nm indicating very smooth films. Although by visual inspection, the grain size seems to decrease as compared to Si (111) as also indicated by the grain size distribution but in reality the crystallite size increases upon introduction of seed layer (see W-H plot in Figure 3.8 (b)). The mean grain size from the grain size distribution is about 32 nm which is smaller than that for without seed layer (~ 40 nm), while the crystallite size increases from 22 nm to 24 nm on adding the seed layer. There occurs a sort of agglomeration of grains during the growth which leads to lower grain sizes in the morphological characterizations but a bigger crystallite size in the structural characterizations. This implies that the grain size from morphological images

Chapter 3: Dependence of performance on the growth of active layer

such as SEM or AFM is not a direct evidence of better growth and lesser strain in the films (as in the case of HSL (111)) but a far better inference can be drawn from calculating the crystallite size which might give a direct evidence of increased crystallinity leading to better performance. The introduction of seed layer leads to a reduced strain in the films which should lead to better film quality and hence, one can expect improved device performance. This is exactly what is observed for devices fabricated on HSL (111).

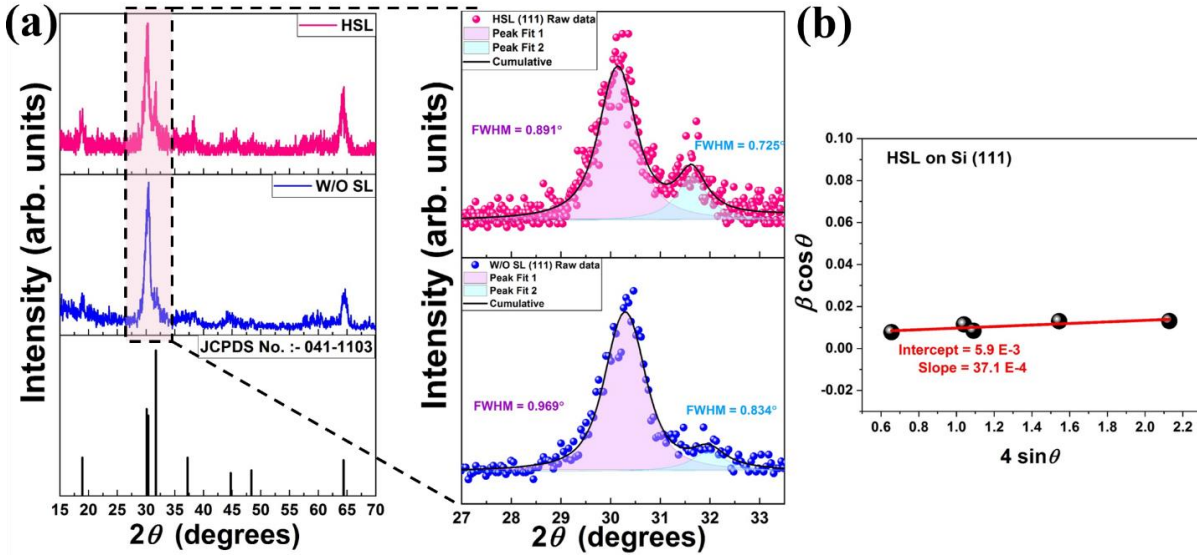


Figure 3.8 (a) GIXRD data of with and without seed layer samples of β -Ga₂O₃ on Si (111). The zoomed-in view of the dominant peaks shows a reduced FWHM (and hence reduced strain) upon introduction of a seed layer and (b) W-H plot of HSL (111) sample showing reduced strain and increased crystallite size.

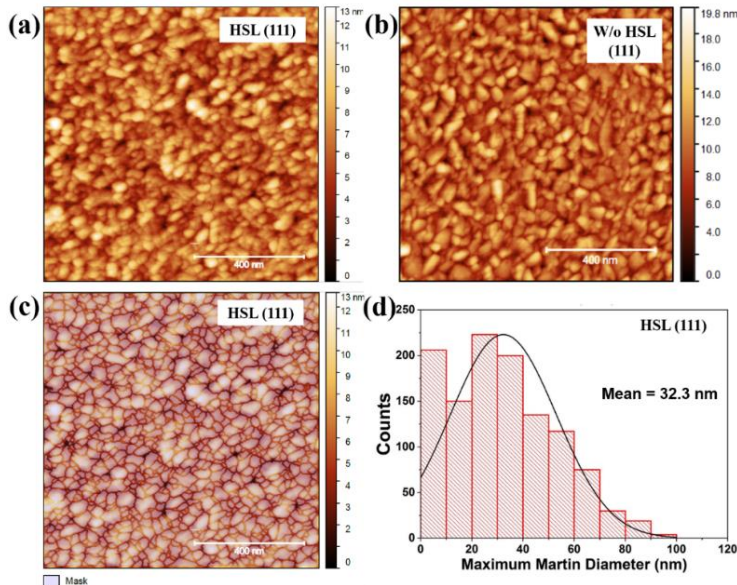


Figure 3.9 AFM micrographs of (a) with and (b) without seed layer samples of β -Ga₂O₃ on Si (111), (c) watershed mask used for calculating the grain size distribution which is shown in (d).

Chapter 3: Dependence of performance on the growth of active layer

The device performance is shown in Figure 3.10 which shows the enhanced performance on the seed layer deposited films. The device not only gives a higher response to light but becomes faster as well, thereby suggesting that indeed, strain in the films is directly related to the device performance and for fabricating high performance photodetectors, strain-free films become an absolute necessity.

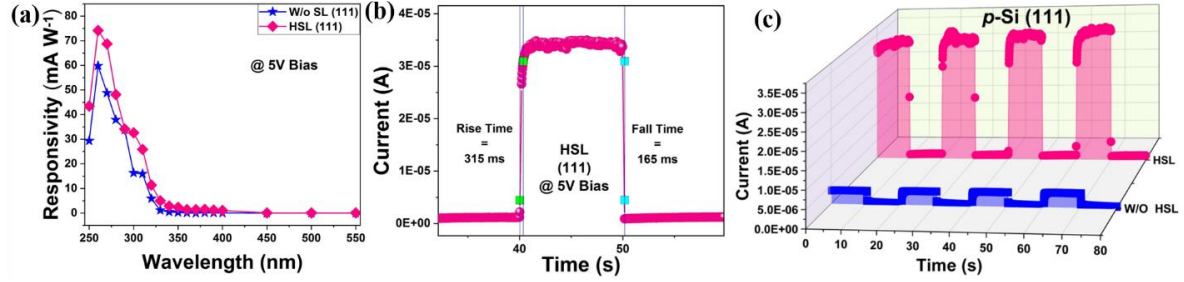


Figure 3.10 Device performance comparison of with and without seed layer in β -Ga₂O₃ on Si (111). (a) Responsivity vs. wavelength showing enhanced performance, (b) improved response times and (c) improved photoresponse.

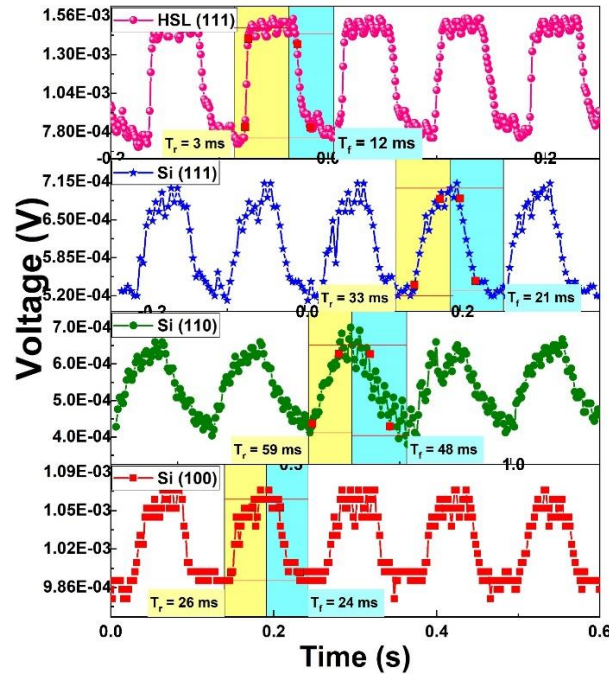


Figure 3.11 Device performance showing excellent stability even after 2100 hours using an optical chopper and oscilloscope. The T_r and T_d represents the rise time and the fall time of the devices, respectively. The x-axis and the y-axis represent different scales for all the four datasets. The data is recorded at 5 V bias under 254 nm UV-C light.

In terms of stability and repeatability, all the devices show excellent stability even after 2100 hours. The photoresponse with 254nm UV-C light chopped by an optical chopper interfaced with an oscilloscope is shown in Figure 3.11. The devices show repeatable trends even after

Chapter 3: Dependence of performance on the growth of active layer

storage under ambient conditions. The best device, HSL (111), shows excellent solar-blind photodetection with a quick response of 3ms and 12ms (rise time and fall time, respectively).

3.1.3 Conclusions

Polycrystalline β -Ga₂O₃ thin films were fabricated on three different orientations of Si – (100), (110) and (111) – at a high temperature of 750°C using RF magnetron sputtering. The subsequent photodetectors grown on the films showed the best performance for the films grown on Si (111). The lower surface energy and the hexagonal projections form a far better growth template for gallium oxide. This is corroborated by the least amount of strain and largest crystallite size for films grown on Si (111) as measured using Williamson-Hall isotropic strain model. In addition, the introduction of a seed layer helps in reducing the strain further which leads to an even bigger crystallite size, reduced strain and hence an enhanced performance. This work leads us to conclude that the performance of Gallium oxide thin films for photodetector applications can be enhanced by simply growing the films on Si (111) which promotes better growth in terms of crystallinity. In addition, it is also found that instead of relying solely on the morphological methods for grain size, a better indicator of good growth would be calculating the crystallite size which plays a far important role in predicting device performance in the case of Ga₂O₃ based solar-blind photodetectors.

3.2 Optimizing thickness of β -Ga₂O₃ film on sapphire substrates

β -Ga₂O₃ thin films can be grown on different substrates such as epitaxial substrates, sapphire, silicon, GaN, PET, etc. leading to homoepitaxial, heteroepitaxial, polycrystalline or even nanocrystalline films.[19, 34-37] Especially for the case of sapphire, crystallinity can be easily achieved because of the relative ease of growth of β -Ga₂O₃ owing to their low lattice mismatch.[38] For the case of oxides which are generally plagued with oxygen vacancies, the ultimate device performance is contingent on these vacancies which act as defect centres and are responsible for the high photoconductive gain in β -Ga₂O₃. [39, 40] They act as trap states for the charge carriers which makes the holes localized and the electrons go around the circuit multi-fold leading to very high external quantum efficiencies, thereby increasing the overall response. However, this trapping is also responsible for the slow response times of the devices since the carriers now take longer than usual to recombine.[41] Additionally, this trapping of the carriers may sometimes lead to an effect called persistent photoconductivity (PPC).[42] PPC is a light-induced effect wherein the photoresponse remains even after switching off the incident light. This leads to an increase in the level of dark current over a number of switching cycles, leading to false logic for the photodetectors.[43] Thus, it poses a serious issue,

especially where the reliability of these photodetectors is concerned. Hence, it becomes imperative to optimize the Ga₂O₃ thin films on sapphire substrates before achieving high performance photodetection.

3.2.1 Experimental section

c-plane sapphire substrates were first cleaned ultrasonically in acetone, methanol and deionized water, successively, for 20 minutes each and blown dry with N₂. These were then loaded into the vacuum chamber which was pumped down to a base vacuum of 8×10^{-7} Torr. Ga₂O₃ was sputtered (using Ga₂O₃ target, 99.9% pure, sourced from K.J. Lesker) on to the substrates using Ar as the working gas with 1% O₂ at a working pressure of 3 mTorr, deposition temperature of 500°C and RF power of 100 W. The thickness of the films was varied by using different deposition times. Films of five different thicknesses – 5 nm, 20 nm, 50 nm, 100 nm, and 300 nm were grown. Subsequent to film growth, photodetectors were fabricated by depositing interdigitated electrodes of Au using a thermal evaporator via a physical shadow mask.

3.2.2 Results and Discussion

Figure 3.12 (a) shows the GIXRD data of the thin films grown on *c*-plane sapphire, depicting the polycrystalline nature of all the grown films. All the thicknesses show a characteristic peak around 37.4° indicative of (401) phase of β -Ga₂O₃ (JCPDS Card No. – 041-1103).

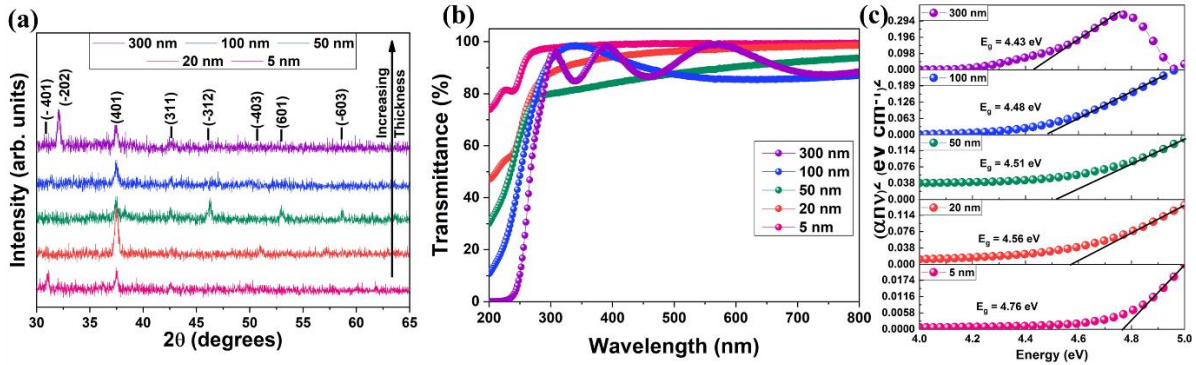


Figure 3.12 (a) GIXRD data of the films of varying thickness showing the formation of β -Ga₂O₃ on *c*-plane sapphire. (b) Transmittance data recorded using UV-Vis spectrophotometer and (c) band gap calculations using Tauc plot for varying film thickness.

Figure 3.12 (b) shows the transmittance data of the grown films, showing that the films absorb only in the UV-C region while they show a transmission above 80 % for higher wavelengths. Figure 3.12 (c) represents the calculation of the bandgap of the films using the absorbance data for all the samples using the Tauc plot and extrapolating the curve for the $h\nu$ vs $(\alpha h\nu)^2$ graphs

Chapter 3: Dependence of performance on the growth of active layer

(where α is the absorption coefficient and $h\nu$ denotes the incident photon energy).[44] The band gap of the films decreases with increasing thickness. This is consistent with literature[45-47] and may be attributed to the reduced crystallite size, high density of localized states within the band gap and an increased defect concentration strongly affecting the quantum confinement leading to an increase in the band gap with reduced thickness.[48]

The evolution of the morphology of the films was studied by using the Atomic Force Microscopy. Figure 3.13 (a-e) represents the AFM micrographs of scan size $1\mu\text{m} \times 1\mu\text{m}$. The films formed are continuous and uniform and there is a clear increase in the size of grains with increasing thickness of $\beta\text{-Ga}_2\text{O}_3$. The RMS roughness of the films remain quite low for film thickness of about 20 nm but then increases for higher thicknesses (see Figure 3.13 (f)). The values of RMS roughness are calculated to be 0.23 ± 0.04 nm, 0.23 ± 0.01 nm, 0.59 ± 0.03 nm, 0.68 ± 0.01 nm, and 1.12 ± 0.12 nm, for 5 nm, 20 nm, 50 nm, 100 nm and 300 nm, respectively.

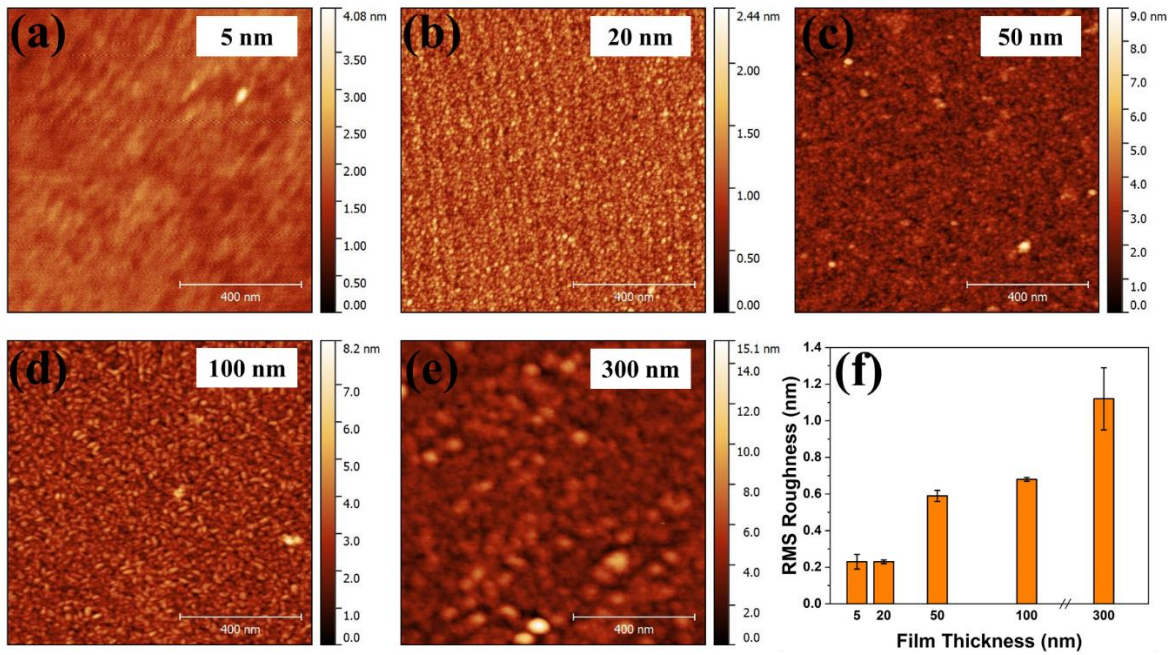


Figure 3.13. AFM micrographs showing the morphology for (a) 5nm, (b) 20 nm, (c) 50 nm, (d) 100 nm and (e) 300 nm. (f) variation of the calculated RMS roughness for the varying thickness of $\beta\text{-Ga}_2\text{O}_3$ thin films.

To check the effect of thickness of $\beta\text{-Ga}_2\text{O}_3$ for photodetection applications, devices were fabricated by using Au electrodes in the form of interdigitated electrodes as shown in the device schematic in Figure 3.14 (a). The I-V response of the devices to 245 nm, 365 nm, 532 nm and 650 nm wavelengths for the different thicknesses is shown in Figure 3.14 (b-f). All the different

devices show excellent solar-blindness and do not respond to UV-A or visible light while producing a photocurrent in the UV-C region.

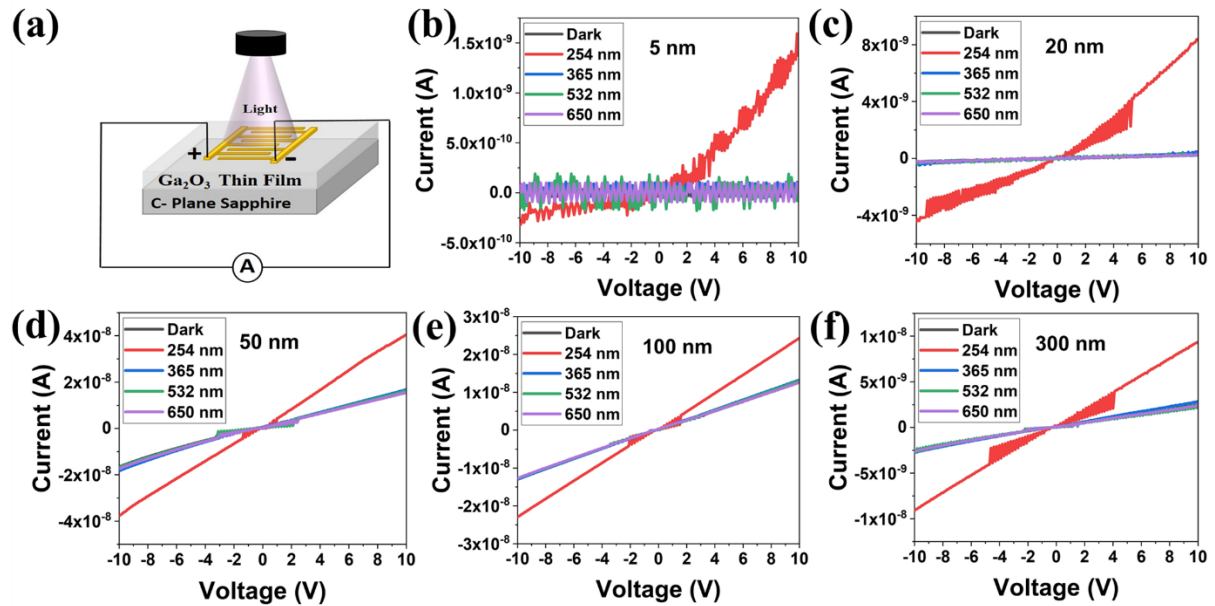


Figure 3.14 (a) Device Schematic. I-V curves under dark and light conditions (254 nm, 365 nm, 532 nm, 650 nm incident light) for devices fabricated on (b) 5 nm, (c) 20 nm, (d) 50 nm, (e) 100 nm and (f) 300 nm thick films of β -Ga₂O₃.

Figure 3.15 (a) shows the temporal response of the photodetectors to repeated switching on and off of 254 nm incident light at 10 sec intervals. The rise time and the fall time reduces with increasing thickness which implies that better and faster devices can be fabricated using thicker films. The rise time decreases from 8.37 s to about 287 ms for 5 nm and 300 nm β -Ga₂O₃ devices, respectively, a reduction of more than 96%. The fall time also reduces from 7.61 s to 178 ms for 5 nm and 300 nm β -Ga₂O₃ devices, respectively, reducing by about 98%. Along with the faster response, another major reduction is in the persistent photoconductivity in the devices. There is a marked trend in the PPC effect observed for increasing thickness. The level of dark current increases continuously with each successive light switching cycle but increment in the dark current becomes smaller and smaller with increasing thickness. The observed PPC though smallest in 300 nm films, is still present in all the devices. Since the photodetectors are fabricated with identical electrodes, this implies that this change in the PPC effect is dependent directly on the growth of the Ga₂O₃ being deposited for different thicknesses.

To probe deeper into the cause of the reduction of the PPC effect, X-ray photoelectron spectroscopy was carried out for all the samples. Figure 3.15 (b) shows the Ga 3d peak of gallium oxide centred around 20 eV which can be decomposed into two peaks. The lower

Chapter 3: Dependence of performance on the growth of active layer

binding energy peak corresponds to the Ga^+ state while the higher binding energy peak is for the Ga^{3+} . [49, 50] The presence of the Ga^+ state shows the film is oxygen deficient or sub-stoichiometric. The ratio of area of peaks for $\text{Ga}^{3+}/\text{Ga}^+$ increases from about 1.3 to 3.8 for 5 nm to 300 nm, respectively, thereby implying that the amount of stoichiometric Ga_2O_3 increases with increasing thickness. For the lower values of thickness, the change in the ratio of $\text{Ga}^{3+}/\text{Ga}^+$ is not that pronounced but it shows a marked improvement for the 300 nm film. Moreover, the O 1s spectra was used to study the oxygen deficiency in the films. As shown in Figure 3.15 (c), the O 1s spectra can be decomposed into two peaks, O(I) peak (lower binding energy) corresponding to the Ga-O bond while the O(II) peak (higher binding energy) corresponds to the O^{2-} ion in the oxygen-deficient region. The oxygen related defects can thus be evaluated by calculating the area ratio of $\text{O(II)}/(\text{O(I)} + \text{O(II)})$. The area ratio for the 5 nm, 20 nm, 50 nm, 100 nm and 300 nm thick films varies from 49.5 %, 46.9 %, 43 %, 39 % and 29.8 %, respectively.

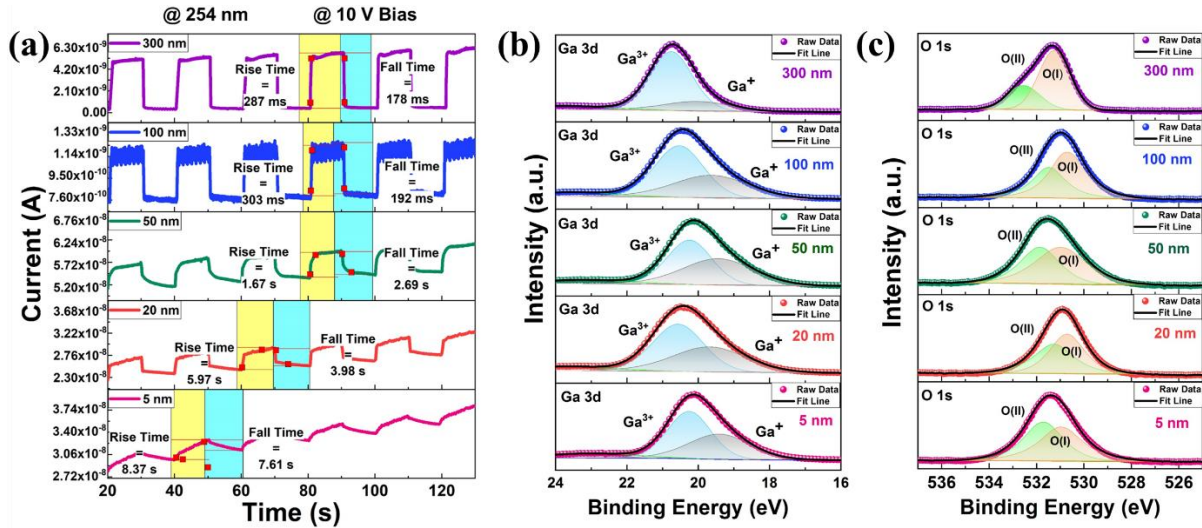


Figure 3.15 (a) Temporal photoresponse of the devices with calculated rise and fall time. Reduction in the PPC effect can be clearly seen with increasing $\beta\text{-Ga}_2\text{O}_3$ film thickness. XPS core level spectra for the (b) Ga 3d and (c) O 1s peaks for the varying film thickness of $\beta\text{-Ga}_2\text{O}_3$.

The decrease in the area ratio implies an improvement in the stoichiometry of the films with lesser number of oxygen vacancies progressively with increasing thickness. This explains that the reduction of the PPC effect with increasing thickness is because of the improvement in the overall quality of the film with thick films having lesser number of oxygen-related defects. Figure 3.16 (a) shows the variation of the PDCR (photo-to-dark-current ratio, calculated as $((I_{\text{light}} - I_{\text{dark}})/I_{\text{dark}}) \times 100$), the area ratio of $\text{O(II)}/(\text{O(I)} + \text{O(II)})$, and the $\text{Ga}^{3+}/\text{Ga}^+$ with increasing thickness of $\beta\text{-Ga}_2\text{O}_3$. There is a clear correlation between the observation of the PPC effect and the oxygen-related defects in the system.

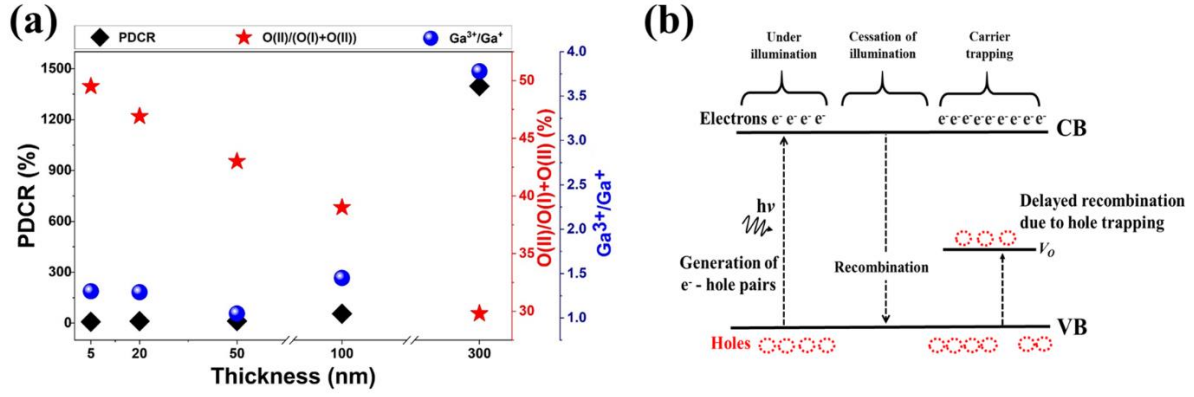


Figure 3.16 (a) Correlation of the photo-to-dark current ratio (PDCR), ratio of O(II)/(O(I) + O(II)) (depicting the oxygen-related defects) and $\text{Ga}^{3+}/\text{Ga}^+$ for the varying film thicknesses and (b) schematic representing the trapping of charge carriers leading to a delayed recombination which is responsible for the observed PPC effect.

The decrease in the PPC (and the consequent increase in the PDCR) can be understood better by looking at Figure 3.16 (b). Upon illumination of light, electron hole pairs are generated which get separated due to the Schottky contact and we get a measureable amount of photocurrent. Upon the cessation of illumination, the carriers should ideally recombine and the photocurrent should come down to the level of dark current. But in the presence of oxygen vacancies which act as trap states, the level does not fall down to the initial value even after the incident light is switched off. The holes in Ga_2O_3 have a very high effective mass and tend to get localized on the lattice distortions such as oxygen vacancies, thereby getting trapped.[41, 51] As long as the hole remains trapped at the trap, the corresponding electron goes around the circuit manifold and leads to a high external quantum efficiency. This leads to a high photoresponse and hence a high PDCR. But at the same time, this trapping leads to an increased carrier lifetime of the hole, thereby delaying the carrier recombination. This leads to slowing down of the device and an increase in the number of such traps (V_o) leads to a PPC effect with the photocurrent still persisting even after the cessation of illumination. More the number of oxygen vacancies, more pronounced is the PPC effect and slower is the response of the device. Therefore, to achieve the best performance with highest photoresponse, fastest photodetection and negligible PPC, it becomes imperative to reduce the oxygen vacancies to a minimum, so that the carrier trapping may be minimized.

3.2.3 Conclusions

β - Ga_2O_3 thin films were fabricated on *c*-plane sapphire via RF Magnetron sputtering at 500°C under 1% O_2 ambient. Five different thicknesses – 5 nm, 20 nm, 50 nm, 100 nm and 300 nm – were fabricated by varying the deposition time. The films turn out polycrystalline, with the

Chapter 3: Dependence of performance on the growth of active layer

band gap decreasing with increasing film thickness. The grain size increases as the thickness increases. Photodetectors fabricated for different thicknesses show excellent solar-blindness but the response time improves with increasing thickness. The PPC effect is more pronounced for thinner films and reduces drastically for the maximum thickness sample. PPC in the devices is directly correlated with the quality of the films and the oxygen-related defects in the system as studied by XPS. The lesser the number of oxygen vacancies, better is the device performance with reduced PPC effect. This work shows that thicker films have a lower number of oxygen vacancies and a better stoichiometric ratio and hence can be utilized for fabricating better and faster optoelectronic devices with minimum PPC.

3.3 Room temperature crystallinity

One of the major challenges for oxide-based devices is its high processing temperatures. Most of the oxide materials crystallize at high temperatures, with room temperature counterparts being restricted to the amorphous phase. This has led to a dearth of crystalline oxides at low temperatures which often have superior properties than their amorphous counterparts. Gallium oxide, Ga_2O_3 , is one such oxide which requires temperatures in excess of 500°C to crystallize into its stable phase – the β phase. Occurring in 5 different phases, only the β phase is stable while the α , ε and γ are meta-stable phases and δ/κ phase is unstable. Nevertheless, all the phases change into the stable β phase at high temperatures or pressures, but room temperature crystallinity in gallium oxide has remained elusive till now.

3.3.1 Experimental details

β - Ga_2O_3 thin films were fabricated on *c*-plane sapphire via RF Magnetron sputtering at room temperature for varied deposition parameters such as RF power and deposition pressure in different combinations using Ar with 1% O_2 . The films were characterized using Panalytical Xpert³ with Cu $K\alpha$ in the Goni mode. High resolution transmission electron microscopy images were recorded using Jeol JEM 2100 PLUS TEM (JEOL USA, Inc., Peabody, MA, USA). Devices were fabricated by using Au interdigitated electrodes on as-deposited samples and tested for photodetection capabilities.

3.3.2 Results and discussion

Figure 3.17 (a) shows the XRD data for the different samples grown on *c*-plane sapphire using different deposition conditions for 90 minutes while providing no external heat to the substrates. It is noteworthy that the substrate temperature even after 90 minutes of continuous deposition does not exceed 32°C , even with the highest deposition power. Upon comparison

with standard data (JCPDS data card number – 00-041-1103 for β -Ga₂O₃, 00-006-0503 for α -Ga₂O₃), it was found that all the films show characteristic peak of both α and β -Ga₂O₃, thereby implying a mixed phase room-temperature poly-crystallinity. Judging from the peak intensity and the full-width at half maxima (FWHM) of the most intense peaks, the RT – 150W was found to be the best sample with the highest crystallinity and was thus chosen for further studies. Figure 3.17 (b) shows the TEM images showing the growth of Ga₂O₃ with about 400 nm thickness for the RT-150W sample. The inset shows the selected area electron diffraction (SAED) patterns of Ga₂O₃ showing the polycrystalline nature of the films. Upon analysis, the calculated d-spacing showed the maximum intensity for the 0.254 nm, which belongs to β -Ga₂O₃. Higher d-spacing is also observed corresponding to α -Ga₂O₃. Figure 3.17 (c) depicts the HRTEM image showing the Ga₂O₃ film and sapphire interface. The insets show the FFT patterns of the Ga₂O₃ and the substrate below. The former corroborates the formation of the mixed-phase crystallinity in gallium oxide. Shown alongside in the zoomed-in image is a mapping of the selected area, studied by taking FFTs of different regions. The mapping shows that the two phases formed are randomly spread across the film.

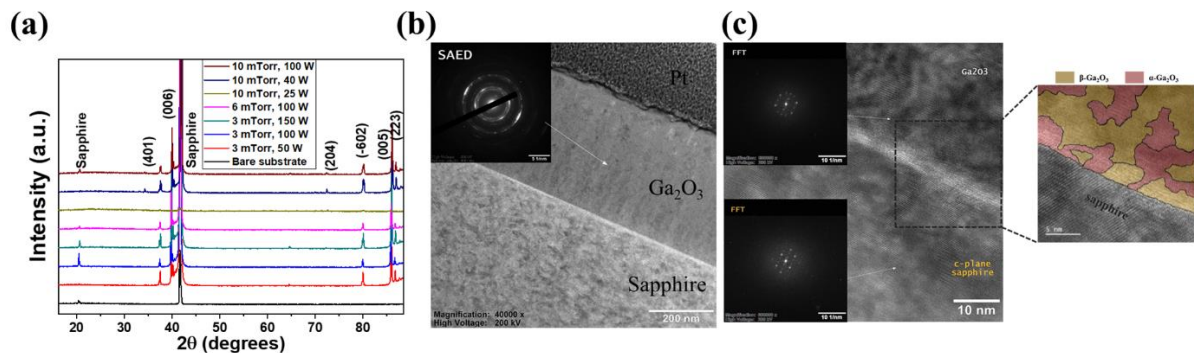


Figure 3.17 (a) XRD spectra for the thin films grown on *c*-plane sapphire at room temperature but different RF powers and deposition pressure. (b) TEM image of the RT-150W sample with the inset showing the SAED pattern. (c) HRTEM image with insets showing the corresponding FFT analysis of Ga₂O₃ and sapphire substrate. The zoomed-in image shows a mapping of the bi-phase polycrystalline films.

The *c*-plane sapphire has an atomic arrangement which is quite similar to that of α -Ga₂O₃ and hence this phase can grow on these substrates with relative ease, but since α -Ga₂O₃ is metastable in nature, it tends to convert into β -Ga₂O₃ as soon as some energy is provided to it. The sputtered atoms, especially at higher powers, are energetic and when these adatoms fall on to the substrate, they rearrange before coalescing to form the thin film. During this rearrangement, it may be possible for some of them to crystallize in to the β -phase. Figure 3.18 (a) shows the

Chapter 3: Dependence of performance on the growth of active layer

AFM micrographs of the RT-150W sample showing the large grain size of the as-deposited films. There seems to be an overgrowth of the films at this sample, but even without the overgrowth, the small grain sizes are also in excess of 40 nm or above with the larger grains being about 130 nm in diameter. The good grain growth is in consonance with the high quality of film growth. The absorbance spectrum of the sample is shown in Figure 3.18 (b) while the inset shows the Tauc plot giving a value of band gap as 4.61 eV.

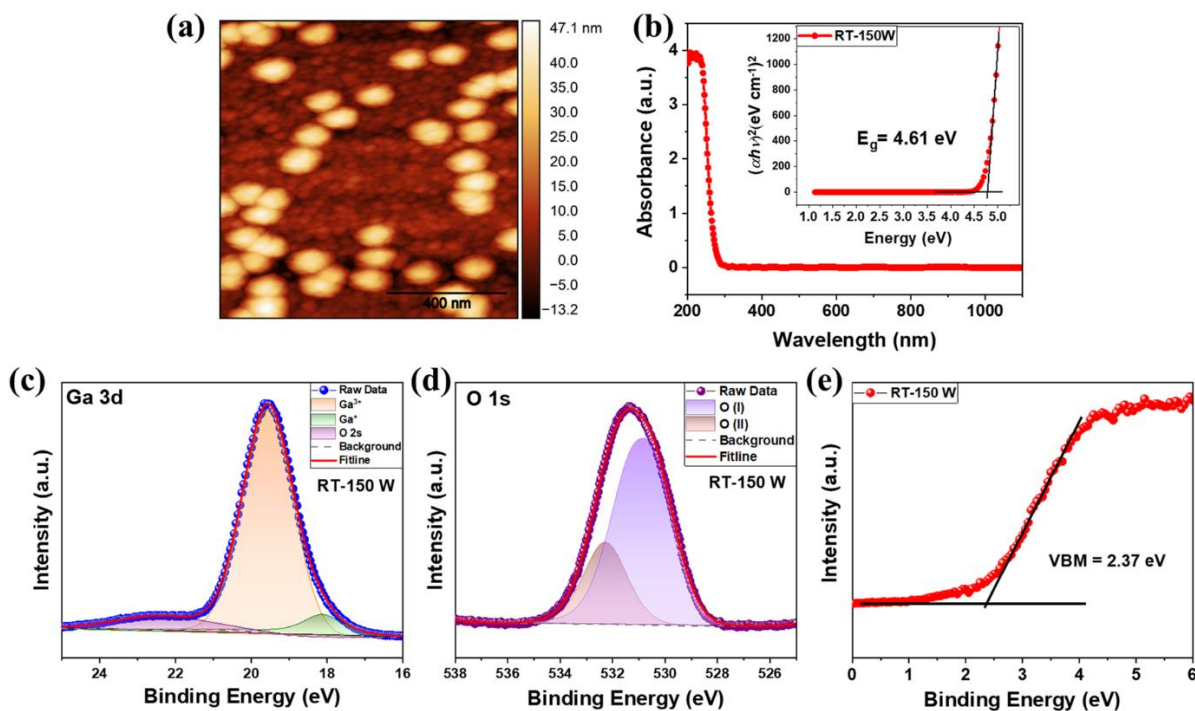


Figure 3.18 (a) AFM micrograph image showing the morphology of RT-150 W. (b) Absorbance spectra with the inset showing the Tauc plot for band gap calculation. XPS core level spectra of (c) Ga 3d and (d) O 1s. (e) VBM calculation using the valence band spectra.

The core level spectra of Ga 3d and O 1s of the samples is provided in Figure 3.18 (c) and (d), respectively. Ga 3d is deconvoluted into two peaks – the lower binding energy peak corresponding to Ga^+ (the sub-stoichiometric gallium oxide) and the higher binding energy curve corresponding to Ga^{3+} (belonging to Ga_2O_3). The ratio of $\text{Ga}^{3+}/\text{Ga}^+$ is found to be 6.77 showing that the films are highly stoichiometric. Similarly, O 1s peak can also be deconvoluted into two peaks – the lower binding energy peak corresponds to the oxygen bonded to gallium whereas the higher binding energy peak belongs to O^{2-} or the oxygen vacancies present in the films. The oxygen vacancy concentration in the films can be estimated using $\text{O}_{\text{II}}/(\text{O}_{\text{I}} + \text{O}_{\text{II}})$ and is found to be ~ 0.24 . Figure 3.18 (e) shows the valence band maxima value as found using the valence band spectra and is found to be 2.37 eV, implying that the fermi level is closer to the

middle of the band gap, slightly towards conduction band, showing that the films turn out to be slightly *n*-type conducting even without any intentional doping.

Photodetector devices were fabricated using RT-150 W by depositing Au electrodes in the interdigitated geometry. Figure 3.19 (a) shows the I-V graphs under dark and illumination conditions. The devices show an ultra-high PDCR of 10^5 at a 10 V bias. The devices show excellent solar-blind nature as seen in Figure 3.19 (b). The peak responsivity was found to be $\sim 0.28 \text{ A W}^{-1}$ at 10 V bias which may be attributed to the low dark current. The devices also show a very stable and repeatable temporal response with repeated switching of incident light with a rise/fall time of 0.57/0.19 s without any PPC (Figure 3.19 (c)).

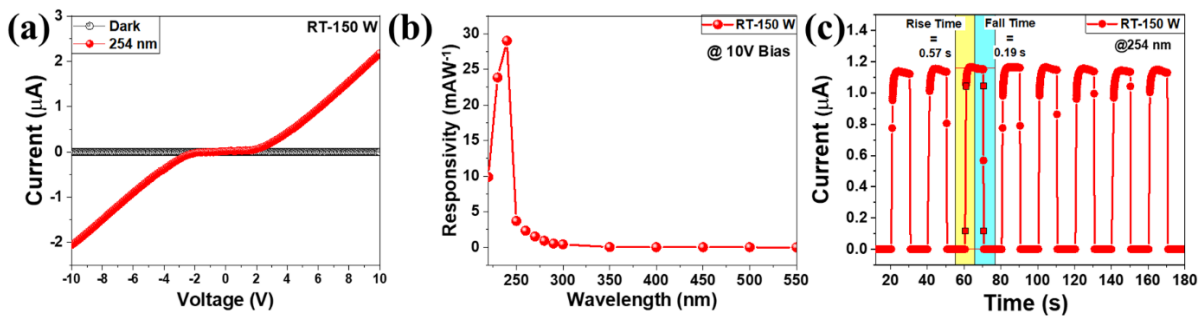


Figure 3.19 For the RT-150W photodetector device, (a) I-V graphs under dark and illuminated conditions. (b) responsivity versus wavelength graph showing the solar-blind nature (c) temporal response of the device to repeated switching of 254 nm incident light.

3.3.3 Conclusions

In conclusion, oxide semiconductors require high temperatures to achieve crystallinity and thus require annealing either during growth or during post-processing. Leading to a dearth of room temperature crystalline oxides with most of them turning out to be amorphous. But we have found room temperature crystallinity in Ga_2O_3 by using a facile fabrication with conventional sputtering. The deposited films on *c*-plane sapphire turn out to be bi-phase mixture of α and β Ga_2O_3 , which is corroborated by XRD and HRTEM data. The subsequently grown photodetectors show an ultra-high photo-to-dark current ratio of over 10^5 at a 10 V bias under 254 nm illumination, thus confirming the high quality of the deposited films. This study shows that it is possible to achieve room temperature crystallinity in Ga_2O_3 by using *c*-plane sapphire substrates and optimizing the deposition parameters to achieve ultra-high photoresponse, thereby providing facile fabrication.

References

1. Pearton, S.J., et al., Exfoliated and bulk β -gallium oxide electronic and photonic devices. *Science Talks* **2022**, 1, 100001.
2. Chen, X., et al., Highly Narrow-Band Polarization-Sensitive Solar-Blind Photodetectors Based on β -Ga₂O₃ Single Crystals. *ACS Applied Materials & Interfaces* **2019**, 11(7), 7131-7137.
3. Xu, Y., et al., Carrier Transport and Gain Mechanisms in β -Ga₂O₃-Based Metal–Semiconductor–Metal Solar-Blind Schottky Photodetectors. *IEEE Transactions on Electron Devices* **2019**, 66(5), 2276-2281.
4. Ghose, S., et al., Growth and characterization of β -Ga₂O₃ thin films by molecular beam epitaxy for deep-UV photodetectors. *Journal of Applied Physics* **2017**, 122(9), 095302.
5. Liu, Z., et al., Construction of a β -Ga₂O₃-based metal–oxide–semiconductor-structured photodiode for high-performance dual-mode solar-blind detector applications. *Journal of Materials Chemistry C* **2020**, 8(15), 5071-5081.
6. Hu, H., et al., Effects of Post Annealing on Electrical Performance of Polycrystalline Ga₂O₃ Photodetector on Sapphire. *Nanoscale Research Letters* **2020**, 15(1), 100.
7. Peng, Y., et al., Arrays of Solar-Blind Ultraviolet Photodetector Based on β -Ga₂O₃ Epitaxial Thin Films. *IEEE Photonics Technology Letters* **2018**, 30(11), 993-996.
8. An, Y.H., et al., Influence of oxygen vacancies on the photoresponse of β -Ga₂O₃/SiCn–n-type heterojunctions. *Journal of Physics D: Applied Physics* **2016**, 49(28), 285111.
9. Kalra, A., et al., Demonstration of high-responsivity epitaxial β -Ga₂O₃/GaN metal–heterojunction-metal broadband UV-A/UV-C detector. *Applied Physics Express* **2018**, 11(6), 064101.
10. Tak, B.R., et al., Photovoltaic and flexible deep ultraviolet wavelength detector based on novel β -Ga₂O₃/muscovite heteroepitaxy. *Scientific Reports* **2020**, 10(1), 16098.
11. Zhang, J.-m., et al., Dependence of stresses on grain orientations in thin polycrystalline films on substrates: an explanation of the relationship between preferred orientations and stresses. *Applied Surface Science* **2001**, 180(1), 1-5.
12. Xie, C., et al., The influence of substrate orientation and annealing condition on the properties of LaMnO₃ thin films grown by polymer-assisted deposition. *Applied Surface Science* **2015**, 351, 188-192.
13. Wang, Q., et al., Influence of growth temperature on the characteristics of β -Ga₂O₃ epitaxial films and related solar-blind photodetectors. *Applied Surface Science* **2019**, 489, 101-109.
14. Doerner, M.F., et al., Stresses and deformation processes in thin films on substrates. *Critical Reviews in Solid State and Materials Sciences* **1988**, 14(3), 225-268.
15. Ohring, M., *Materials science of thin films: deposition & structure*. 2001: Elsevier.
16. Yadav, M.K., et al., Impact of annealing temperature on band-alignment of PLD grown Ga₂O₃/Si (100) heterointerface. *Journal of Alloys and Compounds* **2020**, 819, 153052.
17. Guo, X.C., et al., β -Ga₂O₃/p-Si heterojunction solar-blind ultraviolet photodetector with enhanced photoelectric responsivity. *Journal of Alloys and Compounds* **2016**, 660, 136-140.
18. Kim, H.W., et al., Growth of gallium oxide thin films on silicon by the metal organic chemical vapor deposition method. *Materials Science and Engineering: B* **2004**, 110(1), 34-37.
19. Arora, K., et al., Ultrahigh Performance of Self-Powered β -Ga₂O₃ Thin Film Solar-Blind Photodetector Grown on Cost-Effective Si Substrate Using High-Temperature Seed Layer. *ACS Photonics* **2018**, 5(6), 2391-2401.
20. Anzalone, R., et al., Heteroepitaxy of 3C-SiC on different on-axis oriented silicon substrates. *Journal of Applied Physics* **2009**, 105(8), 084910.

21. Min, Y., et al., Performance dependence of CMOS on silicon substrate orientation for ultrathin oxynitride and HfO₂ gate dielectrics. *IEEE Electron Device Letters* **2003**, 24(5), 339-341.
22. Morita, M., et al., Aluminum Nitride Epitaxially Grown on Silicon: Orientation Relationships. *Japanese Journal of Applied Physics* **1981**, 20(3), L173.
23. Yen, C.-C., et al., Role of Interfacial Oxide in the Preferred Orientation of Ga₂O₃ on Si for Deep Ultraviolet Photodetectors. *ACS Omega* **2021**, 6(43), 29149-29156.
24. Gu, K., et al., Effect of a seed layer on microstructure and electrical properties of Ga₂O₃ films on variously oriented Si substrates. *Vacuum* **2022**, 195, 110671.
25. Yadav, M.K., et al., Substrate orientation dependent current transport mechanisms in β -Ga₂O₃/Si based Schottky barrier diodes. *Journal of Vacuum Science & Technology A* **2021**, 39(3), 033203.
26. Zangwill, A., *Physics at Surfaces*. 1988, Cambridge: Cambridge University Press.
27. Homma, Y., 1 - Measuring nucleation and growth processes in thin films, in *Thin Film Growth*, Z. Cao, Editor. 2011, Woodhead Publishing. p. 3-21.
28. Momma, K., et al., VESTA 3 for three-dimensional visualization of crystal, volumetric and morphology data. *Journal of Applied Crystallography* **2011**, 44(6), 1272-1276.
29. Bean, K.E., et al., The influence of crystal orientation on silicon semiconductor processing. *Proceedings of the IEEE* **1969**, 57(9), 1469-1476.
30. Nečas, D., et al., Gwyddion: an open-source software for SPM data analysis. **2012**, 10(1), 181-188.
31. Malhotra, S.G., et al., Analysis of thin film stress measurement techniques. *Thin Solid Films* **1997**, 301(1), 45-54.
32. Suryanarayana, C., et al., *Determination of Crystallite Size and Lattice Strain*, in *X-Ray Diffraction: A Practical Approach*, C. Suryanarayana and M.G. Norton, Editors. 1998, Springer US: Boston, MA. p. 207-221.
33. Muhammed Shafi, P., et al., Impact of crystalline defects and size on X-ray line broadening: A phenomenological approach for tetragonal SnO₂ nanocrystals. *AIP Advances* **2015**, 5(5), 057137.
34. Bin Anooz, S., et al., Impact of chamber pressure and Si-doping on the surface morphology and electrical properties of homoepitaxial (100) β -Ga₂O₃ thin films grown by MOVPE. *Journal of Physics D: Applied Physics* **2020**, 54(3), 034003.
35. Liu, X.Z., et al., β -Ga₂O₃ thin films on sapphire pre-seeded by homo-self-templated buffer layer for solar-blind UV photodetector. *Optical Materials* **2016**, 51, 203-207.
36. Kumar, S.S., et al., Structure, Morphology, and Optical Properties of Amorphous and Nanocrystalline Gallium Oxide Thin Films. *The Journal of Physical Chemistry C* **2013**, 117(8), 4194-4200.
37. Kaur, D., et al., Strain effects on the optoelectronic performance of ultra-wide band gap polycrystalline β -Ga₂O₃ thin film grown on differently-oriented Silicon substrates for solar blind photodetector. *Applied Surface Science* **2023**, 616, 156446.
38. Nakagomi, S., et al., Crystal orientation of β -Ga₂O₃ thin films formed on c-plane and a-plane sapphire substrate. *Journal of Crystal Growth* **2012**, 349(1), 12-18.
39. Armstrong, A.M., et al., Role of self-trapped holes in the photoconductive gain of β -gallium oxide Schottky diodes. *Journal of Applied Physics* **2016**, 119(10), 103102.
40. Wang, J., et al., Balanced performance for β -Ga₂O₃ solar blind photodetectors: The role of oxygen vacancies. *Optical Materials* **2021**, 112, 110808.
41. Kaur, D., et al., A Strategic Review on Gallium Oxide Based Deep-Ultraviolet Photodetectors: Recent Progress and Future Prospects. *Advanced Optical Materials* **2021**, 9(9), 2002160.

Chapter 3: Dependence of performance on the growth of active layer

42. Yoo, H., et al., A Review of Phototransistors Using Metal Oxide Semiconductors: Research Progress and Future Directions. *Advanced Materials* **2021**, 33(47), 2006091.
43. Sumanth, A., et al., A review on realizing the modern optoelectronic applications through persistent photoconductivity. *Journal of Physics D: Applied Physics* **2022**, 55(39), 393001.
44. Tauc, J., et al., Optical Properties and Electronic Structure of Amorphous Germanium. *physica status solidi (b)* **1966**, 15(2), 627-637.
45. Yang, H., et al., Effects of growth temperature and thickness on structure and optical properties of Ga₂O₃ films grown by pulsed laser deposition. *Superlattices and Microstructures* **2019**, 131, 21-29.
46. An, Y.H., et al., Thickness Tuning Photoelectric Properties of α -Ga₂O₃ Thin Film Based Photodetectors. *Journal of Nanoscience and Nanotechnology* **2017**, 17(12), 9091-9094.
47. Sun, R., et al., Effect of thickness on the microstructure, surface morphology and optical properties of N-incorporated β -Ga₂O₃ films. *Superlattices and Microstructures* **2014**, 65, 146-151.
48. Kossar, S., et al., Study on thickness-dependence characteristics of bismuth ferrite (BFO) for ultraviolet (UV) photodetector application. *Micro and Nano Systems Letters* **2021**, 9(1), 1.
49. Zhang, N., et al., Fabrication and properties of N-doped top layer of Ga₂O₃ films by magnetron sputtering. *Applied Surface Science* **2022**, 604, 154666.
50. Gu, K., et al., Effects of sputtering pressure and oxygen partial pressure on amorphous Ga₂O₃ film-based solar-blind ultraviolet photodetectors. *Applied Surface Science* **2022**, 605, 154606.
51. Varley, J.B., et al., Role of self-trapping in luminescence and *p*-type conductivity of wide-band-gap oxides. *Physical Review B* **2012**, 85(8), 081109.

Chapter 4: Enhancing performance using surface modification

Apart from the crystalline phases, the amorphous phase of gallium oxide is also a viable candidate for the fabrication of solar-blind photodetectors. Its facile fabrication, room temperature growth and independence of the substrate used add to its charm and potential application for flexible and wearable electronics. But amorphous gallium oxide is notoriously known for its high number of oxygen vacancies which gives a high internal photo-gain and hence a higher photoresponse, but at the cost of increased carrier lifetime (due to carrier trapping) leading to slower devices. Therefore, this chapter deals with enhancing the speeds of such amorphous based photodetectors by using surface modification. In the first part, we have modified the surface of a 300 nm amorphous Ga_2O_3 film by nanopatterning it using 500 eV Ar^+ ion beam sputtering.[1] The ripples formed on the surface of gallium oxide thin film lead to the formation of anisotropic conduction channels along with an increase in the surface defects which leads to different performances for the parallel and perpendicular orientation. In the next part of the study, instead of modifying the active layer, we have modified the surface of the substrate used underneath and conformally coated an ultra-thin amorphous Ga_2O_3 on top. Ion-beam sputtering (500eV Ar^+) is utilized to nanopattern SiO_2 coated Si substrate leaving the topmost part rich in elemental Si, as obtained by XPS results. This helps in enhancing the carrier conduction by increasing n -type doping of the subsequently coated 5nm amorphous Ga_2O_3 films, corroborated by room-temperature resistivity measurement and valence band spectra, respectively, while the nanopatterns formed help in better light management. Thus, surface modification using ion-beam sputtering turns out to be a powerful tool in the fabrication of fast speed photodetectors based on gallium oxide.

4.1 Nanopatterning the active layer

The amorphous phase of gallium oxide requires only room temperature fabrication and can be grown on a variety of foreign substrates without the hassle of lattice matching and the subsequent defects and instability.[2] The major concern with the amorphous Ga_2O_3 based PDs is their low performance especially the long response times. Qin et al. have fabricated amorphous gallium oxide SBPD transistors with gate tunability. The device shows a very high responsivity of $4.1 \times 10^3 \text{ A W}^{-1}$ but suffers from a very long response time of $\tau_r = 50 \text{ s}$. [3] The defects associated with these systems are responsible for the long times that these devices take to respond to a change in light from ON-to-OFF mode. Various methods have been developed

to improve the performance of these devices such as the use of a graphene layer [4], chemical etching[5] or external spontaneous polarization.[6]

Surface patterning is another novel method which has been used to improve device performance, especially in the field of photovoltaics and optoelectronics.[7, 8] The surfaces are modified (to increase light absorption or improve the conduction of charge carriers) either by functionalizing the material [9], putting over-layers [10], or nanopatterning [11]. Surface modification using nanopatterning is a much more controlled technique which can be used to pattern the surfaces using either etching methods (such as Reactive ion etching, ion beam sputtering), self-assembly processes, photolithography or scanning probe techniques.[12] Out of these, low energy ion beam sputtering (IBS) is a particularly interesting and universal method to create self-ordered patterns on surfaces without the need of a mask or photoresist.[13] Thus, we have employed IBS as a means to modify the surface of amorphous Ga_2O_3

4.1.1 Experimental details

Amorphous Ga_2O_3 thin films (approx. 300 nm thickness) were deposited on SiO_2 coated Si substrate by RF Magnetron Sputtering using a Gallium oxide target (99.99% purity, supplied by K. J. Lesker).

Prior to deposition, the substrates were cleaned ultrasonically in soap solution, de-ionized water, acetone and propanol for 30 minutes each and finally dried with N_2 gun. After achieving a base vacuum of 8×10^{-7} Torr, deposition was done at room temperature with 100 W RF power and 3 mTorr working pressure using Ar gas. The films were then nanopatterned using a broad ion beam inside a vacuum chamber housing a Kaufman ion source and irradiated at room temperature with 500 eV Ar^+ ions at an incident angle of 67° with respect to the surface normal for 15 minutes. The experimental set-up for the irradiation process can be found in a previously reported study.[14] An unirradiated sample was kept as a control for the measurements. Subsequently, photodetectors were fabricated on the control and irradiated samples (henceforth named “bare” and “rippled”) by forming Cr/Au strip electrodes (with an interspacing of 3.5 mm in between) via a physical shadow mask using a thermal evaporator (see Figure 4.1). The diffuse reflectance spectra were recorded using an UV–Vis spectrophotometer (Perkin Elmer, Lambda 950), and the bandgap was calculated by using the Kubelka-Munk function.

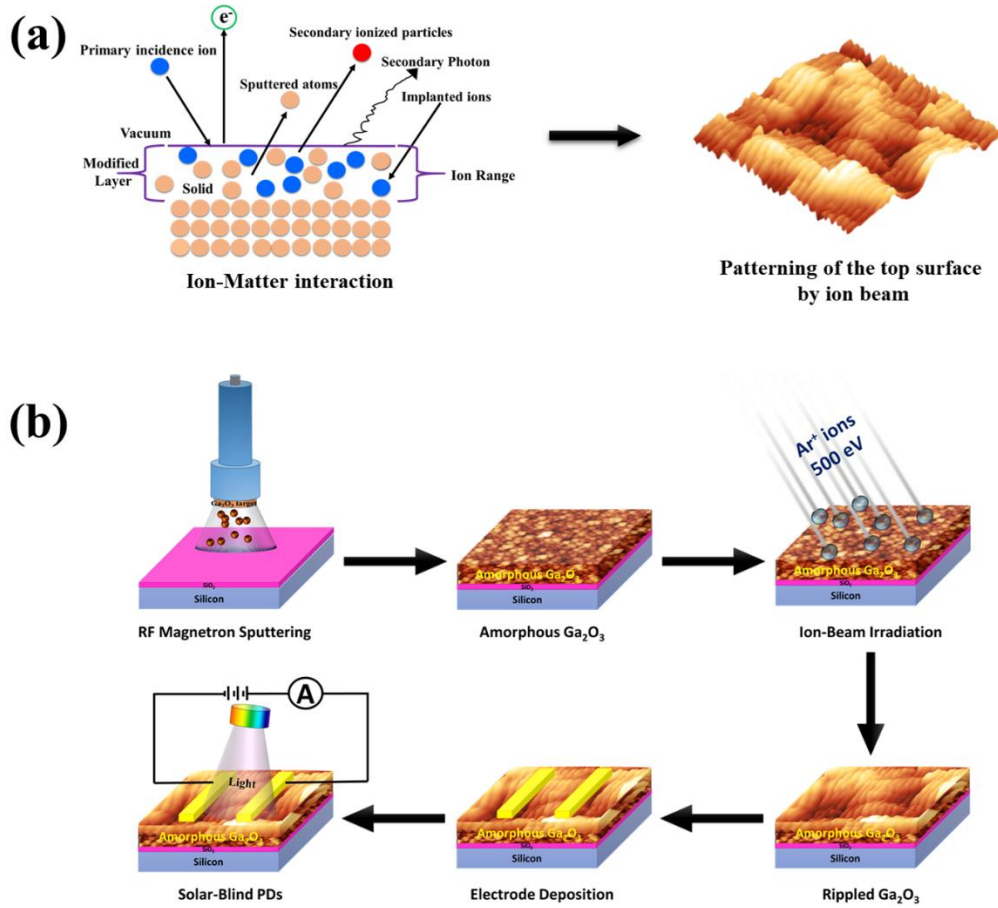


Figure 4.1 (a) Schematic depicting atomic level changes during ion-matter interaction. (b) Schematic for the growth of amorphous gallium oxide thin film with subsequent nanopatterning by broad Ar^+ ion beam sputtering (IBS). The photodetectors were fabricated to evaluate the effect of nanopatterning on device performance.

4.1.2 Results and discussion

Figure 4.2 depicts the change in morphology upon irradiation as studied using AFM micrographs. The amorphous thin film (Figure 4.2 (a)) is uniformly deposited on the substrate without any cracks or discontinuities and possesses a root mean square (RMS) roughness of 1.85 ± 0.12 nm. Figure 4.2 (b) shows the formation of a rippled or nanopatterned structure formed after low-energy ion beam irradiation of Ar^+ with 500 eV energy. The black arrow indicates the direction of the incident ion beam. After irradiation, the RMS roughness of the rippled film increases to 3.64 ± 0.17 nm. The rippled films show a homogenous distribution of the nanoripples in the direction of the incident beam. The bottom-left insets of the AFM images show the 2-dimensional FFTs depicting the periodicity of the surface morphologies. The amorphous film exhibits no such periodicity with the FFT consisting of randomly oriented dots while the rippled film reveals a clear periodicity and alignment of the nanoripples in the direction of the irradiation. Figure 4.2 (c) shows the log-log plot of power spectral density

(PSD) versus the spatial frequency q calculated in the direction parallel to the incident ion beam. The first-order peak positions in the PSD curves can be used to determine the wavelength of the best ordered ripples. The inverse of the peak position is equal to the ripple wavelength with a sharper peak usually indicating a better ordering.[15, 16]

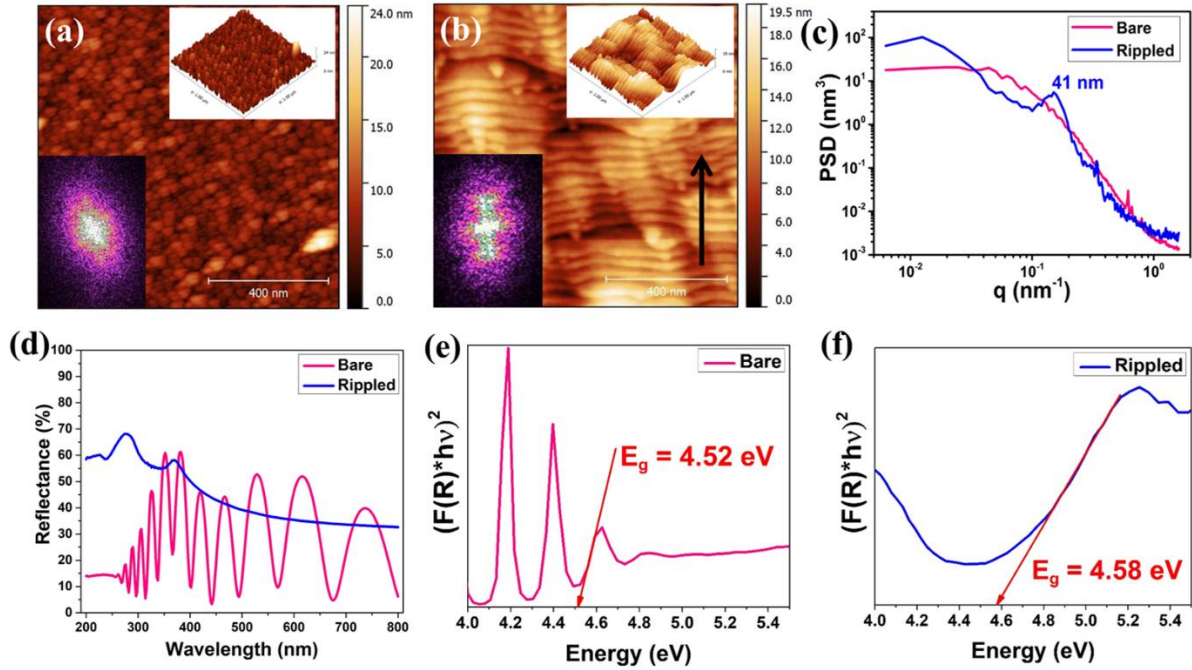


Figure 4.2 (a,b) AFM scans ($1\mu\text{m} \times 1\mu\text{m}$) of amorphous Ga_2O_3 thin film (bare) and irradiated thin film (rippled), respectively, showing the formation of nanopatterns using IBS. The top-right insets represent the corresponding 3-D mapping while the bottom-left insets depict the FFT of the corresponding AFM images. The black arrow indicates the direction of the incident ion beam. (c) log-log plot of power spectral density (PSD) versus the spectral frequency q as extracted from the AFM data. (d) The diffuse reflectance spectra of the thin films on SiO_2/Si substrate. The estimated band gap of (e) bare and (f) rippled gallium oxide thin films.

From Figure 4.2 (c), it is evident that for the bare amorphous films, the graph is relatively smooth with no visible peak pointing to the absence of any characteristic ordering whereas the rippled film shows a distinct peak with a ripple wavelength of about 41 nm. The optical properties of the thin films were investigated to check the suitability of nanopatterning of gallium oxide for optoelectronic applications. The reflectance spectra of the thin films are shown in Figure 4.2 (d). The modified Kubelka–Munk function obtained by multiplying the $F(R)$ (Kubelka-Munk function) by hv , was used for the calculation of the optical band gap. A plot of $(F(R) \times hv)^n$ (where $n=2$ for indirect transitions) as a function of energy in eV gives the required band gap.[17] The shape of the spectra is in consonance with that reported in literature for micro-size structures[18] as well as for thin films[19] of gallium oxide, corroborating again the formation of ordered or rippled structure after irradiation. The band gap of the bare and

rippled films lies in the solar-blind region, as expected for Ga_2O_3 (see Figure 4.2 (e,f)). The optically active defects in the system and their lifetimes were probed using room-temperature steady-state photoluminescence (PL) and time-resolved photoluminescence (TRPL), respectively. Figure 4.3 (a) shows the PL emission spectra for the films recorded for an excitation wavelength of 266 nm. There occurs an increase in the intensity for the characteristic UV-A band of Ga_2O_3 while the blue-green bands show quenching. The near UV band (UV-A) in the PL spectra of gallium oxide has previously been attributed to the surface or near-surface defects present in system, which may be enhanced by a Ga-rich environment.[20, 21] Upon irradiation, it is very much plausible for the surface of the thin films to loose oxygen much faster (oxygen being the lighter atom) leading to a Ga-rich surface, responsible for the corresponding increase in the PL intensity. The change in the decay of the carriers in the system was studied via the TRPL measurement as shown in Figure 4.3 (b). The decay curves were fitted using a bi-exponential function, $y = y_0 + A_1 \exp\left(-\frac{t}{\tau_1}\right) + A_2 \exp\left(-\frac{t}{\tau_2}\right)$, where τ_1 and τ_2 are time decay constants while A_1 and A_2 are appropriate constants. The black line represents the fitting result of each curve. The τ_1 corresponds to the fast decay component which is usually attributed to the surface recombination of the carriers while the τ_2 is the slow component, corresponding to the delayed recombination of carrier due to defects within the bulk.[22] Both the fast and the slow component show a marked decrease with τ_1 changing from 1.28 ns to 0.65 ns while τ_2 goes from 11.13 ns to 3.07 ns. A shortened carrier decay time is usually ascribed to the presence of defects in the system which behave as recombination centers. In the present case, the charge carriers in the thin films recombine much faster for a rippled surface as compared to that for the bare one due to an increase in the defects introduced in the system by incidence of energetic Ar ions and a consequently enhanced surface recombination, in line with the steady-state PL data.

To ascertain the effect of nanopatterning on the device performance, solar-blind photodetectors (PD) were fabricated on both (bare and rippled) samples by depositing Cr/Au electrodes in the form of strips with an interspacing of 3.5 mm. For nanopatterned surfaces, anisotropy in the electrical conduction with respect to the ripple orientation has been reported before.[23, 24] This is often attributed to the conduction channels formed on the surfaces having different conductivities along and across the channels as a result of structural anisotropy. To fully comprehend this, photodetectors were fabricated with electrodes parallel and perpendicular to the ripple direction (equivalent to the direction of the incident ion beam). As shown in Figure 4.4 (a), the PD with the current measured in the direction perpendicular to the ripples is labelled

henceforth as “perpendicular” while that with current measured parallelly is labelled as “parallel”.

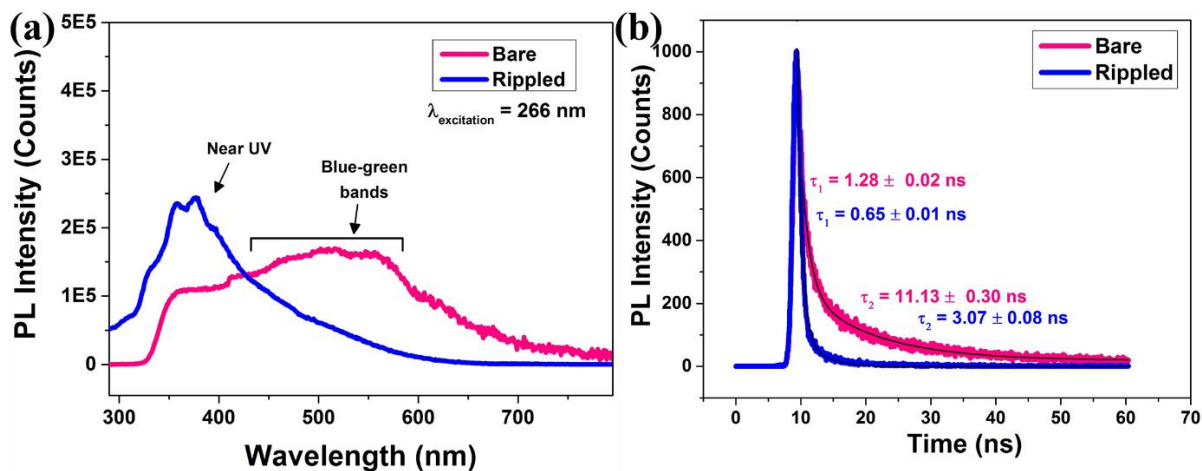


Figure 4.3. (a) Photoluminescence spectra and (b) time-resolved PL of amorphous Ga_2O_3 films before and after IBS.

Figure 4.4 (b) shows the current versus voltage graph of the three fabricated detectors. The increase in the dark current upon nanopatterning can be attributed to the change in the conductivity of the films due to the formation of conduction channels. The conductivity is anisotropic in this case as well, as is evident from the different dark currents obtained for parallel and perpendicular orientations. Illuminating the PDs with UV-C source (254 nm) leads to an increase in the measured current. The different orientations of rippled Ga_2O_3 give rise to an enhanced photocurrent as compared to bare sample. Figure 4.4 (c) shows the spectral response of the PDs with different wavelengths revealing excellent solar-blind nature of all the fabricated devices, even at self-biased operation. The rippled devices show an enhanced performance in terms of an increase in responsivity in the suitable spectrum. The responsivity increases from 0.35 mA W^{-1} for bare to 1.78 mA W^{-1} for rippled perpendicular and 6.08 mA W^{-1} for rippled parallel at 0 V bias and 250 nm, $4.6 \mu\text{W cm}^{-2}$ illumination (an increase of 5-fold and 19-fold, respectively). The responsivity also increases when a bias is applied across the electrodes (see Figure 4.4 (d)). The increase in the responsivity is credited to the introduction of defects in the system which is more often than not responsible for the high photoconductive gain in gallium oxide.

In addition to the light detection via an increase in the current after illumination, an equally important parameter is the response time of the photodetectors – how quickly the PD responds to a switching of the light source. Figure 4.5 (a) shows the temporal response of the PDs at zero-bias under 254 nm illumination (10 second on-off interval) with a single cycle depicted

in Figure 4.5 (b). The fabricated photodetectors showed good switching speeds with minimum persistent photoconductivity and stable response after repeated switching cycles.

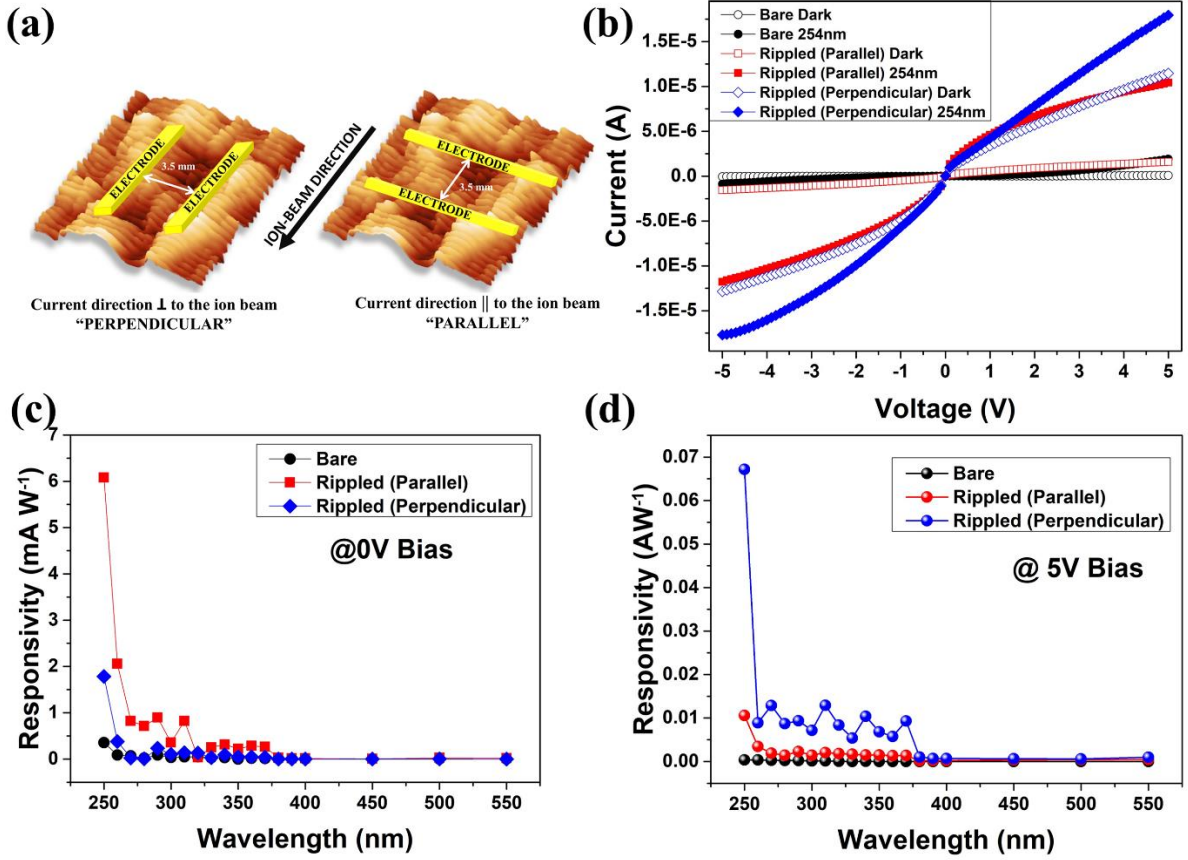


Figure 4.4 (a) Schematic of “perpendicular” and “parallel” oriented device structures of rippled surfaces of amorphous Ga_2O_3 (b) I-V characteristics. Responsivity versus wavelength of the fabricated solar-blind photodetectors at (c) 0 V bias and (d) 5 V bias.

Whenever a PD is illuminated with above band gap illumination, the photons are absorbed by the active layer resulting in the generation of electron-hole pairs. The photogenerated charge carriers then travel across the active layer to the electrodes where they are collected giving rise to a photocurrent. Upon the removal of the incident light, new carriers are no longer generated while the already present electrons and holes move towards each other to recombine. The former part constitutes the rise time of the device while the latter corresponds to the fall time. The nanopatterning of the amorphous Ga_2O_3 thin film leads to a faster recombination of the charge carriers as ascertained by the decrease in decay time constants of TRPL measurements (see Figure 4.3 (b)). Thus, a corresponding decrease in the fall time is to be expected for the rippled devices implying that the charges recombine faster once the light is switched off. Figure 4.5 (c,d) show the decay edges of the bare and rippled devices on the light off-part of the switching cycle at self-bias (0 V) and at 5 V bias, respectively. The fall time of the rippled

devices show a much faster response as compared to bare and the decrement is even more pronounced at 5 V applied bias. It reduces more than one order of magnitude with the bare device having a fall time of 3472 ms as compared to about 243 ms and 169 ms for the parallel and perpendicular ones. This implies that a faster surface recombination of the charge carriers occurs for nanopatterned films as compared to bare flat surface.

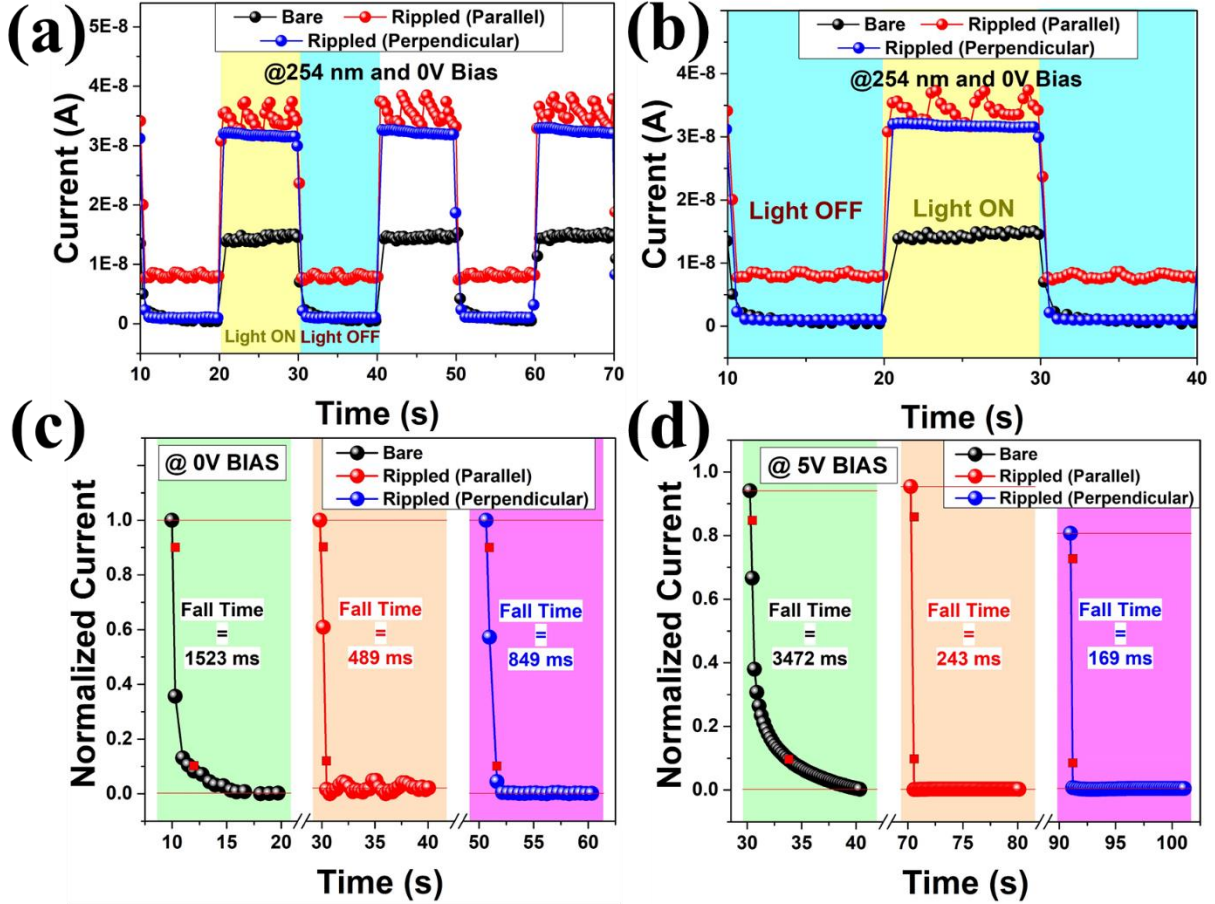


Figure 4.5. (a) Temporal response at zero-bias (b) single-cycle for the temporal response at zero-bias (c) decay edges showing the fall time at zero-bias (d) decay edges showing the fall time at 5 V bias for the fabricated SBPDs under 254 nm illumination.

4.1.3 Conclusions

Surface nanopatterning of amorphous gallium oxide thin film was carried out via ion beam sputtering. A low energy (500 eV) broad Ar^+ ion beam was irradiated upon amorphous films grown via sputtering on SiO_2/Si substrates, giving rise to nano-ripples on the surface of the thin film. Solar-blind photodetectors fabricated on rippled thin film showed an enhancement in performance both in terms of responsivity and response time as compared to the flat reference, even at self-bias. The devices showed one order of magnitude decrease in the fall time at moderate bias of 5 V. The surface defects generated as a result of ion irradiation was found to

be the cause of the improved performance which were corroborated by PL and TRPL study. This study opens up new avenues for using surface modification as a tool for improving the performance of amorphous materials based photodetectors which is the utmost requirement for the fabrication of next-generation devices such as flexible optoelectronics.

4.2 Nanopatterning the substrate below

Amorphous oxide films have garnered high interest in the recent past partly due to the fact that these can be grown even on a wide variety of non-native substrates at room temperature (thereby reducing the overall complexity of the growth process) and partly due to the potential application in flexible electronics (crucial for the wearable industry).[25, 26] Being less conducting, efforts have been made to increase the electrical conductivity of amorphous gallium oxide thin films using conventional methods such as tuning metal/oxide ratio and elemental doping.[27, 28] But still, majority of the reported literature points to amorphous films exhibiting insulating behavior with currents reaching below nA levels.[5, 29, 30] As a solution to the high resistivity, doping during growth of amorphous films has been reported by incorporating dopant atoms during growth and/or controlling the oxygen partial pressure for appropriate charge compensation.[31, 32] This has had some success but requires more attention due to lack of universality. Ion implantation, although a preferred method of doping for β -Ga₂O₃, usually involves heating at high temperatures to introduce the donor properties, and is therefore not that appealing for room temperature fabricated amorphous films. Hence, some novel ways to circumvent this shortcoming are required so that amorphous gallium oxide films may be used for device purposes. In this part of the study, we found an easy and facile way to inadvertently dope amorphous Ga₂O₃ films along with obtaining better light management using IBS. Ion beam sputtering (IBS) technique is often used as a cost effective method to fabricate large area nanopatterns on solid surfaces. The ion-matter interaction between the surfaces and the incoming ions tends to change the morphology of the surface.[14] In general, the topmost layer of the sample subject to irradiation undergoes amorphization due to the high energy transfer by the incoming atoms. For the case of inherently amorphous materials, it has been reported that the kinetics of pattern formation are relatively slower and consequently, shallow ripples are formed.[33] Since IBS requires only low-energy, defocussed ion beam for the formation of nanopatterns, it has the potential to create large area patterned surfaces. Herein, we make use of the ease of IBS for patterning the SiO₂ coated Si substrates.

4.2.1 Experimental details

SiO₂ coated Si substrates (~280 nm SiO₂) were first cut and cleaned sequentially in industrial grade soap solution, deionized water, acetone and propanol for 30 minutes each in an ultrasonicator before being blown dry by N₂ gun. The cleaned samples were loaded into a vacuum chamber housing a Kaufman ion source. The substrates were irradiated with a broad ion beam of 500 eV Ar⁺ ions at an angle of 67° with respect to the surface normal for 5 minutes, 10 minutes, and 15 minutes, respectively. The experimental set-up for the irradiation process can be found in a previously reported study.[34] Amorphous Gallium oxide thin films (~5nm) were deposited on the non-rippled and rippled substrates using RF Magnetron Sputtering. A ceramic target of Ga₂O₃ (sourced from K.J.Lesker) with 99.9% purity was used for the deposition. The base vacuum achieved was 8×10^{-7} Torr, while the working pressure was kept at 3 mTorr. The RF power used was 100 W while the depositions were done at room temperature. The conductivity measurements were carried out in the van der Pauw geometry using an in-house DC Hall measurement technique equipped with a Keithley 2450 source meter and a Keithley 2182A nanovoltmeter). Au interdigitated electrodes (IDE ~120 nm thick) were fabricated using a thermal evaporator via physical shadow mask. Simulations were carried out using the FDTD simulation software package as available in commercially available Lumerical. The simulations were performed using periodic boundary conditions with perfectly matched layers (PML) conditions utilized along the z-axis along which the electromagnetic waves propagate. Plane waves are made incident normal to the surfaces along z-direction and reflectance data is collected with power monitors placed behind the radiation source. The complex refractive index of SiO₂ is taken from the data of Palik as available in the Lumerical software and while that for Ga₂O₃ is taken from Paskaleva et al.[35]

4.2.2 Results and discussion

Figure 4.6 (a) shows the schematic of the experimental steps used for achieving this. Briefly, cleaned SiO₂ (280 nm) coated Si substrates were irradiated with a broad ion beam of 500 eV Ar⁺ ions at an angle of 67° with respect to the surface normal for 5 minutes, 10 minutes and 15 minutes, respectively, using a Kaufman ion source, corresponding to an ion fluence of 2.5×10^{22} , 5×10^{22} and 7.5×10^{22} ions cm⁻². The incident ions tend to erode the surface and since the ions are falling at an angle, it leads to pattern formation. Figure 4.6 (b-e) shows the 3 μm x 3 μm AFM micrographs of the bare substrates and the nanoripples formed on the SiO₂ coated Si substrate with the black arrow indicating the direction of the incident ion beam. Bottom-left insets of these figures depict the Fast Fourier transforms of these images showing the

periodicity of the ripples formed and/or the roughness distribution while the top-right insets show the magnified images of the nanoripples. There is not much difference between the characteristic patterns formed for varying ion fluence. The formation of these ripples is fundamentally explained by the theory put forward by Bradley and Harper (B-H), which uses the Sigmund's theory of sputtering as the underpinning model.[36] B-H model traces the origin of the pattern formation to the surface instability as a result of the competing processes of erosion (or roughening; curvature dependent sputtering) and smoothing (or the surface diffusion)[37] and is quite successful in predicting the ripple direction and wavelength. Figure 4.6 (f) represents the power spectral density (PSD) versus spatial frequency q calculated in the direction parallel to the incident beam. The peak in the PSD curve represents the ordering of the ripples in terms of its wavelength which is found to be around 39 nm.[38] Figure 4.6 (g) shows the root mean square (RMS) roughness which decreases with increasing irradiation time.

The decreasing roughness trend observed with increasing sputtering times for SiO₂ during Ar⁺ ion beam irradiation is likely due to a process known as ion beam-induced smoothing. This occurs via ion bombardment induced viscous flow and surface diffusion of disturbed atoms.[39] During ion beam irradiation, energetic ions bombard the surface of the material, causing sputtering and surface rearrangement. With commencement of irradiation, there is an initial increase in roughness, followed by a subsequent decrease over time. This decrease in roughness is attributed to the increased mobility of surface atoms induced by surface diffusion processes. As a result, higher fluence levels can lead to decreased roughness due to enhanced surface diffusion and smoothing effects. A comparison may be drawn with the non-rippled bare substrate as shown in the AFM image in Figure 4.6 (b) which has a very small surface roughness ($\sim 0.27 \pm 0.05$ nm).

Consequent to the ripple formation, ultra-thin amorphous Ga₂O₃ films (~ 5 nm) were deposited via RF Magnetron Sputtering at room temperature on rippled and non-rippled substrate as well. Sputtering as a physical vapor deposition process has limited scope when it comes to conformally coat surfaces such as deep trenches due to the shadowing effect at the edges, due to the difference in the incoming flux at the sidewalls and the planar surface.[40, 41] However, in our case, the low aspect ratio of the ripples (about ~ 0.8 nm height to ~ 43 nm width of a ripple) allows for a smooth Ga₂O₃ film depositing over the underlying rippled substrates. The incoming flux of sputtered materials does not face too much of a shadowing effect and the low thickness of the deposited layer ensures that the films emulates the features below. The films get conformally coated on the substrates which is evident from the AFM micrographs that show

a similar pattern for the samples with and without the Ga_2O_3 coating (Figure 4.7 (a)) for the samples irradiated for 5, 10 and 15 minutes. Since all the samples have the similar morphological characteristics and get conformally coated, for simplicity, the 5 minute irradiated sample will be chosen for further discussion. To further confirm the uniformity of Ga_2O_3 , Energy Dispersive X-ray Spectroscopy studies were carried out and are shown in Figure 4.7 (b).

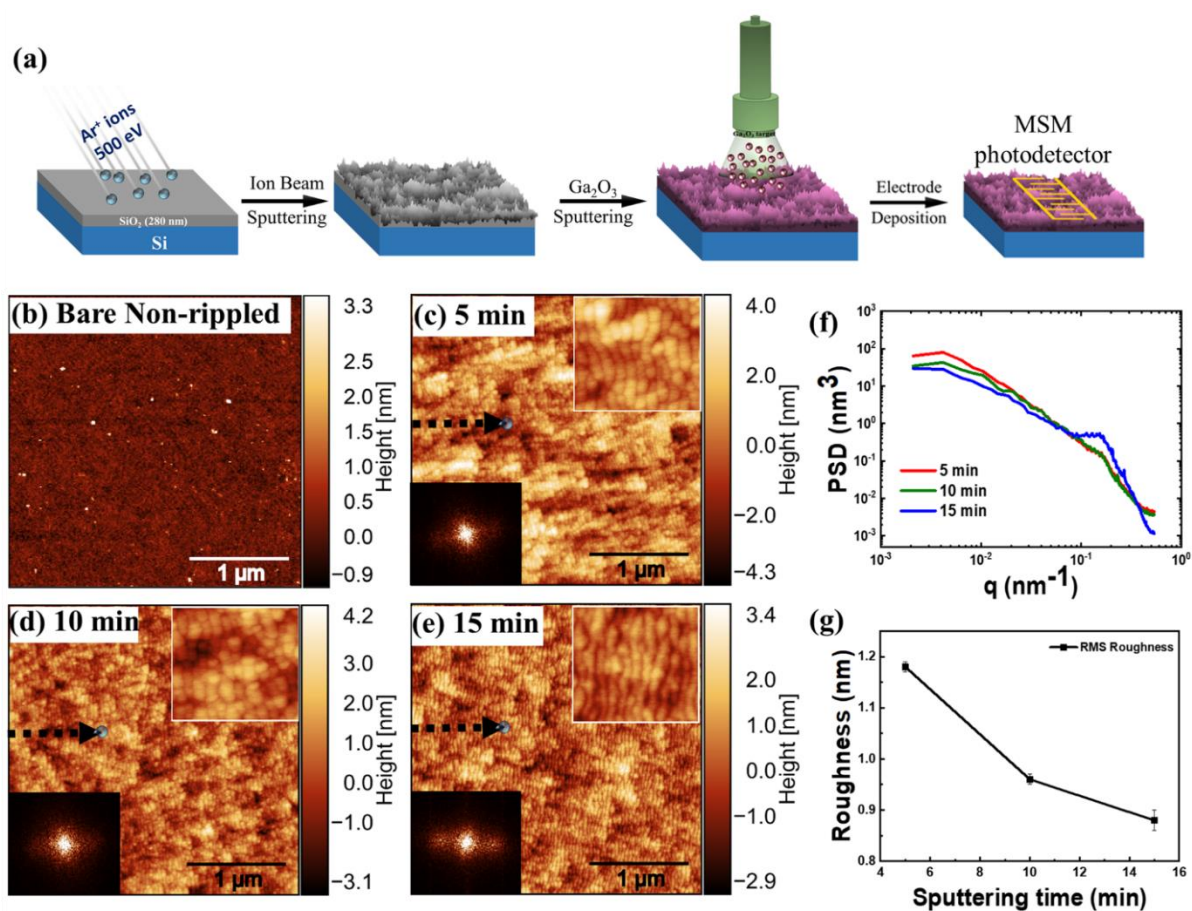


Figure 4.6 (a) Schematic showing the fabrication of nanoripples and the consequent majority carrier MSM photoconductor devices. 3 μm x 3 μm AFM micrographs for the irradiation times of (b) 0 min (or bare substrate), (c) 5 min, (d) 10 min and (e) 15 min. Bottom-left insets of the respective micrographs shows the FFT images showing the periodicity of the nanoripples while the top-right insets show the magnified images of the nanoripples. Black arrow depicts the direction of the incident ion beam. (f) Log-log plot of power spectral density versus spatial frequency q as extracted from AFM data. (g) Variation of RMS roughness with increasing ion beam sputtering times.

To look at the changes in the chemistry of the films, X-ray photoelectron spectroscopy studies were carried out. Figure 4.8 (a) shows the core level spectra of rippled 5 min with Ga_2O_3 sample and the peaks were deconvoluted into the core levels of Ga 3p and Si 2p. The non-rippled sample shows the characteristic peak for SiO_2 and Ga_2O_3 but upon irradiation, an additional

peak of Si starts to appear. The Ga 3p peaks at around 105.5 eV (Ga 3p_{3/2}) and around 109 eV (Ga 3p_{1/2}) produce no shift in the binding energy upon irradiation, thereby implying that the above deposited gallium oxide experiences no chemical change. In addition to the SiO₂ peak around 103 eV, there occurs an additional peak at 99.5 eV in the irradiated sample, corresponding to elemental silicon.

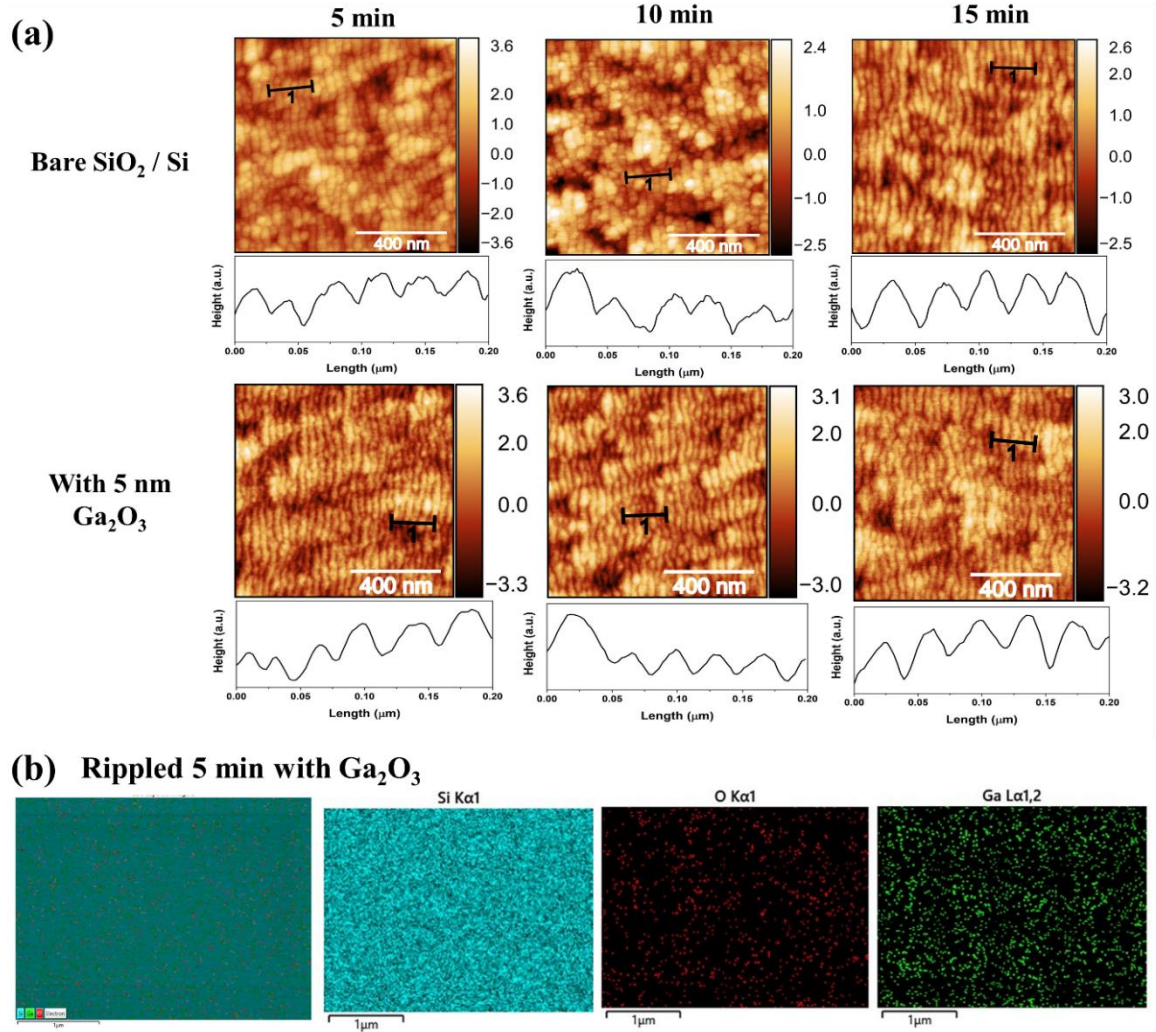


Figure 4.7 (a) 1 μm x 1 μm AFM micrographs for the varying irradiation times without and with Ga₂O₃ coating showing the conformality of the films. Below the micrographs are the respective line scans showing that the Ga₂O₃ films get conformally-coated (for 5-15min) since the nature of the ripples remain same before and after Ga₂O₃ deposition. (b) EDX mapping of the 5 min rippled substrates with Ga₂O₃ showing the uniformity of the films.

During IBS of compound semiconductors, there often occurs preferential sputtering wherein one of the elements is sputtered more than the other since they are bound differently to the solid.[42] The highly energetic ions may break the bonds between the compound leading to preferential sputtering. In this case, oxygen being the lighter element can easily sputter out leaving the surface behind Si rich. The same characteristic peak of elemental Si is also found

in 10 min and 15 min rippled samples with Ga_2O_3 (see Figure 4.8 (b)). This addition of Si in the films above leads to an increase in the valence band maxima of Ga_2O_3 (as shown in Figure 4.8 (c)) depicting the Si doping which leads to an increasing shift in the fermi level towards the conduction band, implying more *n*-type conductivity. Thus, the ion-beam sputtering on the underlying substrates facilitates the incorporation of Si into the Ga_2O_3 films above because of the enhanced adatom diffusion since the presence of nanoripples alters the diffusion pathways and kinetics of Si atoms on the surface of the substrate.[43] The ripples may, therefore, act as channels or traps that guide Si towards specific regions of Ga_2O_3 facilitating their incorporation. Moreover, the increased effective surface area also enhances the chances of incorporation of Si. All these factors are highly influenced by the ripple dimensions as well. For example, the height and spacing of the nanoripples can affect how the Si atoms diffuse along the surface and get incorporated, thereby altering the surface states as well as the electrical conductivity.[24]

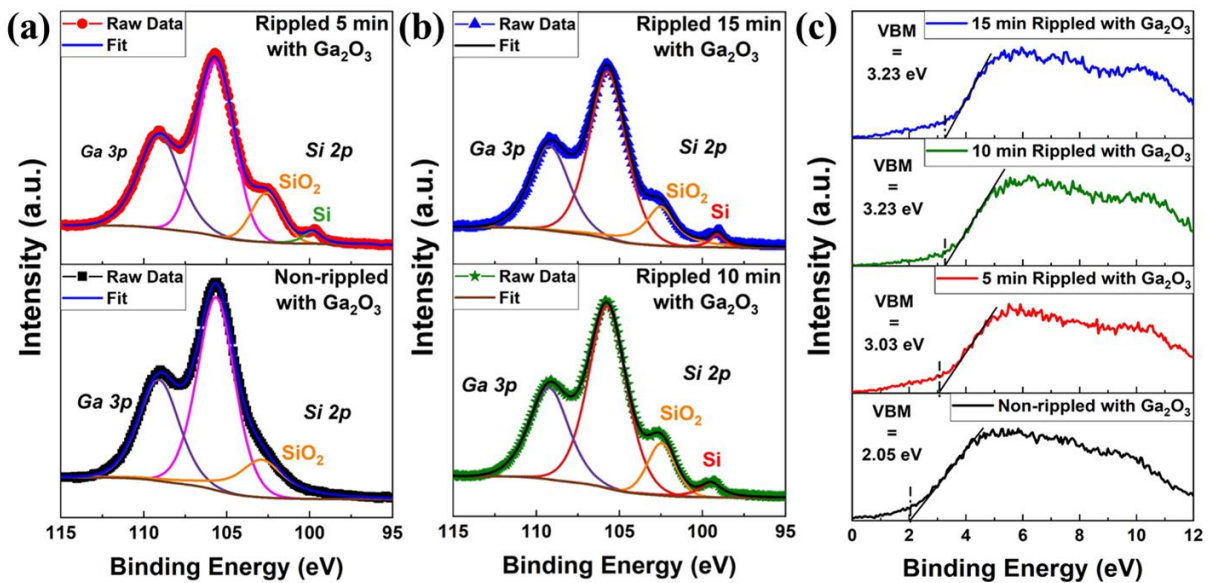


Figure 4.8. (a) XPS core level spectra of Ga 3p and Si 2p for the non-rippled and rippled 5 minute with Ga_2O_3 samples showing the additional peak of elemental silicon in the latter (b) XPS core level spectra of Ga 3p and Si 2p for rippled 10 and 15 minute with Ga_2O_3 samples (c) Valence band maxima of the various samples showing increasing *n*-type doping.

The doping of Si in gallium oxide has been previously reported to increase the carrier concentration.[44-46] Si acts as a substitutional dopant replacing Ga and forming a shallow donor. Since the fermi level shifts towards the conduction band, the electrical properties of the films may get augmented. Thus, the electrical conductivity of the 5 min rippled Ga_2O_3 film was checked using the hall measurement setup in the van der Pauw geometry. The resistivity of the gallium oxide turns out to be of the order of $10^5 \Omega \text{ cm}$ whereas the carrier concentration of the

films was found to be of the order of 10^{19} cm^{-3} , implying enhanced conductivity. In contrast, the non-rippled films of Ga_2O_3 , were found to be highly insulating with the currents dropping to levels beyond detection capabilities of the measuring equipment. Once the improvement in carrier concentration was ascertained, the doped films were then utilized for the fabrication of real-world applications.

The improvement in the resistivity of the amorphous Ga_2O_3 films due to the introduction of Si can have far reaching implications, especially for devices based on gallium oxide. One such device is the solar-blind photodetectors which uses Ga_2O_3 as the active layer.

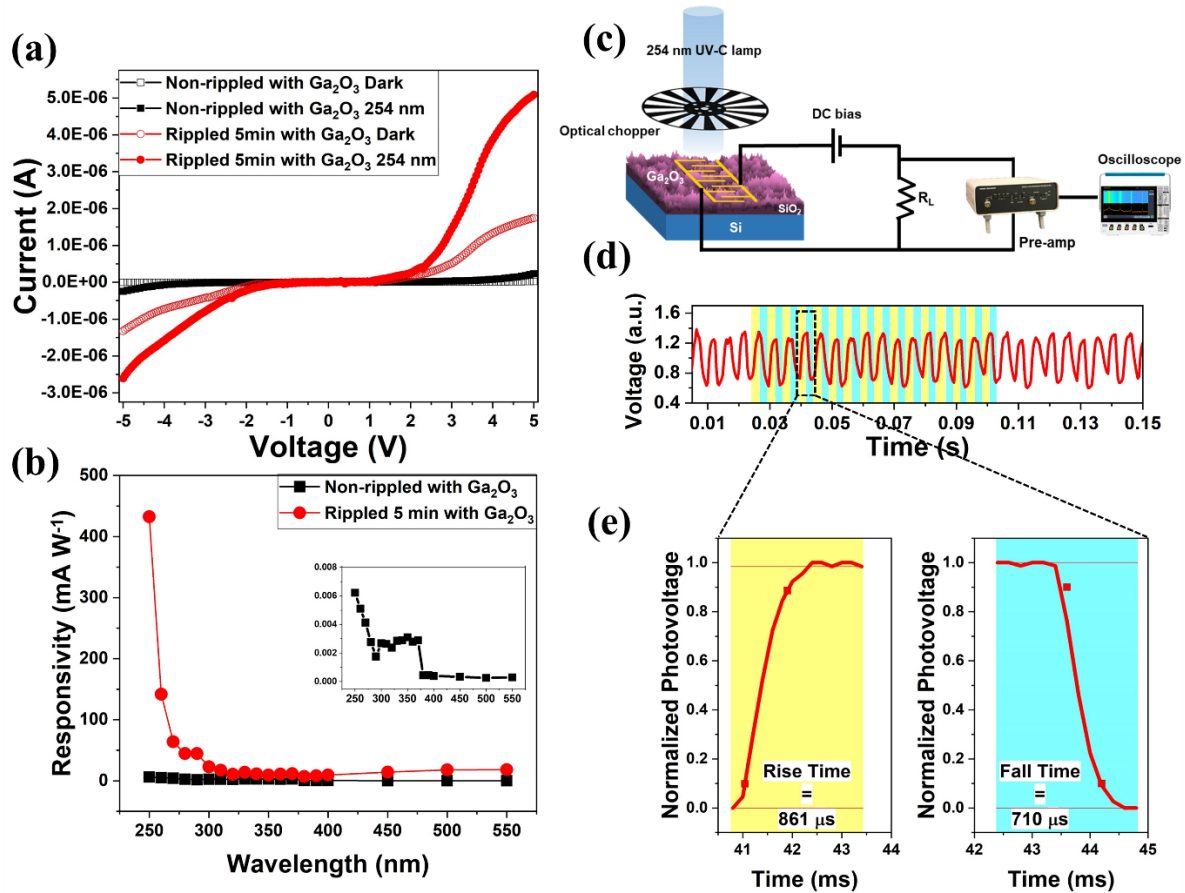


Figure 4.9 (a) Current versus voltage graph under dark conditions and 254 nm light for non-rippled and rippled 5min with Ga_2O_3 . (b) Responsivity versus wavelength of the rippled 5 minute device with Ga_2O_3 . Inset shows the responsivity of the non-rippled with Ga_2O_3 device. (c) Schematic of the experimental set up for carrying out the temporal responses of the devices. (d) Temporal response of the rippled 5 minute device with (e) showing the single cycle of the temporal response to 254 nm of wavelength of light at 200 Hz chopping frequency.

Figure 4.9 (a) shows the dark current and the photocurrent under 254 nm illumination of Ga_2O_3 devices on non-rippled as well as 5 min rippled substrate. An increase is observed in both the dark current as well as photocurrent upon using the nanorippled substrates. The increase in

dark current signifies an improvement in the charge carrier conduction in the films whereas the photocurrent may be enhanced because of the improved light management for patterned substrates.[47] The photocurrent enhances by about 22 times for the conformally coated films. The responsivity (R) at 250 nm increases from 6 mA W^{-1} to about 433 mA W^{-1} at a moderate bias of 5V by simply using the patterned substrate, an increment of 72 times while maintaining excellent cut-off for solar-blindness (Figure 4.9 (b)). The UV-Visible rejection ratio (R_{250}/R_{400}) is found to be ~ 46 for the 5 minute rippled sample as compared to 16 for the non-rippled devices. The temporal response of the rippled 5 minute device to an incident radiation of 254 nm (with the high speed testing setup in Figure 4.9 (c)) is shown in Figure 4.9 (d,e). The rippled substrate device shows a fast rise time of 861 μs along with a fast fall time of 710 μs as opposed to the non-rippled device which has a slow rise and fall time of 377 ms and 392 ms, respectively. This is a three order of magnitude decrease in the response times. This decrement may be attributed to the decreased resistivity of the samples with doping as well as the increased effective area of the electrodes for charge carrier extraction.[48] Moreover, the decrease in resistivity also reduces the dielectric relaxation component of the displacement current which is otherwise reported to lead to higher response times.[49] Since a broad source of light – a 254 nm pen-ray UV lamp (Cole-Parmer) is employed, the chopping frequency of light incident on the devices is limited. The devices are therefore, expected to perform much faster if lasers are employed but the present reported values are limited by the testing equipment used.

Doping of Si in the films explains why the dark current and current under illumination of the devices increases in the rippled substrate devices while it is quite low for the non-rippled devices, leading to an increase in the overall device performance. The other rippled devices (10 min and 15 min) also boast of an enhancement in the UV-C region but with increasing irradiation times, the devices start responding to the visible spectra as well (15 minutes of ion beam sputtering) (Figure 4.10 (a,b)). The incident ions erode the SiO_2 layer which adds elemental Si in the layer above. With increasing irradiation times, the SiO_2 might get eroded to an extent where the underlying Si substrate might even get exposed leading to a response in the visible spectra. Nevertheless, for up to 10 minutes of IBS, the introduction of elemental Si is just enough to increase the performance without hampering the solar-blind nature of the devices. The response of the devices to repeated switching of the incident 254 nm light is shown in Figure 4.10 (c). The devices show negligible persistent photoconductivity (PPC) with the current levels under illumination and dark conditions repeating itself after successive cycles. All the devices show a fast response speed to repeated switching of the incident UV-C light.

With increasing irradiation times, the RMS roughness of the ripples reduces while the incoming energetic ions tend to introduce more and more Si into the overlying Ga_2O_3 layer, responsible for the response to the visible light in 15 minute rippled with Ga_2O_3 sample. The conspicuous absence of any persistent photoconductivity in all the samples show the high quality of the fabricated amorphous films which are otherwise quite prone to PPC. The superior photodetection of the devices may also be attributed to the changing oxygen vacancy concentration as shown in Figure 4.10 (d). The O1s core level spectra is deconvoluted into three peaks corresponding to oxygen being bonded to Ga (around ~ 530 eV), oxygen being bonded to Si (around ~ 532 eV) and the oxygen vacancies present in the sample (around ~ 531 eV).[50] The area percentage attributed to the oxygen vacancies in the O 1s spectra changes from $\sim 11\%$ non-rippled with Ga_2O_3 sample to about 39% in 5 minute rippled with Ga_2O_3 sample. This increase in oxygen vacancies for the rippled samples may be attributed to the preferential sputtering of oxygen atoms due to the incoming ion beam sputtering. The increase in oxygen vacancies has already been reported to be the reason for the high photoconductive gain in Ga_2O_3 [51, 52] and is also responsible for the improved photodetection in our devices.

Figure 4.10 (e) shows the temporal response of the devices taken after substantial passage of time which proves the excellent stability of the devices even after storing in air ambient, implying their robustness and durability. Although, the introduction of Si in the films corroborates the improved electrical performance of the devices, but the increase in the photocurrent of the devices may not be solely due to doping. This increase may partly be attributed to the better light-matter interaction as the increased absorption by multiple scattering and reflections and increased surface area may also contribute to the enhancement in the photocurrent. To study the changes that the patterning has on the light absorption by the material, UV-Vis spectroscopy in the reflectance mode was carried out. Figure 4.11 (a) shows the reflectance data for the non-rippled and the 5 minute rippled samples with Ga_2O_3 . The nature of the reflectance of non-rippled and rippled substrates is in line with those previously reported in literature and may be attributed to the formation of thin film and micro-size structures, respectively.[1] Figure 4.11 (c,e) shows the reflectance data for the bare substrates as well as the rippled 5 min substrate, both with and without coating the Ga_2O_3 film. Upon deposition of Ga_2O_3 , the reflectance of the films reduces in the UV-C region, since gallium oxide absorbs this particular spectrum.

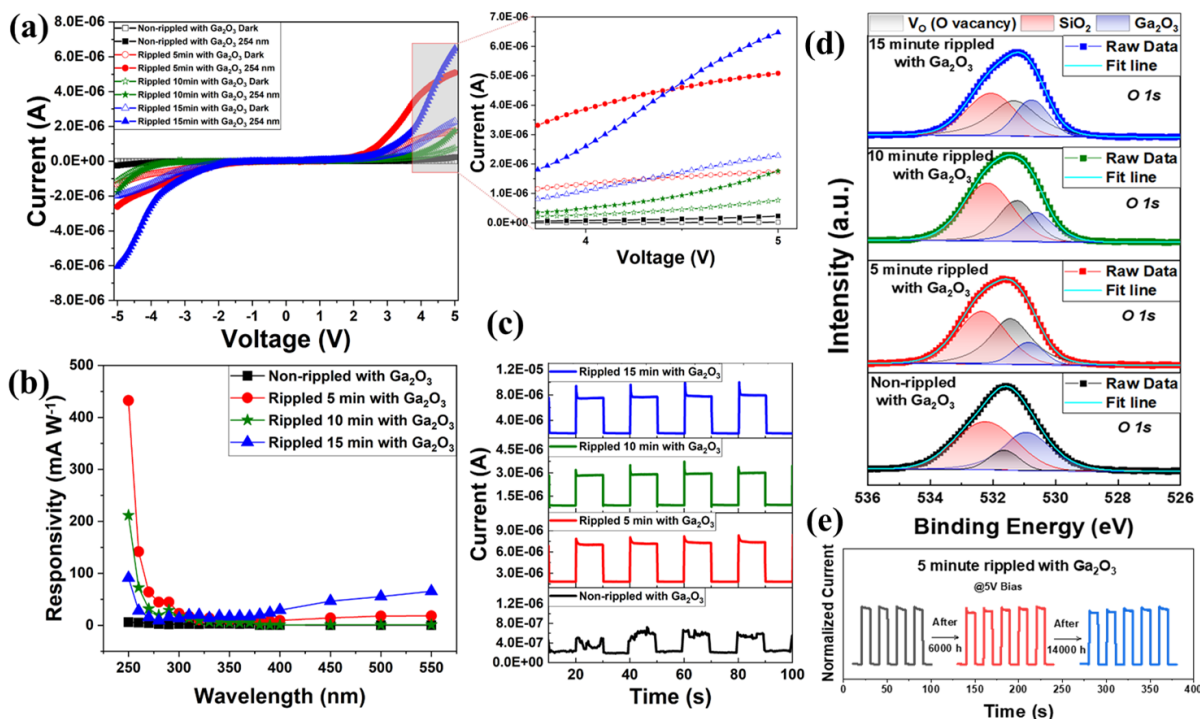


Figure 4.10. (a) Dark current and light current (under 254 nm illumination) of the devices of rippled substrates with Ga₂O₃ along with a zoomed-in image. (b) Responsivity versus wavelength of the bare and rippled devices with Ga₂O₃. The erosion of the SiO₂ layer exposes the underlying Si substrate leading to a response in the visible spectrum for the 15 min rippled devices. (c) Temporal response of the non-rippled and rippled devices to repeated switching of the incident 254 nm wavelength of light. (d) XPS core level spectra of O1s of the non-rippled and rippled samples with Ga₂O₃ and its deconvolution into three peaks corresponding to oxygen bonded to Ga, Si and the oxygen vacancies. (e) Temporal response of the devices after prolonged storage in air ambient showing high stability and robustness of the fabricated device.

To ascertain the increment in the absorption, Finite-Difference Time-Domain (FDTD) simulations were carried out using Lumerical Software and the simulated reflectance is shown in Figure 4.11 (b,d,f). The active layers were irradiated with a plane wave source and the surface was modified while conforming to the ripples generated experimentally (Figure 4.11 (g)). The side view of the model employed for the simulations is shown in Figure 4.11 (h). The simulations were carried out for varying thickness of SiO₂ (Figure 4.12 (1-h)). It was found that the erosion caused by the incoming Ar⁺ ions decreases the thickness from 280 nm to less than 150 nm upon irradiation. The simulated data for the reflectance is thus, in line with the experimental data for thicknesses less than 150 nm. In corroboration with the simulated data, a cross-sectional FESEM was also employed for determining the thickness of the films left after irradiation and the consequent Ga₂O₃ film deposition. Figure 4.12 (i) shows the cross-

sectional FESEM clearly showing the reduced thickness for the 5-minute sample. Irradiating for 5 minutes leads to a reduced thickness of about 145 nm SiO_2 .

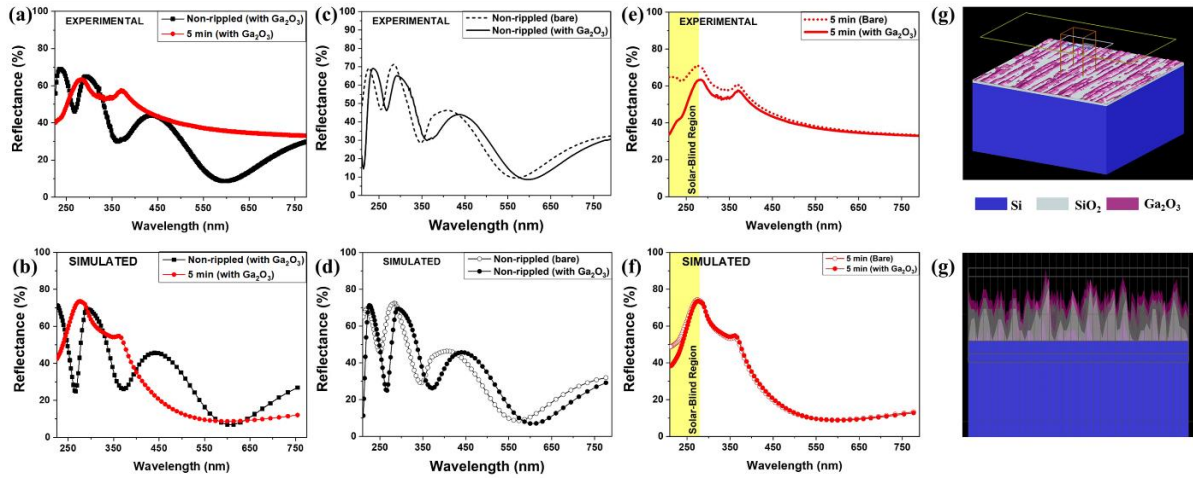


Figure 4.11. (a) Experimental reflectance data showing the difference in reflectance for non-rippled and 5 min rippled samples with Ga_2O_3 and (b) its simulated reflectance data. (c) Experimental reflectance spectra of non-rippled SiO_2 coated Si substrate with and without Ga_2O_3 . (d) Simulated reflectance spectra of non-rippled SiO_2 coated Si substrate with and without Ga_2O_3 . (e) Experimental reflectance spectra of rippled 5 min SiO_2 coated Si substrate with and without Ga_2O_3 . (f) Simulated reflectance spectra of rippled 5 min SiO_2 coated Si substrate with and without Ga_2O_3 . (g) Model used for carrying out FDTD calculations and (h) side-view of the model used for simulations showing the rippled substrate and conformally-coated Ga_2O_3 .

The thickness reduces because of the competing processes involving erosion and surface diffusion. Initially, when the surface is flat or non-patterned, the incoming ions tend to erode the surface at a much faster rate. Once patterns start appearing, the curvature/slope of the patterns reduce the erosion and surface diffusion rate which leads to a linear regime of the ripple amplitude being followed as compared to an exponential increase at the beginning of irradiation.[53] Thus, there is no marked change in the morphology of the ripples or its amplitude for increasing irradiation times as seen in Figure 4.6. This also explains why we may not be able to increase doping beyond a certain level by using higher fluences, as this would eventually erode the SiO_2 film completely, exposing the bare Si substrate below. Nevertheless, for nanopatterning using optimum fluences, the enhancement in absorption by Ga_2O_3 can be attributed to the increased surface area for absorption, multiple reflection, refractions and enhanced scatterings.[54] Light falling on the subwavelength nanoripples leads to increased multiple scatterings from the patterned substrate which is ultimately re-absorbed by the active material. Although this does not vary the band gap of the material above, it does lead to a better light management on the device which is an added advantage to the photodetection capability.

Especially for the case of SBPDs based on Ga_2O_3 films used in this work, the method of doping offers twin benefits. IBS introduces Si in the films which takes an active part in conduction thereby improving the electrical conductivity of the films by increasing the n -type doping. The second would be the formation of patterns leads to an increased absorption due to the multiple scatterings.

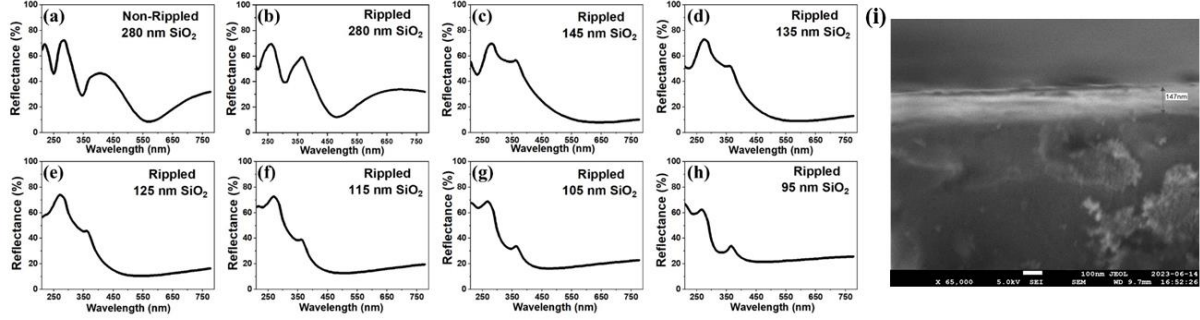


Figure 4.12 Simulated reflectance spectra using FDTD simulations for (a) non-rippled SiO_2/Si (~ 280 nm thick) and (b-h) rippled SiO_2/Si for varying thicknesses of SiO_2 from 280 nm to 95 nm. (i) FESEM image of rippled 5nm with Ga_2O_3 showing the reduction in thickness after irradiation.

A comparison of the device performance with those reported in literature is presented in Table 4.1 which clearly shows the rippled devices outperform various amorphous Ga_2O_3 based thin-film photodetectors in terms of response times. Achieving such low response times with appreciable responsivity using ultra-thin films is an interesting application of surface modification since amorphous oxide materials are notoriously known for forming slower speed devices. In this particular study, we have been able to achieve fast response times of few hundred μs simply by using ion beam sputtering as an unconventional way to dope films with free elemental Si. This method of doping may also find resonance with doping of elements in amorphous films of other materials as well which are difficult to dope via conventional methods.

Table 4.1: Comparison of the photodetectors in the present work with those reported in literature.

Material	Thickness	Method used	Geometry used	Responsivity	Rise time	Fall Time	Ref
Amorphous Ga_2O_3	100nm	Sputtering	MSM IDE	70.26 @ 10V	0.41/2.04 s	0.02/0.3 s	[28]
Amorphous Ga_2O_3	208nm	Sputtering	Phototransistor	4100 @ $V_G = -30$ V, $V_{DS} = 10$ V	50s	>400s	[3]
Amorphous Ga_2O_3	232nm	PLD	MSM IDE	9.7 @ 5V	1/7.5 s	1.1/12.7 s	[2]

Amorphous Ga ₂ O ₃	120μm	Sputtering	MSM IDE	8.9 @ 15V	<15μs	308μs/1.7ms	[55]
Amorphous Core–Shell Ga ₂ O ₃ Nanoparticles	-	FLAL and spray-coating method	MSM IDE	778 mA/W @ 3 V	0.088 s	0.23 s	[56]
Amorphous Ga ₂ O ₃	-	Sputtering	Photoelectrochemical-type	12.9 mA/W @0V	0.15 s	0.13 s	[57]
Amorphous Ga ₂ O ₃	-	Sputtering	Phototransistor	151.56 @ VGS = -1V and VDS = 40 V	3.18 s	3.05 s	[30]
Amorphous Ga ₂ O ₃	28 nm	ALD	MSM	33.9 @ 10V	0.02/0.07 s	0.02/0.04 s	[58]
β-Ga ₂ O ₃	90nm	PLD	MSM	18.23 @ 10V	0.06/0.38 s	0.06/0.66 s	[59]
β-Ga ₂ O ₃	150nm	MBE	MSM IDE	1.5 @ 4V	3.33 s	0.4 s	[60]
2D β-Ga ₂ O ₃ nanosheet	10nm	Oxidation of GaSe	Phototransistor	3.3 @ V _{DS} = 10V	0.03 s	0.06 s	[61]
Ga ₂ O ₃ /NS TO	1.324 μm	Sputtering	Heterojunction	43.31(-10 V)	0.21 s	0.07 s	[62]
Graphene / β-Ga ₂ O ₃ wafer	0.6mm	Wafer purchased	Heterojunction	39.3 @ 20V	94.83 s	219.19 s	[63]
α/β-Ga ₂ O ₃ phase junction nanorods	-	Hydrothermal reaction followed by annealing	Heterojunction	0.26@0V	0.54/3.32 s	1.63/6.79 s	[64]
Amorphous Ga ₂ O ₃	5nm	Sputtering	MSM IDE	0.43@5V	861 μs	710 μs	This work

4.2.3 Conclusions

In conclusion, this work shows the use of a low-cost, large area method of surface modification – ion-beam sputtering – as a way to dope amorphous oxide films with Si. This leads to an enhanced carrier concentration, thereby effectively enhancing the performance of a next-generation, ultra-wide band semiconductor. The preferential sputtering by IBS leads to preferential sputtering of oxygen, thereby incorporating elemental silicon into the films above which may not be possible using other etching techniques available for surface modification. Solar-blind photodetectors fabricated on these doped ultra-thin films show an enhanced performance in terms of both responsivity and response time. The responsivity of the rippled devices increases from 6 mA W⁻¹ to 433 mA W⁻¹ (~ 72 times) with fast detection speeds of 861

μs / 710 μs (rise/fall time) as opposed to the non-rippled devices which are quite slow (377 ms/392 ms). This way of doping amorphous films may be utilized for other amorphous materials as well, especially those which cannot be subjected to harsh ion implantations or high temperatures during growth.

References

1. Kaur, D., et al., Surface nanopatterning of amorphous gallium oxide thin film for enhanced solar-blind photodetection. *Nanotechnology* **2022**, 33(37), 375302.
2. Tak, B.R., et al., Wearable Gallium Oxide Solar-Blind Photodetectors on Muscovite Mica Having Ultrahigh Photoresponsivity and Detectivity with Added High-Temperature Functionalities. *ACS Applied Electronic Materials* **2019**, 1(11), 2463-2470.
3. Qin, Y., et al., Amorphous Gallium Oxide-Based Gate-Tunable High-Performance Thin Film Phototransistor for Solar-Blind Imaging. *Advanced Electronic Materials* **2019**, 5(7), 1900389.
4. Wang, Y., et al., Ultrasensitive Flexible Solar-Blind Photodetectors Based on Graphene/Amorphous Ga₂O₃ van der Waals Heterojunctions. *ACS Applied Materials & Interfaces* **2020**, 12(42), 47714-47720.
5. Han, Z., et al., Boosted UV Photodetection Performance in Chemically Etched Amorphous Ga₂O₃ Thin-Film Transistors. *Advanced Optical Materials* **2020**, 8(8), 1901833.
6. Liu, N., et al., Fast-Response Amorphous Ga₂O₃ Solar-Blind Ultraviolet Photodetectors Tuned by a Polar AlN Template. *IEEE Electron Device Letters* **2022**, 43(1), 68-71.
7. Menard, E., et al., Micro- and Nanopatterning Techniques for Organic Electronic and Optoelectronic Systems. *Chemical Reviews* **2007**, 107(4), 1117-1160.
8. Guijarro, N., et al., Surface modification of semiconductor photoelectrodes. *Physical Chemistry Chemical Physics* **2015**, 17(24), 15655-15674.
9. Chirilă, A., et al., Potassium-induced surface modification of Cu(In,Ga)Se₂ thin films for high-efficiency solar cells. *Nature Materials* **2013**, 12(12), 1107-1111.
10. Xiang, D., et al., Surface Transfer Doping-Induced, High-Performance Graphene/Silicon Schottky Junction-Based, Self-Powered Photodetector. *Small* **2015**, 11(37), 4829-4836.
11. Jeong, B., et al., Micro- and Nanopatterning of Halide Perovskites Where Crystal Engineering for Emerging Photoelectronics Meets Integrated Device Array Technology. *Advanced Materials* **2020**, 32(30), 2000597.
12. Lei, Y., et al., Highly ordered nanostructures with tunable size, shape and properties: A new way to surface nano-patterning using ultra-thin alumina masks. *Progress in Materials Science* **2007**, 52(4), 465-539.
13. Muñoz-García, J., et al., Self-organized nanopatterning of silicon surfaces by ion beam sputtering. *Materials Science and Engineering: R: Reports* **2014**, 86, 1-44.
14. Rakhi, et al., Abrupt pattern transitions in argon ion bombarded swinging Si substrates. *Physical Review B* **2022**, 106(24), 245420.
15. Redondo-Cubero, A., et al., Nanopatterning dynamics on Si(100) during oblique 40-keV Ar⁺ erosion with metal codeposition: Morphological and compositional correlation. *Physical Review B* **2012**, 86(8), 085436.
16. Gago, R., et al., Production of ordered silicon nanocrystals by low-energy ion sputtering. *Applied Physics Letters* **2001**, 78(21), 3316-3318.
17. López, R., et al., Band-gap energy estimation from diffuse reflectance measurements on sol-gel and commercial TiO₂: a comparative study. *Journal of Sol-Gel Science and Technology* **2012**, 61(1), 1-7.
18. Rex, J.P., et al., The influence of deposition temperature on the structural, morphological and optical properties of micro-size structures of beta-Ga₂O₃. *Results in Physics* **2019**, 14, 102475.

19. Hassanien, A.M., et al., Effect of annealing temperature on structural and optical properties of gallium oxide thin films deposited by RF-sputtering. *Optical and Quantum Electronics* **2020**, 52(4), 194.
20. Huso, J., et al., Localized UV emitters on the surface of β -Ga₂O₃. *Scientific Reports* **2020**, 10(1), 21022.
21. Mi, W., et al., Ultraviolet–green photoluminescence of β -Ga₂O₃ films deposited on MgAl₆O₁₀ (100) substrate. *Optical Materials* **2013**, 35(12), 2624–2628.
22. Zhang, J., et al., Solution-Processed Epitaxial Growth of Arbitrary Surface Nanopatterns on Hybrid Perovskite Monocrystalline Thin Films. *ACS Nano* **2020**, 14(9), 11029–11039.
23. Giordano, M.C., et al., Self-Organized Tailoring of Faceted Glass Nanowrinkles for Organic Nanoelectronics. *ACS Applied Nano Materials* **2021**, 4(2), 1940–1950.
24. Parida, B.K., et al., Anisotropic electrical conduction on ion induced nanorippled CoSi surface. *Applied Physics A* **2021**, 127(12), 972.
25. Dearnaley, G., et al., Electrical phenomena in amorphous oxide films. *Reports on Progress in Physics* **1970**, 33(3), 1129.
26. Nomura, K., et al., Room-temperature fabrication of transparent flexible thin-film transistors using amorphous oxide semiconductors. *Nature* **2004**, 432(7016), 488–492.
27. Ide, K., et al., Transition Metal-Doped Amorphous Oxide Semiconductor Thin-Film Phosphor, Chromium-Doped Amorphous Gallium Oxide. *physica status solidi (a)* **2019**, 216(5), 1800198.
28. Qian, L.-X., et al., Ultrahigh-Responsivity, Rapid-Recovery, Solar-Blind Photodetector Based on Highly Nonstoichiometric Amorphous Gallium Oxide. *ACS Photonics* **2017**, 4(9), 2203–2211.
29. Qin, Y., et al., Ultra-High Performance Amorphous Ga₂O₃ Photodetector Arrays for Solar-Blind Imaging. *Advanced Science* **2021**, 8(20), 2101106.
30. Wang, Y., et al., Realization of cost-effective and high-performance solar-blind ultraviolet photodetectors based on amorphous Ga₂O₃ prepared at room temperature. *Materials Today Advances* **2022**, 16, 100324.
31. Villora, E.G., et al., Electrical conductivity and carrier concentration control in β -Ga₂O₃ by Si doping. *Applied Physics Letters* **2008**, 92(20), 202120.
32. Heinemann, M.D., et al., Oxygen deficiency and Sn doping of amorphous Ga₂O₃. *Applied Physics Letters* **2016**, 108(2), 022107.
33. Ou, X., et al., Reverse Epitaxy of Ge: Ordered and Faceted Surface Patterns. *Physical Review Letters* **2013**, 111(1), 016101.
34. Rakhi, et al., Towards ordered Si surface nanostructuring: role of an intermittent ion beam irradiation approach. *Physica Scripta* **2023**, 98(5), 055902.
35. Paskaleva, A., et al., Electric, dielectric and optical properties of Ga₂O₃ grown by metal organic chemical vapour deposition. *Journal of Physics: Conference Series* **2017**, 794(1), 012017.
36. Bradley, R.M., et al., Theory of ripple topography induced by ion bombardment. *Journal of Vacuum Science & Technology A* **1988**, 6(4), 2390–2395.
37. Bradley, R.M., et al., Spontaneous Pattern Formation Induced by Ion Bombardment of Binary Compounds. *Physical Review Letters* **2010**, 105(14), 145501.
38. Castro, M., et al., Self-Organized Ordering of Nanostructures Produced by Ion-Beam Sputtering. *Physical Review Letters* **2005**, 94(1), 016102.
39. Makeev, M.A., et al., Morphology of ion-sputtered surfaces. *Nuclear Instruments and Methods in Physics Research Section B: Beam Interactions with Materials and Atoms* **2002**, 197(3), 185–227.

40. Karabacak, T., et al., Enhanced step coverage by oblique angle physical vapor deposition. *Journal of Applied Physics* **2005**, 97(12), 124504.
41. Grigoros, K., et al., Coating of Nanoporous Membranes: Atomic Layer Deposition versus Sputtering. *Journal of Nanoscience and Nanotechnology* **2009**, 9(6), 3763-3770.
42. Seah, M.P., et al., Sputtering yields of compounds using argon ions. *Journal of Physics D: Applied Physics* **2010**, 43(25), 253001.
43. Stefanos, C., et al., *Growth Study and Characterization of Single-Layer Graphene Structures Deposited on Copper Substrate by Chemical Vapour Deposition*, in *Graphene Materials*, Z.K. George and M. Athanasios Ch, Editors. 2017, IntechOpen: Rijeka. p. Ch. 5.
44. Leedy, K.D., et al., Highly conductive homoepitaxial Si-doped Ga₂O₃ films on (010) β -Ga₂O₃ by pulsed laser deposition. *Applied Physics Letters* **2017**, 111(1), 012103.
45. Rafique, S., et al., LPCVD homoepitaxy of Si doped β -Ga₂O₃ thin films on (010) and (001) substrates. *Applied Physics Letters* **2018**, 112(5), 052104.
46. Zhang, F., et al., Toward controlling the carrier density of Si doped Ga₂O₃ films by pulsed laser deposition. *Applied Physics Letters* **2016**, 109(10), 102105.
47. Wang, H., et al., Nanoimprinted Perovskite Nanograting Photodetector with Improved Efficiency. *ACS Nano* **2016**, 10(12), 10921-10928.
48. Shkir, M., et al., High-performance visible light photodetectors based on inorganic CZT and InCZT single crystals. *Scientific Reports* **2019**, 9(1), 12436.
49. Alexander, O.G., et al., On response time of semiconductor photodiodes. *Optical Engineering* **2017**, 56(9), 097101.
50. Mativenga, M., et al., Origin of light instability in amorphous IGZO thin-film transistors and its suppression. *Scientific Reports* **2021**, 11(1), 14618.
51. Hou, X., et al., High-Performance Harsh-Environment-Resistant GaOX Solar-Blind Photodetectors via Defect and Doping Engineering. *Advanced Materials* **2022**, 34(1), 2106923.
52. Kaur, D., et al., A Strategic Review on Gallium Oxide Based Deep-Ultraviolet Photodetectors: Recent Progress and Future Prospects. *Advanced Optical Materials* **2021**, 9(9), 2002160.
53. Ziberi, B., et al., Ripple pattern formation on silicon surfaces by low-energy ion-beam erosion: Experiment and theory. *Physical Review B* **2005**, 72(23), 235310.
54. Wang, W., et al., Light Management with Patterned Micro- and Nanostructure Arrays for Photocatalysis, Photovoltaics, and Optoelectronic and Optical Devices. *Advanced Functional Materials* **2019**, 29(25), 1807275.
55. Chen, Y., et al., 3D Solar-Blind Ga₂O₃ Photodetector Array Realized Via Origami Method. *Advanced Functional Materials* **2019**, 29(50), 1906040.
56. Mitra, S., et al., Solar-Blind Self-Powered Photodetector Using Solution-Processed Amorphous Core-Shell Gallium Oxide Nanoparticles. *ACS Applied Materials & Interfaces* **2019**, 11(42), 38921-38928.
57. Huang, L., et al., A simple, repeatable and highly stable self-powered solar-blind photoelectrochemical-type photodetector using amorphous Ga₂O₃ films grown on 3D carbon fiber paper. *Journal of Materials Chemistry C* **2021**, 9(32), 10354-10360.
58. Yang, Y., et al., Low Deposition Temperature Amorphous ALD-Ga₂O₃ Thin Films and Decoration with MoS₂ Multilayers toward Flexible Solar-Blind Photodetectors. *ACS Applied Materials & Interfaces* **2021**, 13(35), 41802-41809.
59. Wang, Q., et al., Influence of growth temperature on the characteristics of β -Ga₂O₃ epitaxial films and related solar-blind photodetectors. *Applied Surface Science* **2019**, 489, 101-109.

60. Pratiyush, A.S., et al., High responsivity in molecular beam epitaxy grown β -Ga₂O₃ metal semiconductor metal solar blind deep-UV photodetector. *Applied Physics Letters* **2017**, *110*(22), 221107.
61. Feng, W., et al., Synthesis of two-dimensional β -Ga₂O₃ nanosheets for high-performance solar blind photodetectors. *Journal of Materials Chemistry C* **2014**, *2*(17), 3254-3259.
62. Guo, D., et al., Zero-Power-Consumption Solar-Blind Photodetector Based on β -Ga₂O₃/NSTO Heterojunction. *ACS Applied Materials & Interfaces* **2017**, *9*(2), 1619-1628.
63. Kong, W.-Y., et al., Graphene- β -Ga₂O₃ Heterojunction for Highly Sensitive Deep UV Photodetector Application. *Advanced Materials* **2016**, *28*(48), 10725-10731.
64. Wu, C., et al., Vertical α/β -Ga₂O₃ phase junction nanorods array with graphene-silver nanowire hybrid conductive electrode for high-performance self-powered solar-blind photodetectors. *Materials Today Physics* **2020**, *12*, 100193.

Chapter 5: Interface engineering via heterostructures of gallium oxide

Heterostructures are a novel way to assimilate the superior properties of two dissimilar materials and form an integral part of modern-day research in optoelectronics. But the amalgamation of two different materials is highly dependent on the interface between the two materials and the charge carrier dynamics due to a suitable band alignment. The end result of how two different materials will integrate is highly dependent on their interface chemistry. This chapter shows this by interfacing amorphous Ga_2O_3 with two different sulfide materials – CdS and PtS. Both the sulfide materials have different properties due to their band gaps (CdS – 2.2 eV and PtS – 1.65 eV).

For the CdS- Ga_2O_3 heterostructure, the resultant devices remain solar-blind and outperform the singular bare photodetectors.[1] To further improve upon device performance, the heterostructure is subjected to a moderate annealing of 300 °C. The annealed heterojunction device shows a reduction in dark current by more than 1 order of magnitude along with an enhanced photocurrent. To study this change in the device performance between the pristine and the annealed interface, the two heterojunctions are compared using X-ray photoelectron spectroscopy depth profiling, and results show that the pristine heterostructure has a sharp interface whereas upon annealing, it leads to a sort of diffuse interface. This produces a reduced valence band offset, resulting in a change in the band alignment from type II to type I. For the PtS- Ga_2O_3 heterostructure, even though the band alignment still remains type I, the resultant devices show a broadband photoresponse instead of the solar-blind nature. Here, the charge carrier dynamics are more favorable for the narrow bandgap material PtS and thus, this particular heterojunction gives broadband photoresponse. Therefore, this chapter shows that the interfacing of the two materials for enhanced photodetection requires a thorough and complete understanding of the interfacial dynamics and charge transfer from one material to another and requires careful consideration of optimization parameters before implementation.

5.1 CdS – amorphous Ga_2O_3 heterointerface

The absence of *p*-type doping in gallium oxide has led to unipolar devices being fabricated.[2] To improve upon the existing performance, fabrication of heterostructures of Ga_2O_3 with various materials of different dimensionality and different optoelectronic properties are being pursued.[3-6] Amongst this vast repository of literature for heterostructures, it becomes imperative to study what actually happens at the core of these heterojunctions – the interface.

Gallium oxide has previously been heterointerfaced with various materials such as *p*-type traditional oxides (NiO, CuO, etc.) [7, 8] for bipolar devices, 2D materials (MoS₂, PtSe₂, etc.) [9-11] for enhanced charge carrier extraction, or even functionalized with materials like Quantum Dots and nanoparticles for obtaining novel effects. [12-17] Cadmium Sulfide, on the other hand, is an intermediate band gap material with low resistivity, high optical absorbance and high chemical and thermal stability. These properties have proliferated its use in solar cells, photodetectors, LEDs, lasers, etc. [18, 19] The integration of Gallium oxide with Cadmium Sulfide leads to the formation of a *n-n* heterojunction, since both of these are intrinsically *n*-type materials. The advantage of forming isotype heterojunctions is that the devices formed are now governed by majority carriers (as opposed to minority carrier conduction). [20] The combination of CdS and Ga₂O₃ has already been explored for photocatalytic evolution of H₂ [21] while Ga₂O₃ as a nanolayer has been utilized for enhancing the open circuit voltage of solar cells by passivating the interfacial layers. [22, 23] However, this particular combination of the oxide-sulfide materials for solar-blind photodetection remains unexplored. Moreover, the detailed studies into the interface and its critical role in governing device performance remains underreported.

5.1.1 Experimental details

SiO₂ coated Si substrates were first cleaned ultrasonically using industrial grade soap solution, deionized water, acetone, and propanol for 30 minutes successively and finally blown dry with N₂ gun. The CdS of 70-80 nm thickness were then grown using the chemical bath deposition at 85°C for 7 minutes. An aqueous solution of DI water (155 ml), aqueous ammonium hydroxide (15 ml), CdSO₄ (79.6 mM), and thiourea (2 M) was used for CdS deposition. [24] Subsequent to CdS deposition, the deposited samples were rinsed using de-ionized water to remove extra CdS particulates from the surface. Half side of the CdS film was coated with amorphous Gallium Oxide using RF Magnetron Sputtering, while the other half was physically shadowed. Ar with 3% O₂ was used as the working gas at a deposition pressure of 3 mTorr at 100 W and room temperature (after achieving a base pressure of 7 x 10⁻⁷ Torr). Indium electrodes were then fabricated in the form of strip electrodes with an inter-electrode spacing of 3.5 mm using a physical shadow mask and thermal evaporator (see Figure 5.1 (a)).

5.1.2 Results and discussion

Figure 5.1 (a) shows a comparison of the temporal response of the heterostructures of amorphous Ga₂O₃/CdS with the bare Ga₂O₃ and bare CdS based photodetectors. The fabricated

PDs showed an improved performance of the heterostructures as compared to the individual materials. The dark current of the heterostructures is found to be higher as compared to the bare Ga_2O_3 or bare CdS because of the formation of a $n-n$ heterojunction.[25] Since both CdS as well as Ga_2O_3 are intrinsically n -type in nature, the carrier conduction is led by majority carriers in the heterostructure (as opposed to the minority carriers in a conventional $p-n$ heterojunction) and hence the level of dark current rises.

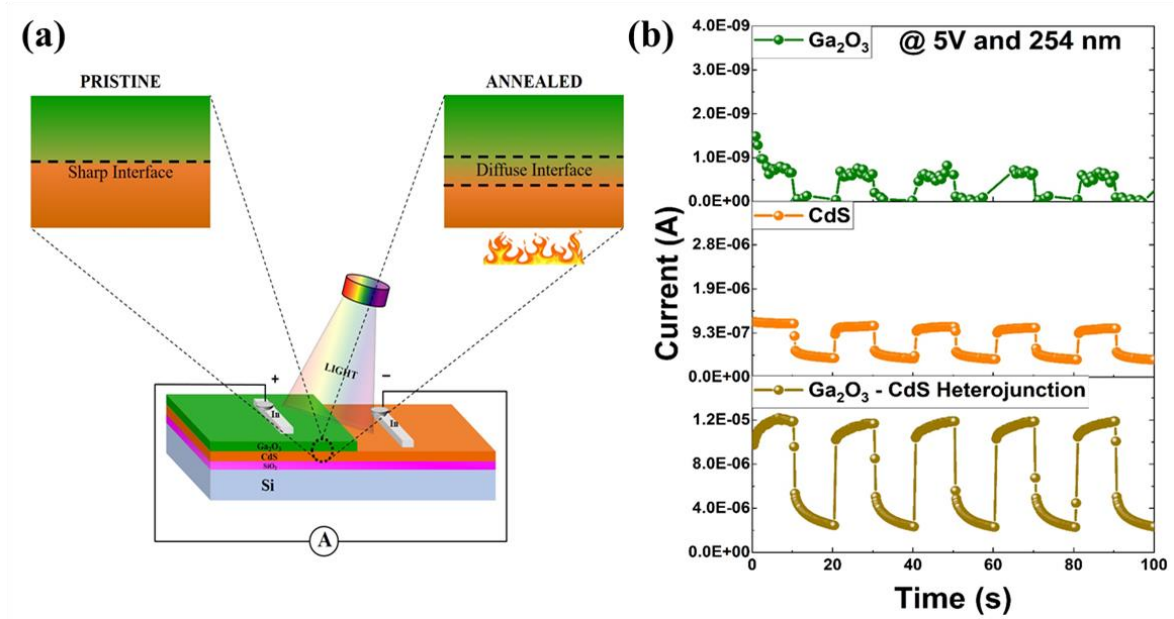


Figure 5.1 (a) Schematic of the device structure showing the pristine and annealed interface. (b) Temporal response of the bare Ga_2O_3 , bare CdS and Ga_2O_3 -CdS heterostructure based solar-blind photodetectors under 254 nm illumination and 5 V bias.

To study the effect that the interface has on the device performance, the pristine interface was tweaked by carrying out post-deposition annealing at a moderate temperature of 300°C in air ambient for about 20 minutes. This led to two different set of samples – one with a sharp interface (@pristine) and the other with a relatively diffused interface (@annealed). The schematic of the heterojunction layers is shown in Figure 5.2 (a) while the optical images of the interface of the pristine and annealed heterostructure are shown in Figure 5.2 (b) and 5.2 (c), respectively. The diffusiveness of the interface is clearly visible even with the optical images. The atomic concentration of the different constituent elements as obtained by XPS depth profile upon going from Ga_2O_3 to CdS (going from top to bottom in Figure 5.2 (a)) is also shown in Figure 5.2 (d,e). Clearly, the diffusion of the various elements starts to occur earlier in the annealed interface as compared to the pristine one. The lateral diffusion is apparent from the optical images while the atomic concentration profiles show that after around 12-14 minutes of etching, the concentrations of Cd, S, Ga and O start to show a larger variation

for the annealed interface, implying more diffusion and intermixing of the elements as compared to the pristine interface, wherein the relative concentration of the elements remain with same ratio as shown by the coloured columns in Figure 5.2 (d,e).

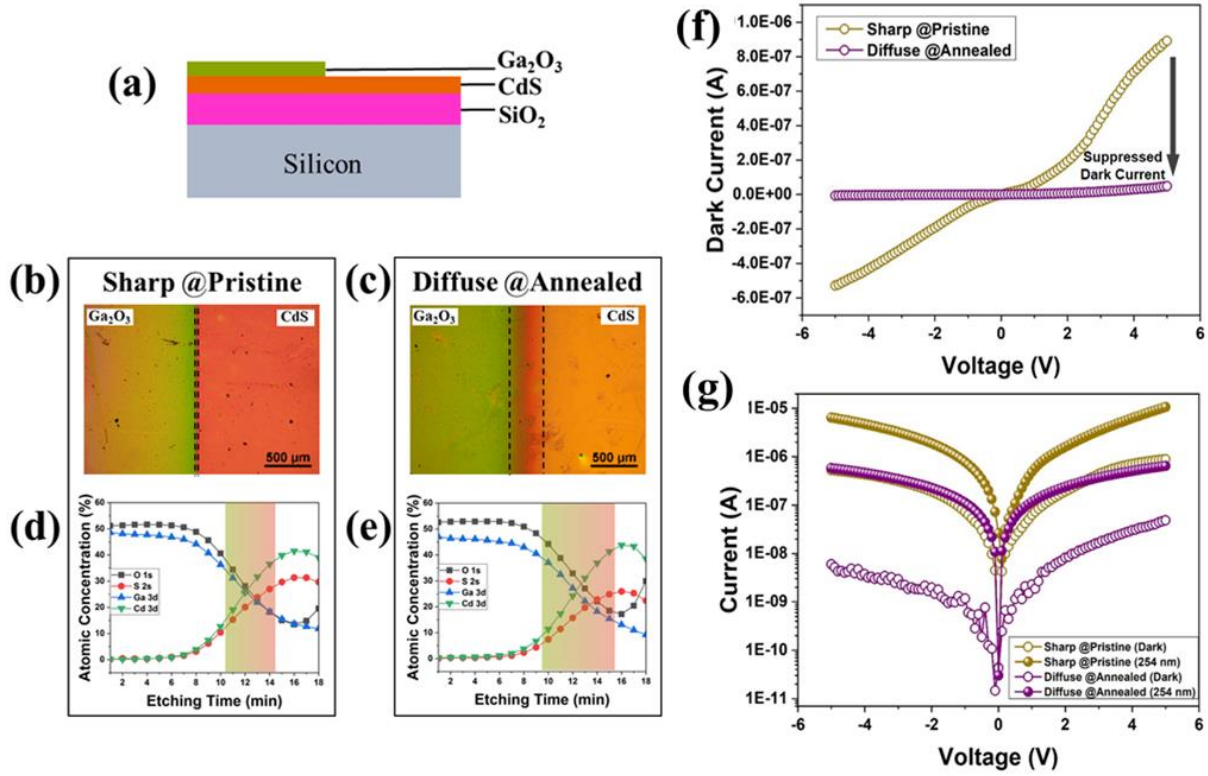


Figure 5.2. (a) Cross-sectional image of the thin film structure. Optical images of (b) pristine and (c) annealed interface. Atomic concentration of the (d) pristine and (e) annealed interfaces as determined by XPS depth profiling. (f) I-V graph under dark conditions and (g) log I vs. V plot under dark and 254 nm illumination for the pristine and annealed interface based devices.

Figure 5.2 (f) shows the dark current for the pristine and annealed heterostructures devices. The dark current reduces drastically after annealing while maintaining its Schottky nature. The reduction in dark current upon annealing has been reported in literature for other materials as well.[26] This is usually attributed to the passivation of the defects present at the interface and/or improvement in the interface quality.[27, 28] The dark current at 5V bias reduces from 0.89 μA (for the pristine interface) to about 48 nA upon annealing. Upon illumination with 254 nm incident light, the devices show an increase in the photocurrent as shown in Figure 5.2 (g). The photoresponse ($I_{ph} - I_{dark}$) also increases upon annealing with the annealed devices showing a higher increment than the pristine devices. Since annealing is performed on the heterostructures and not the devices per se, the improvement in the nature of contacts as a reason for the change in performance may be ruled out. Moreover, since the relative levels of dark current as well as photocurrent change in both the interfaces, the passivation of defects at

the interface cannot be the sole reason for the change in device performance. If only the defects were passivated or reduced, the order of magnitude of the photocurrent should have remained the same as before passivation, if not higher.[29] In this case, the level of the photocurrent also reduces (in addition to the reduction of dark current). This implies that a change in the material property at the interface must play a crucial role in determining the device performance.

Figure 5.3 (a) shows the photo-to-dark current ratio (PDCR) (calculated as $(I_{ph} - I_{dark})/I_{dark}$) for the pristine and annealed devices with the annealed device showing a higher PDCR as compared to the pristine one. Inset of Figure 5.3 (a) shows the responsivity vs. wavelength graph for the devices at 5 V bias, both of which show excellent solar-blindness. The higher magnitude of the absolute responsivity for the pristine sample is due to the larger dark current which leads to a higher value of I_{ph} even though the photo-to-dark current ratio is higher for the annealed sample.

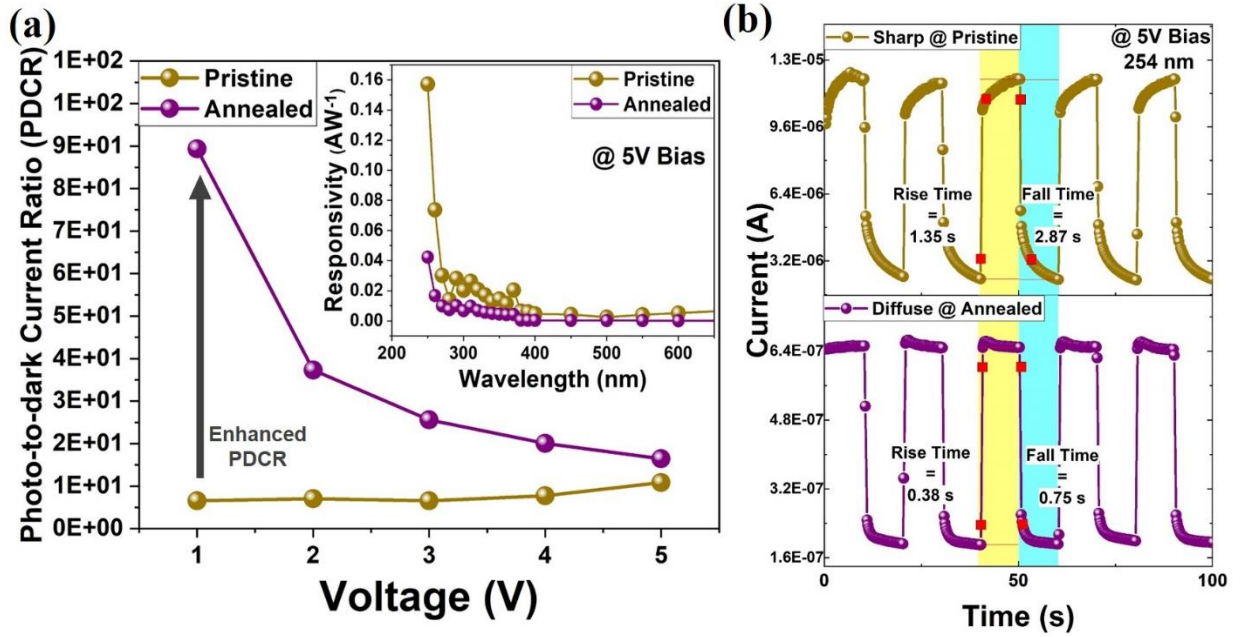


Figure 5.3. (a) PDCR for different applied voltages for the pristine and annealed interface. Inset shows the responsivity vs. wavelength plot at 5 V bias and (b) temporal response under 254 nm illumination with the rise and fall times for the pristine and annealed interface based devices.

Figure 5.3 (b) shows temporal response of the devices for repeated switching on and off of the incident UV-C light. The rise time of the devices reduces from 1.35 s to 0.38 s upon annealing while the fall time reduces from 2.87 s to about 0.75 s for the pristine and annealed devices, respectively. Thus, the annealed devices with a diffuse interface show a lower dark current, higher photoresponse and faster speed as compared to the pristine devices with a sharp

interface. The improvement in interface quality and/or a reduction in defects at the interface reduces the dark current and may also be the reason for the faster devices as the charge carrier trapping at the interface is now lowered.

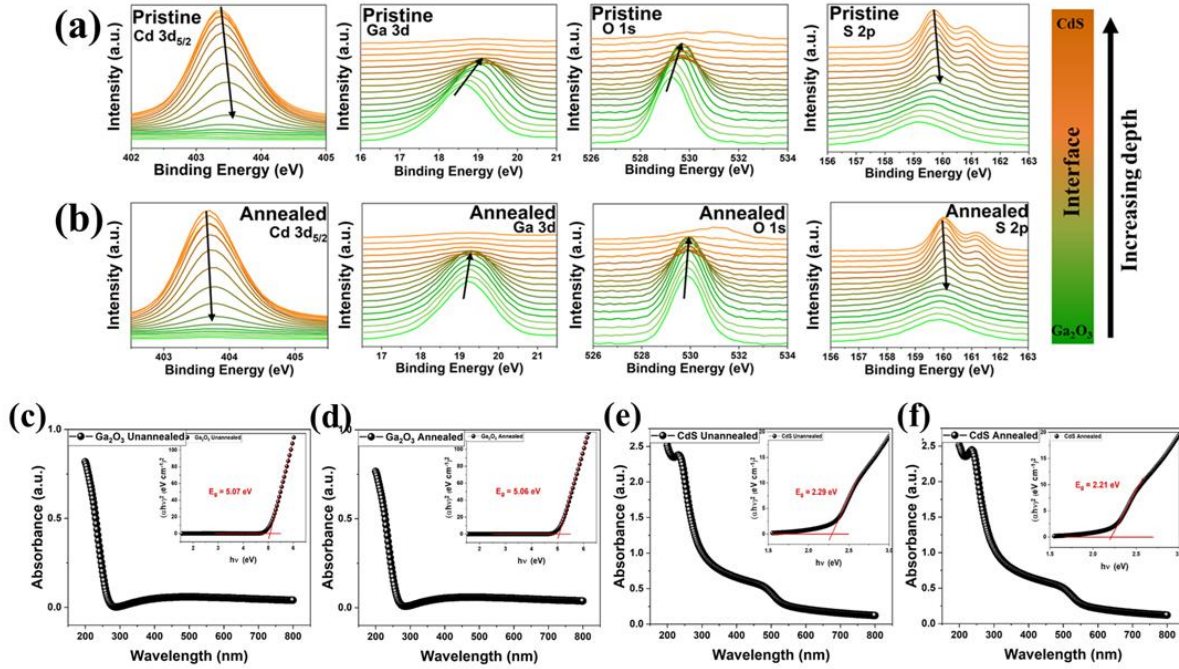


Figure 5.4. XPS depth profile for the core level spectra of Cd 3d_{5/2}, Ga 3d, O 1s and S 2p for the (a) pristine and (b) annealed interface. Absorbance spectra for (c) Ga₂O₃ unannealed or pristine, (d) Ga₂O₃ Annealed, (e) CdS unannealed or pristine and (f) CdS annealed films. The insets show the Tauc plots with the corresponding calculated band gaps.

To probe into the reason for change in the device performance upon annealing of the heterostructures, the interfacial studies were carried out using XPS depth profiling.[30, 31] The thickness of the amorphous gallium oxide film is roughly 70-80 nm and hence, to move towards the vicinity of the true interface, some of the top film on the Ga₂O₃ side was etched with Ar ion sputtering prior to XPS depth profiling. Thereafter, the levels were etched for 60 s each and the XPS was recorded after each etch level. Figure 5.4 (a-b) shows the XPS depth profile for the pristine and annealed interface displaying the core level spectra of Cd 3d_{5/2}, Ga 3d, O 1s and S 2p. There is a positive shift in all of the core level spectra but the relative shift is higher in pristine samples (as indicated by the black arrows in Figure 5.4 (a-b)) as we go down from gallium oxide to CdS at the interface. This implies that the heterostructure interface is much sharper in the pristine sample leading to a more pronounced shift in the core level spectra. The interface spectra differ more because of the change in the chemical state in pristine sample but upon annealing, the interface diffuses to a sort of homogeneity, thereby leading to a relatively small shift.

To study the band alignment at the interface, core level spectra of Cd 3d_{5/2} and Ga 3d was utilized. The valence band maximum (VBM) was calculated by extrapolating a linear fit of the leading edge of the valence band spectra. The VBM of CdS and Ga₂O₃ was found to be 1.76 eV and 4.16 eV for the pristine samples while it decreased to 2.1 eV and 4.19 eV for the annealed ones. The valence band offset (VBO) at both the sharp and diffuse interfaces was determined by using the Kraut's rule[32]:

$$VBO = (E_{Ga\ 3d}^{Ga_2O_3} - E_{VBM}^{Ga_2O_3}) - (E_{Cd\ 3d_{5/2}}^{CdS} - E_{VBM}^{CdS}) + \Delta E_{CL}(i) \quad (5.1)$$

where, $\Delta E_{CL}(i) = (E_{Cd\ 3d_{5/2}}^{Ga_2O_3/CdS} - E_{Ga\ 3d_{5/2}}^{Ga_2O_3/CdS})$ is the binding energy difference between Cd 3d_{5/2} and Ga 3d core levels at the interface. The term $(E_{Ga\ 3d}^{Ga_2O_3} - E_{VBM}^{Ga_2O_3})$ and $(E_{Cd\ 3d_{5/2}}^{CdS} - E_{VBM}^{CdS})$ and represent valence band edges with reference to core levels of Ga₂O₃ and CdS, respectively.

For the pristine interface, the VBO was calculated to be 2.81 eV while for the annealed interface, it was found to be 2.08 eV. To calculate the conduction band offset (CBO), the following equation was used:

$$CBO = E_g^{Ga_2O_3} - E_g^{CdS} + VBO \quad (5.2)$$

where $E_g^{Ga_2O_3}$ and E_g^{CdS} represents the bandgap of Ga₂O₃ and CdS, respectively. The band gaps of CdS and Ga₂O₃ were determined using the Tauc plots (Figure 5.4 (c-f)). Ga₂O₃ band gap remained almost constant even after annealing, changing slightly from 5.07 to 5.06 eV. The consistent band gap is to be expected as the annealing temperature of 300°C is too low for any sort of major change to occur in Ga₂O₃. CdS on the other hand, has a reduction in band gap from 2.29 eV to 2.21 eV, consistent with the reported literature.[33-35] These values of band gaps were utilized to find the CBO which was 0.03 eV and – 0.77 eV for the pristine and annealed samples, respectively. The resultant band alignments are shown in Figure 5.5 (c). The pristine interface shows a type II band alignment which changes into a type I alignment upon annealing. The reduced band gap and the lower VBO lead to a shifting down of CdS bands and hence leads to a change in the nature of the band alignment. In addition to the band alignment, the shifts in the core level spectra can also provide important information about the charge transfer occurring at the interface. The shift in the binding energies often give information about the charge states of the materials along with how the electronic environment of the chemical components changes with a change in their surroundings.[36-38]

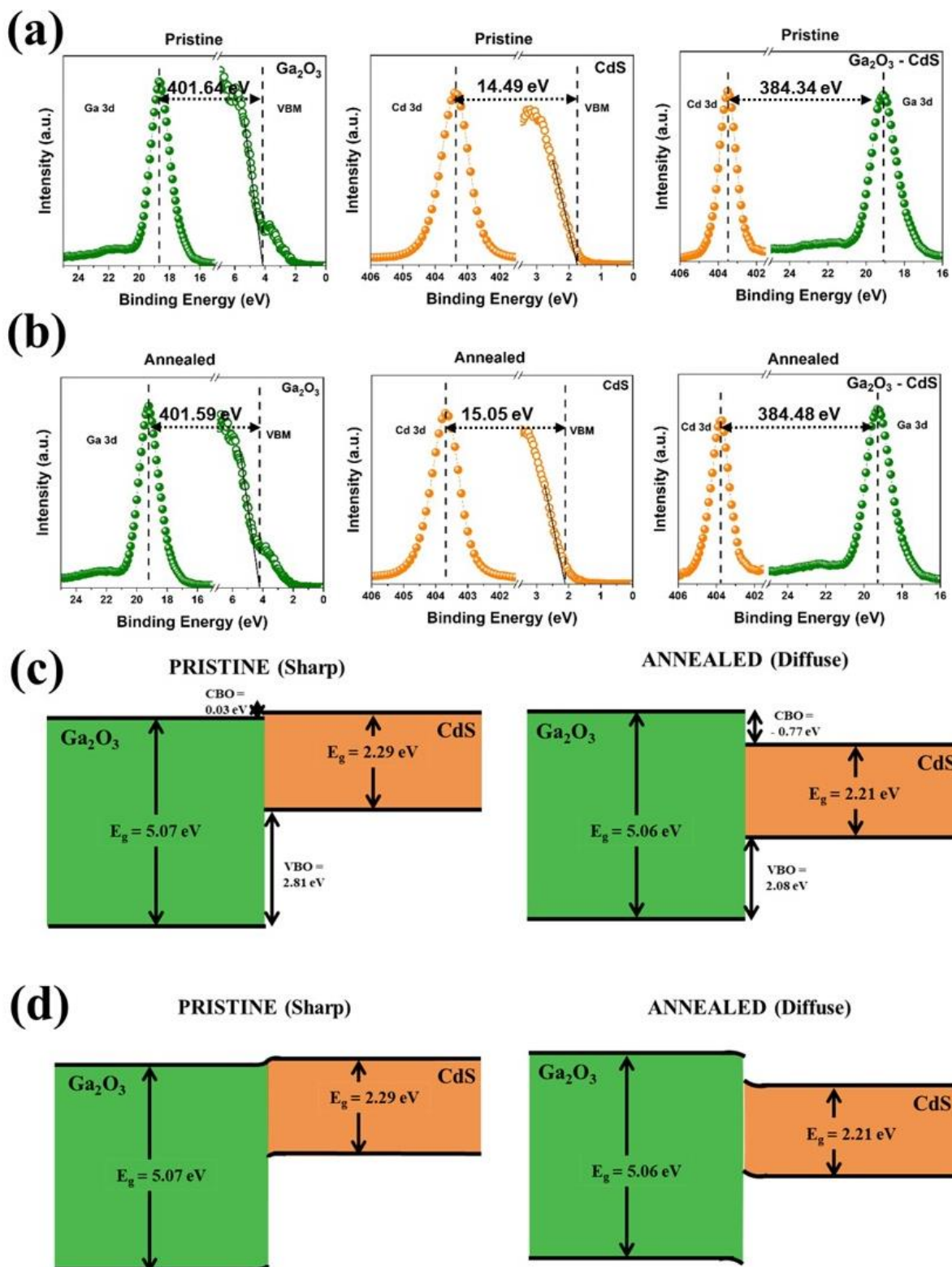


Figure 5.5. XPS core level spectra and valence band maxima calculation at the bulk and interface for (a) pristine and (b) annealed interfaces. (c) Band alignment diagrams for the pristine and annealed interfaces found using the binding energy measurements carried out via XPS and VBS spectra (d) Band alignments along with the obtained band bending.

Looking closely at the shifts in the core level spectra of the Cd 3d_{5/2} and Ga 3d, the change in the charge transfer of the pristine and annealed interfaces can be easily understood. In Figure 5.6 (a,c), for the case of pristine interface, the relative shift of the Cd 3d_{5/2} is 0.14 eV towards higher binding energy (BE), while the Ga 3d shows a shift of 0.48 eV towards higher BE. Since higher binding energy shift corresponds to *n*-doping or a higher number of electrons, the charge transfer in the pristine interface takes place from CdS to Ga₂O₃. [39] For the case of annealed interface (Figure 5.6 (b,d)), the relative shift in the Cd 3d_{5/2} and Ga 3d core level spectra is 0.07 eV and 0.03 eV towards higher BE, and hence the charge transfer occurs from Ga₂O₃ to CdS.

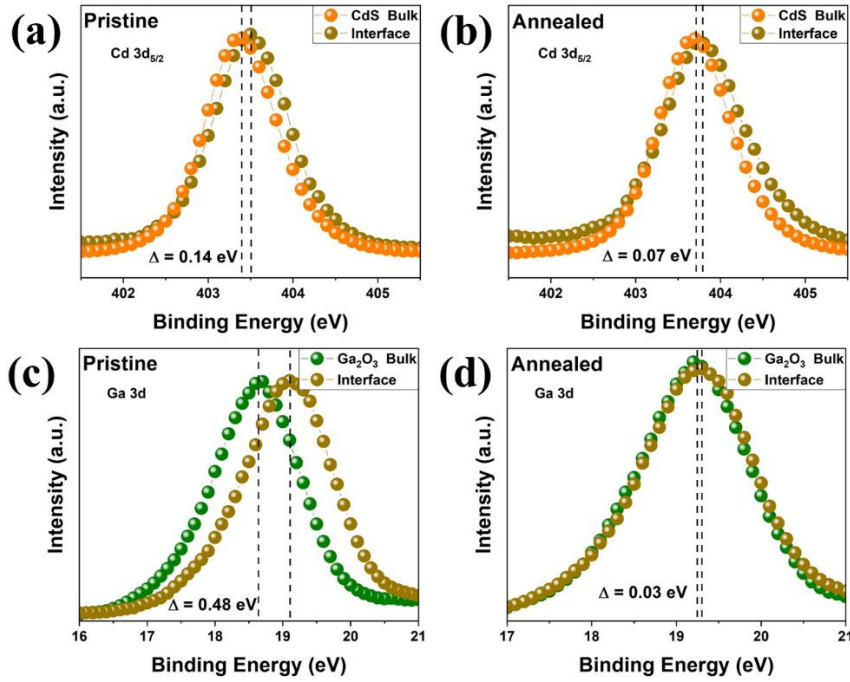


Figure 5.6 XPS core level spectra of Cd 3d_{5/2} and Ga 3d for the (a,c) pristine and (b,d) annealed interfaces showing the relative shift from the bulk to the interface.

To study the charge dynamics and corroborate the results found using the XPS depth profiling, Kelvin Force Probe Microscopy was carried out on the two heterointerfaces under dark and light conditions. [40]. For KPFM, the V_{CPD} or the contact potential difference is calculated as [41]:

$$eV_{CPD} = \phi_t - \phi_s \quad (5.4)$$

where, ϕ_t is the work function of the tip, ϕ_s is the work function of the sample and e is the electronic charge. Since the work function of the tip remains same, any change in the V_{CPD} corresponds to a change in the work function of the sample. [42] The higher V_{CPD} means a lower work function of the sample, while a lower V_{CPD} corresponds to a higher work function of the sample. Thus, the Fermi level of a bigger ϕ_s would be lower than the fermi level of a smaller

ϕ_s and upon the formation of equilibrium, the charges would be transferred from one material to the other.[43, 44] Figure 5.7 (a,b) shows the surface potential maps of the bare CdS and Ga₂O₃-CdS heterojunction for the pristine interface, respectively, while Figure 5.7 (c) represents the surface potential distribution curve. It can be seen that the surface potential is more positive for the Ga₂O₃-CdS as compared to the bare CdS, implying a charge transfer from CdS to Ga₂O₃ to form the equilibrium. For the case of annealed interface (Figure 5.7 (d-f)), the V_{CPD} for Ga₂O₃-CdS is lower than that of bare CdS implying a charge transfer from Ga₂O₃ to CdS. This is in-line with the band alignment as obtained from XPS data. There is a huge change observed in the surface potential even under dark conditions for the Ga₂O₃-CdS of pristine and annealed interface (Figure 5.7 (g)) which may be attributed to the vast difference in the charge carrier dynamics.

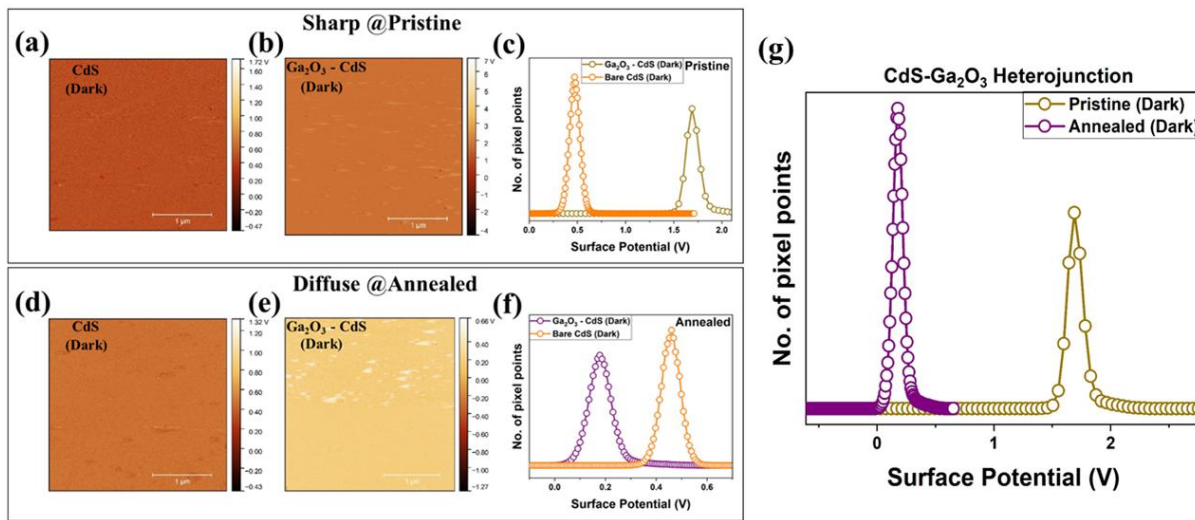


Figure 5.7. Surface potential maps in dark of (a) CdS and (b) Ga₂O₃ - CdS pristine interface along with the corresponding (c) surface potential distribution. Surface potential maps in dark of (d) CdS and (e) Ga₂O₃ - CdS annealed interface along with the corresponding (f) surface potential distribution. (g) Surface potential distribution under dark conditions of the Ga₂O₃ - CdS pristine and annealed interface.

To understand the changes under light, KPFM was conducted using white light illumination. For the case of bare CdS, the surface potential does not change drastically under dark or light conditions, primarily because there is no change in the material property (Figure 5.8 (a,b)). But for the case of heterostructures, the surface potential of the Ga₂O₃-CdS changes because of a charge transfer at the interface under dark and light conditions. Figure 5.8 (c-e) and Figure 5.8 (f-h) show the surface potential maps and distribution of the pristine and annealed interfaces, respectively, under dark and light conditions. The negative shift in the surface potential of the pristine interface shows that upon incidence of light, more photogenerated charge carriers are

transferred from CdS to Ga_2O_3 while the positive shift in the case of annealed interface represents the charge transfer from Ga_2O_3 to CdS.

The correlation of the device performance with the change in carrier dynamics can be understood by the shift in the KPFM. The huge change in the surface potential under dark condition is representative of the change in the charge dynamics across the two interfaces which eventually leads to a reduction in dark current of the annealed device. The relative change in the surface potential values under light illumination is less and hence the enhancement in photocurrent for the two interfaces remain less pronounced.

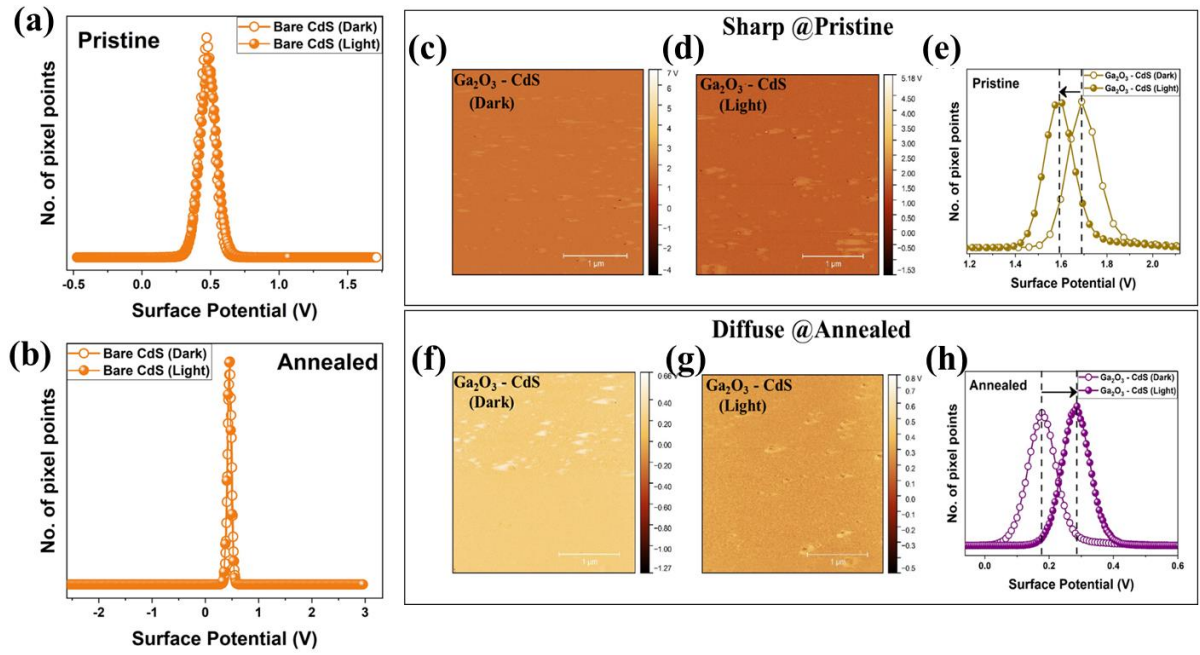


Figure 5.8. Surface potential distribution of the bare CdS (a) pristine and (b) annealed interface showing almost negligible change under dark and light conditions. Surface potential maps under illumination of (c) CdS and (d) Ga_2O_3 - CdS pristine interface along with the corresponding (e) surface potential distribution. Surface potential maps under illumination of (f) CdS and (g) Ga_2O_3 - CdS annealed interface along with the corresponding (h) surface potential distribution.

Thus, the change in the nature of band alignment with moderate annealing is adjudged to be the reason for the change in device performance. The type II band alignment of the pristine interface, leads to a separation of charge carriers with the electrons easily going from the CB of CdS to the CB of Ga_2O_3 while the holes go from the VB of Ga_2O_3 to the VB of CdS. The very small CBO enhances the flow of electrons across the interface with a relative ease, leading to an increased dark current as well as an enhanced photocurrent. Since the carriers are efficiently separated, their recombination upon the switching off of the incident light is slower leading to slow response times. On the other hand, annealing the samples leads to a diffuse

interface having a sort of homogeneity at the interface and a type I band alignment. This provides a barrier to the flow of electrons and holes across the interface, leading to decreased dark currents. The electrons can go from CB of Ga_2O_3 to CB of CdS, but the holes face a huge barrier and may get accumulated in the VB of CdS. This accumulation leads to higher chances of recombination for the electrons in the CB and hence the device gives much faster response speed. Thus, from the XPS and KPFM studies, it can be clearly seen that the change in device performance upon annealing can be attributed to the change in the interfacial chemistry represented by band alignment modification. Moreover, annealing the heterostructures may not necessarily lead to only a reduction in the interfacial defects but can also significantly alter the interface chemistry.

5.1.3 Conclusions

Amorphous Ga_2O_3 is heterointerfaced with CdS for achieving solar-blind photodetection. The *n-n* heterojunction formed leads to an improved performance as compared to the single material photodetectors. Annealing the interface leads to a reduced dark current, enhanced photocurrent and faster devices as compared to pristine interface. Interfacial studies were carried out to investigate the reason for the enhanced performance. XPS depth profiling studies showed that the diffuse interface has a sort of homogenized interface with less relative shift in the peak positions leading to a type I alignment while the sharp interface has a more pronounced higher binding energy shift leading to a type II band alignment. The change in the alignment also leads to a change in the charge carrier dynamics which is also corroborated by KPFM studies. The ultimate device performance is intimately linked with the band alignment that is formed at the heterointerface. For the specific case of Ga_2O_3 -CdS interface, the nature of the band alignment can be altered with annealing at moderate temperatures.

5.2 PtS – amorphous Ga_2O_3

For the next study, we introduce a heterojunction interfacing narrow band gap semiconductor PtS with wide band gap semiconductor Ga_2O_3 , which does not lead to solar-blind photodetection but instead gives rise to fast speed broadband photodetectors, working even at self-bias. The thin layer of Ga_2O_3 provides oxide passivation to the ample of defects present on the surface of PtS. Consequently, the resultant broadband photodetector gives an enhanced responsivity at 300 nm of incident light for PtS from about 2 mAW^{-1} to about 252 mAW^{-1} for the heterojunction device at moderate bias of 5V bias, an increase of more than 120 times while the responsivity at 780 nm rises from 5 mAW^{-1} to 173 mAW^{-1} for PtS- Ga_2O_3 . Additionally,

for the visible region, the response time reduces from 42 ms/46ms (rise/fall time) for PtS to 277 μ s/258 μ s for PtS- Ga₂O₃, a reduction of more than 150 times. Band alignment studies using XPS depth profiling show a type I band alignment in the *n-n* heterojunction. Thus, this study reveals that the interfacing of any material with Ga₂O₃ for enhanced photodetection requires a thorough and complete understanding of the interfacial dynamics and charge transfer from one material to another and requires careful consideration of optimization parameters before implementation.

5.2.1 Experimental details

SiO₂ coated Si substrates were ultrasonically cleaned in soap-solution, deionized water, acetone and propanol, for 30 minutes each successively and then blown-dry with N₂. PtS was grown using thermal assisted conversion (TAC) method. Pt was coated on the substrates using RF Magnetron Sputtering at 30 W and 3.75 mTorr at room temperature after reaching a base pressure of 2.8 x 10⁻⁶ Torr. These Pt coated substrates were then sulfurized using Ar gas (75 sccm) in a CVD tube keeping the substrates at a temperature of 500°C while the sulfur powder is vaporized at 300°C. Further details regarding sulfurization set up is reported elsewhere.[45] A 3 nm ultra-thin amorphous Ga₂O₃ films were coated on half of PtS films (while physically shadowing the other half) using RF Magnetron Sputtering at low power of 50 W and deposition pressure of 3 mTorr at room temperature. Photodetectors were then fabricated by employing strip electrodes of Au with 3.5 mm inter-strip spacing using thermal evaporator and a physical shadow mask.

5.2.2 Results and discussion

Figure 5.9 (a) shows the schematic depicting the synthesis of the PtS- Ga₂O₃ films while Figure 5.9 (b) shows the optical image of the films. Ga₂O₃ film covers half of the PtS film while exposing the other half.

The growth of PtS on the SiO₂/Si samples was confirmed using the Raman spectra (Figure 5.9 (c)). There occurs a small intensity peak at ~ 333 cm⁻¹ which corresponds to B_{1g} peak of PtS.[46] Even upon coating the PtS with Ga₂O₃, the Raman peak remains consistently at the same peak position without showing any shift depicting that the overlying Ga₂O₃ produces no strain on the underlying PtS.[47] Figure 5.9 (d) shows the AFM micrographs of PtS and PtS- Ga₂O₃, both showing no distinct change in morphology implying that the amorphous Ga₂O₃ is coated evenly on PtS without any major change. The RMS roughness of the films turn out to be 1.63 ± 0.15 nm and 1.73 ± 0.39 nm with and without coating with Ga₂O₃ whose thickness is measured to be ~ 3 nm.

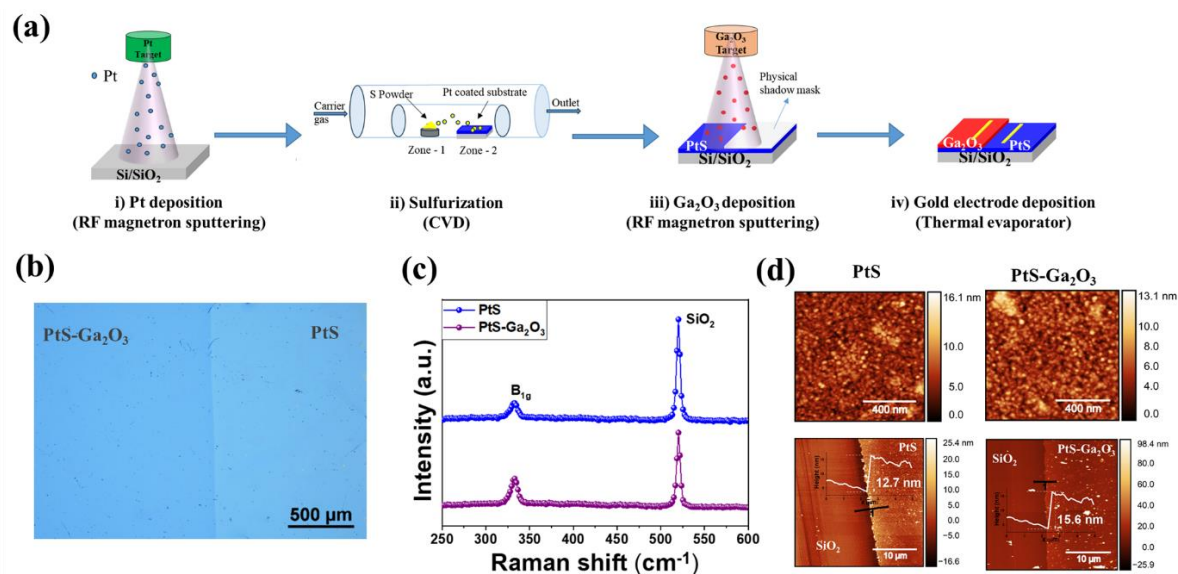


Figure 5.9. (a) Schematic showing the growth of PtS and PtS-Ga₂O₃ thin films and photodetectors thereof. (b) Optical image of the actual thin film heterostructure. (c) Raman spectra showing the B_{1g} peak proving the formation of PtS. (d) AFM micrographs showing the surface morphology of PtS and PtS-Ga₂O₃ films along with the height profiles to measure the thickness of Ga₂O₃ film.

To study the chemical changes occurring at the heterojunction, XPS depth profiling was carried out going from Ga₂O₃ layer to the PtS below. Since the Ga₂O₃ film is quite thin, the heterojunction is reached after about 50 sec of etching with 1000 eV Ar⁺ ions in a raster size of 2 mm². Figure 5.10 shows the core-level spectra of the main elements of PtS and gallium oxide while going downwards in depth from gallium oxide. The top level shows the presence of both PtS and Ga₂O₃ since the oxide film is too thin and the XPS detects the underlying layer as well. As we go deeper into the films, the Ga 3d simply disappears implying that the Ga₂O₃ is etched away reaching down to PtS layer. Further etching leads to un-sulfurized Pt which is followed by the substrate of SiO₂/Si. Figure 5.10 (a) shows the Pt 4f spectra for the different etch levels. The top most level shows Pt 4f_{7/2} peak around 72 eV which corresponds to Pt(II) or PtS, whereas higher levels also show the presence of an additional peak around 71 eV corresponding to metallic Pt.[48] The latter becomes more prominent as the etching is continued, implying that some of the deposited Pt remains un-sulfurized, even with the formation of PtS. Figure 5.10 (b) shows the core level spectra of S 2p where the first level also contains a small peak of Ga 3s at 160 eV in addition to those for sulfide and polysulfide.[49] The Ga 3s peak almost disappears in the second level itself which is also evident in the core-level spectra of Ga 3d as shown in figure 5.10 (c). For the core level of O 1s, the same trend is seen, where O 1s is deconvoluted into two peak, lower binding energy peak is corresponding

to the Ga-O bonding and the higher energy peak is corresponding to the oxygen vacancy. The area of the lower binding energy peak decreases with etching and complete disappears at level 4 as shown in Figure 5.10 (d). Where the topmost level corresponds to Ga_2O_3 , level 3 belongs to PtS while the interface between them is represented by level 2. The peak binding energies of the Pt $4f_{7/2}$ corresponding to PtS shifts by about 0.06 eV (from bulk towards interface) towards higher binding energy while Ga 3d shows a shift of about 0.04 eV.

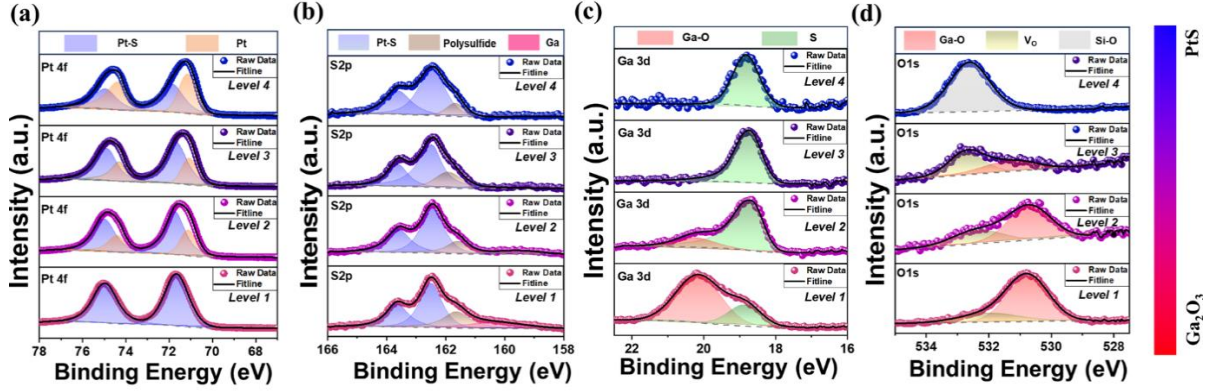


Figure 5.10. Core-level spectra of (a) Pt 4f, (b) S 2p, (c) Ga 3d and (d) O 1s for the PtS- Ga_2O_3 heterostructure measured during XPS depth profiling.

Figure 5.11 (a-c) shows the relative difference between the core level spectra and the valence band maxima (as obtained from extrapolating the linear region in UPS spectra) for the PtS and Ga_2O_3 and the relative difference between the Ga 3d and Pt 4f at the interface. Using Kraut's rule for determining the valence band offset:

$$VBO = (E_{Pt\ 4f}^{PtS} - E_{VBM}^{PtS}) - (E_{Ga\ 3d}^{Ga_2O_3} - E_{VBM}^{Ga_2O_3}) + \Delta E_{CL} (i) \quad (5.5)$$

where, $\Delta E_{CL} (i) = (E_{Ga\ 3d}^{Ga_2O_3/PtS} - E_{Pt\ 4f}^{Ga_2O_3/PtS})$ is the binding energy difference between Ga 3d and Pt 4f core levels at the interface. The terms $(E_{Pt\ 4f}^{PtS} - E_{VBM}^{PtS})$ and $(E_{Ga\ 3d}^{Ga_2O_3} - E_{VBM}^{Ga_2O_3})$ represent valence band edges with reference to core levels of PtS and Ga_2O_3 , respectively. The VBO was found to be 2.17 eV. Using the band gap values as extracted from the REELS spectra (see figure S2) for PtS and Ga_2O_3 , the conduction band offset was calculated as:

$$CBO = E_g^{PtS} - E_g^{Ga_2O_3} + VBO \quad (5.6)$$

where E_g^{PtS} and $E_g^{Ga_2O_3}$ represents the bandgap of PtS and Ga_2O_3 , respectively.

The CBO was found to be -0.93 eV. Figure 3 (d) shows the calculated band alignment at the interface of PtS and Ga_2O_3 which turns out to be a type I band alignment. Since both the materials employed are *n*-type in nature, the carrier conduction changes from minority type to

a majority type conduction, implying that the electrons alone are majorly responsible for conduction.[1] Under equilibrium, Ga_2O_3 shows an upward band bending while PtS shows a downward band bending once the two materials are interfaced.

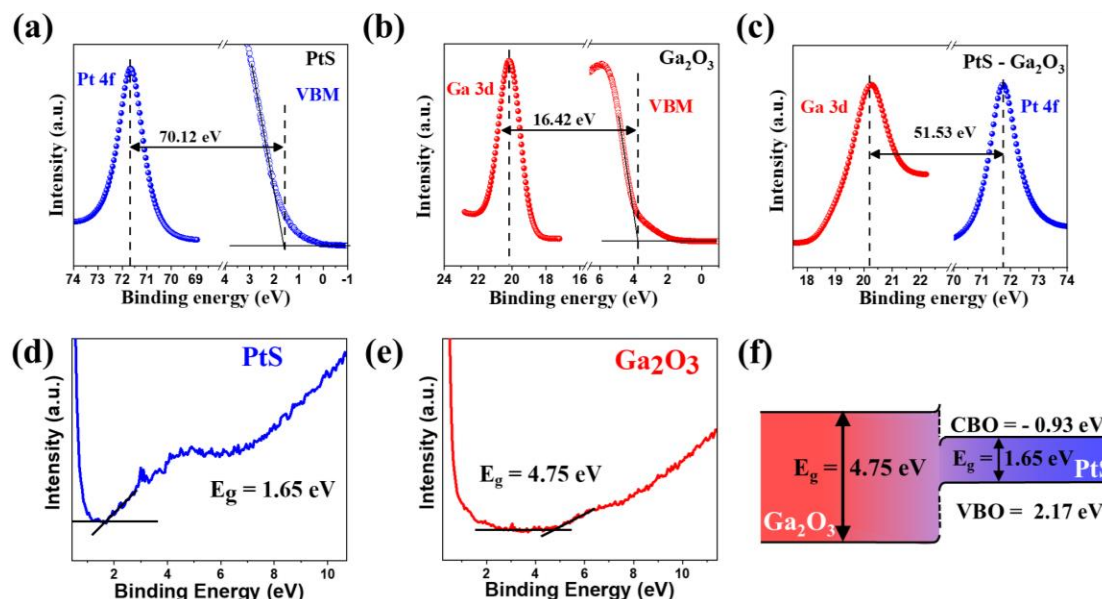


Figure 5.11. XPS core level spectra and valence band maxima calculation at the bulk for (a) bare PtS and (b) PtS- Ga_2O_3 heterojunction. (c) XPS core level spectra difference at the interface. REELS data showing the band gap values of (d) PtS and (e) Ga_2O_3 . (f) Calculated band alignment diagram for the heterojunction found using the binding energy measurements carried out via XPS and VBS spectra.

Figure 5.12 (a,b) shows the current versus voltage characteristics of the devices (see inset) of PtS and PtS- Ga_2O_3 . Due to the *n*-type nature of both the materials, the dark current of the heterostructure increases due to the conduction changing from minority to majority carrier conduction. Upon illumination under different wavelengths, the current in the devices increases due to the generation of electron-hole pairs. Figure 5.12 (c) depicts the responsivity versus wavelength graph of the bare PtS and PtS- Ga_2O_3 heterojunction device, showing an increment in the responsivity across the entire wavelength spectrum. In the UV region, the peak responsivity at 300 nm of incident light increases from about 2 mAW^{-1} to about 252 mAW^{-1} for the heterojunction device at 5V bias, an increase of more than 120 times. For the visible region, the peak responsivity at 780 nm rises from 5 mAW^{-1} to 173 mAW^{-1} for PtS- Ga_2O_3 heterojunction. Thus, showing that heterointerfacing Ga_2O_3 with PtS does not lead to solar-blind photodetection.

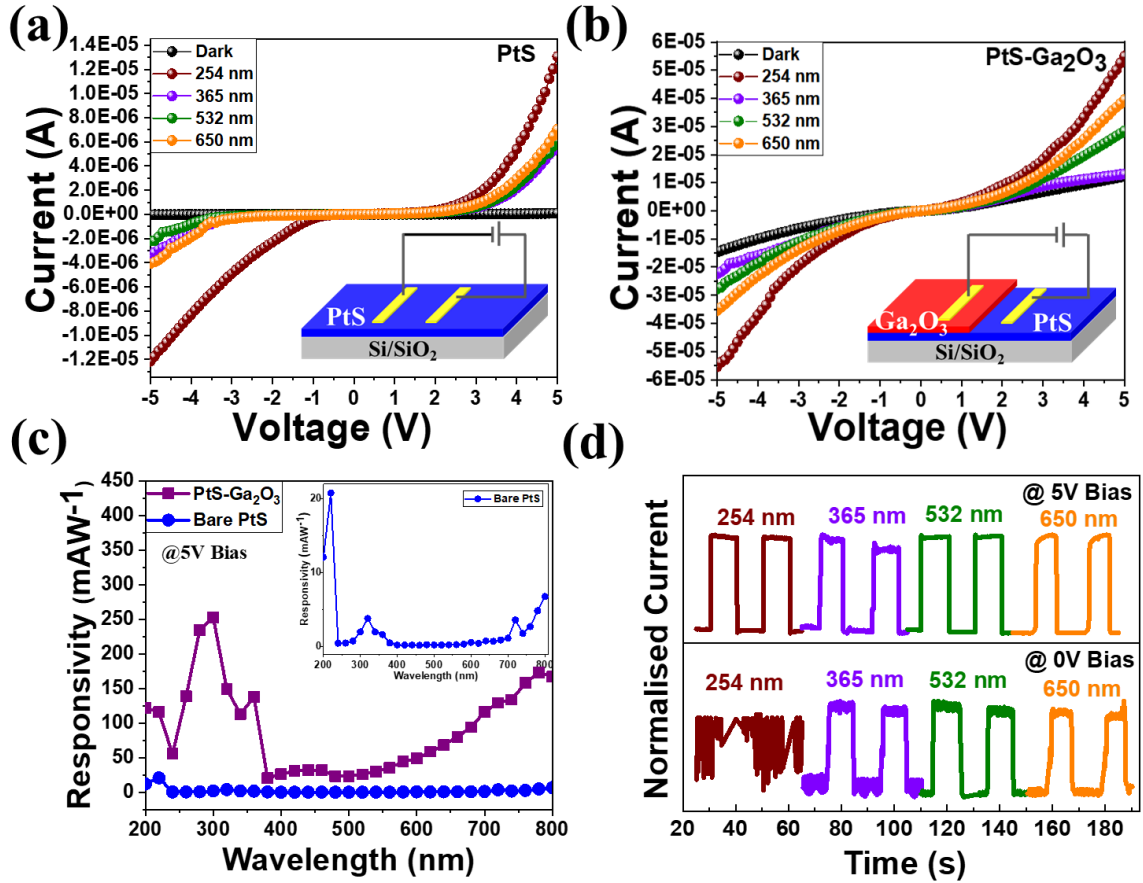


Figure 5.12 I-V characteristics under dark and light conditions of different wavelengths for (a) bare PtS and (b) PtS-Ga₂O₃ heterojunction. The insets show the schematic used for device testing. (c) Responsivity versus wavelength graph of the bare PtS and heterojunction device. (d) Temporal response of the heterojunction device to different wavelengths of incident light at zero-bias and 5V bias.

The temporal response of the devices was measured using lamps and lasers of different wavelengths in the UV to visible spectra while switching on and off the incident light. Figure 5.12 (d) shows two cycles of the temporal response of the heterojunction device under self-bias and 5 V bias under different illumination wavelengths emphasizing its broadband capability and negligible persistent photoconductivity. working principle of the device may be judged from the band alignment. Figure 5.13 (a) shows the heterojunction under dark and light conditions. Under equilibrium conditions, the Ga₂O₃ band bends upwards while the PtS band bends downwards. Under illumination of 254 nm, electron-hole pairs are generated both in Ga₂O₃ and PtS because of the above band gap illumination. Since electrons are present in the conduction bands of both the materials, due to the upward bending, the flow of electrons is restricted. This is the reason why the PtS-Ga₂O₃ heterojunction does not work at self-bias conditions under 254 nm illumination. Applying a bias gives rise to a driving force to the carriers in one direction giving rise to a measurable photoresponse. In case of visible region,

the carriers are photogenerated only in PtS (since the band gap of Ga_2O_3 is larger than the excitation wavelength). But due to the downward band bending of PtS, photogenerated electrons accumulate at the interface on the PtS side, leading to an upward shift in the fermi level.

To understand the increment in the device performance due to the formation of heterostructure,

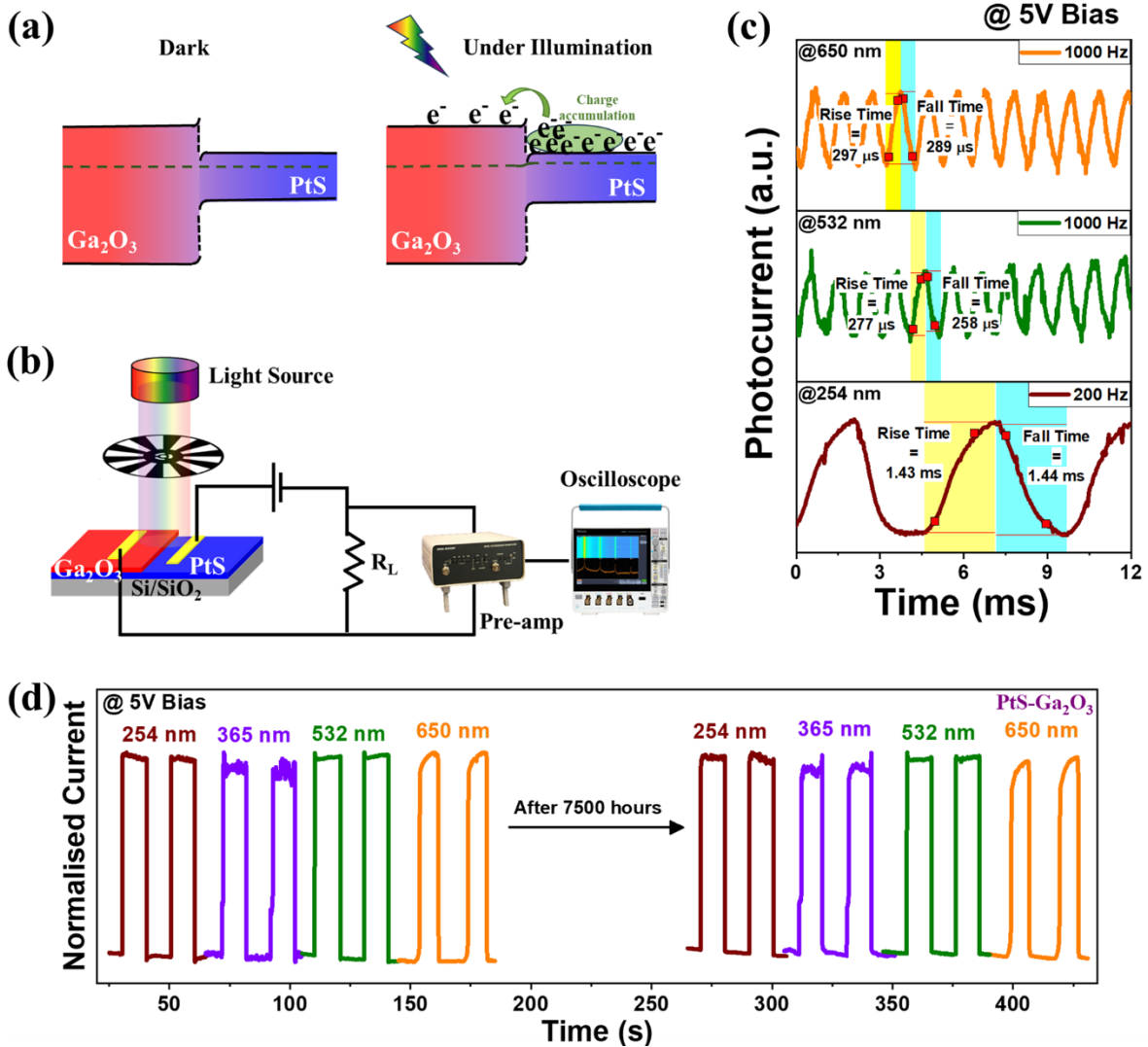


Figure 5.12 Working principle of heterojunction device under dark and illumination. (b) Experimental set-up for high speed photodetection measurements. (c) Temporal response of the heterojunction device to different wavelengths of incident light using the mentioned set-up. (d) Temporal response of PtS-Ga₂O₃ heterojunction devices to different wavelengths of incident light after 7500 hours of ambient storage.

Thus, the fermi level of PtS moves upwards to the fermi level of Ga₂O₃ leading to a flow of electrons from PtS to Ga₂O₃ leading to an increase in the photocurrent, leading to a photoresponse even at self-bias. The external bias only adds on to the driving force of the built-in potential giving a much higher photoresponse than that obtained in the self-bias mode.[50]

The heterojunction devices were tested for faster speeds using an optical chopper interfaced with oscilloscope as shown in Figure 5.12 (b). PtS-Ga₂O₃ photodetectors indeed perform at much faster speeds as can be seen in Figure 5.12 (c). For 650 nm laser illumination at a frequency of 1 KHz, the rise/fall time of the device at 5V bias was found to be 297 μ s/289 μ s while under 532 nm laser illumination, the rise/fall time reached 277 μ s/258 μ s at the same chopping frequency. For 254 nm, since a broad source in the form of pen-ray UV lamp is used, the chopping frequency is limited to 200 Hz and the consequent device speed is found to be 1.43 ms/1.44 ms.

5.2.3 Conclusion

In this study, heterojunction of 2D non-layered semiconductor PtS is fabricated with ultra-thin amorphous Ga₂O₃ which leads to fast speed broadband photodetection capabilities. The *n-n* heterojunction driven by majority carrier conduction boasts of an increment of more than 120 time in responsivity (252 mA W⁻¹ as compared to 2 mA W⁻¹ for bare PtS) and a reduction in response times by more than 150 time (277 μ s/258 μ s rise/fall time as compared to 42ms/45ms for bare PtS). The heterojunction is a type I alignment as studied from XPS depth profiling. The charge accumulation at the downwards band bending on PtS side due to photogenerated electrons under illumination leads to raising of fermi level of PtS over Ga₂O₃. This leads to an ease in the flow of electrons from PtS to Ga₂O₃ leading to fast speed broadband photodetector.

References

1. Kaur, D., et al., Interfacial-Mixing and Band Engineering Induced by Annealing of CdS and α -Ga₂O₃ n-n-Type Thin-Film Heterojunction and Its Impact on Carrier Dynamics for High-Performance Solar-Blind Photodetection. *ACS Applied Electronic Materials* **2023**, 5(7), 3798-3808.
2. Stepanov, S.I.N., V. I.; Bougrov, V. E.; Romanov, A. E., Gallium Oxide: Properties and Applications - A Review. *Reviews on Advanced Materials Science* **2016**, 44, 63-86.
3. Ayhan, M.E., et al., Ultraviolet radiation-induced photovoltaic action in γ -CuI/ β -Ga₂O₃ heterojunction. *Materials Letters* **2020**, 262, 127074.
4. Guo, D., et al., Review of Ga₂O₃-based optoelectronic devices. *Materials Today Physics* **2019**, 11, 100157.
5. Guo, D., et al., Zero-Power-Consumption Solar-Blind Photodetector Based on β -Ga₂O₃/NSTO Heterojunction. *ACS Applied Materials & Interfaces* **2017**, 9(2), 1619-1628.
6. Kan, H., et al., Ultrafast Photovoltaic-Type Deep Ultraviolet Photodetectors Using Hybrid Zero-/Two-Dimensional Heterojunctions. *ACS Applied Materials & Interfaces* **2019**, 11(8), 8412-8418.
7. Li, K.-H., et al., Deep-Ultraviolet Photodetection Using Single-Crystalline β -Ga₂O₃/NiO Heterojunctions. *ACS Applied Materials & Interfaces* **2019**, 11(38), 35095-35104.
8. Bae, H., et al., Solar-Blind UV Photodetector Based on Atomic Layer-Deposited Cu₂O and Nanomembrane β -Ga₂O₃ pn Oxide Heterojunction. *ACS Omega* **2019**, 4(24), 20756-20761.
9. Zhuo, R., et al., A self-powered solar-blind photodetector based on a MoS₂/ β -Ga₂O₃ heterojunction. *Journal of Materials Chemistry C* **2018**, 6(41), 10982-10986.
10. Wu, D., et al., Highly sensitive solar-blind deep ultraviolet photodetector based on graphene/PtSe₂/ β -Ga₂O₃ 2D/3D Schottky junction with ultrafast speed. *Nano Research* **2021**, 14(6), 1973-1979.
11. Wadhwa, R., et al., A strategic review of recent progress, prospects and challenges of MoS₂-based photodetectors. *Journal of Physics D: Applied Physics* **2021**, 55(6), 063002.
12. Alwadaï, N., et al., Enhanced Photoresponsivity UV-C Photodetectors Using a p-n Junction Based on Ultra-Wide-Band Gap Sn-Doped β -Ga₂O₃ Microflake/MnO Quantum Dots. *ACS Applied Materials & Interfaces* **2023**, 15(9), 12127-12136.
13. Arora, K., et al., Spectrally Selective and Highly Sensitive UV Photodetection with UV-A,C Band Specific Polarity Switching in Silver Plasmonic Nanoparticle Enhanced Gallium Oxide Thin-Film. *Advanced Optical Materials* **2020**, 8(16), 2000212.
14. An, Y.H., et al., Dual-band photodetector with a hybrid Au-nanoparticles/ β -Ga₂O₃ structure. *RSC Advances* **2016**, 6(71), 66924-66929.
15. Yu, J., et al., Improved Photoresponse Performance of Self-Powered β -Ga₂O₃/NiO Heterojunction UV Photodetector by Surface Plasmonic Effect of Pt Nanoparticles. *IEEE Transactions on Electron Devices* **2020**, 67(8), 3199-3204.
16. Wu, C., et al., Work function tunable laser induced graphene electrodes for Schottky type solar-blind photodetectors. *Applied Physics Letters* **2022**, 120(10), 101102.
17. Wu, C., et al., A general strategy to ultrasensitive Ga₂O₃ based self-powered solar-blind photodetectors. *Materials Today Physics* **2022**, 23, 100643.
18. Yuan, Y.-J., et al., Cadmium sulfide-based nanomaterials for photocatalytic hydrogen production. *Journal of Materials Chemistry A* **2018**, 6(25), 11606-11630.

19. Zhao, W., et al., Single CdS Nanorod for High Responsivity UV–Visible Photodetector. *Advanced Optical Materials* **2017**, 5(12), 1700159.
20. Kaur, D., et al., A Strategic Review on Gallium Oxide Based Deep-Ultraviolet Photodetectors: Recent Progress and Future Prospects. *Advanced Optical Materials* **2021**, 9(9), 2002160.
21. Pan, Y.-x., et al., Cadmium Sulfide Quantum Dots Supported on Gallium and Indium Oxide for Visible-Light-Driven Hydrogen Evolution from Water. *ChemSusChem* **2014**, 7(9), 2537-2544.
22. Lee, Y.S., et al., Atomic Layer Deposited Gallium Oxide Buffer Layer Enables 1.2 V Open-Circuit Voltage in Cuprous Oxide Solar Cells. *Advanced Materials* **2014**, 26(27), 4704-4710.
23. Nisika, et al., Interface Engineering of CZTS/TiO₂ Heterojunction Using Wide-Bandgap Ga₂O₃ Passivation Interlayer for Efficient Charge Extraction. *physica status solidi (a)* **2022**, 219(14), 2200001.
24. Nisika, et al., Energy level alignment and nanoscale investigation of a-TiO₂/Cu-Zn-Sn-S interface for alternative electron transport layer in earth abundant Cu-Zn-Sn-S solar cells. *Journal of Applied Physics* **2019**, 126(19), 193104.
25. Oldham, W.G., et al., n-n Semiconductor heterojunctions. *Solid-State Electronics* **1963**, 6(2), 121-132.
26. Ajisawa, A., et al., Improvement in HgCdTe diode characteristics by low temperature post-implantation annealing. *Journal of Electronic Materials* **1995**, 24(9), 1105-1111.
27. Yu, J., et al., Influence of annealing temperature on structure and photoelectrical performance of β -Ga₂O₃/4H-SiC heterojunction photodetectors. *Journal of Alloys and Compounds* **2019**, 798, 458-466.
28. Alnuaimi, A., et al., Reduction of interface traps at the amorphous-silicon/crystalline-silicon interface by hydrogen and nitrogen annealing. *Solar Energy* **2013**, 98, 236-240.
29. Solanke, S.V., et al., UV/Near-IR dual band photodetector based on p-GaN/ α -In₂Se₃ heterojunction. *Sensors and Actuators A: Physical* **2021**, 317, 112455.
30. Oswald, S., et al., Binding state information from XPS depth profiling: capabilities and limits. *Applied Surface Science* **2001**, 179(1), 307-315.
31. Chambers, S.A., et al., Introductory guide to the application of XPS to epitaxial films and heterostructures. *Journal of Vacuum Science & Technology A* **2020**, 38(6), 061201.
32. Kraut, E.A., et al., Precise Determination of the Valence-Band Edge in X-Ray Photoemission Spectra: Application to Measurement of Semiconductor Interface Potentials. *Physical Review Letters* **1980**, 44(24), 1620-1623.
33. Metin, H., et al., The effect of annealing temperature on the structural, optical, and electrical properties of CdS films. *Journal of Materials Research* **2010**, 25(1), 189-196.
34. Metin, H., et al., Annealing effects on optical and crystallographic properties of CBD grown CdS films. *Semiconductor Science and Technology* **2003**, 18(7), 647.
35. Çetinörgü, E., et al., Effects of deposition time and temperature on the optical properties of air-annealed chemical bath deposited CdS films. *Thin Solid Films* **2006**, 515(4), 1688-1693.
36. Jiang, Z., et al., Direct XPS Evidence for Charge Transfer from a Reduced Rutile TiO₂(110) Surface to Au Clusters. *The Journal of Physical Chemistry C* **2007**, 111(33), 12434-12439.
37. Chiu, M.-H., et al., Band Alignment of 2D Transition Metal Dichalcogenide Heterojunctions. *Advanced Functional Materials* **2017**, 27(19), 1603756.
38. Zhang, P., et al., Photogenerated Electron Transfer Process in Heterojunctions: In Situ Irradiation XPS. *Small Methods* **2020**, 4(9), 2000214.

39. Wadhwa, R., et al., Investigation of charge transport and band alignment of MoS₂-ReS₂ heterointerface for high performance and self-driven broadband photodetection. *Applied Surface Science* **2021**, 569, 150949.
40. Melitz, W., et al., Kelvin probe force microscopy and its application. *Surface Science Reports* **2011**, 66(1), 1-27.
41. Nony, L., et al., On the relevance of the atomic-scale contact potential difference by amplitude-modulation and frequency-modulation Kelvin probe force microscopy. *Nanotechnology* **2009**, 20(26), 264014.
42. Xu, Z., et al., Ultrafast Charge Transfer 2D MoS₂/Organic Heterojunction for Sensitive Photodetector. *Advanced Science* **2023**, n/a(n/a), 2207743.
43. Wang, G., et al., Interlayer Coupling Induced Infrared Response in WS₂/MoS₂ Heterostructures Enhanced by Surface Plasmon Resonance. *Advanced Functional Materials* **2018**, 28(22), 1800339.
44. Xue, J., et al., Interfacial charge transfer of heterojunction photocatalysts: Characterization and calculation. *Surfaces and Interfaces* **2021**, 25, 101265.
45. Bassi, G., et al., Controlled and tunable growth of ambient stable 2D PtS₂ thin film and its high-performance broadband photodetectors. *Journal of Alloys and Compounds* **2023**, 955, 170233.
46. Cullen, C.P., et al., Synthesis and characterisation of thin-film platinum disulfide and platinum sulfide. *Nanoscale* **2021**, 13(15), 7403-7411.
47. Wadhwa, R., et al., Fast response and high-performance UV-C to NIR broadband photodetector based on MoS₂/a-Ga₂O₃ heterostructures and impact of band-alignment and charge carrier dynamics. *Applied Surface Science* **2023**, 632, 157597.
48. Dembowski, J., et al., Platinum Sulfide by XPS. *Surface Science Spectra* **1993**, 2(2), 104-108.
49. Liu, K.Z., et al., AES and XPS studies of a GaP(001) surface treated by S₂Cl₂ and P₂S₅/(NH₄)₂Sx. *Applied Surface Science* **2004**, 237(1), 623-626.
50. Gui, T., et al., In-situ fabrication of PtSe₂/MoS₂ van der Waals heterojunction for self-powered and broadband photodetector. *Materials & Design* **2024**, 238, 112722.

Chapter 6: Photodetectors under extreme environments

In this chapter, we try to look at the impact of extreme environments such as high temperatures and high radiation on the fabricated photodetectors, since the active layer itself is extremely resilient to extreme temperatures and radiation doses. In the first part, we study the origin of the near-failure of conventional Au contacts to β -Ga₂O₃ at high temperatures using interfacial studies. For this purpose, β -Ga₂O₃ with Au interdigitated electrodes is subjected to high temperature annealing and their interface chemistry is studied and correlated with device performance for solar-blind photodetection. The second part of this chapter involves using an unconventional transparent conducting oxide contact of IZO to β -Ga₂O₃ and studying its behavior under high temperatures.[1] The devices show a unique conversion from Schottky-to-Ohmic by annealing at an optimized temperature of 650°C, while changing back to Schottky at higher temperatures. The third part of this chapter involves testing the resilience of the films against swift heavy ions (Ag⁷⁺) of 100 MeV energy.[2] The preservation of device integrity and the other results show that the gallium oxide as a material shows excellent radiation hardness against SHI and is highly suitable for the fabrication of the Solar-blind photodetectors to be used in extreme and harsh environments.

6.1 Au contacts under high temperatures

Ga₂O₃ as a material itself can sustain the high temperatures but actual devices are limited more by the electrical contacts which are susceptible to damage by heat. Most of the conventional metal contacts to β -Ga₂O₃ are Au or some combination with Au since it provides stability and may even be used as a capping layer.[3, 4] Pure Au electrodes show Schottky behavior while Ti/Au exhibits Ohmic nature, which sometimes requires annealing at 400-500°C, especially for undoped films as this leads to a lowering of the barrier height due to Ti-Ga₂O₃ chemical reaction.[5] In addition to Ti/Au, other stacks such as Ti/Al/Ni/Au is also used for forming Ohmic devices where the additional layers are added to prevent the out-diffusion of Ti into the Au overlayer.[6] As a Schottky contact, Ni/Au has also been utilized, but at around 500°C, Ni also shows diffusion and ultimate device breakdown.[7] Oxidized electrodes such as PtO_x, IrO_x and PdO_x show good stability as Schottky contacts at higher temperatures up to 330°C.[8]

Especially with industrial-standard metal contacts such as Au, the electrodes after being subjected to high temperatures requires an in-depth analysis to truly understand its efficacy for real-world applications. Lyle et al. have reported the nanoscale characterization of the Au/ β -

Ga₂O₃ interface in the as-deposited condition and found Ga diffusion into Au.[9] Another report suggests that Au contacts start diffusion after 500°C and leads to reduced device performance.[10] Most of these studies only speculate the reasons for the decreased device performance and the true reaction dynamics at higher temperatures are severely under-studied in all these contacts with little knowledge about their material chemistry and the stability of their electrical characterizations for gallium oxide. Hence it becomes imperative to study what actually happens to the semiconductor-metal interface at higher temperatures which decides the fate of the working device for any extreme environment applications.

6.1.1 Experimental details

To investigate the behavior of the contacts and their chemistry at the metal-semiconductor interface, Au contacts (~120 nm thick) in the form of interdigitated metal electrodes are thermally evaporated on top of polycrystalline β -Ga₂O₃ thin films (~300nm). The stability, performance and resilience of the contacts was tested against high temperatures by comparing their performance for solar-blind photodetection. Details of growth of β -Ga₂O₃ thin films on Si (100) may be found elsewhere.[11] These are then subjected to annealing at 450°C, 650°C and extreme temperature of 850°C for 1 hour under Ar ambient (with natural cooling) and compared with the as-deposited samples. The temperatures are chosen specifically such that they lie in the range of acceptable optimized annealing temperatures of 400-500°C, an intermediate higher temperature of 650°C while the extreme temperature of 850°C is fixed at maximum, considering equipment limitations.

6.1.2 Results and discussion

Figure 6.1 (a) shows the schematic depicting the device structure used for the study. Given alongside in Figure 6.1 (b-e) are the optical images of the damage to the devices after annealing under 450°C, 650°C and 850°C. As compared to the @RT sample, the @450°C shows no significant change in the morphology with the contacts staying intact even after annealing. The @650°C, starts showing diffusion in the narrower fingers of the electrode but do not show diffusion on the main strips. On the other hand, @850°C clearly shows the extended diffusion of the gold into the Ga₂O₃ film. The contact shows excessive damage with the pores forming throughout the electrode. The physical damage to the contacts and the interfacial diffusion has been reported at lower temperatures (upto 500°C) previously but has not been studied at higher temperatures.[12, 13] This pore/crater formation due to the diffusion of gold inside the film requires particular attention as this might ultimately disrupt the device performance. For this, XPS depth profiling was carried out to check the variation in the chemical composition across

the metal-semiconductor interface. Figure 6.1 (f-i) shows the atomic concentration of Ga, O and Au as a function of depth as one moves through the metal contact and into the Ga_2O_3 thin film. @RT and @450°C shows a clear demarcation of the different elements across the two films with the interface showing an abrupt change from Au to Ga_2O_3 , whereas @850°C shows a pronounced in-diffusion of Au. In addition to the gold, Ga also shows an out-diffusion into Au as seen by the change in its atomic concentration across the electrode and Ga_2O_3 . [14]

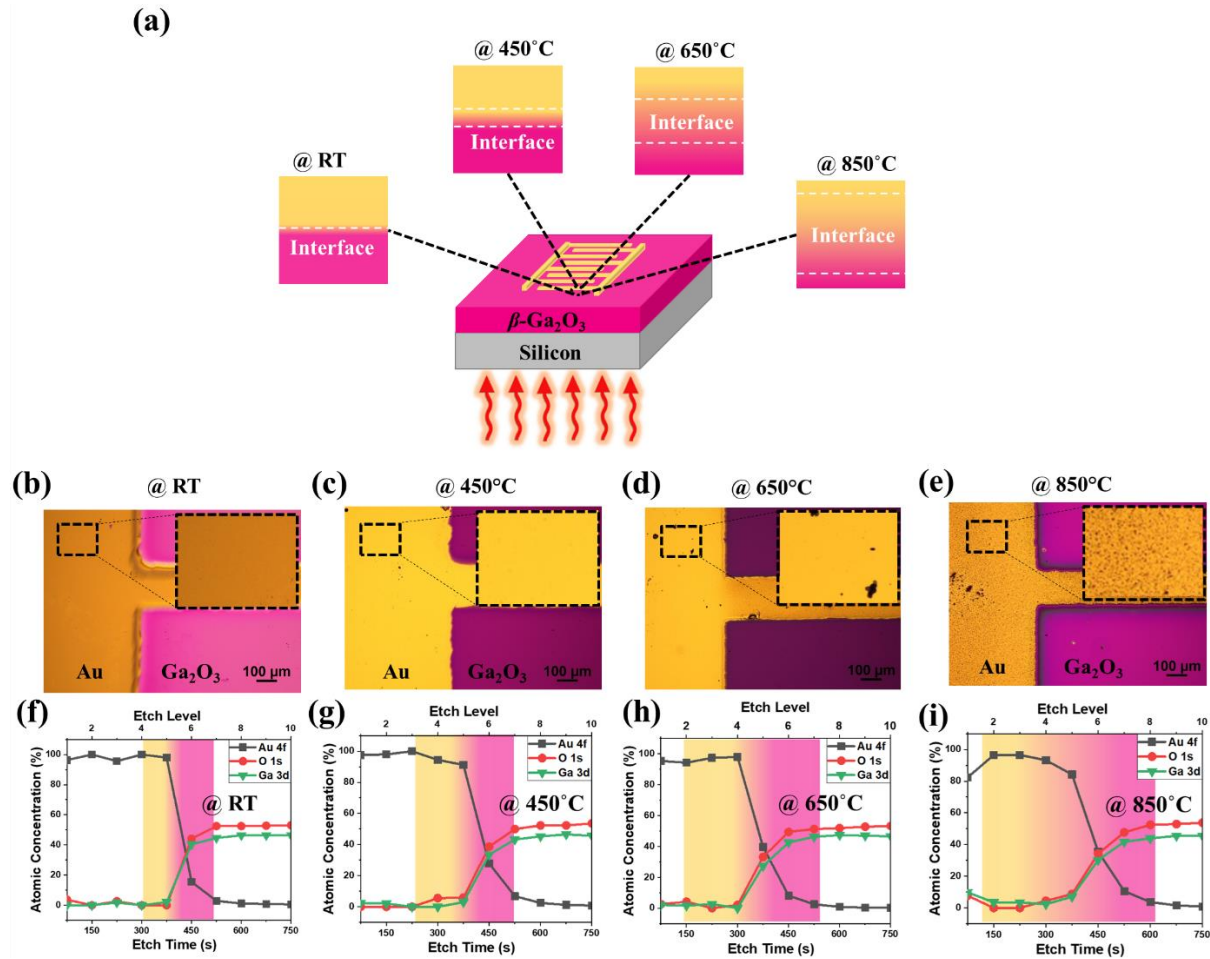


Figure 6.1 (a) Device schematic used for this study. Optical images of the actual devices showing finger electrodes for (b) room temperature as-deposited, (c) 450°C, (d) 650°C and (e) 850°C annealed devices. Atomic concentration profiles as determined by XPS depth profile for (f) room temperature as-deposited, (g) 450°C, (h) 650°C and (i) 850°C annealed devices.

Figure 6.2 represents the contact behavior in terms of device performance in the fabricated solar-blind photodetectors with Au electrodes under different annealing conditions. Figure 6.2 (a) represents the dark current of the devices which is the current without any illumination. For the @RT and @450°C, the devices show almost equivalent levels of dark current, ~8 nA for the @RT and ~4 nA for @450°C at 5V bias. The lower dark current for @450°C can be associated with better electrical contact formation due to optimized annealing conditions of the

device. Moderate annealing is usually applied to improve the defect density at the metal-semiconductor interface which leads to a better quality at the interface giving a superior performance.[2, 15] Upon higher annealing at 650°C, the devices show a much higher dark current with levels rising to $\sim 0.1 \mu\text{A}$ for a similar bias of 5 V. It increases even further at 850°C when the dark current doubles to $0.2 \mu\text{A}$ at 5 V bias. This increase in the current is of particular concern since an increase in the leakage or the dark current reduces the sensitivity of the devices.

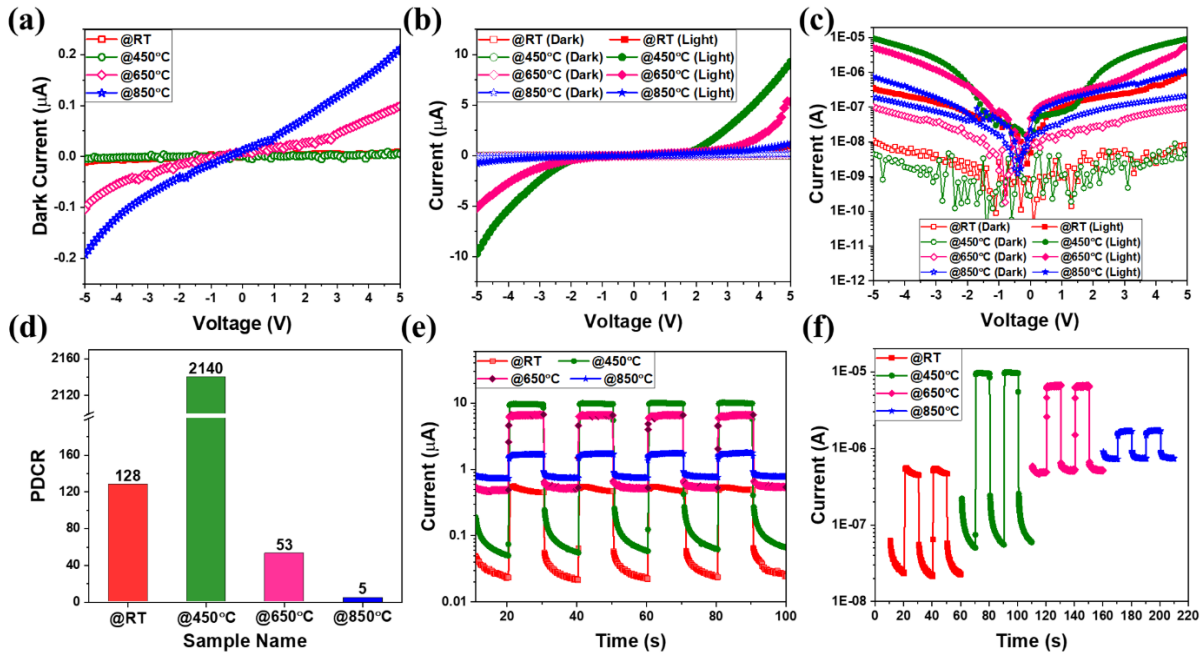


Figure 6.2 (a) Dark current of the devices without illumination, (b) I-V curves under dark and light conditions (254 nm), (c) Log I vs. voltage graph showing the relative increment in the photocurrent, (d) photo-to-dark-current ratio for the devices, (e) temporal response of the devices to repeated switching of incident light and (f) time-cycles of the devices showing excellent stability.

Figure 6.2 (b,c) shows the current of the devices under dark and illumination of 254 nm light. The relative enhancement in the photocurrent is maximum for @450°C which boasts of the lowest dark current and the highest light current. For the case of @850°C, the higher darker current along with a relatively lower light current reduces the photo-to-dark current ratio (PDCR) ($= (I_{\text{light}} - I_{\text{dark}})/I_{\text{dark}}$) as depicted in Figure 6.2 (d). The PDCR reduces to a miniscule value of just 5 for @850°C, as compared to 2140 for @450°C, 128 for @RT and 53 for @650°C, signifying a drastic decrement in the device performance at higher temperatures. Figure 6.2 (e,f) shows the temporal response of the devices to repeated periodic switching of incident light which again corroborates the supremacy of @450°C device. Contrary to a

previous report by Seyidov et al.[16], where they explicitly mention the instability of the Au electrode as a Schottky contact for applications exceeding 200°C, our devices show excellent resilience at temperatures around 450°C.

To ascertain the reason for the decreased performance, and find the origin for the near-failure of @850°C, in-depth analysis of the metal-semiconductor interface was carried out using XPS depth profile. Figure 6.3 shows the core-level spectra of Au 4f as we move through the thickness of the electrode. The doublet of Au_{7/2} and Au_{5/2} at the binding energies around 84 eV and 88 eV belong to the Au in its metallic state. In the case of @RT and @450°C, the Au 4f metallic peaks are visible which drastically reduce in intensity once Ga₂O₃ is reached. But a peculiar aspect is seen in the @650°C and @850°C samples where additional peaks in Au 4f are observed at the interface. These peaks start to emerge in @650°C while they become prominent in @850°C. The additional peaks at the lower binding energy may belong to Au forming an alloy/compound with another element. To probe the origin of these peaks further, the other elements namely Ga 3d and O 1s were also studied at the interface. Looking at the core level spectra of Ga 3d, a similar additional peak is observed (see Figure 6.4). @RT and @450°C possess the usual peaks of Ga 3d with them being deconvoluted into two peaks – the lower binding energy peak belonging to the Ga⁺ oxidation state while the higher binding energy peak corresponding to the Ga³⁺ state. For the case of @650°C and @850°C, an additional peak around 21 eV is observed as we go towards the metal-semiconductor interface. It should be noted that this feature of an additional peak is observed only in Au 4f and Ga 3d while no such peak is observed for O 1s, implying that the new peaks may be corresponding to an intermetallic compound or alloy between Au and Ga. The higher binding energy shift in the Ga 3d implies a higher oxidation state while the lower binding energy shift implies a lower oxidation state, indicating a charge transfer from Ga to Au.[17] The formation of Au-Ga alloy at higher temperatures has previously been reported in literature with the intermetallic compound of Gold-Gallium used as a novel, high temperature solder with high eutectic temperature.[18] In a work done by Liu et al. concerning the Au₃₀Ga alloy where they have discussed the binary phase diagram[19], they have showed that higher concentrations of Ga (by atomic %) and higher temperatures (in excess of ~ 500°C) are conducive to the formation of Au-Ga alloy.[18] In our case, temperatures higher than the said temperature results in the formation of the alloy. Evidently, the formation of gold-gallium alloy has previously been reported for Au films on GaAs substrates as well as GaN, but has never been studied in gallium oxide-based systems.[20, 21] For Au on GaN, the alloy formation occurs above 500°C while

the GaAs suffers from the alloy formation at just 300°C. Judging from our XPS studies, the chemical composition of the interface after exposure to high temperature (> 650°C) is a mix of metallic Au, an intermetallic compound of Au-Ga and gallium oxide. This varied mixture is what leads to a change in device performance at 650°C and the near-failure of the devices at high temperatures.

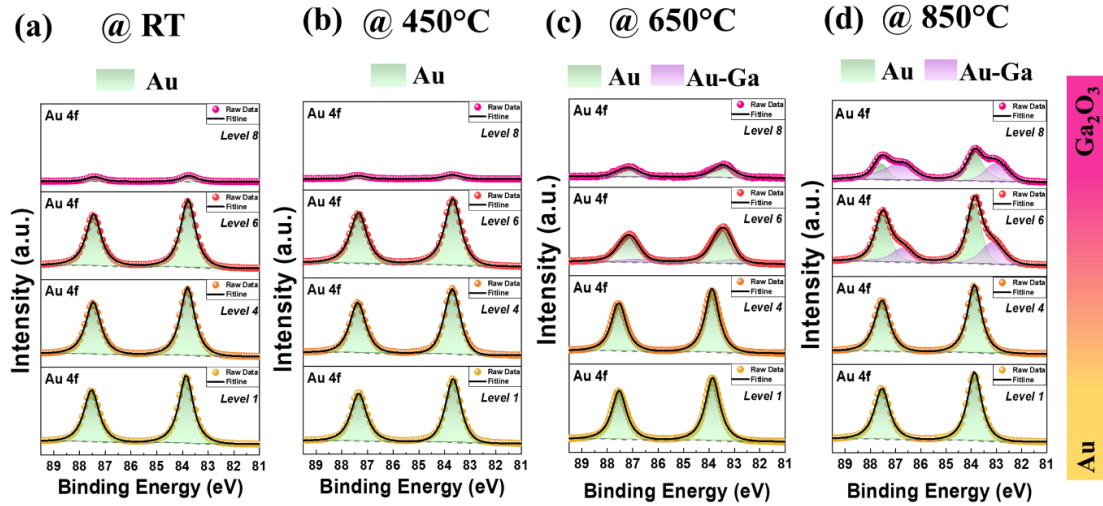


Figure 6.3 XPS core level spectra of Au 4f for increasing depths for (a) room temperature as-deposited, (b) 450°C, (c) 650°C and (d) 850°C annealed devices.

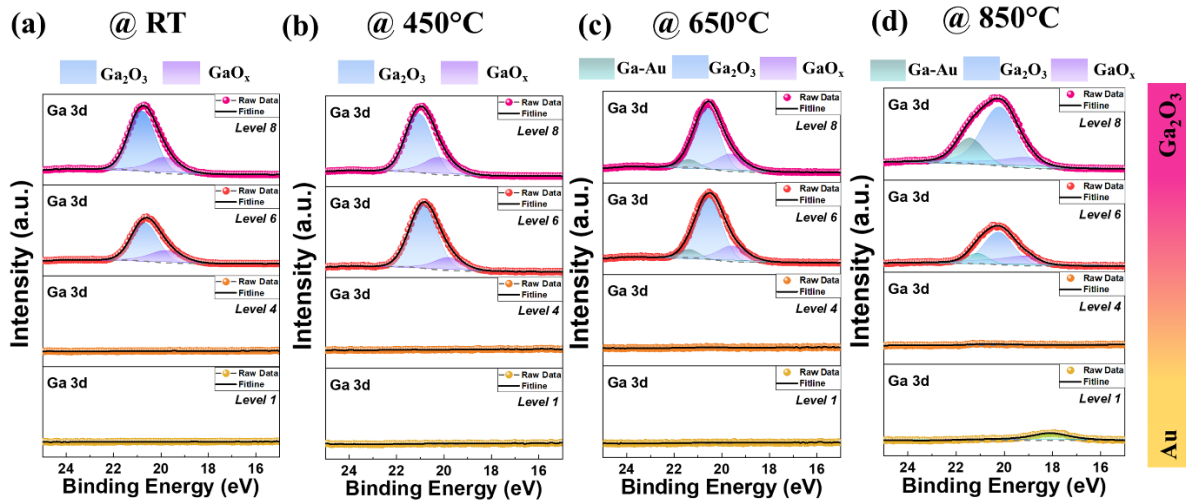


Figure 6.4 XPS core level spectra of Ga 3d for increasing depths for (a) room temperature as-deposited, (b) 450°C, (c) 650°C and (d) 850°C annealed devices.

Since the Ga is now bonded to not just oxygen but also Au, it leads to a change in the local charge density at the interface. This is also indicated by the change in the valence band maxima values which were probed across the metal-semiconductor interface. Figure 6.5 shows the variation of VBM where @RT and @450°C shows an abrupt change in the VBM values across Au and Ga₂O₃ whereas the @650°C and @850°C shows a decrease in the VBM value with a

steady increase thereafter. It is noteworthy that these values are used only for indicative purposes and have not been corrected with respect to a reference. The different values of VBM obtained for @650°C and @850°C are indicative of different electronic structure for these particular samples as compared to the others.[22] The initial lowering of the VBM may be attributed to the introduction of additional electronic states due to the formation of Au-Ga alloy at the interface. With increasing depth, the relative percentage of the alloy formation decreases as compared to the present Ga_2O_3 and the VBM thereby increases beyond a certain depth.

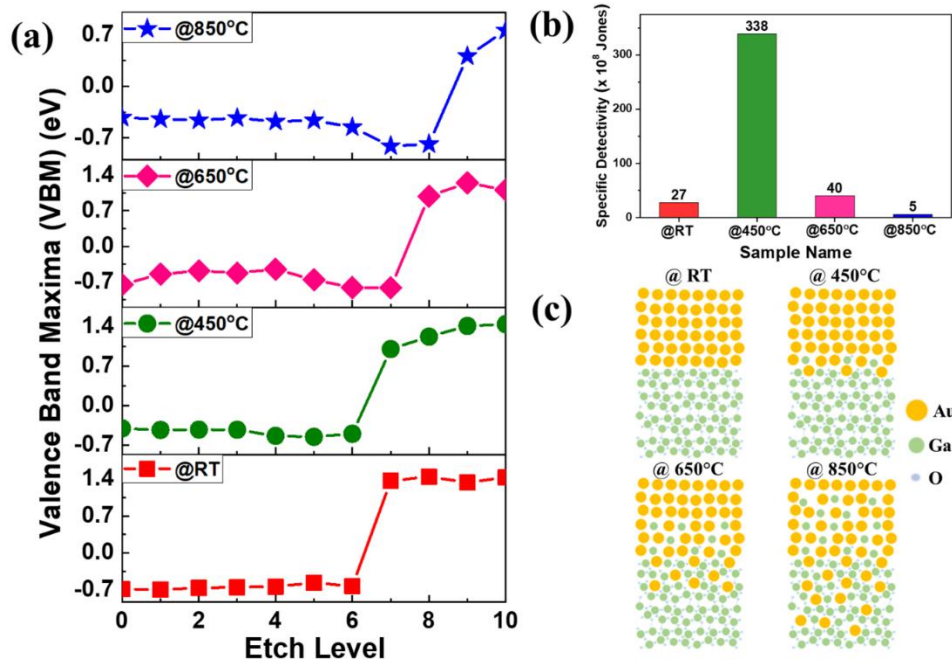


Figure 6.5 (a) Variation in the VBM values as a function of depth for the different samples (b) Specific detectivity of the different device and (c) schematic representing the diffusion and alloy formation at the interface.

The formation of gold-gallium phase in GaAs-Au interface has been shown to lower the Schottky barrier height.[23] Similarly, here also, the Au-Ga alloy might lower the Schottky barrier height leading to an increased flow of electrons across the metal-semiconductor interface, thereby resulting in a higher dark (or leakage) current in @650°C and @850°C, resulting in the near failure of Au contacts to $\beta\text{-Ga}_2\text{O}_3$ at higher temperatures. Figure 6.5 (b) shows the specific detectivity of the devices which re-asserts the dominance of @450°C while depicting the near-failure of @850°C. The origin of the near-failure of the devices at such high temperatures may be attributed to the interfacial reaction dynamics which favors the formation of the Au-Ga alloy at higher temperatures (Figure 6.5 (c)). At 650°C, the interfacial reactions lead to beginning of alloy formation which reduces the performance, which then accelerates at 850°C leading to the near-failure.

6.1.3 Conclusions

This work provides insight into the origin of the interface chemistry between pure Au Schottky contacts to β -Ga₂O₃ at the near-failure temperature of 850°C. The interfacial studies at the contact-semiconductor interface using XPS depth profiling point out to the formation of Au-Ga alloy (above 650°C) which increases the leakage current of the devices. At far higher temperatures of 850°C, the alloy formation starts dominating leading to the ultimate device near-failure. Unlike the case of GaN or GaAs which suffers from the alloy formation at far lower temperatures, the reaction dynamics between Ga₂O₃ and Au is favorable for a delayed alloy formation, leading to operation of Ga₂O₃ based devices at higher temperatures. Thus, this work not only delves into the changes in the performance of the devices after being subjected to high temperatures but also probes into the origin of the hitherto unknown mechanism of the near-failure of Ga₂O₃ based devices.

6.2 Indium Zinc Oxide (IZO) contact under high temperatures

Although the progress of devices based on gallium oxide has been scaling up rampantly but one of key bottlenecks remains the choice of electrode materials used for device fabrication, since the ultimate performance of any device is governed by the electrical characteristics of the contacts.[3] To begin with, the nature of metallic electrodes with Gallium oxide is quite varied.[4, 5, 24] Moreover, the same metallic structures can show either Ohmic or Schottky behaviour since it depends heavily on the interface chemistry between Ga₂O₃ and metal.[25] The surface states play an ever-important role in determining the behaviour of the electrode and since the surface states of gallium oxide vary according to the deposition technique used and the chosen deposition parameters, it becomes even more difficult to predict the electrode behaviour.[26] Different studies have been conducted using different metals which may show Ohmic as well as Schottky contacts depending on the post-processing techniques.[27, 28] Mostly, multi-metallic stacks such as Ti/Au are being utilized as Ohmic contacts for Ga₂O₃ based devices after annealing at 400-500°C.[29] A lot of research in understanding how these contacts behave under elevated temperatures is also being done, but actual devices using metallic contacts seem to fail under extreme temperatures, primarily due to their high diffusion in active layer.[10] Nowadays, alternatives for metal contacts are also being explored. Unconventional electrodes such as graphene, transparent conducting oxides, etc. are also being researched as potential contacts to Ga₂O₃. [30-32] The flexibility that the TCOs offer in terms of better stability, high optical transparency and interesting oxide interfaces surpasses the traditional metal contacts, but controlling their behaviour is still challenging. Mostly, these

TCOs show Schottky behaviour with some such as ITO or AZO being employed as an interlayer between metal-semiconductor to improve the Ohmic contact [30, 32-34], but using them primarily as the contact with controllable behaviour still remains unexplored. Additionally, most of these studies have shown the introduction of an interlayer of TCOs as an effective tool for interface engineering of the Schottky barrier height but seldom report the origin for the actual behaviour.

6.2.1 Experimental details

β -Ga₂O₃ films (~300nm thick) were grown on Si substrates by using a high temperature seed layer method via RF Magnetron Sputtering. The experimental details can be found in previously reported study.[15] On top of these films, IZO (In₂O₃/ZnO – 87/13wt%) was deposited using RF superimposed DC sputtering at 35 W ((RF/(RF+DC)) = 75%), room temperature and 5 mTorr working pressure, in the form of interdigitated electrodes.[35] The devices are then subjected to annealing at different temperatures of 450°C, 650°C and 850°C under Ar ambient using a tube furnace with natural cooling. One sample without any annealing is kept as the control device of room temperature and named as @RT henceforth.

6.2.2 Results and discussion

Figure 6.6 (a,b) shows the device schematic utilized for this study. The deposited devices were annealed at different temperatures for 1 hour. IZO electrodes fabricated at room temperature on β -Ga₂O₃ show Schottky behaviour as illustrated in Figure 6.6 (b) where the dark currents of the devices are shown. As compared to @RT, the annealed devices @450°C, @650°C and @850°C shows higher dark currents, probably due to the diffusion of the electrodes inside the Ga₂O₃ films. The dark current of @RT, @450°C, @650°C and @850°C at 5V bias is found to be 1.79×10^{-8} A, 2.69×10^{-7} A, 3.15×10^{-6} A and 3.92×10^{-8} A, respectively. Interestingly, the devices show a variation in the behaviour of electrodes. While @RT and @450°C show Schottky behaviour, the @650°C shows an Ohmic behaviour which again changes to Schottky at higher annealing of 850°C. The devices were then subjected to UV-C light from a pen-ray lamp. Upon incidence of light (254 nm), the devices show photodetecting abilities with the current rising in all the devices (Figure 6.6 (d)). The corresponding photocurrents of the devices is found to be 3.45×10^{-5} A, 3.92×10^{-5} A, 8.44×10^{-5} A and 3.49×10^{-6} A, respectively. The increment is above two orders of magnitude for all the devices, showing the excellent resilience of IZO as electrodes even after annealing at such high temperatures. Figure 6.6 (e) shows the temporal response of the devices to repeated switching of the incident light at regular intervals of 10 seconds. Up to 650°C, we see negligible persistent photoconductivity, with the devices

showing repeatable switching. The stability of the devices can also be corroborated from the rise and fall time of the devices which show the same order of magnitude. For the extremely high temperature of @850°C, the device shows a very slow fall time and some remnant photoconductivity but still with a high photoresponse, implying that the devices do not fail even after annealing at 850°C.

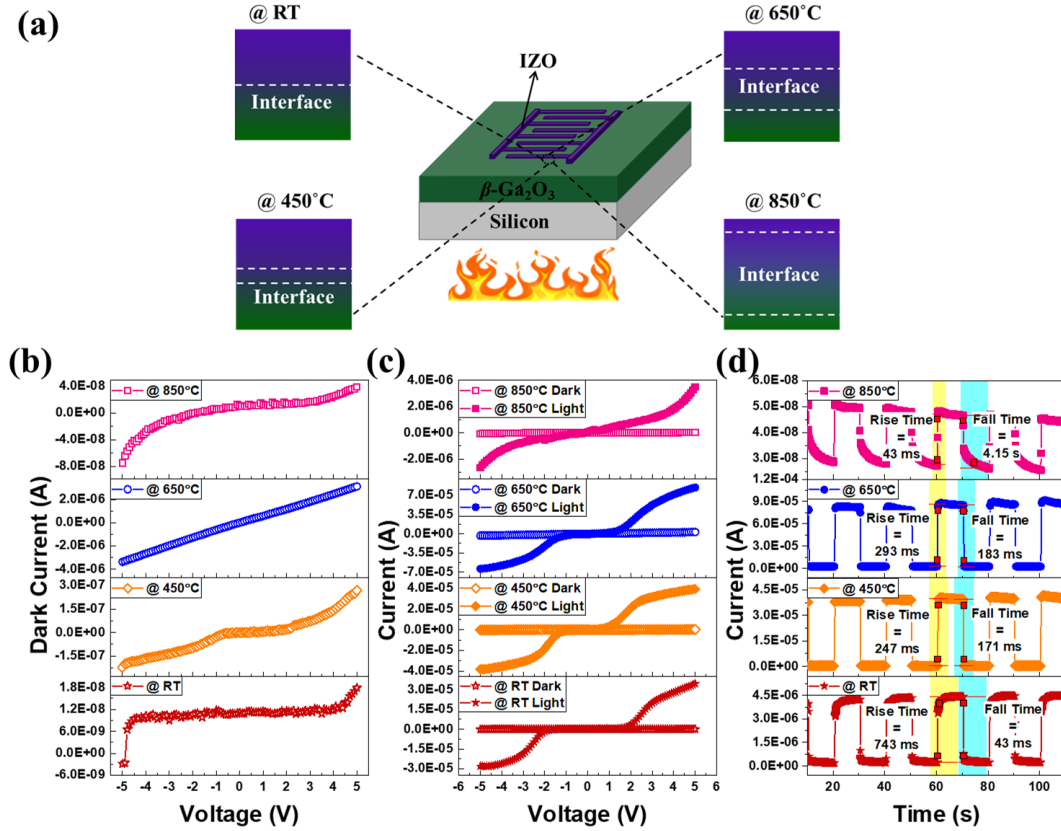


Figure 6.6. (a) Device schematic of the experimental conditions. Here green colour represents Ga₂O₃ while purple colour is indicative of IZO. (b) Dark current of the devices using IZO electrodes annealed under different temperatures (c) Photoresponse of the devices to 254 nm incident light (e) temporal response of the devices to repeated switching of incident light.

Figure 6.7 (a) shows the optical images of the actual devices showing few of the finger electrodes. As is clearly visible, the devices start showing damage after annealing. The @RT shows completely intact electrodes with uniform shape and width, but upon annealing, the electrodes start getting faded due to diffusion. Especially at higher temperatures, the physical damage is much more pronounced with the @850°C device having extreme diffusion of the electrodes and hence the faintest looking electrodes. Diffusion being a natural process, is expedited at higher temperatures. In case of metallic contacts, the metal atoms diffuse inside the layers to form oxidized metal cations and hence lose their conductive properties. But in the case of oxide electrodes, the diffusion inside the active layer is different since the metal cations

are already bonded to oxygen. The metal cations diffuse through the active layer and change the oxide-oxide interface which determines the final device performance, whether the device ultimately works or fails altogether. Thus, it becomes imperative to probe the oxide-oxide interface and hence, to study the changes that take place at the electrode-semiconductor interface, XPS depth profile was carried out on the actual electrodes.

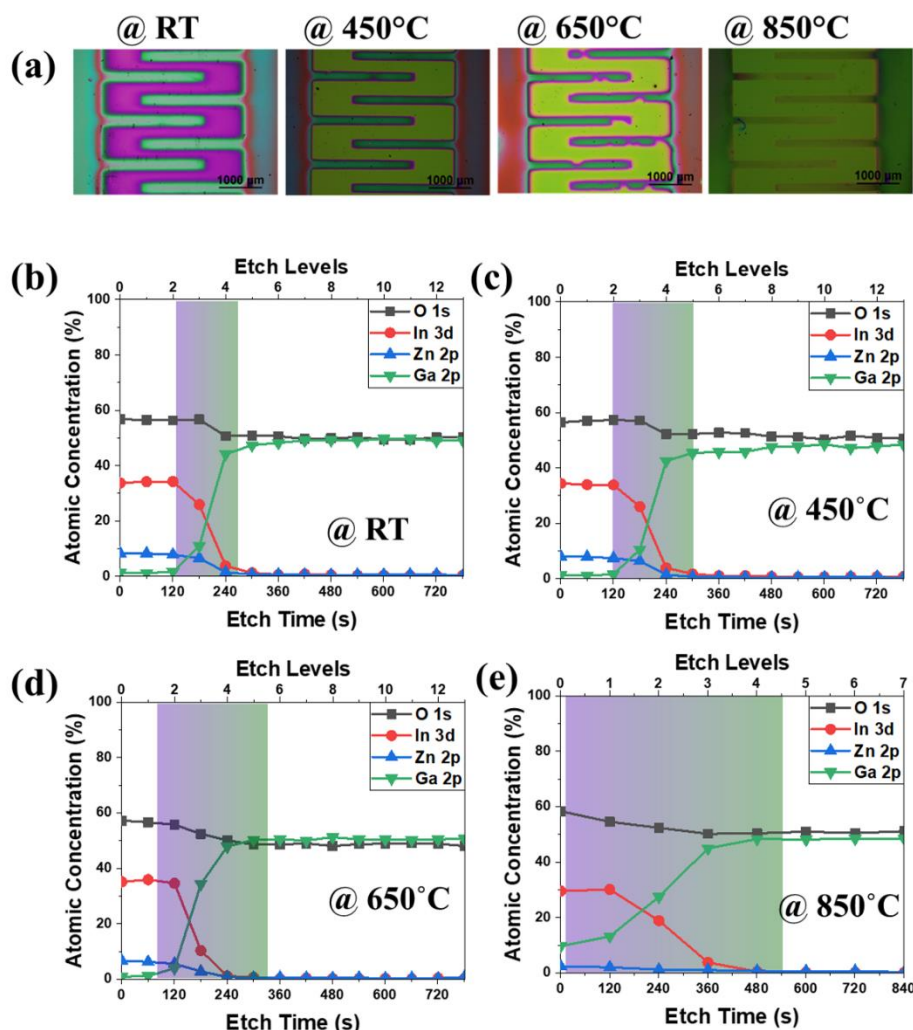


Figure 6.7 (a) Optical images of the devices showing physical damage after annealing. Atomic concentrations of various elements with increasing depth found using XPS depth profile for (b) room temperature (c) 450°C (d) 650°C and (e) 850°C annealed samples.

The variation in the atomic concentration going from IZO to Ga₂O₃ is shown in Figure 6.7 (b-d). Except for @850°C which showed signature of Ga right on the surface, some of the top IZO was etched out (for about 5 minutes using 1000 eV Ar⁺ in a 1 mm² raster area) in the remaining samples to reach the interface before the data was recorded. For @850°C, the diffusion of the electrodes and the film was enormous and the film and electrode showed a diffused interface up to 480 seconds of etching (with 1000 eV Ar⁺ in a 1 mm² area) whereas the others showed a

gradual interface. The @RT showed a relatively sharper interface as compared to the @450°C and @650°C. This differential diffusion of IZO into Ga_2O_3 might be the reason for the different behaviours found in the devices.

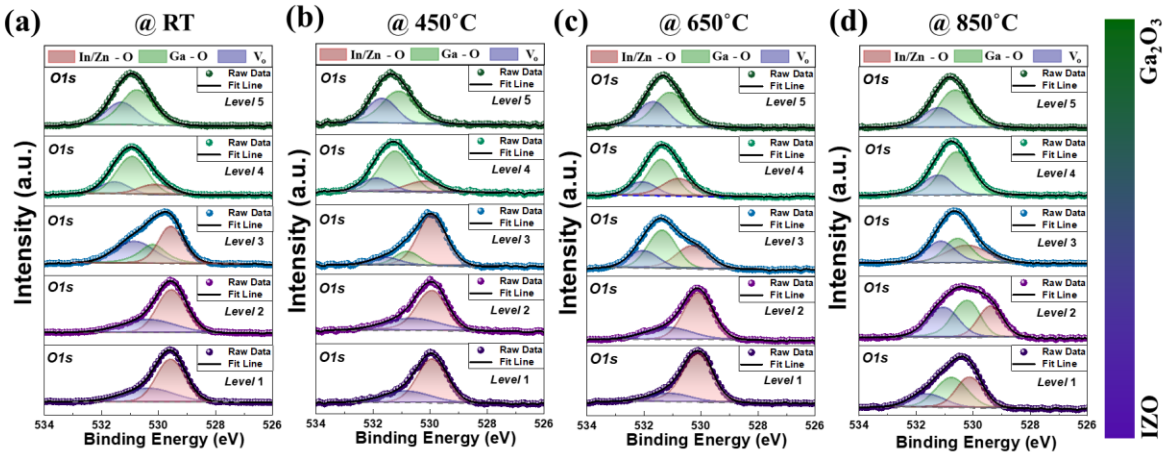


Figure 6.8 Core-level spectra of O1s for the interface of the (a) room temperature (b) 450°C (c) 650°C and (d) 850°C annealed samples.

To further probe the trends in diffusion, core level spectra of various elements such as In, Zn, Ga and O at the interface were studied. The O1s core level spectra of the interface of the devices are shown in Figure 6.8 (a-d). For any oxide system, the O1s levels may be deconvoluted into two peaks – the lower binding energy peak corresponding to the metal-oxide peak and the higher energy peak corresponding to the oxygen vacancies.[36] For these samples, the O1s on the top levels show the presence of the In/Zn bonded to oxygen while containing oxygen vacancies. As we go deeper into the electrodes at the interface, the oxygen now starts bonding with all the three cations – In, Zn and Ga. For @RT, the oxygen vacancies at the interface are aplenty because of the pristine interface of Ga_2O_3 and IZO which individually contain a lot of vacancies. For the case of @450°C, the heat anneals some of the oxygen vacancies present at the interface while the oxygen is still predominantly bonded to In/Zn as compared to Ga, as in the case of @RT. However, once annealing is done at @650°C, the interface now consists of oxygen bonded more to Ga than to In/Zn, along with having a higher number of oxygen vacancies at the interface. Decrease in oxygen vacancies has previously been reported to be responsible for the Ohmic to Schottky conversion[37] and this seems to be the case here as well. For @850°C, the diffusion starts to occur right from the surface of the electrodes with oxygen being bonded to Ga, In and Zn altogether. Since the interface chemistry is different for @RT, @450°C and @650°C, and so is the nature of the electrodes, the change in the trend of the valence band maxima was also studied. For the case of @850°C, the diffusion of elements

is entirely throughout the thickness of the electrode, with no clear demarcation between the individual materials and the heterointerface and hence, it has no clear trend in the VBM.

Figure 6.9 (a) shows the changing VBM at the interface. For @RT and @450°C, the VBM increases across the interface whereas for the @650°C, the VBM decreases. The change in the diffusion of elements, their intermixing and bonding with oxygen leads to a charge transfer to occur at the interface, leading to changing VBM across the depth. The shifts in the VBM are indicative of the local charge distribution due to the band bending at the interface. Since the trend of VBM followed is different for the samples, the band alignment between the interfaces was studied to look at the charge transfer and the band bending occurring at the interface. Core level spectra of In 3d and Ga 2p were used for determining the valence band offset (VBO) using Kraut's rule:

$$VBO = \left(E_{Ga\ 2p_{3/2}}^{Ga_2O_3} - E_{VBM}^{Ga_2O_3} \right) - \left(E_{In\ 3d}^{IZO} - E_{VBM}^{IZO} \right) + \Delta E_{CL} (i) \quad (6.1)$$

where, $\Delta E_{CL} (i) = (E_{In\ 3d}^{Ga_2O_3/IZO} - E_{Ga\ 2p_{3/2}}^{Ga_2O_3/IZO})$ is the binding energy difference between In 3d and Ga 2p_{3/2} core levels at the interface. The term $(E_{Ga\ 2p_{3/2}}^{Ga_2O_3} - E_{VBM}^{Ga_2O_3})$ and $(E_{In\ 3d}^{IZO} - E_{VBM}^{IZO})$ represent valence band edges with reference to core levels of Ga₂O₃ and IZO, respectively.

The VBO was found to be -0.54 eV, -0.37 eV, +0.79 eV and +0.36 eV for @RT, @450°C, @650°C and @850°C, respectively. Using the band gap values obtained from absorbance spectra (see Figure 6.9 (b,c)) for Ga₂O₃ and IZO, the conduction band offset was calculated as:

$$CBO = E_g^{Ga_2O_3} - E_g^{IZO} + VBO \quad (6.2)$$

where $E_g^{Ga_2O_3}$ and E_g^{IZO} represents the bandgap of Ga₂O₃ and IZO, respectively. The CBO was found to be 0.94 eV, 1.11 eV, 2.27 eV and 1.22 eV for @RT, @450°C, @650°C and @850°C, respectively. Figure 6.9 (b-d) shows the calculated band alignments for the three samples. As can be clearly seen, the @RT, @450°C and @850°C show a type I band alignment while @650°C shows a type II band alignment. The former band alignment has a barrier to the flow of electrons due to the upward band bending of the conduction band of Ga₂O₃. This is the reason for the electrodes showing the Schottky behaviour for @RT, @450°C and @850°C samples. For the @650°C sample, the alignment is type II which is favourable for a smooth flow of electrons and holes from one material to another. The downward bending of the Ga₂O₃ obstructs no electrons which can easily move from Ga₂O₃ to IZO, thereby exhibiting Ohmic behaviour of the electrodes. From Figure 6.8 (a-c), the interface data (level 3) shows the relative

amount of Ga and In/Zn bonded to oxygen. The dominance of Ga-O bonding to In/Zn-O in @650°C may be responsible for the change in the band alignment at this temperature.

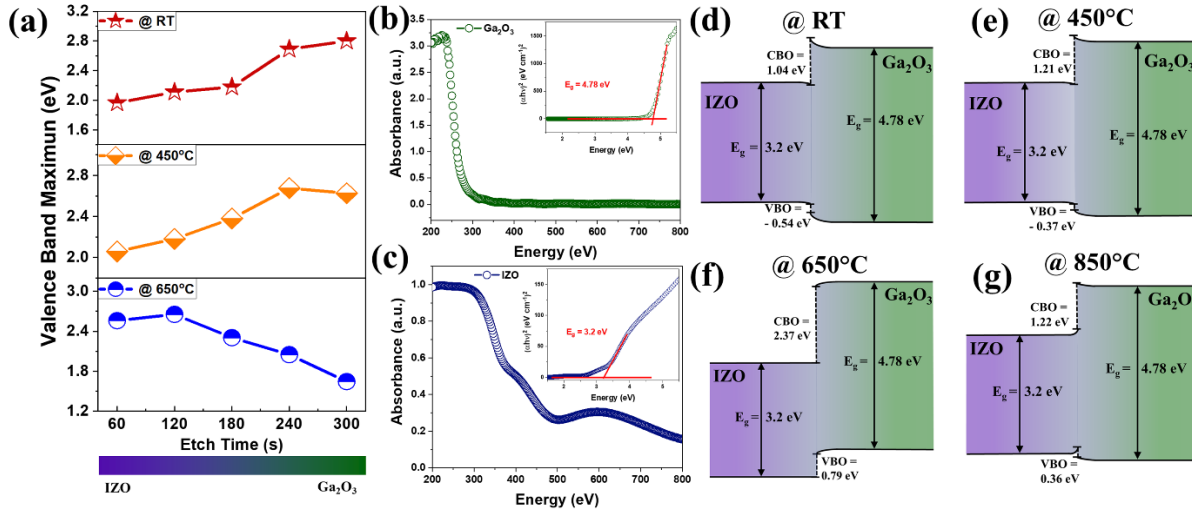


Figure 6.9 (a) Variation in the valence band maxima values for the different samples. Absorbance spectra of (b) Ga₂O₃ and (b) IZO with the insets showing the corresponding band gaps using Tauc plot method. Calculated band alignments for the (d) room temperature (e) 450°C, (f) 650°C and (g) 850°C annealed samples.

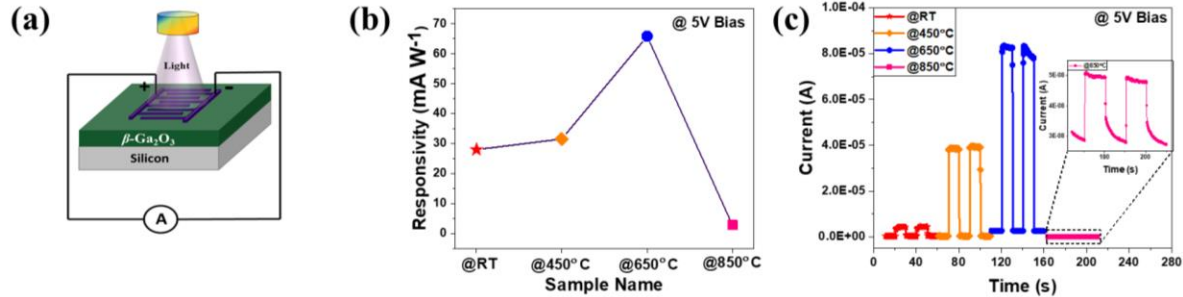


Figure 6.10 (a) Schematic of the device under testing. (b) Variation in responsivity of the different samples and (c) temporal response of the devices showing resilience under high temperature annealing.

Figure 6.10 shows the resilience of the devices after the high annealing temperatures. The responsivity of the devices increases till 650°C reaching up to 65 mA W⁻¹ from around 28 mA W⁻¹ at room temperature. For the highest temperature of 850°C, the responsivity decreases but is still appreciable at 2.8 mA W⁻¹. Figure 6.10 (c) reveals that although the devices degrade a bit at the highest annealing temperature, they still perform well.

6.2.3 Conclusions

This work shows that transparent IZO electrodes can be used as a potential contact to β -Ga₂O₃ with tunable Schottky-to-Ohmic conversion at 650°C which is due to the change in the interfacial chemistry between the semiconductor and the electrode. The dominance of Ga

bonding to oxygen more than In/Zn was found to change the band alignment from type I to type II while changing the band bending from upwards to downwards upon annealing at 650°C. The results show that IZO, as a contact material, may be employed as either a Schottky or Ohmic contact to β -Ga₂O₃ by simply tuning the annealing temperature post deposition with relative ease.

6.3 Radiation hardness under swift heavy ions

For extreme environment applications such as those in the nuclear reactor infrastructures, geothermal applications or space explorations, it becomes imperative for the functional material (here Ga₂O₃) to be immune (at least partially) to damage caused by any type of radiations. Various studies have been performed to check the radiation hardness of gallium oxide and devices thereof. Irradiation studies of Ga₂O₃ using alpha particles[38], neutrons[39], electrons[40], protons[41] and gamma[42] radiation of different energies and fluences have been done. However, most of these studies have been focused on energies in the range of 1 eV – 20 MeV. Yang et.al.[43] studied the damage caused by 10 MeV protons in β -Ga₂O₃ Schottky rectifiers where they found that proton damage induced point defects which created trap states leading to a decrease in carrier concentration. In another study, Lee et.al.[44] investigated the effect on the β -Ga₂O₃ carrier lifetime by 1.5 MeV electron irradiation. Another seldom chartered territory in the field of radiation damage is the swift heavy ions (SHI) and the material modifications by the high energy, heavy-ions is well known.[45] In contrast to the other type of radiations, SHI are massive and have huge energies that cause high radiation damage in the materials. Any material that can withstand such extreme radiation can prove its mettle for being used in extremely harsh environments. Tracy et.al.[46] irradiated β -Ga₂O₃ with 946 MeV Au ions and studied its structural response. They found that amorphization was induced and each ion produced an amorphous track along its path, leading to a phase transformation and an increase in the unit cell volume of the material. Ai et.al.[47] studied the amorphous latent tracks formed in β -Ga₂O₃ single crystal irradiated with $\sim 5\text{--}10\text{ MeV u}^{-1}$ ¹⁸¹Ta and ⁸⁶Kr ions and found the latent track size using electron microscopy and the Thermal Spike model. Although there have been a few studies related to the irradiation of SHI on gallium oxide and investigating their structural properties.[46-48] However, to the best of our knowledge, no study has been reported to investigate the radiation hardness and performance analysis of Ga₂O₃ based solar-blind photodetector against swift heavy ion irradiation.

6.3.1 Experimental details

The Ga_2O_3 thin films were deposited on *p*-type (100) Silicon substrates using RF magnetron sputtering. Prior to deposition, the substrates were cleaned by ultrasonicing in industrial grade soap solution, deionised water, acetone followed by propanol for 30 minutes each and then blow-dried with N_2 jet. Sputtering of the pure (99.99%) Ga_2O_3 2" target was done with Ar plasma at 100 W RF power. The base vacuum achieved in the chamber was 2×10^{-6} Torr while the deposition was done at a pressure of 3 mTorr. Two different sets of deposition were done by varying the growth temperature of the substrate.

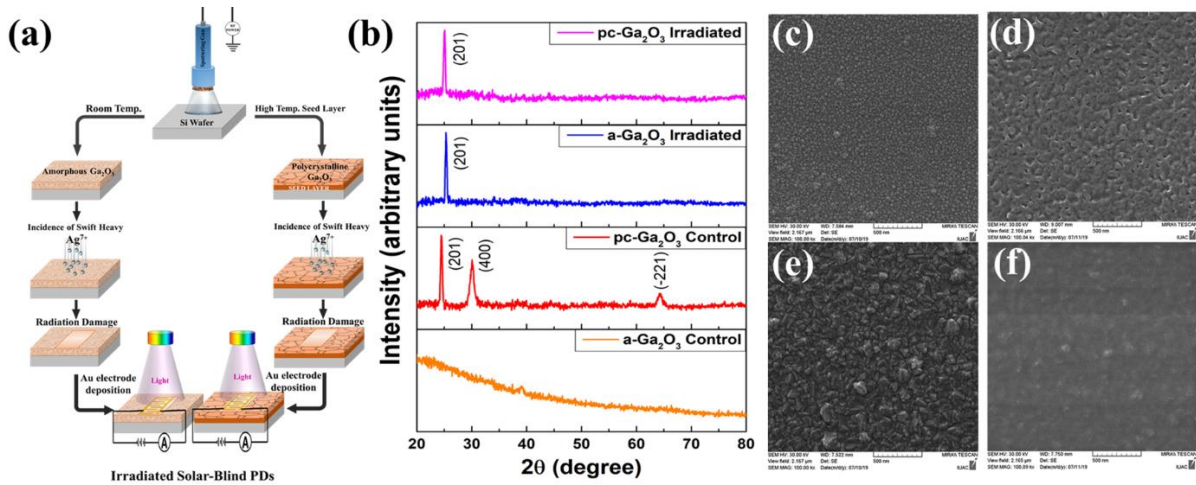


Figure 6.11 (a) Schematic for the growth amorphous and polycrystalline gallium oxide thin film and irradiation procedure with swift heavy ion irradiation. The photodetector was fabricated for final performance measurement. (b) GIXRD of control and irradiated amorphous and polycrystalline gallium oxide thin films. FE-SEM images of (c) control a- Ga_2O_3 , (d) irradiated a- Ga_2O_3 , (e) control pc- Ga_2O_3 and (f) irradiated pc- Ga_2O_3 thin films.

Amorphous gallium oxide (a- Ga_2O_3) thin film was deposited when substrate was kept at room temperature while a polycrystalline gallium oxide (pc- Ga_2O_3) thin film was deposited using a high temperature seed layer of gallium oxide followed by the growth of gallium oxide thin film at high temperature. The growth of polycrystalline gallium oxide is discussed elsewhere in details.[15] In brief, a seed layer of gallium oxide (~ 15 nm) is deposited at 700°C followed by the post-annealing at 650°C for 30 mins. The gallium oxide thin film, ~ 300 nm, is deposited at 650°C on top of gallium oxide seed-layer. The schematic for the growth of amorphous and polycrystalline gallium oxide thin film is shown in Figure 1.

The amorphous and polycrystalline β - Ga_2O_3 samples (hereafter referred to as a- Ga_2O_3 and pc- Ga_2O_3 , respectively) were then irradiated with swift heavy ions using the Pelletron accelerator facility at Inter-University Accelerator Centre (IUAC), New Delhi, India. A Silver (Ag^{7+}) ion

beam of energy 100 MeV and fluence of 10^{13} ions per cm^2 with a beam current of 7 pA (particle nanoampere) was scanned over an area of $1 \times 1 \text{ cm}^2$ of the samples. The temperature of the samples was kept at LN2 ($\sim 80 \text{ K}$) during the entire irradiation process. The identical samples of amorphous and polycrystalline gallium oxide were kept unirradiated and used as the control samples. Subsequent to irradiation, photodetectors were fabricated on control and irradiated a- Ga_2O_3 and pc- Ga_2O_3 samples by thermally depositing Cr/Au (5nm/150nm) interdigitated electrodes using a physical shadow mask. The devices were then annealed at 250°C for 20 minutes to have better adhesion of the electrodes.

6.3.2 Results and discussion

The crystallographic orientation of the samples was studied using GIXRD. The diffraction patterns of non-irradiated (control) and irradiated samples are shown in Figure 6.11 (b). It can be clearly seen that there is a broad hump with no visible sharp peak depicting the amorphous nature of the gallium oxide thin film deposited at room temperature (a- Ga_2O_3) whereas the pc- Ga_2O_3 sample (Fig. 2) shows distinctive peaks at (2θ) 24.46° , 30.05° and 64.24° corresponding to the (201), (400) and (-221) of β - Ga_2O_3 phase (pc- Ga_2O_3) (JCPDS 00-041-1103). Upon irradiation with Ag^{7+} ions, the a- Ga_2O_3 sample recrystallizes and shows a sharp peak of crystallization at 25.32° which correspond to (201) peak. This seems to be the preferred orientation as the pc- Ga_2O_3 sample also shows this single peak after the irradiation indicating that it must correspond to the lowest energy orientation in gallium oxide thin film.

However, there appears to be a slight right shift in the XRD peaks, approx. 0.6 - 0.9° in (2θ) because of internal compressive stress induced by the SHI radiation. Since there is no peak broadening and only a peak shift, this implies that the compressive stress is homogenous in nature.[49] The incident ions seem to have suppressed or destroyed the other orientations leaving only (201) intact. The morphological changes in amorphous and polycrystalline gallium oxide thin film before and after irradiation are investigated using FE-SEM and the results of the samples are shown in Figure 6.11 (c-f). The scans reveal that there is a considerable change in the surface morphologies of the thin films upon irradiation. Figure 6.11 (c) shows the amorphous nature of the RT deposited film which upon irradiation changes to a sort of nano-porous structure (Figure 6.11 (d)). This is somehow similar to the process of agglomeration and coalescence which occurs during the sintering procedure.[50] Figure 6.11 (e) shows the pc- Ga_2O_3 thin film having visibly larger crystallites in the thin film. However, upon irradiation the polycrystalline surface is highly damaged with visible destruction of the

large grains. Also, noteworthy is the fact that both the a-Ga₂O₃ and pc-Ga₂O₃ have a continuous film distribution without any cracks or voids.

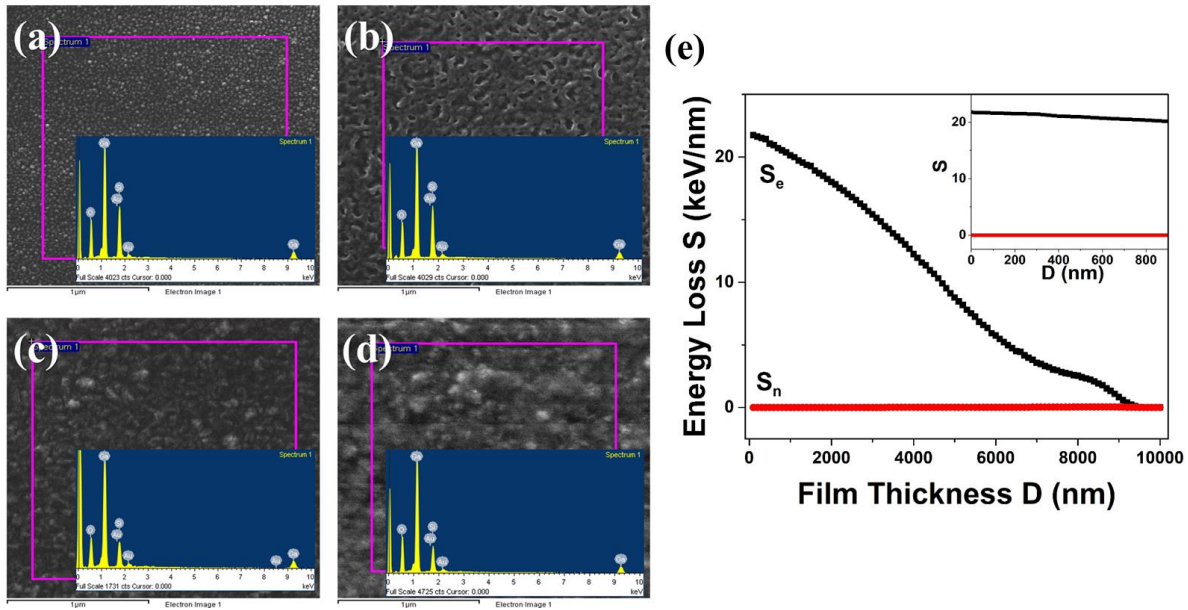


Figure 6.12 EDX Spectra of (a) a-Ga₂O₃ control (b) a-Ga₂O₃ irradiated (c) pc-Ga₂O₃ control and (d) pc-Ga₂O₃ irradiated. The absence of silver in any of these shows that all the Ag⁷⁺ ions simply pass through without getting deposited in the samples. (e) Variation of the electronic energy loss (S_e) and nuclear energy loss (S_n) of 100 MeV Ag⁷⁺ ions incident on gallium oxide film as a function of film thickness. The inset shows the almost constant and dominated value of electronic energy loss for entire thickness of gallium oxide deposited on silicon substrate.

The absence of any silver in the EDX spectrum (Figure 6.12 (a-d)) implies that most of the incident Ag⁷⁺ ions simply pass through without getting deposited in the gallium oxide thin film. This is also confirmed by the Stopping and Range of Ions in Matter (SRIM) software calculations.[51] The projected range of 100 MeV silver in gallium oxide is about 8.70 μm which is much larger than the deposited thin films (the maximum thickness of the gallium oxide film is around 300 nm).

The structural modifications upon SHI irradiation of amorphous and polycrystalline gallium oxide thin film are due to the deposition of high energy by the incoming ions locally in the system. The interaction of an ion traversing through a solid is indeed a complicated process. The mechanism of the energy deposited by the ion is highly dependent on the energy that it possesses. At intermediate energies (such as those which are involved in neutron studies), the energy is transferred to both the electronic as well as atomic sub-systems. However, at the higher end of the energy spectra (such as SHI), the energy is primarily transferred to the electronic subsystem only.[52] This leads to electronic excitations, electron-electron scattering,

electron-phonon coupling and electronic and atomic defect formations.[53] The exact exchange of energy between the electronic and atomic sub-systems is still unknown. However, attempts have been made to understand the process of the transfer of electronic excitation to displacement of atoms via two models viz. the Coulomb Explosion[54] model and the Thermal Spike[55] model, of which the latter is of particular interest. According to this model, an ion in its path gives rise to highly excited electrons via inelastic scattering and electron-electron scattering. The excited electronic subsystem transfers its energy to the atoms in the immediate vicinity via the electron-phonon coupling, thereby causing local heating and a consequent sudden rise in temperature, sometimes even above the melting point of the material. The temperature increase is then followed by a rapid quenching ($10^{13} - 10^{14}$ K/s) that results in change in phase when the melt solidifies. In our case, the energy losses of SHI ion are predominantly electronic energy losses, inelastic collision of the incoming ions with the electronic subsystem, in contrast to the nuclear energy losses, elastic collision with the atom subsystems of the solid, which dominates at low energy scale. SRIM calculations for the electronic and nuclear energy losses also confirm the same. The calculated nuclear stopping power (S_n) is 0.12 keV/nm which is negligible as compared to the electronic stopping power (S_e) of 21.73 keV/nm. Figure 6.12 (e) shows the comparative S_e and S_n as a function of depth with the inset showing that it is nearly constant for the relevant film thickness. Therefore, the morphological, structural and electronic changes in the gallium oxide thin film correspond to electronic energy loss of incident SHI ions.

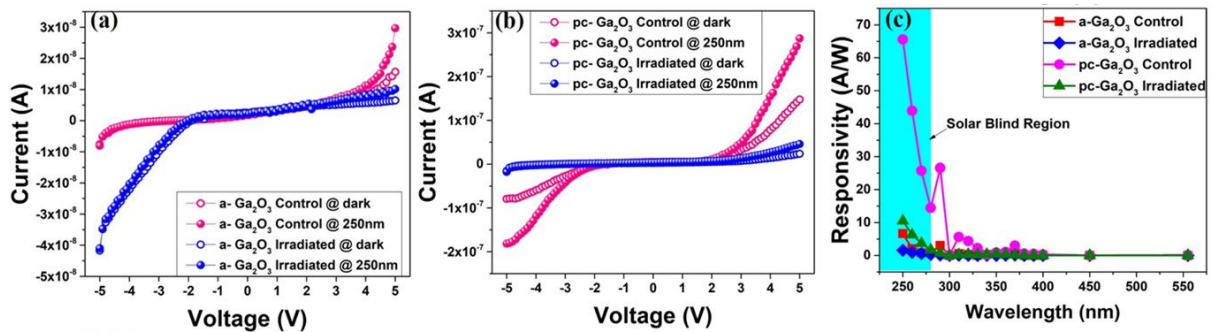


Figure 6.13 IV curves for (a) amorphous and (b) polycrystalline Ga₂O₃ based photodetectors and (c) Comparison of photoresponsivity vs. wavelength at an input bias of 5V.

Solar-blind photodetectors fabricated on irradiated samples were tested and compared to the ones made on control samples. Figure 6.13 (a-b) shows the I-V curves for the photodetectors which are all non-linear in nature, thereby confirming the Schottky contact with gold electrode. The performance was measured on two main parameters viz. the responsivity and the response

time. The spectral response of the device with variable input wavelengths is shown in Figure 6.13 (c). The measurements were taken at 5V input bias and all the SBPDs show the maximum responsivity at 250 nm (solar-blindness).

The transient response of the photodetectors was measured by periodically switching a 254 nm UV-C lamp after every 30 seconds. Figure 6.14 (a-b) shows the comparison of the real-time photocurrent for the different SBPDs. The pc-Ga₂O₃ clearly shows a much better and stable response than the a-Ga₂O₃ prior to and even after radiation damage.

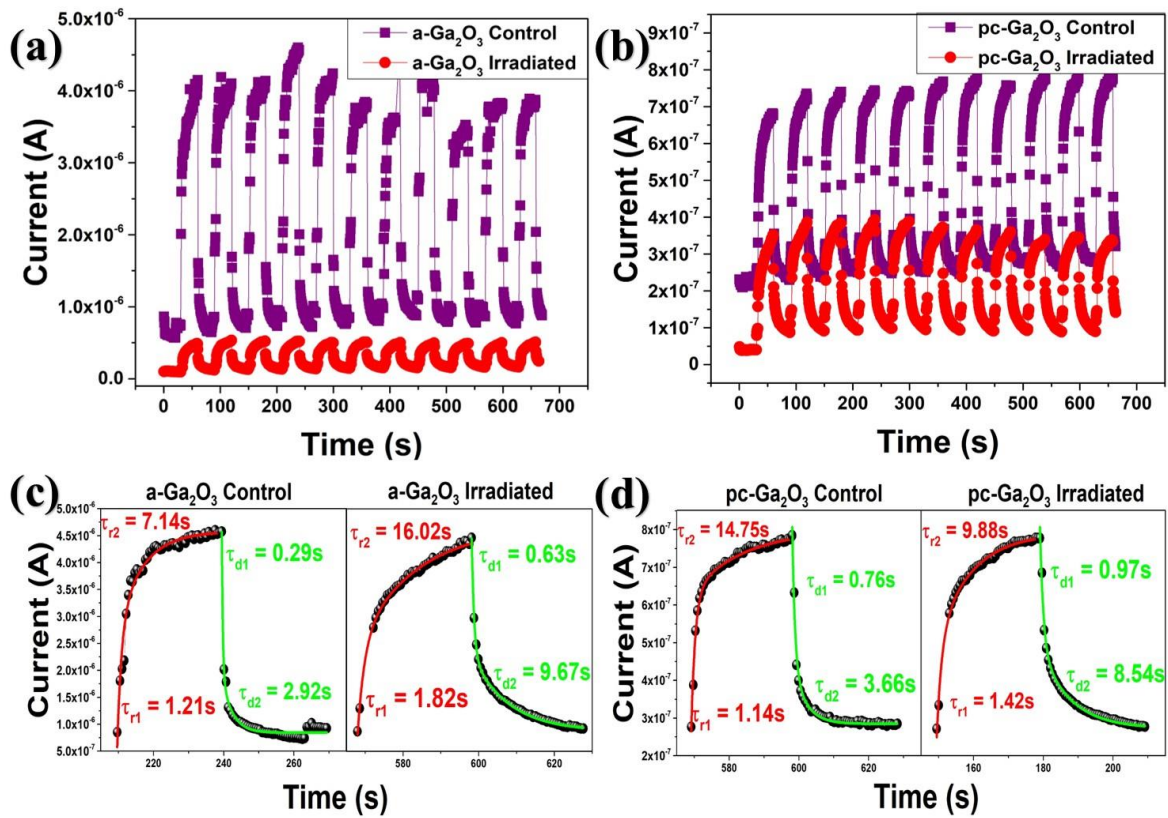


Figure 6.14 (a,b) Comparison of transient photoresponse and (c,d) fitted single cycle photoresponse of amorphous and polycrystalline based SBPD.

To get a quantitative estimate on the effect that SHI irradiation has on the response time, the single-cycle photoresponse for the samples is plotted by fitting the rising and falling edges (Figure 6.14 (c-d)), using the equation:

$$I = I_o + Ae^{-t/\tau_1} + Be^{-t/\tau_2}, \quad (6.3)$$

where I_o is the steady-state current, A and B are constants, t is the time, and τ_1 and τ_2 are relaxation-time constants.[37] The rise and decay edges both consist of the fast component and the slow component (τ_{r1} , τ_{r2} , τ_{d1} and τ_{d2} respectively). The fast component is attributed to the change in carrier density, while the slow component is due to the carrier trapping/releasing

owing to the defects in the system.[15] From Figure 6.14 (c-d), it is clearly visible that upon irradiation there is a marked decrease in responsivity and an increase in the time constants. This can be attributed to a possible change in the defect density in irradiated gallium oxide thin films. The defects present in the system may lead to a change in its basic properties.

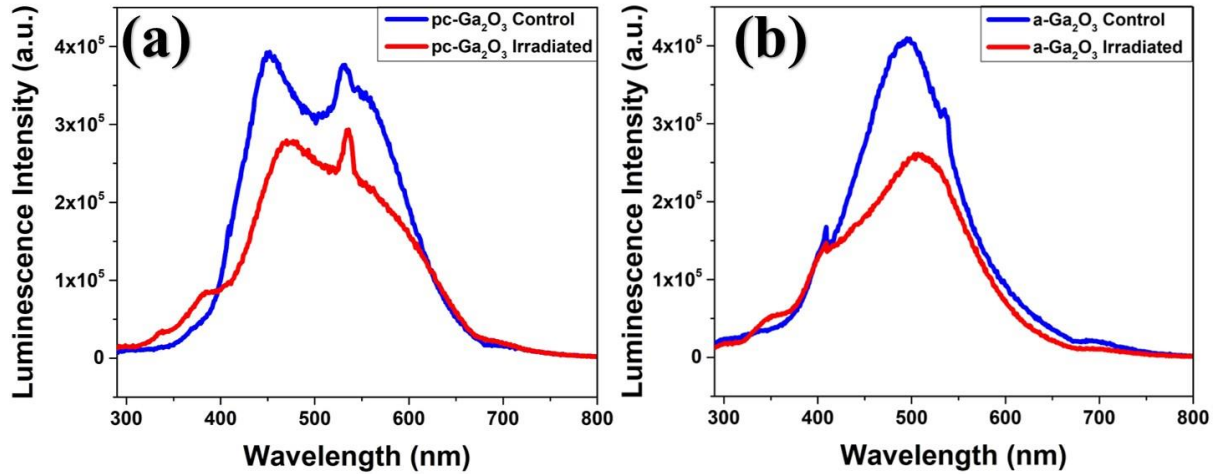


Figure 6.15 PL spectra for (a) polycrystalline and (b) amorphous before and after irradiation.

For gallium oxide, it has been reported that an increase in the oxygen vacancies tend to increase the electrical conductivity while the gallium vacancies have an opposite effect because these act as trapping centres for the charge carriers.[46, 56] To confirm the change in defect density upon irradiation and correlate with the performance of the photodetector, detailed Photoluminescence (PL) studies were done on all the samples.[57] Figure 6.15 (a) depicts the room temperature PL study for the pc-Ga₂O₃ sample. The spectra show the UV, blue and green emission bands, characteristic of the β -Ga₂O₃. The UV band is attributed to the intrinsic defects in gallium oxide and are independent of doping and growth conditions. The blue and the green bands are usually attributed to the donor-acceptor pair transitions involving deep donors (oxygen vacancies) and deep acceptors (gallium vacancies or gallium oxygen vacancy pairs).[58, 59] Control and irradiated pc-Ga₂O₃ both show this characteristic, however, the intensity of blue and green band decreases upon irradiation with a slight increase in the UV band intensity. The change in intensity can be attributed to the increase in some of intrinsic defects (responsible for UV emission) and the thermal quenching of some of the point defects (which cause the blue and green emission). This can occur simultaneously by an electron de-trapping from a donor to the conduction band or by hole de-trapping from an acceptor to the valence band.[58] The increase in local temperature due to irradiation may have caused certain point defects (such as the oxygen vacancies or gallium vacancies)[60] to anneal thereby

reducing the overall optical defect density. This ionization-induced annealing of defects has been previously reported in other wide band gap semiconductors such as SiC, both theoretically and experimentally.[61, 62] Zhang et.al.[53] have studied the annealing of pre-existing defects in SiC which restores the structural disorder. In the case of gallium oxide (also a wide band gap material), a similar process might occur wherein the oxygen and gallium vacancies may have annealed under the influence of the local thermal spike. It has been reported by Armstrong et.al.[63] that the photoconductive gain in Ga_2O_3 based Schottky diodes is primarily due to the self-trapped holes. Cui et.al.[64] have also reported that the high responsivity and the slow response times in Ga_2O_3 PDs are because of the persistent photo conductivity (PPC) which is attributable to the deep traps formed by the oxygen vacancies. In our irradiation study, we have found the responsivity of the detectors decreases upon irradiation. PL study suggests that a decrease in oxygen and gallium vacancies and other optical defects (due to annealing of these pre-existing defects via the thermal spike) must be the reason for the consequent decrease in the responsivity. The slight changes in the fast components (due to band-to-band transitions) of the response time as compared to the marked change in the slow component (due to traps) also corroborate these findings. PL study was also carried out for the amorphous gallium oxide samples which shows a similar trend. Although these measurements show the decrease in optical defect density by annealing, these in no way imply the complete return of lattice order. There are still defects and vacancies present even after irradiation and we also cannot completely rule out the formation of non-optical defects. These non-optical defects may have a role in the response of the photodetector upon irradiation such as leading to a slight increase in the time constants of the photoresponse. Some of these defects have previously been reported in literature.[65-68] Ingebrigtsen et.al.[65] have studied the impact of proton irradiation on deep level defects in gallium oxide where they have reported a change in charge carrier concentration and hence in conductivity attributable to gallium vacancies and vacancy-complex formation. Gao et.al.[66] have also reported the generation and enhancement of electrically active defects upon neutron irradiation with a possible passivation with annealing. The defect study in Ga_2O_3 oxide is still a new topic of research and the exact mechanism of creation and destruction of defects remain unknown. Extensive studies are required to fill this gap.

Some radiation studies[56, 69] have suggested that annealing at elevated temperatures tends to recover device performance up to a certain level. With this aim, we have studied the effect of time on the irradiated samples. So these were left undisturbed for > 3600 hours to study whether

these would self-anneal and stabilize themselves. Subsequently, the irradiated samples were then annealed in air ambient for different temperatures and durations (100°C, 175°C and 250°C for 30 minutes and 60 minutes each) to expedite the recovery process. However, the post-annealing temperature for irradiated gallium oxide photodetector was kept same as the annealing temperature for metal electrode made in control device (250°C for 20 mins). Table II shows the comparison in the performance of the photodetectors after self-annealing and annealing at moderate temperatures. After self-annealing, the a-Ga₂O₃ sample showed a slight increase in responsivity and response time, however the pc-Ga₂O₃ showed a huge decrease in responsivity. This can be attributed to the fact that leaving the devices alone gives them time to stabilize and come to the lowest energy configuration. Since the amorphous sample was fabricated at RT, it has a better chance of self-stabilizing.

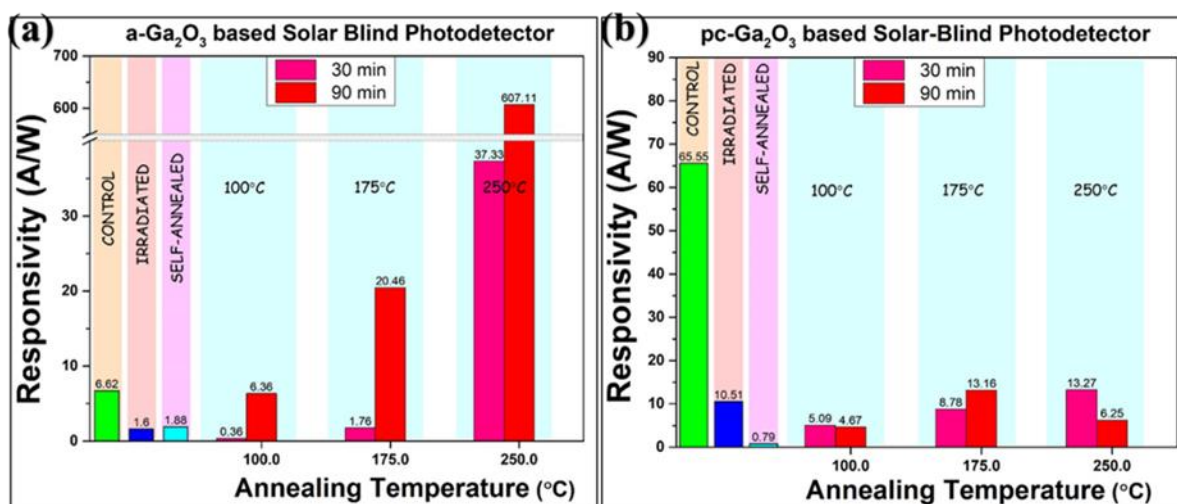


Figure 6.16 Comparison of peak responsivity @ 250 nm (at 5 V bias) for (a) amorphous Ga₂O₃ based photodetector and (b) polycrystalline Ga₂O₃ based photodetector, respectively. The responsivity values are reported for control and irradiated samples along with those after annealing.

The effect of annealing at moderate temperature on responsivity is shown in Figure 6.16. Whereas the a-Ga₂O₃ based device shows a steady increment in the responsivity with a dramatic increase of responsivity at 250°C, the pc-Ga₂O₃ sample show no such marked trend. This huge jump in responsivity in a-Ga₂O₃ can be attributed to the diffusion of gold atoms in the gallium oxide layer through nano-pores formed due to irradiation process. Suzuki et.al.[10] also predicted such a process in a single crystal β -Ga₂O₃ based photodiode. Although they reported that the diffusion occurred at a temperature of 500°C, however in the present study, the diffusion at a lower temperature is possible in irradiated a-Ga₂O₃ devices primarily because of its nano-porous structure as compared to the rigid structure of a single crystal β -Ga₂O₃. No

similar jump in responsivity was observed for the pc-Ga₂O₃, primarily due to non-formation of nano-pores facilitating the diffusion of gold atoms at a temperature much lower than 500°C.[10] It should be noted that a possible change in crystal structure of the thin films upon annealing is ruled out because the annealing temperatures were intentionally kept low so as to avoid the same. Also, prior to testing, all the devices were annealed at the same temperature to make the adherence of the deposited electrodes stronger. This is a routine procedure which has never shown to induce any change in the crystal structure of gallium oxide thin film.

The transient response time constants of the irradiated samples upon annealing show that there is a significant decrease in the rise time after heating at 250°C. The rise time constants (τ_{r1}/τ_{r2}) for the irradiated, annealed samples are 0.65s/3.85s for a-Ga₂O₃ and 0.59s/7.78s for pc-Ga₂O₃ which are far better as compared to even the control samples. Since annealing provides thermal energy to the samples, this energy may be used to create some new defects as well as the annealing of certain pre-existing non-optical defects. The annealing temperatures are moderate enough to induce only small changes in the overall structure as opposed to a complete structural or phase change which might occur at temperatures greater than 300°C.[10]

6.3.3 Conclusions

The swift heavy ions (Ag⁷⁺) are irradiated upon amorphous and polycrystalline gallium oxide thin-films and its impact on the performance of the solar-blind photodetector is investigated. The highly energetic irradiation leads to significant morphological and structural changes in the films which are explained via the thermal spike model. The increase in local lattice temperature anneals some of the pre-existing defects which is confirmed by the PL studies. These optical defects are responsible for the photoconductive gain and their reduction degrades the photodetector performance. Nano-pores formed in the irradiated amorphous thin-film facilitates the diffusion of gold atoms leading to an enhanced recovery of responsivity even at moderate annealing temperatures. The preservation of device integrity and the other results show that the gallium oxide as a material shows excellent radiation hardness against SHI and is highly suitable for the fabrication of the Solar-blind photodetectors to be used in extreme and harsh environments. Also, the partial annealing of defects upon irradiation presented in this study may pave the way for ionization-induced elimination of intrinsic defects in gallium oxide in the future.

References

1. Kaur, D., et al., Interface-induced origin of Schottky-to-Ohmic-to-Schottky conversion in non-conventional contact to β -Ga₂O₃. *Applied Physics Letters* **2024**, 124(2), 021601.
2. Kaur, D., et al., Phase dependent radiation hardness and performance analysis of amorphous and polycrystalline Ga₂O₃ solar-blind photodetector against swift heavy ion irradiation. *Journal of Applied Physics* **2020**, 128(6), 065902.
3. Huan, Y.-W., et al., Recent Advances in β -Ga₂O₃–Metal Contacts. *Nanoscale Research Letters* **2018**, 13(1), 246.
4. Lyle, L.A.M., Critical review of Ohmic and Schottky contacts to β -Ga₂O₃. *Journal of Vacuum Science & Technology A* **2022**, 40(6), 060802.
5. Tadjer, M.J., 10 - Ohmic contacts to gallium oxide, in *Gallium Oxide*, S. Pearton, F. Ren, and M. Mastro, Editors. 2019, Elsevier. p. 211-230.
6. Chen, J.-X., et al., Investigation of the Mechanism for Ohmic Contact Formation in Ti/Al/Ni/Au Contacts to β -Ga₂O₃ Nanobelt Field-Effect Transistors. *ACS Applied Materials & Interfaces* **2019**, 11(35), 32127-32134.
7. Favela, E.V., et al., Effects of Annealing on Co/Au and Ni/Au Schottky Contacts on β -Ga₂O₃. *Journal of Electronic Materials* **2023**, 52(3), 1927-1936.
8. Hou, C., et al., High temperature (500 °C) operating limits of oxidized platinum group metal (PtOx, IrOx, PdOx, RuOx) Schottky contacts on β -Ga₂O₃. *Applied Physics Letters* **2020**, 117(20), 203502.
9. Lyle, L.A.M., et al., Nanoscale Characterization of Chemical and Structural Properties of the Au/(100) β -Ga₂O₃ Interface. *ACS Applied Electronic Materials* **2022**, 4(9), 4471-4481.
10. Suzuki, R., et al., Enhancement of responsivity in solar-blind β -Ga₂O₃ photodiodes with a Au Schottky contact fabricated on single crystal substrates by annealing. *Applied Physics Letters* **2009**, 94(22), 222102.
11. Kaur, D., et al., Strain effects on the optoelectronic performance of ultra-wide band gap polycrystalline β -Ga₂O₃ thin film grown on differently-oriented Silicon substrates for solar blind photodetector. *Applied Surface Science* **2023**, 616, 156446.
12. Li, J.-S., et al. *Annealing Stability of NiO/Ga₂O₃ Vertical Heterojunction Rectifiers*. Crystals, 2023. **13**, DOI: 10.3390/cryst13081174.
13. Lee, M.-H., et al., Interfacial reactions of titanium/gold ohmic contacts with Sn-doped β -Ga₂O₃. *APL Materials* **2019**, 7(2), 022524.
14. Xing, Z., et al., Liesegang Phenomenon of Liquid Metals on Au Film. *Advanced Materials* **2023**, 35(7), 2209392.
15. Arora, K., et al., Ultrahigh Performance of Self-Powered β -Ga₂O₃ Thin Film Solar-Blind Photodetector Grown on Cost-Effective Si Substrate Using High-Temperature Seed Layer. *ACS Photonics* **2018**, 5(6), 2391-2401.
16. Seyidov, P., et al., Thermal Stability of Schottky Contacts and Rearrangement of Defects in β -Ga₂O₃ Crystals. *Advanced Electronic Materials* **2023**, n/a(n/a), 2300428.
17. Greczynski, G., et al., X-ray photoelectron spectroscopy: Towards reliable binding energy referencing. *Progress in Materials Science* **2020**, 107, 100591.
18. Liu, H., et al., Design and solderability characterization of novel Au–30Ga solder for high-temperature packaging. *Journal of Materials Science: Materials in Electronics* **2020**, 31(3), 2514-2522.
19. Elliott, R.P., et al., The Au–Ga (Gold-Gallium) system. *Bulletin of Alloy Phase Diagrams* **1981**, 2(3), 356-358.
20. Barinov, A., et al., Stages of formation and thermal stability of a gold-n-GaN interface. *Journal of Physics D: Applied Physics* **2001**, 34(3), 279.

21. Weizer, V.G., et al., The interaction of gold with gallium arsenide. *Journal of Applied Physics* **1988**, 64(9), 4618-4623.
22. González-Elipé, A.R., et al., *Chapter 4 - SPECTROSCOPIC CHARACTERIZATION OF OXIDE/OXIDE INTERFACES*, in *Handbook of Surfaces and Interfaces of Materials*, H.S. Nalwa, Editor. 2001, Academic Press: Burlington. p. 147-194.
23. Leung, S., et al., Electrical Properties, Structure, and Phase Morphology of Au-Ga Alloy Films Codeposited on GaAs Substrates. *Journal of The Electrochemical Society* **1985**, 132(4), 898.
24. Lu, C., et al., A review of metal–semiconductor contacts for β -Ga₂O₃. *Journal of Physics D: Applied Physics* **2022**, 55(46), 463002.
25. Shivani, et al., A strategic review on gallium oxide based power electronics: Recent progress and future prospects. *Materials Today Communications* **2022**, 33, 104244.
26. Kaur, D., et al., A Strategic Review on Gallium Oxide Based Deep-Ultraviolet Photodetectors: Recent Progress and Future Prospects. *Advanced Optical Materials* **2021**, 9(9), 2002160.
27. Yao, Y., et al., Electrical behavior of β -Ga₂O₃ Schottky diodes with different Schottky metals. *Journal of Vacuum Science & Technology B* **2017**, 35(3), 03D113.
28. Yao, Y., et al., Investigation of Different Metals as Ohmic Contacts to β -Ga₂O₃: Comparison and Analysis of Electrical Behavior, Morphology, and Other Physical Properties. *Journal of Electronic Materials* **2017**, 46(4), 2053-2060.
29. Lyle, L.A.M., et al., Electrical and chemical analysis of Ti/Au contacts to β -Ga₂O₃. *APL Materials* **2021**, 9(6), 061104.
30. Carey, P.H., et al., Ohmic contacts on n-type β -Ga₂O₃ using AZO/Ti/Au. *AIP Advances* **2017**, 7(9), 095313.
31. Li, Y., et al., Graphene Interdigital Electrodes for Improving Sensitivity in a Ga₂O₃:Zn Deep-Ultraviolet Photoconductive Detector. *ACS Applied Materials & Interfaces* **2019**, 11(1), 1013-1020.
32. Kumar, N., et al., High performance, flexible and room temperature grown amorphous Ga₂O₃ solar-blind photodetector with amorphous indium-zinc-oxide transparent conducting electrodes. *Journal of Physics D: Applied Physics* **2019**, 52(33), 335103.
33. Oshima, T., et al., Formation of indium–tin oxide ohmic contacts for β -Ga₂O₃. *Japanese Journal of Applied Physics* **2016**, 55(12), 1202B7.
34. Carey, P.H., et al., Improvement of Ohmic contacts on Ga₂O₃ through use of ITO-interlayers. *Journal of Vacuum Science & Technology B* **2017**, 35(6), 061201.
35. Kumar, N., et al., Design of low surface roughness-low residual stress-high optoelectronic merit a-IZO thin films for flexible OLEDs. *Journal of Applied Physics* **2016**, 119(22), 225303.
36. Kaur, D., et al., Dependence of persistent photoconductivity on the thickness of β -Ga₂O₃ thin film photodetectors on c-plane sapphire via magnetron sputtering. *Journal of Vacuum Science & Technology A* **2023**, 41(4), 043410.
37. Guo, D.Y., et al., Oxygen vacancy tuned Ohmic-Schottky conversion for enhanced performance in β -Ga₂O₃ solar-blind ultraviolet photodetectors. *Applied Physics Letters* **2014**, 105(2), 023507.
38. Yang, J., et al., Eighteen mega-electron-volt alpha-particle damage in homoepitaxial β -Ga₂O₃ Schottky rectifiers. *Journal of Vacuum Science & Technology B* **2018**, 36(3), 031205.
39. Farzana, E., et al., Impact of deep level defects induced by high energy neutron radiation in β -Ga₂O₃. *APL Materials* **2019**, 7(2), 022502.
40. Yang, J., et al., 1.5 MeV electron irradiation damage in β -Ga₂O₃ vertical rectifiers. *Journal of Vacuum Science & Technology B* **2017**, 35(3), 031208.

41. Ahn, S., et al., Effect of 5 MeV proton irradiation damage on performance of β -Ga₂O₃ photodetectors. *Journal of Vacuum Science & Technology B* **2016**, 34(4), 041213.
42. Wong, M.H., et al., Radiation hardness of β -Ga₂O₃ metal-oxide-semiconductor field-effect transistors against gamma-ray irradiation. *Applied Physics Letters* **2018**, 112(2), 023503.
43. Yang, J., et al., 10 MeV proton damage in β -Ga₂O₃ Schottky rectifiers. *Journal of Vacuum Science & Technology B* **2018**, 36(1), 011206.
44. Lee, J., et al., Effect of 1.5 MeV electron irradiation on β -Ga₂O₃ carrier lifetime and diffusion length. *Applied Physics Letters* **2018**, 112(8), 082104.
45. Kanjilal, D., Swift heavy ion-induced modification and track formation in materials. *Current Science (Bangalore)* **2001**, 80(12), 1560-1566.
46. Tracy, C.L., et al., Anisotropic expansion and amorphization of Ga₂O₃ irradiated with 946 MeV Au ions. *Nuclear Instruments and Methods in Physics Research Section B: Beam Interactions with Materials and Atoms* **2016**, 374, 40-44.
47. Ai, W., et al., Radiation damage in β -Ga₂O₃ induced by swift heavy ions. *Japanese Journal of Applied Physics* **2019**, 58(12), 120914.
48. Yadav, S., et al., Effects of Energetic Ion Irradiation on β -Ga₂O₃ Thin Films. *ECS Journal of Solid State Science and Technology* **2020**, 9(4), 045015.
49. Ungár, T., Microstructural parameters from X-ray diffraction peak broadening. *Scripta Materialia* **2004**, 51(8), 777-781.
50. Kocjan, A., et al., The agglomeration, coalescence and sliding of nanoparticles, leading to the rapid sintering of zirconia nanoceramics. *Scientific Reports* **2017**, 7(1), 2541.
51. Ziegler, J.F., et al., SRIM - The stopping and range of ions in matter (2010). *Nuclear Instruments and Methods in Physics Research B* **2010**, 268, 1818.
52. Kumar, M., et al., Nanoparticle formation by swift heavy ion irradiation of indium oxide thin film. *Nanotechnology* **2008**, 19(17), 175606.
53. Zhang, Y., et al., Ionization-induced annealing of pre-existing defects in silicon carbide. *Nature Communications* **2015**, 6(1), 8049.
54. Lesueur, D., et al., Damage creation via electronic excitations in metallic targets part II : A theoretical model. *Radiation Effects and Defects in Solids* **1993**, 126(1-4), 163-172.
55. Szenes, G., General features of latent track formation in magnetic insulators irradiated with swift heavy ions. *Physical Review B* **1995**, 51(13), 8026-8029.
56. Cojocaru, L.N., Defect-annealing in neutron-damaged β -Ga₂O₃. *Radiation Effects* **1974**, 21(3), 157-160.
57. Chandrinou, C., et al., PL study of oxygen defect formation in ZnO nanorods. *Microelectronics Journal* **2009**, 40(2), 296-298.
58. Binet, L., et al., ORIGIN OF THE BLUE LUMINESCENCE OF β -Ga₂O₃. *Journal of Physics and Chemistry of Solids* **1998**, 59(8), 1241-1249.
59. Shi, Q., et al., Structural, optical and photoluminescence properties of Ga₂O₃ thin films deposited by vacuum thermal evaporation. *Journal of Luminescence* **2019**, 206, 53-58.
60. Guzmán-Navarro, G., et al., CL study of blue and UV emissions in β -Ga₂O₃ nanowires grown by thermal evaporation of GaN. *Journal of Applied Physics* **2011**, 110(3), 034315.
61. Backman, M., et al., Molecular dynamics simulations of swift heavy ion induced defect recovery in SiC. *Computational Materials Science* **2013**, 67, 261-265.
62. Debelles, A., et al., Combined experimental and computational study of the recrystallization process induced by electronic interactions of swift heavy ions with silicon carbide crystals. *Physical Review B* **2012**, 86(10), 100102.
63. Armstrong, A.M., et al., Role of self-trapped holes in the photoconductive gain of β -gallium oxide Schottky diodes. *Journal of Applied Physics* **2016**, 119(10), 103102.

64. Cui, S., et al., Room-Temperature Fabricated Amorphous Ga₂O₃ High-Response-Speed Solar-Blind Photodetector on Rigid and Flexible Substrates. *Advanced Optical Materials* **2017**, 5(19), 1700454.
65. Ingebrigtsen, M.E., et al., Impact of proton irradiation on conductivity and deep level defects in β -Ga₂O₃. *APL Materials* **2018**, 7(2), 022510.
66. Gao, H., et al., Optical signatures of deep level defects in Ga₂O₃. *Applied Physics Letters* **2018**, 112(24), 242102.
67. Ingebrigtsen, M.E., et al., Iron and intrinsic deep level states in Ga₂O₃. *Applied Physics Letters* **2018**, 112(4), 042104.
68. Ingebrigtsen, M.E., et al., Bulk β -Ga₂O₃ with (010) and (201) Surface Orientation: Schottky Contacts and Point Defects. *Materials Science Forum* **2017**, 897, 755-758.
69. Yang, G., et al., Influence of High-Energy Proton Irradiation on β -Ga₂O₃ Nanobelt Field-Effect Transistors. *ACS Applied Materials & Interfaces* **2017**, 9(46), 40471-40476.

Chapter 7: Summary and Scope for Future Studies

The present thesis focused on the fabrication and development of high performance solar-blind photodetectors based on gallium oxide thin film. All the three components including the substrate used, active layer as well as contact electrodes were studied for their dependency of the ultimate device performance. The active layer of gallium oxide is optimized on different substrates such as Si (differently oriented), *c*-plane sapphire, SiO₂ coated Si, etc. to realize its different phases (crystalline as well as amorphous) for enhanced photodetection. Moreover, surface modification and heterostructures are also employed for enhancing the performance of amorphous based SBPDs. Finally, the devices and the active layer is also tested under extreme environmental conditions including high temperatures and under high radiation to check their resilience against harsh conditions. Ultimately, we have been able to reach sub-millisecond response times which is now restricted by testing equipment.

7.1 Summary

7.1.1 Dependence of performance on the growth of active layer

This chapter investigates systematically the active layer involved – gallium oxide. It begins by building upon the growth of polycrystalline β -Ga₂O₃ on different orientations of Si substrate and studying how the performance changes with the strain produced in the films. This is followed by optimizing the growth of β -Ga₂O₃ on a more lattice matched substrate – sapphire – by varying the thickness of the film and studying its impact on PDs. Additionally, a facile fabrication of mixed-phase (α – β) is done on room temperature on sapphire substrates, thus, opening the doors for room temperature crystallinity being achieved in Ga₂O₃

- Photodetector performance is highly dependent on orientation of substrate used as the strain induced ultimately affects active layer film growth.
- Strain in the films should be minimized to achieve high performance.
- From the thickness dependent study, thicker films have a lower number of oxygen vacancies and a better stoichiometric ratio and hence can be utilized for fabricating better and faster optoelectronic devices with minimum persistent photoconductivity.
- It is possible to achieve room temperature crystallinity in Ga₂O₃ by using sapphire substrates and optimizing the deposition parameters to achieve ultra-high photoresponse, thereby providing facile fabrication.

- We were ultimately able to achieve a rise time of 3 ms and fall time of 12 ms using a high temperature seed layer of β -Ga₂O₃ deposited on Si (111), having the minimum amount of strain in the grown films.
- We also achieved an ultra-high photo-to-dark-current ratio of 10⁵ using a facile fabrication of mixed-phase, polycrystalline Ga₂O₃ deposited at room temperature.

7.1.2 Enhancing performance using surface modification

In this chapter, surface modification of amorphous films of gallium oxide are undertaken in two different approaches. First, the surface of amorphous Ga₂O₃ film is modified and nanoripples are created using ion beam sputtering and the dependence on photodetector performance is studied. In the second approach, ultra-thin Ga₂O₃ film is conformally coated on a nanopatterned substrate, giving rise to fast speed photodetectors

- Surface modification using ion-beam sputtering turns out to be a powerful tool in the fabrication of fast speed photodetectors based on gallium oxide.
- Patterning the active layer with an incident ion beam can lead to creation of surface defects which act as recombination centers and reduce the carrier lifetime, thereby improving the ultimate device speed.
- Patterning the substrate below demonstrates a facile, cost-effective and large-area approach to enhance speeds of amorphous Ga₂O₃ based devices by amalgamating twin benefits of better light management with inadvertent Si doping, taking it a step closer towards commercialization.
- We were able to achieve one order of magnitude decrease in response times by nanopatterning the active layer and a three orders of magnitude decrease in response times by nanopatterning the substrate
- The lowest response time achieved was – 861 μ s / 710 μ s (rise/fall time) which is limited by testing equipment used.

7.1.3 Interface engineering via heterostructures of gallium oxide

This chapter studies the importance of interfaces, charge carrier dynamics and energy level alignment in the heterostructures of Ga₂O₃, taking the case of sulphide materials. The first part includes the study of a heterostructure of amorphous Ga₂O₃ with CdS, giving rise to a solar-blind photodetector while the second part deals with a heterostructure of amorphous Ga₂O₃ with PtS but now giving a broadband photoresponse.

- Amorphous Ga_2O_3 when interfaced with CdS gives rise to a solar-blind nature while interfacing it with PtS gives rise to broadband photodetection, even though both of them form n - n heterojunction and exhibit type 1 band alignment.
- Heterojunctions give superior performance than singular PDs which may be further enhanced by post-processing techniques such as annealing.
- The interfacing of the two materials for enhanced photodetection requires a thorough and complete understanding of the interfacial dynamics and charge transfer from one material to another and requires careful consideration of optimization parameters before implementation.
- Response times (rise/fall time) decrease from 1.35/2.87 s to 0.38/0.75 s by moderately annealing the solar-blind CdS- Ga_2O_3 interface.
- PtS- Ga_2O_3 heterojunction based devices, although broadband, show a fast speed of 277 μs /258 μs (rise/fall) as compared to 42 ms/46ms for bare PtS at 532 nm light, a reduction of more than 150 times, along with an enhancement in the peak responsivity of about 120 times reaching upto 0.25 AW^{-1} at 300 nm.

7.1.4 Photodetectors under extreme environments

This chapter touches upon the extreme environment applicability of Ga_2O_3 . Although the material itself is extremely thermally stable, the devices sometimes fail due to other components of the PD. In the first part, a study on the origin of near-failure of Au contacts to β - Ga_2O_3 at high temperatures is studied. The second part involves the change in the behaviour of IZO transparent electrodes from Schottky-Ohmic-Schottky upon increasing the temperatures, studied using interfacial studies. The third part involves the radiation hardness resilience of Ga_2O_3 films against swift heavy ions of 100 MeV energy and photodetectors thereof.

- Unlike its counterparts GaN and GaAs, which have reported alloy formation at lower temperatures, β - Ga_2O_3 shows a higher resilience to formation of Au-Ga alloy and can withstand higher temperatures before the actual device failure is reached.
- IZO layer as an alternate contact material to β - Ga_2O_3 whose behaviour as Ohmic or Schottky contact may be tuned by simply varying the annealing temperature and inducing interfacial changes at the semiconductor-electrode interface, while maintaining excellent device resilience.

- SHI radiation (100 MeV Ag^{7+}) induces structural and morphological changes which can be explained by Thermal Spike Model.
- The performance of the PD decreases upon irradiation which is attributable to the decrease in optical defect density (otherwise responsible for the huge photoconductive gain in gallium oxide) and can be recovered using annealing at moderate temperatures.

7.2 Scope for future studies

The present thesis has aimed to achieve enhanced performance of gallium oxide based solar-blind photodetectors and has fulfilled its objectives to a great extent and contributed significantly to the advancement of the field. Further studies as indicated below may help to further these objectives and move a step closer towards commercialization of SBPDs based on gallium oxide thin films

- Doping of the active layer to increase the carrier concentration. Since the material itself is highly insulating, suitable doping of the active layer can help in improving the electrical properties and thus carrier conduction in the devices.
- Use of asymmetric Schottky electrodes or different contact geometry for improving the performance of PD. The edges of the contacts usually lead to an electric field crowding thereby leading to localized breakdown at certain points, which may be averted by varied contact geometry.
- The formation of heterostructures between the different polymorphs of Ga_2O_3 to induce localized built-in fields since the material properties and charge transfer properties between the two interfaced polymorphs will remain more or less similar.
- Using plasmonics for obtaining novel phenomenon such as hot carrier injection using quantum dots to achieve unique photodetectors.
- Fabrication of a fully transparent, flexible and fast photodetector for use in wearable technologies which would require a suitable substrate, optimized active layer as well as flexible electrodes.

List of Publications

PUBLISHED:

1. **Damanpreet Kaur**, Pargam Vashishtha, Saif Ahmad Khan, Pawan K. Kulriya, Govind Gupta and Mukesh Kumar, Phase dependent radiation hardness and performance analysis of amorphous and polycrystalline Ga₂O₃ solar-blind photodetector against swift heavy ion irradiation, *Journal of Applied Physics* **2020**, 128, 065902
2. **Damanpreet Kaur** and Mukesh Kumar, A Strategic Review on Gallium Oxide Based Deep-Ultraviolet Photodetectors: Recent Progress and Future Prospects, *Advanced Optical Materials* **2021**, 9, 2002160
3. **Damanpreet Kaur**, Rakhi, Pargam Vashishtha, Govind Gupta, Subhendu Sarkar and Mukesh Kumar, Surface nanopatterning of amorphous gallium oxide thin film for enhanced solar-blind photodetection, *Nanotechnology* **2022**, 33, 375302
4. Shivani*, **Damanpreet Kaur***, Anupam Ghosh and Mukesh Kumar, A strategic review on gallium oxide based power electronics: Recent progress and future prospects, *Materials Today Communications* **2022**, 33, 104244 (*equal contribution)
5. **Damanpreet Kaur**, Srikanta Debata, Dhruv Pratap Singh and Mukesh Kumar, Strain effects on the optoelectronic performance of ultra-wide band gap polycrystalline β -Ga₂O₃ thin film grown on differently-oriented Silicon substrates for solar blind photodetector, *Applied Surface Science* **2023**, 616, 156446
6. **Damanpreet Kaur**, Rohit Dahiya and Mukesh Kumar, Dependence of persistent photoconductivity on the thickness of β -Ga₂O₃ thin film photodetectors on c -plane sapphire via magnetron sputtering, *Journal of Vacuum Science & Technology A: Vacuum Surfaces and Films* **2023**, 41, 043410
7. **Damanpreet Kaur**, Riya Wadhwa, Nisika, Yuchen Zhang, Poojan Indrajeet Kaswekar, Quinn Qiao, Anju Sharma, Mark D. Poliks, and Mukesh Kumar, Interfacial-Mixing and Band Engineering Induced by Annealing of CdS and α -Ga₂O₃ n-n-Type Thin-Film Heterojunction and Its Impact on Carrier Dynamics for High-Performance Solar-Blind Photodetection, *ACS Applied Electronic Materials* **2023**, 5, 3798
8. **Damanpreet Kaur**, Rohit Dahiya, Shivani and Mukesh Kumar, Interface-induced origin of Schottky-to-Ohmic-to-Schottky conversion in non-conventional contact to β -Ga₂O₃, *Applied Physics Letters* **2024**, 124, 021601
9. **Damanpreet Kaur**, Rohit Dahiya, Shivani and Mukesh Kumar, Origin of near-failure in Au contacts to polycrystalline β -Ga₂O₃ at high temperatures using interfacial studies, *Applied Physics Letters* **2024**, 124, 151601
10. **Damanpreet Kaur**, Rakhi, Raghvendra Posti, Jaspreet Singh, Debansu Roy, Subhendu Sarkar and Mukesh Kumar, Nanopatterning induced Si doping in amorphous Ga₂O₃ for enhanced electrical properties and ultra-fast photodetection, *Small* **2024**, 2309277.
11. **Damanpreet Kaur**, Rohit Dahiya Nadeem Ahmed and Mukesh Kumar, Vertically graded oxygen vacancies in amorphous Ga₂O₃ for offsetting the conventional trade-off between photoresponse and response time in solar-blind photodetectors, *ACS Applied Electronic Materials* **2024** (Just Accepted) (<https://doi.org/10.1021/acsaelm.4c00759>) (2024)

12. Nisika, Anupam Ghosh, **Damanpreet Kaur**, Kulwinder Kaur, Manoj K. Yadav, Ankush Bag and Mukesh Kumar, Interface Engineering of CZTS/TiO₂ Heterojunction using Wide-Bandgap Ga₂O₃ Passivation Interlayer for Efficient Charge Extraction, *Physica Status Solidi A* **2022**, 219, 2200001
13. Riya Wadhwa, **Damanpreet Kaur**, Yuchen Zhang, Akhil Alexender, Deepu Kumar, Pradeep Kumar, Manoj A.G. Namboothiry, Quinn Qiao and Mukesh Kumar, Fast response and high-performance UV-C to NIR broadband photodetector based on MoS₂/a-Ga₂O₃ heterostructures and impact of band-alignment and charge carrier dynamics, *Applied Surface Science* **2023**, 632, 157597
14. Gaurav Bassi, **Damanpreet Kaur**, Rohit Dahiya, and Mukesh Kumar, 2D-3D heterostructure of PtS_{2-x}/Ga₂O₃ and their band alignment studies for high performance and broadband photodetector, *Nanotechnology* **2024**, 35, 325706

UNDER PREPARATION:

1. **Damanpreet Kaur**, Rohit Dahiya, Vinit Sheokand, Gaurav Bassi and Mukesh Kumar, Two-dimensional non-layered PtS heterointerfaced with amorphous Ga₂O₃ for highly stable, ultra-fast and broadband photodetector
2. **Damanpreet Kaur**, Rohit Dahiya, Manish Kumar Singh, Verkholetov Maksim, Litvinova Kristina, Poliakov Maksim, Alexei Almaev, Rajendra S. Dhaka and Mukesh Kumar, Room-temperature crystallinity in oxide semiconductor.

BOOK CHAPTER:

1. **Damanpreet Kaur**, Abhay Vivek Agrawal and Mukesh Kumar, (2022), Next-Generation Materials for Broadband Photodetection: From Solar-blind to NIR”, Chapter - 6, Types of Photodetectors and their Applications, Nova Science Publishers, 175-201.

Conferences/Workshops Attended

1. **Damanpreet Kaur** and Mukesh Kumar, Poster presentation, Radiation hardness of Ga₂O₃ thin films and photodetectors against swift heavy ions, International Symposium on Semiconductor Materials and Devices (ISSMD-2020), October 31-November 2, 2020, NIT Jalandhar.
2. **Damanpreet Kaur** and Mukesh Kumar, Poster presentation, Effect of Swift Heavy Ion Irradiation on Gallium oxide thin films and photodetectors thereof, 5th International Conference on Emerging Electronics (IEEE-ICEE 2020), November 26-28, 2020, IIT Delhi.
3. **Damanpreet Kaur** and Mukesh Kumar, Oral presentation, Performance Analysis of Gallium Oxide Thin films and Photodetectors thereof against Swift Heavy Ions, Ion beams in Materials Engineering and Characterizations (IBMEC-2020), December 8-11, 2020, IUAC New Delhi.
4. **Damanpreet Kaur** and Mukesh Kumar, Poster presentation, Solar-Blind Photodetectors Based on Gallium Oxide and Their Performance Analysis against Swift Heavy Ions, 2021 MRS Fall meeting & Exhibit, December 6-8, 2021, Boston Massachusetts.
5. **Damanpreet Kaur** and Mukesh Kumar, Poster presentation, Enhanced performance in gallium oxide based photodetectors via surface nanopatterning, IUMRS-ICA 2022, December 19-23, 2022, IIT Jodhpur.
6. **Damanpreet Kaur** and Mukesh Kumar, Poster presentation, Enhanced Solar-blind photodetection of amorphous gallium oxide thin film using nanopatterned surface, Anusandhan 1.0 Research Fair 2023, June 23-25, 2023, IIT Mandi
7. **Damanpreet Kaur** and Mukesh Kumar, Poster presentation, Growth of Room Temperature Polycrystalline β -Gallium Oxide Thin Film, 6th U.S. Gallium Oxide Workshop (GOX 2023), August 13-16, 2023. Buffalo, New York, USA.
8. **Damanpreet Kaur** and Mukesh Kumar, Poster presentation, Ultrathin Films of Amorphous Gallium Oxide for Ultra-Fast Solar-Blind Photodetectors, 6th U.S. Gallium Oxide Workshop (GOX 2023), August 13-16, 2023. Buffalo, New York, USA.
9. **Damanpreet Kaur** and Mukesh Kumar, Oral presentation, Enhanced solar-blind photodetection of amorphous gallium oxide thin film using nanopatterned surface, Student Conference on Optics and Photonics (SCOP-2023), September 27-29, 2023, PRL Ahmedabad.
10. **Damanpreet Kaur** and Mukesh Kumar, Poster presentation, Ultrathin Films of Amorphous Gallium Oxide for Ultra-Fast Solar-Blind Photodetectors, ISRAPS Discussion Meeting-Cum-One-Day Symposium, October 21, 2023, IIT Ropar.
11. **Damanpreet Kaur** and Mukesh Kumar, Oral presentation, Fast speed solar-blind photodetectors using ultra-thin amorphous gallium oxide films on patterned substrates, International Conference on Materials for Energy and Sustainable Development (MESD-2023), October 27-29, 2023, JNU New Delhi.
12. **Damanpreet Kaur** and Mukesh Kumar, Poster presentation, Enhanced solar-blind photodetection of amorphous gallium oxide thin film using nanopatterned surface, DAE

Solid State Physics Symposium (DAE-SSPS 2023), December 20-24, 2023, GITAM Institute Vishakhapatnam

13. INUP Familiarisation workshop on “*Basic training program on Nano Science and Technology*”, 2019, IISC Bangalore
14. Online Short-term course on “*Nanotechnology for Electronic and Photonic Devices*”, 2020, PEC, Chandigarh

Curriculum Vitae

Damanpreet Kaur

Research Scholar

Functional and Renewable Energy Materials Laboratory (FREM Lab)

Department of Physics

Indian Institute of Technology Ropar, Rupnagar, Punjab, 140001, India

Researchgate: <https://www.researchgate.net/profile/Damanpreet-Kaur-8>

Google Scholar: <https://scholar.google.com/citations?user=QQzzFp4AAAAJ&hl=en>

Email: 2018phz0010@iitrpr.ac.in & damanpreetkaur92@yahoo.com

ORCID: 0000-0002-9788-3211

Date of Birth: December 2, 1992

RESEARCH INTEREST

- Ultra-wide band gap materials
- Synthesis and characterization of UWBG thin films, especially Ga₂O₃
- Photodetectors
- High power devices
- High performance sensors
- Physical Vapor Deposition techniques

EDUCATION

Doctor of Philosophy | Physics

January 19 – Present

Dissertation: Strategies towards Realization of High Performance Solar-blind

Photodetectors based on Gallium Oxide Thin Films

Indian Institute of Technology Ropar, India

Performance/CGPA: 9.55

Master of Science (Honour School) | Physics (2014-2016)

Dept. of Physics, Panjab University, Chandigarh, India **Performance/Percentage: 77.25%**

Bachelor of Science (Honour School) | Physics (2011-2014)

Dept. of Physics, Panjab University, Chandigarh, India **Performance/Percentage: 82.2%**

ACADEMIC ACHIEVEMENTS

- Qualified national exams GATE Physics in 2017, CSIR UGC NET (LS) in 2018
- Secured 2nd position in SARANSH: 2022 Thesis Presentation Competition organized by INYAS, India
- First prize in poster presentation in ISSMD-2020, organized by NIT Jalandhar.
- First prize in Dare2Dream4.0 competition organized by DRDO.

RESEARCH EXPERIENCE AND TECHNICAL SKILLS

- Expertise in synthesis of oxides through sputtering and other PVD methods
- Experience in thin film process development

- Expertise in vacuum equipment troubleshooting
- Other methods known: spin coating, chemical bath deposition, chemical vapour deposition
- Expertise in device fabrication: photodetector, in-house prototype fabrication
- Equipment handling experience: Keithley, Bentham PVE 300 and TMc 300, High-performance photodetector measurement with optical chopper interface with an oscilloscope, NANOMAGNETICS INSTRUMENTS ezHEMS (Hall effect set up)
- Characterization tools known: Raman and PL spectroscopy, XRD, XPS and UPS, KPFM with hands-on experience in SEM, AFM, and UV-Vis-NIR spectroscopy
- Expertise in Data Analysis Software: MS Office, Origin, XPS Peak fit, Advantage, Gatan Microscopy Suite, Gwyddion, ImageJ, AutoCAD, VESTA, EagleCAD

OTHER COMPETENCIES

- Confident in taking independent initiatives for research activities
- Proficient team player – can work and co-ordinate within a group
- Willing to take new challenges
- Curiosity and ability to learn new skills
- Leadership skills: Guided five master's students for their master thesis projects

TEACHING EXPERIENCE

Teaching Assistant at IIT Ropar

- Jul – Dec 2022 TA for PH510 (Physics Lab – II (Optics)) – (Lab Course)
- Jul 2021 – Jul 2022 TA for PH101 – Physics for Engineering (Theory Course)
- Jun – Jul 2021 TA for PH420 – Physics (CMP) Lab -I (Lab Course)
- Jan – May 2021 TA for PH452 – Physics of Materials (Theory Course)
- Jul – Dec 2020 TA for PH512 – Statistical Mechanics (Theory Course)
- Jan – May 2020 TA for PH452 – Physics of Materials (Theory Course)
- Jul – Dec 2019 TA for PH101 – Physics Lab for Engineers (Lab Course)